NUMERICAL METHODOLOGIES FOR MODELLING THE KEY ASPECTS RELATED TO FLOW AND GEOMETRY IN EXTERNAL GEAR MACHINES

A Dissertation

Submitted to the Faculty

of

Purdue University

by

Rituraj

In Partial Fulfillment of the

Requirements for the Degree

of

Doctor of Philosophy

May 2020

Purdue University

West Lafayette, Indiana

THE PURDUE UNIVERSITY GRADUATE SCHOOL
STATEMENT OF DISSERTATION APPROVAL

Dr. Andrea Vacca, Chair

School of Mechanical Engineering

Dr. Arezoo Ardekani

School of Mechanical Engineering

Dr. John Lumkes

School of Agricultural and Biological Engineering

Dr. Carlo Scalo

School of Mechanical Engineering

Approved by:

Dr. Nicole Key

Head of the School Graduate Program

To my parents

ACKNOWLEDGMENTS

First of all, I would like to thank my advisor Prof. Andrea Vacca for providing me the opportunity to pursue my PhD under his supervision. He has been a constant source of inspiration, motivation and guidance throughout the duration of my stay at Purdue. Several advice from him will stay with me forever. I would also like to express my great appreciation to all the professors that I interacted with during my research and coursework. Their guidance and suggestions were of significant help during my PhD. Moreover, I am thankful to all the industry collaborators I worked with, for helping me in gaining insights from their perspective.

I am extremely grateful to the lab mates at Maha who helped me during my PhD in several ways. Divya helped me in my initial months in getting used to the lab environment and her hard-working attitude motivated me in tough times. Tim's guidance was critical in my initial understanding of the HYGESim tool. Matteo's mischievous attitude ensured that the life in the lab was always fun and unpredictable. A number of technical and non-technical conversations with my desk-neighbors: Tom and Sangbeom significantly enriched my PhD experience. I am further grateful to have shared several unforgettable memories with Gautham, Srinath, Yash, Andrew, Meike, Xin, Annalisa, Federico and the Indian contingent of Harish, Shanmukh and Swarnava.

I would like to recognize the assistance that I received from the lab technician David with the test rigs and the staff: Susan, Connie and Deb with several administrative tasks.

Finally, I want to thank my parents for their endless love and unconditional support in my every decision.

TABLE OF CONTENTS

Page

LIST OF TABLES

LIST OF FIGURES

Figure Page

SYMBOLS

A	Area of the flow
a	Index that controls the transition from Newtonian plateau to the power-law region
b	Gear face width
b_b	Width of the journal bearing
C_f	Flow coefficient
$\angle C$	Angular span of the casing
c	Radial clearance at the journal bearing
c_p	Specific heat of the fluid
D	Pipe diameter
d_o	Orifice diameter
d	Gear diameter
e	Eccentricity of shaft from casing's center, eccentricity of shaft/journal from bearing center
E	Modulus of elasticity
Eu	Euler number
F, f	Force
F_{cp}	Ratio of Couette and Poiseuille components for flow between parallel surfaces
F, f	Unknown functions
$\dot{H}$	Enthalpy flow rate
h	Height of the gap
i, j	Iterators
K	Bulk modulus
K_L, K_{or}	Loss coefficient

k	Flow consistency index
L	Length of the gap
l	Thickness of the orifice
L_t	Equivalent length of the gap
M	Moment (Torque)
m	Mass
n	Power law (flow behavior) index
N	Number of resistances
N_r	Shaft speed in RPM
O_B	Center of the bearing
O_C	Center of the casing
O_G	Center of the gear
O_J	Center of the journal
O_S	Center of the shaft
P	Power
p	Pressure
Q	Volumetric flow rate
$\dot{Q}$	Heat flow rate
q''	Heat flux
R, r	Radius
$\mathcal{R}$	Flow resistance
Re	Reynolds number
Re_3	Slatter Reynolds number
r_d	Drain radius
r_g	Gear outer radius
r_p	Pitch circle radius of the gear
r_r	Root radius of the gear
R_c	Radius of the casing
r_C	Distance of tooth tip from casing center

r_S	Distance of tooth tip from shaft center
r_s	Radius of the shaft
T	Temperature
t	Time
U	Journal speed
u	Internal energy
V	Volume
V_D	Displacement of the EGM
v	Flow velocity
v	Velocity of the tooth tip
w_z	Load per unit length
x, y	Cartesian coordinates
y^+	Dimensionless distance from the wall
z	Number of teeth in a gear

Greek letters

α	Pressure angle
α_1	Pressure-viscosity coefficient
β	Orifice diameter ratio (d/D)
γ	Limiting shear stress proportionality constant
$\dot{\gamma}$	Shear rate
δ	Conicity error
δ_1, δ_2	Roughness amplitudes of surfaces
ϵ	Concentricity error (Chapter 5), Journal bearing eccentricity ratio (Chapter 7)
ϵ_h	Parameter in Pellegri et. al.'s leakage flow model
η_v	Volumetric efficiency
η_{hm}	Hydro-mechanical efficiency
θ	Angle of rotation
θ_S	Angular position of tooth tip from from $\vec{\epsilon}$

κ	Curvature
λ_n	Natural time constant (inverse of the shear rate at which power law region starts)
μ	Viscosity
μ_0	Zero shear rate viscosity (Chapter 3), viscosity at 0 bar pressure (Chapter 7)
μ_∞	Infinite shear rate viscosity
μ_r	Viscosity ratio
μ_f	Friction coefficient
ν	Kinematic viscosity
ν_p	Poisson's ratio
ξ	Dimensionless coordinate in gap height direction
Π	Dimensionless number
ρ	Density
σ	Composite RMS roughness
σ_1, σ_2	Standard deviations of δ_1, δ_2
τ	Shear stress
τ_w	Wall shear stress
ϕ	angular coordinate
ϕ_f, ϕ_{fs}, ϕ_{fp}	Shear stress factors
Ω	Area
ω	Shaft speed

ABBREVIATIONS

CFD	Computational Fluid Dynamics
CV	Control Volume
DNS	Direct numerical simulations
EGM	External Gear Machine
EHL	Elastohydrodynamic lubrication
RANS	Reynolds Averaged Navier-Stokes
TSV	Tooth Space Volume

ABSTRACT

Rituraj, PhD, Purdue University, May 2020. Numerical Methodologies for Modelling the Key Aspects Related to Flow and Geometry in External Gear Machines. Major Professor: Andrea Vacca, School of Mechanical Engineering.

External gear machines (EGMs) are used in a variety of industries ranging from fluid power machinery to fluid handling systems and fuel injection applications. Energy efficiency requirements and new trends in hydraulic technology necessitate the development of novel EGMs optimized for efficiency and reliability in all of these applications. A crucial piece in the novel EGM development process is a numerical model that can simulate the operation of EGM and predict its volumetric and hydro-mechanical performance.

The EGM simulation models developed in the past have focused mostly on the challenges related to the modeling of the theoretical behavior and elementary fluid dynamics, and determining appropriate modeling schemes. Key aspects related to the flow and geometry are either considered in a simplified manner or not considered at all. In particular, the current simulation models assume the fluid to be Newtonian and the leakage flows to be laminar. However, EGMs working in fluid handling applications operate with non-Newtonian fluids. Further, in fuel injection applications, due to low fluid viscosity and high operating speed, the internal leakage flows may not remain laminar.

With respect to the geometric aspects, the gears in EGMs are prone to manufacturing errors that are not accounted by any simulation model. In addition, there is no method available in the literature for accurately modeling the leakage flows through curve-constricted geometries in EGMs. Further, the goal of current simulation tools is related to the prediction of the volumetric performance of EGMs. However, an equally important characteristic, hydro-mechanical performance, is often ignored. Fi-

nally, the energy flow during EGM operation can result in the variation of the fluid temperature. Thus, the isothermal assumption of current simulation tools is another major limitation.

The work presented in this dissertation is focused on developing numerical methodologies for the modeling of EGMs that addresses all the aforementioned limitations of the current models. In this work, techniques for evaluating non-Newtonian internal flows in EGMs is developed to permit an accurate modelling of EGMs working with non-Newtonian fluids. For fuel injection EGMs, flow regime at the tooth tips of the gears is investigated and it is shown that the flow becomes turbulent for such EGMs. A methodology for modeling this turbulent flow is proposed and its impact on the performance of EGMs is described. To include gear manufacturing errors in the simulation model, numerical techniques are developed for modeling the effects of two common gear manufacturing errors: conicity and concentricity. These two errors are shown to have an opposite impact on the volumetric efficiency of the EGM. For the evaluation of flows through curve-constricted leakage paths in EGMs, a novel flow model is developed in this work that is applicable for a wide range of geometry and flow conditions. Modeling of the hydro-mechanical efficiency of EGMs is accomplished by developing methodologies for the evaluation of torque losses at key interfaces. Finally, to account for the thermal effects in EGMs, a thermal model is developed to predict the temperature distribution in the EGM and its impact on the EGM performance.

To validate the numerical methodologies developed in this work, several experiments are conducted on commercial gear pumps as well as on a custom apparatus designed and manufactured in the course of this research work. The results from the experiments are found to match those obtained from the simulations which indicates the validity of the methodologies developed in this work.

These numerical methodologies are based on the lumped parameter approach to allow the coupling with mechanical models for gear micromotion and permit fast

computations so that the model can be used in optimization algorithms to develop energy efficient and reliable EGMs.

The methodologies described in the dissertation are useful for accurate analysis of a variety of EGMs working with different types of fluids and at wide range of operating conditions. This capability will be valuable for pump designers in developing novel better performing EGM designs optimized for various applications.

1. INTRODUCTION

External gear machines (EGMs) are one of the most popular positive displacement machines. They are compact, robust, inexpensive and easy to manufacture. Due to these advantages, they are used in a wide range of applications. In industrial fluid power applications (e.g. hydraulic press and forming) and mobile fluid power applications (e.g. agricultural, mining and construction equipment), EGMs are used in the transmission of power from engines to the actuators. In automotive and aerospace applications, they are used as fuel injection devices to supply the fuel to IC/jet engines. Moreover, in vehicles, EGMs are often used in lubrication systems and all wheel drive systems. Finally, in chemical and food processing industries, EGMs are used for dosing, filling, extrusion and other fluid handling purposes.

1.1 Construction and principle of operation of EGMs

EGMs consist of two meshed external gears which are surrounded on the radial side by the casing and on axial sides by front and end covers (Figure 1.1). The shafts of the gears are supported by bearings (journal or needle-roller type) present in the front and the end cover. For EGMs operating at very high pressures ($>$ 200 bar), floating elements (called bushings) are added on each side of the gears to minimize the gap on the axial side of the gears [1]. Such units are called pressure compensated EGMs (Figure 1.2).

The fluid displacing action of EGMs is simple and can be understood via Figure 1.3. The volume between consecutive teeth of a gear forms the displacement chamber. In this dissertation, this volume is referred to as the tooth space volume (TSV). As the gears rotate, the teeth of the gears enter and leave the meshing zone. When the teeth leave the meshing zone, the volume between the teeth increases leading to the

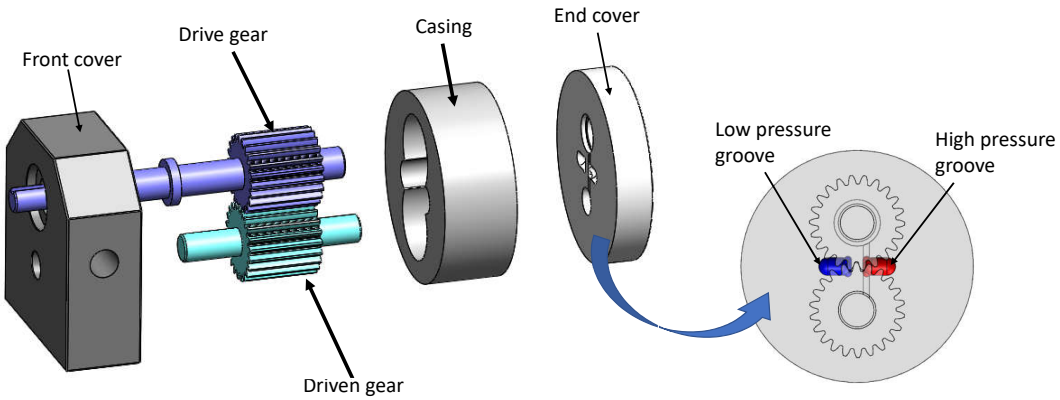

Figure 1.1. Exploded view of a reference external gear machine (E1 in Table 1.1). Relief grooves on the end cover are shown in the front view on the right for clarity

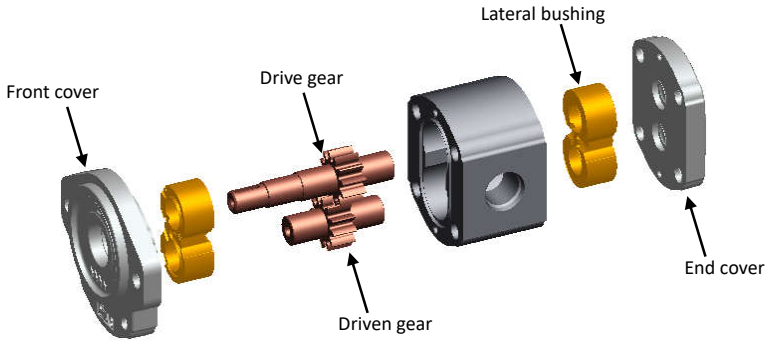

Figure 1.2. Exploded view of a pressure compensated external gear machine

suction of the fluid from the inlet. The fluid between the gear teeth is carried from the inlet side to the outlet side along gears' periphery. When the teeth enter the meshing zone, the volume between the teeth decreases leading to the delivery of the fluid to the outlet.

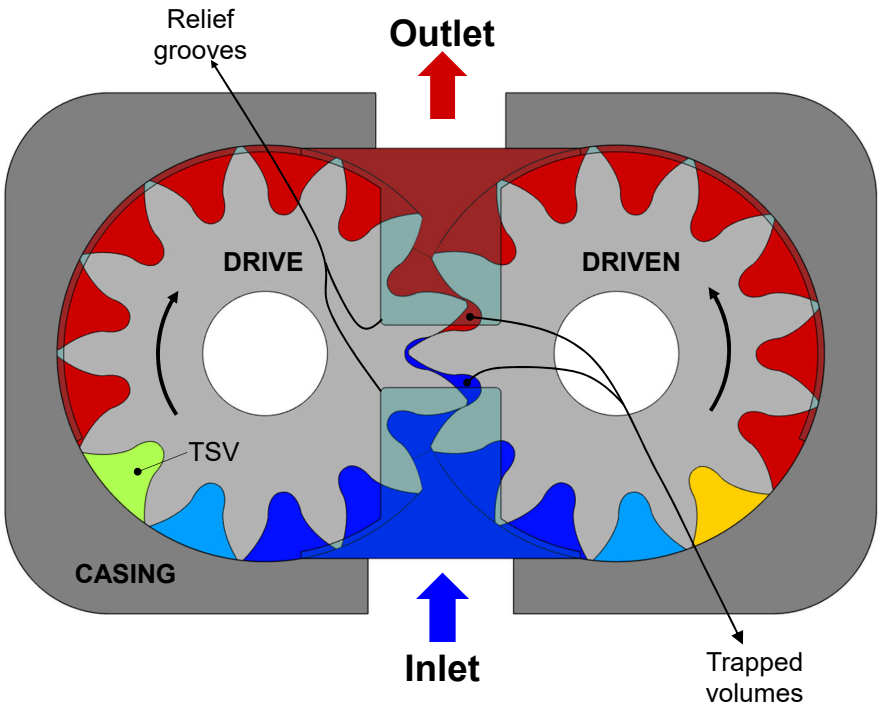

Figure 1.3. Principle of operation of EGMs.

In the meshing zone, the fluid in the TSV is trapped between the gear teeth as shown in Figure 1.3. To ensure that the suction and delivery of the fluid occurs even in this configuration, relief grooves are provided on the front and the end covers as shown in Figure 1.1. In pressure compensated EGMs, these grooves are present on the floating elements. These grooves realize the flow connections between the trapped TSVs and inlet/outlet of the EGM. A proper profile of such grooves permits a smooth transition for the displacement chambers from high pressure to low pressure during the meshing region, and avoids the occurrence of internal pressure spikes and localized cavitation.

When the EGM works as a pump, a mechanical energy source provides rotary motion to the drive shaft. The gears rotate in response and the working fluid is sucked from the low pressure inlet port and is delivered to the high pressure delivery port. In contrast, when the machine works as a motor, the pressure difference between

the inlet and the outlet ports drives the gears and the rotational mechanical energy at the drive shaft is then used to actuate a rotary load. In this dissertation, to avoid any confusion, all the methodologies and results are presented considering EGMs working as a pump. However, these methodologies are applicable for EGMs working as a motor too.

1.2 Energy losses in EGMs

The operation of EGMs involves relative motion between the gears and the casing (and the bushings in pressure compensated EGMs). To avoid contact between these parts, the EGMs are manufactured such that there are clearances between them along both the radial and the axial direction (an exaggerated clearance between the gear tooth tip and the casing can be seen in Figure 1.4). These clearances, however, become the source of energy losses in EGMs.

The clearances allow the working fluid to leak from the high pressure environment to the low pressure one, negatively affecting the volumetric efficiency of EGMs. The volumetric efficiency of a pump is defined as

$$\eta_v = \frac{Q_{actual}}{Q_{th}} = 1 - \frac{Q_{loss}}{Q_{th}} \tag{1.1}$$

where Q_{loss} is the volumetric loss due to leakage flows and Q_{th} is the theoretical amount of flow delivered at a given operating speed, N_r:

$$Q_{th} = V_D N_r \tag{1.2}$$

V_D is the displacement of the pump (defined as the amount of fluid displaced per shaft revolution).

The leakage flow is categorized into three groups. The leakage flow between the adjacent TSVs through the clearance at the tooth tip is referred to as the tooth tip leakage. The leakage flow between the adjacent TSVs through the axial gap is referred to as the lateral leakage. The axial gap also allows the fluid to leak from the TSVs

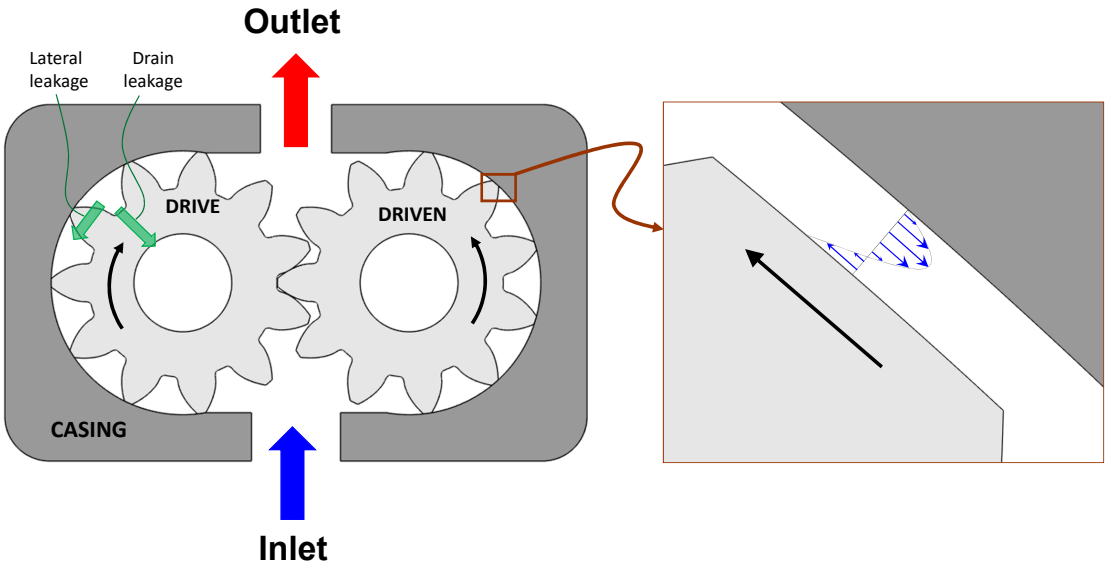

Figure 1.4. Leakages in EGMs (in pumping mode). Inset shows the clearance at the tooth tip and the typical flow profile of tooth tip leakage. The directions of lateral and drain leakages are shown via green arrows.

to the shafts of the gears. This portion of the leakage is called drain leakage as this flow is used to flush the bearings that support the shafts.

The leakage flows through the clearances also give rise to the friction forces on the surfaces involved. Moreover, as the gears mesh, relative motion between the teeth surfaces of drive and driven gears too result in friction. In the pumping operation, to overcome these friction forces, an additional amount of torque is required at the pump shaft. This torque is not doing any useful work and hence is referred to as torque loss (M_{loss}). Existence of torque loss leads to the definition of hydro-mechanical (or torque) efficiency (for pumps):

$$\eta_{hm} = \frac{M_{th}}{M_{actual}} = \frac{M_{th}}{M_{th} + M_{loss}} \tag{1.3}$$

Here, M_{th} is the torque theoretically required to displace the fluid against a given pressure difference Δp:

$$M_{th} = V_D \Delta p \tag{1.4}$$

The total efficiency of the EGM is

$$\eta = \eta_v \cdot \eta_{hm} \tag{1.5}$$

1.3 Gear micromotion

Due to the difference in the pressure at the inlet and outlet ports of the EGM, the gears are subject to radial forces that push the gears towards the low pressure side (Figure 1.5). In response to these forces, the clearances between the gear shafts and the bearings supporting them allow changes in the radial position of the gears on the order of few microns. This phenomenon is referred to as "gear micromotion". Gear micromotion has an important implication on the clearance at the tooth tips of the gears. As shown in Figure 1.6, due to gear micromotion, the gap height at the tooth tip is high at certain locations and low at other locations. This phenomenon has a significant impact on the leakage flow and friction at the gear tooth tips and hence the efficiency of EGMs.

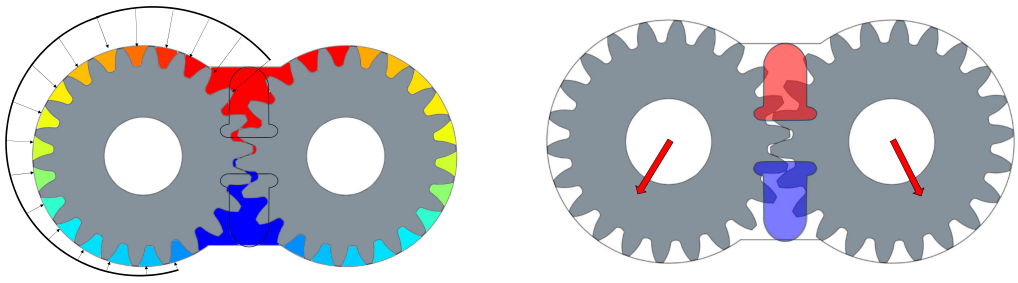

(a) Pressure forces acting on a gear. (b) Net force acting on both gears.

Figure 1.5. Illustration of pressure forces and net force on gears

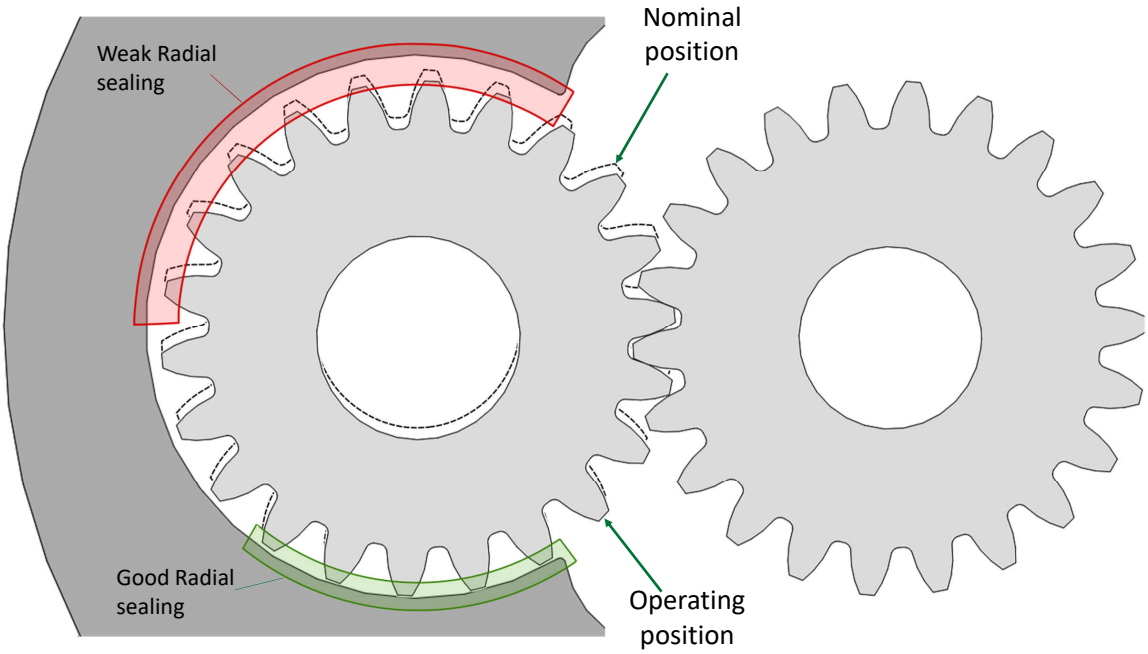

Figure 1.6. Gear micromotion and its impact on the sealing at the tooth tips

1.4 Research motivation

In 21st century, when the energy demands are at all time high [2], it is crucial to identify the sources of energy losses in all machines and develop technologies to minimize these losses. Like every machine, EGMs suffer from energy losses coming from a variety of sources as described in section 1.2. Despite this drawback, EGMs' applications remain widespread due to a number of advantages that they bring (reliability, inexpensiveness, compactness, etc.). However, there is a push in the industry towards the development of novel EGMs designs with minimal losses. Designing such energy efficient EGMs is a challenging problem since often there is a trade-off between the energy efficiency and other advantages such as reliability and low cost. Current EGM designs are based on simplified numerical procedures and a lot of empirical tests which limits the scope of obtaining the true optimal design as well as increases the cost of the design exploration process. To develop optimal energy efficient EGMs in a

cost-effective manner, accurate simulation models are necessary that can be capable of analyzing the operation of EGMs and predicting their efficiency.

Moreover, new technology trends too require expertise in the designing of novel EGMs that can operate reliably with different working fluids and at different operating conditions. For instance, the latest trend towards the electrification of mobile equipment requires EGMs coupled with electric motors. To design efficient and reliable units of such type, numerical models are required that can be used in virtual prototyping and developing EGM designs optimized for high performance.

In recent years, several numerical tools for modelling the behavior of EGMs have have been developed. However, all of them are isothermal models focused on the prediction of volumetric efficiency of traditional EGMs operating in the fluid power applications. They do not consider the effects of different operating fluids (present in fluid handling and fuel injection applications), manufacturing errors, hydro-mechanical losses and localized temperature variations.

To highlight and later address these limitations, in this research, five reference EGMs are selected that cover a wide range of applications. The details of these EGMs are presented in Table 1.1.

Table 1.1.
Reference EGMs selected for numerical modelling in this work. The identifiers are used for refer to these EGMs throughout the dissertation.

Identifier	Name/Description	Working fluid	Applications
E1	Zenith pump	Non-Newtonian fluids	Fluid handling
E2	Aero fuel pump	Fuel	Fuel injection
E3	Concentric GC pump	Mineral oil	Mobile equipment
E4	Continuous contact helical gear pump	Mineral oil	Industrial equipment
E5	Casappa PHP20 pump	Mineral oil	Mobile equipment

Current EGM simulation models make certain assumptions related to key flow and geometric aspects that inhibits accurate modelling of these EGMs. These flow and geometric aspects and the limitations of current models in each aspect are explained below:

A1. **Nature of fluid**: In fluid power applications, the operating fluids behave as Newtonian fluids. However, in chemical and food processing industries, EGMs like the Zenith pump (E1) have to work with fluids that are non-Newtonian i.e. their viscosity varies with shear rate.

The current simulation models consider the operating fluid to be Newtonian in nature and thus are unusable for simulating the operation of EGMs used in these industries. So, there is a need of a simulation tool that can model the operation of the EGMs working with non-Newtonian fluids.

A2. **Leakage flow regime**: The gap heights at the tooth tips of the gears (Figure 1.4) are typically on the order of few microns. At such small length scales, the flow typically stays laminar. However, EGMs used in fuel injection systems, operate at very high speeds. Moreover, the operating fluid, fuel, has very low viscosity. Owing to these factors, the flow at the tooth tip can become turbulent.

The current simulation models assume that this flow is always laminar in nature and hence fail to accurately predict the volumetric efficiency for these EGMs. Thus, a proper leakage flow model for EGMs needs to be developed that accounts for the turbulence of flow at the tooth tip.

A3. **Manufacturing errors**: The gears in EGMs suffer from certain common manufacturing errors. These errors directly impact the geometry of the clearance between the gears and the casing and hence the volumetric efficiency of the EGMs.

The current simulation models ignore these manufacturing errors and hence their applicability is limited to the theoretical gear geometries. Thus, to allow

an accurate performance prediction of actual EGMs, a simulation model needs to developed that can include the effects of these manufacturing errors.

A4. **Leakage flow geometry**: For a typical EGM, the tooth tip is a planar surface parallel to the casing's internal surface (Figure 1.4). However, EGMs with circular arc gear profiles, namely continuous-contact type EGMs [3], are becoming increasingly popular due to their low noise emission. Instead of flat surface, the tooth tip of these EGMs are circular.

The current simulation models provide only an approximate method to model the leakage flow through such curved geometries. Thus, a technique of modelling the flow through such geometries needs to be developed to permit an accurate prediction of the efficiency of EGMs with non-traditional gear tooth.

A5. **Frictional losses**: During the operation of EGMs, the friction between the internal components result in the loss of hydro-mechanical performance of these units.

A majority of the current simulation models do not consider these losses at all. Few models that do consider these losses have key limitations that hinder their accuracy. Thus, a simulation model needs to be developed that incorporates proper methodologies for the modelling of all the sources of frictional losses in EGM to allow an accurate prediction of the EGM hydro-mechanical efficiency.

A6. **Fluid Temperature**: During the operation of EGMs, due to compression /expansion of the fluid and power losses, the fluid temperature varies significantly in the EGM (especially in low efficiency operating conditions). Fluid temperature effects the fluid properties, especially viscosity, that in turn impacts the volumetric and frictional losses in the EGM.

The current simulation models assume constant fluid temperature in the EGM which limits their accuracy. Thus, to allow an accurate prediction of the EGM

performance, numerical techniques needs to be developed to model the temperature distribution in EGMs.

It is to be noted that going forward in this dissertation, these six aspects are always referred to by their identifiers A1 through A6.

1.5 Research objectives

The objective of the work presented in this dissertation is to develop and validate the numerical techniques to model the operation of EGMs with focus on key aspects of fluid flow and geometry (A1 through A6) that significantly influence the performance of the reference EGMs. In particular, following are the research goals of this work:

1. To develop a model that can accurately simulate the operation of EGMs working with non-Newtonian fluids.

2. To investigate the flow regime at the tooth tips of EGMs and develop a numerical technique that can predict the leakage flow for a variety of flow conditions.

3. To investigate the effects of manufacturing errors on the performance of EGMs by developing a numerical technique that includes these effects in the modelling of EGMs.

4. To develop a leakage flow model for EGMs with curved tooth tip geometry.

5. To develop the methodology for the evaluation of frictional losses in EGMs thereby, allowing the prediction of the hydro-mechanical efficiency of these machines.

6. To develop the thermal model of the EGM allowing the prediction of fluid temperature in the EGMs.

1.6 State of the art

In this section, a brief summary of past works done towards analyzing and modelling the operation of EGMs is presented.

The first published work related to the analysis of the performance of EGMs was the one done by Beacham [4] via graphical methods. Later, researchers studied the basics of EGM operation via theoretical approaches. Bonacini [5] used energy method to develop an analytical expression for the theoretical flow of EGMs. Ivantysyn and Ivantysynova [6] and Manring and Kasaragadda [7] proposed similar models for the theoretical flow of EGMs.

First efforts towards modelling the real behavior of EGMs were done by Foster et al. and Manco and Nervegna. Foster et al. [8] developed a mathematical model to predict the tooth space pressure and outlet flow of EGMs. The model considered the leakage flow at the tooth tip but it assumed the connection of the trapped volume to inlet/outlet to be ideal. That is, the TSV was assumed to be fully open to the relief groove when it is trapped between the lines of contact of the gears. Manco and Nervegna [9] were the first researchers to propose a lumped parameter based simulation method of modeling the dynamics of fluid flow in EGMs. This method used a linear relation to model the flow from the trapped TSV to the ports and neglected the flow at the axial sides of gears. Despite these simplifications, the results showed a fair match with the experiments. Realizing the potential of the lumped parameter approach in accurate modeling of EGMs, researchers developed numerous models with various improvements over the original approach.

Eaton et al. [10, 11] and Borghi et al. [12, 13] developed models that focused on predicting TSV pressure in the meshing zone and the impact of cavitation on it.

Preliminary efforts to incorporate the radial forces on gears and associated gear micromotion in the lumped parameter based models were done by Zardin and Borghi [14], Falfari and Pelloni [15], and Casoli et al. [16]. Mucchi et al. published a set of papers on elastodynamic analysis of gear pumps where they developed a model

that integrated the dynamics of gear motion with the lumped parameter based fluid dynamic model [17–19]. The model incorporated the effects of tooth profile errors on the dynamic behavior of EGMs. Later, they also extended the model to helical gears [20].

In the past decade, Dr. Vacca and his research group have developed their own lumped parameter based EGM simulation tool called HYGESim (HYdraulic GEar machines Simulator) [21]. This simulation tool has successfully demonstrated an active coupling of the fluid dynamic model (based on lumped parameter approach) and the mechanical model for micromotion of the gears. Via experiments, the coupled model has proved to accurately predict the volumetric efficiency, port flow pulsation, gear radial micromotion and case wear due to the break-in process. In recent years, further advancements have been made on the tool. The dynamics of cavitation phenomenon has been developed and implemented in this tool by Zhou and Vacca [22] and Shah et al. [23]. New capabilities have been added in the tool to permit the simulation of both traditional helical gear pumps [24] and continuous-contact helical gear pumps [25]. The success of HYGESim simulation tool has allowed it to be used in various optimization studies [26, 27] to develop novel EGM designs.

With significant advancements in computational power, CFD based methods to model the displacing action of EGMs have become popular. The commercial tool Fluent has been used to develop 2D CFD models by Strasser [28] to study the mixing of flow in EGMs and by Castilla et al. to investigate the nature of flow at the suction region [29] accounting for the effects of cavitation [30]. Castilla et al. later demonstrated a 3D CFD model of EGM using OpenFOAM libraries [31,32]. Recently, another commercial software PumpLinx [33] has become a popular tool for modelling and detailed flow analysis of EGMs [34, 35].

The biggest downside of CFD based models is the high simulation setup and execution time. The computational expensiveness comes from the high number of grid points required to capture the complexity of the geometry of fluid domain (especially the small gaps between the gears and the casing). This renders CFD based methods

unsuitable for design and optimization algorithms. In contrast, lumped parameter based models are very fast and yet pretty accurate and reliable as demonstrated by multiple researchers mentioned above. Many articles can been found in the literature that show using lumped parameter based models in optimization algorithms [26, 27, 36, 37], whereas instances of using CFD models in optimization algorithms are rare.

Moreover, CFD based methods do not model the radial micromotion of the gears. As discussed in section 1.3, this phenomenon significantly impacts the gaps at the tooth tips hence influencing the efficiency of EGMs. Lumped parameter based models, on the contrary, can easily be coupled with the mechanical models that evaluate the gear micromotion. Furthermore, the fluid mesh in CFD based methods cannot have discontinuities. This make it impossible to simulate the contact between the gears. For these reasons, this dissertation is focused on investigation and development of numerical techniques for lumped parameter based modelling of EGMs.

1.7 Structure of the dissertation

The dissertation is divided into 10 chapters (including this introduction section):

In Chapter 2, an overview of the simulation tool, HYGESim is provided. The dissertation uses this simulation tool to investigate the limitations of the current modelling approach and the numerical techniques developed in this dissertation are integrated with this tool.

Chapter 3 focuses on the development and validation of the numerical model for EGMs working with non-Newtonian fluids (Aspect A1).

In Chapter 4, an investigation of the nature of flow at the tooth tip is conducted and methods for modelling of the leakage flow in turbulent flow conditions is presented (Aspect A2).

Chapter 5 describes the numerical techniques developed to model the effects of common gear manufacturing errors (Aspect A3). The technique is validated via a

set of experiments and is used to analyze the effect of manufacturing errors on the performance of EGMs.

Chapter 6 deals with the modelling of tooth tip leakage flow for gear machines with curved tooth tip geometry (Aspect A4). The model is validated via experiments on a specialized test apparatus.

In Chapter 7, the methodology for the evaluation of frictional losses in EGMs is developed and validated (Aspect A5).

Chapter 8 focuses on the development and validation of the thermal model for EGMs (Aspect A6).

Finally, Chapter 9 provides a brief summary of the work presented in the dissertation, whereas, Chapter 10 provides recommendations on future research directions.

2. OVERVIEW OF HYGESIM SIMULATION TOOL

The numerical techniques developed in this work to accomplish the goals in section 1.5 will be presented in Chapters 3 to 8. However, since those techniques are integrated in the HYGESim tool, it is imperative to provide a description of this simulation tool before the aforementioned numerical techniques. It is important to note that the version of HYGESim tool described here is the one that existed before the numerical techniques developed in this research work were integrated.

HYGESim (HYdraulic GEar machines Simulator) is the EGM simulation tool developed by Dr. Vacca's research team in past decade. HYGESim consists of multiple modules, each handling a particular aspect of gear machine modelling (Figure 2.1). The research work presented in this dissertation mostly interacts with the Fluid Dynamic Module. Hence, a detailed description of this module is provided in the following section. A condensed description of other modules is provided in later sections to explain the whole simulation framework and the interaction between different modules.

2.1 Fluid Dynamic Module

The Fluid Dynamic Module is the central module in HYGESim. It uses a lumped parameter based approach to determine the pressure in all the control volumes and the flow between the control volumes. Figure 2.2 shows various control volumes (CVs) in an EGM. The CVs corresponding to the tooth space volumes (TSVs) are identified as $V_{1,j}$ for the drive gear and $V_{2,j}$ for the driven gear where $j = 1, 2$, etc. increasing in the direction of rotation of the gears. These two volumes pair, connected through gear backlash, work together in realizing the fluid displacing action. Apart from TSVs,

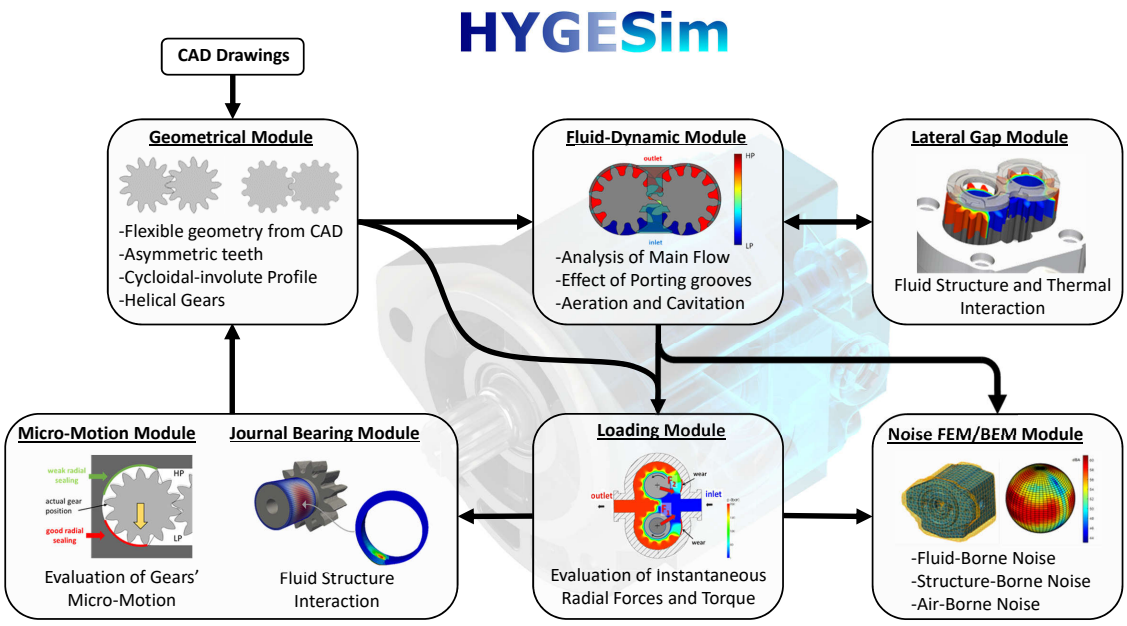

Figure 2.1. Modules in HYGESim simulation tool

the fluid volumes on both the inlet and the outlet side are considered as separate CVs too.

In each CV, the properties are assumed to be uniform and are dependent on time only. The pressure build up equation, which is derived from the conservation of mass law and the equation of state, is used to determine the pressure in each CV:

$$\frac{dp_j}{dt} = \frac{K}{V_j}\left[\sum Q_{in,j} - \sum Q_{out,j} - \left(\frac{dV_j}{dt}\right)\right] \tag{2.1}$$

The first two terms in the square brackets represent the flow coming into the CV and going out of the CV, respectively. The change in the volume of a CV also results in the change of the fluid pressure and the third term represents this volume change.

The flow connections between the CVs are modelled as either orifices or Couette-Poiseuille flow connections. The orifice connections are shown in Figure 2.3. FG represents the connection between a tooth space volume (TSV) of the drive gear and the corresponding TSV of the driven gear. LV represents the connection between

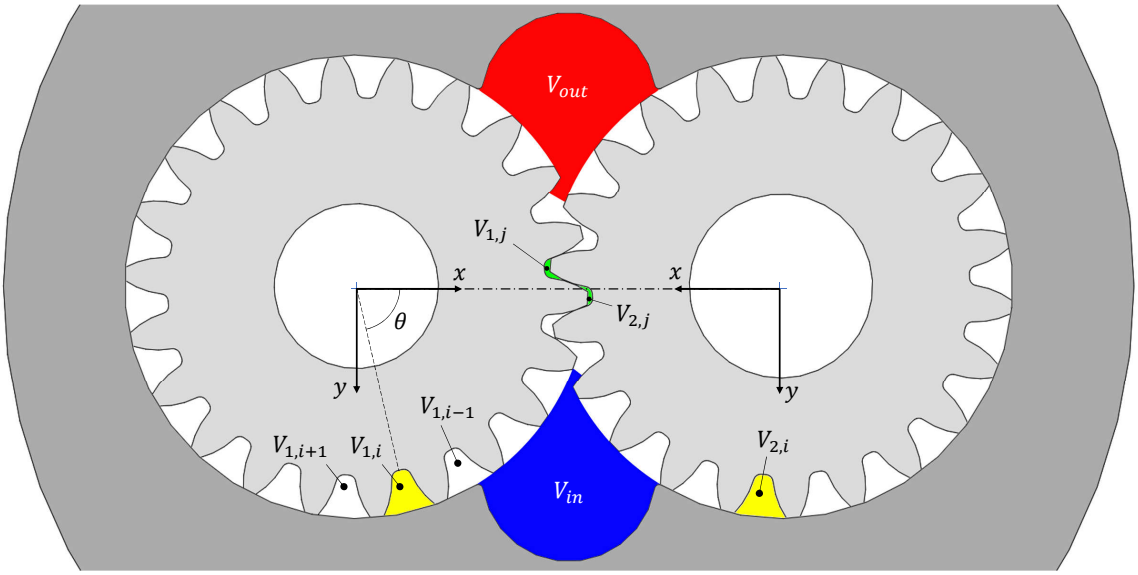

Figure 2.2. Fluid domain of EGM segregated into different control volumes

a TSV and the inlet volume. Similarly, HV represents the connection between a TSV and the outlet volume. FG, LV and HV connections are along the depth of the gears. In contrast, LG represents the connection between a TSV and the inlet volume via the low pressure grooves present on the lateral sides of the gears. Similarly, HG represents the connection between a TSV and the outlet volume via the high pressure grooves present on the lateral sides of the gears. The flow through these connections is modelled using the orifice equation:

$$Q_{i,j} = \text{sign}(p_i - p_j) \cdot C_f \cdot \Omega_{i,j} \cdot \sqrt{\frac{2 \cdot (p_i - p_j)}{\rho}} \tag{2.2}$$

Here the orifice flow coefficient C_f is dependent on flow Reynolds number as reported in [38].

In Figure 2.3, areas of some of the highlighted connections may seem too big to be regarded as orifices. Obviously, these areas increase from zero to maximum and

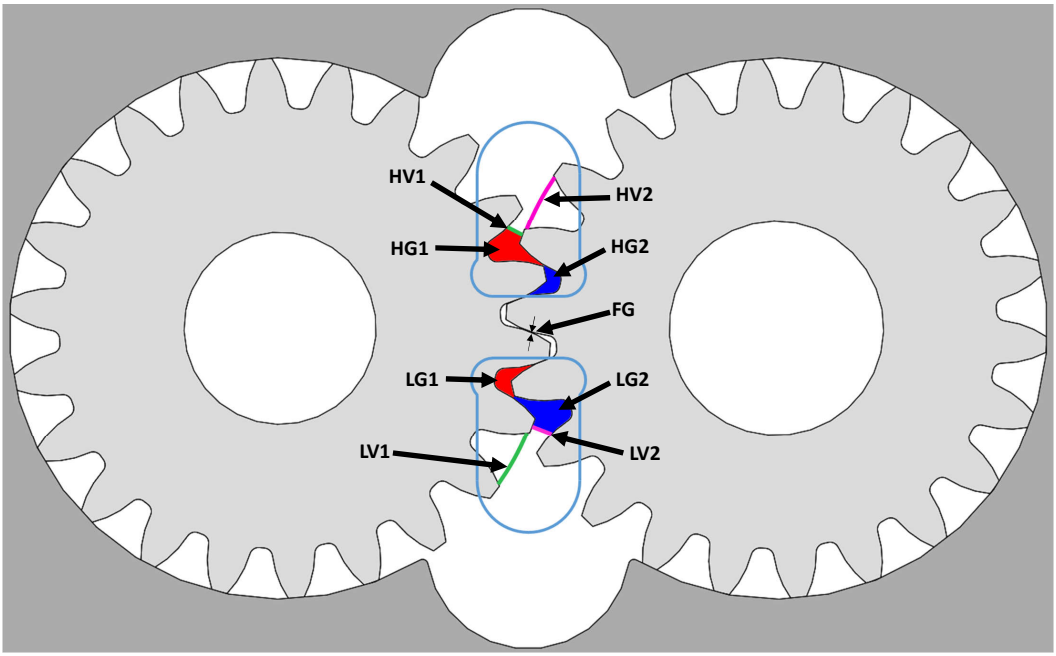

Figure 2.3. Connections between CVs modelled as orifices. HG and LG connections are highlighted through the trace of the high pressure and low pressure grooves (these grooves are shown in Figure 1.1)

then decrease from maximum to zero as the gears rotate. It is important to note that the orifice equation Eq. 2.2 comes into effect for a given orifice connecting two CVs only when the pressures in two CVs are different. This happens only when the area of the orifice is very small. If the area of the orifice is very big, the pressure in the two CVs would equalize instantaneously and the orifice equation will cease to apply.

The flow connection between adjacent tooth space volumes via the gap at the tooth tip (Figure 1.4) permits the flow due to the pressure difference between the two TSVs (Poiseuille flow) and the flow due to the relative motion of the tooth tip with respect to the casing (Couette flow). This flow is assumed to be laminar (this assumption is investigated later in this dissertation) and is modelled using the combined Couette-Poiseuille equation.

$$Q_{i,j} = \left[-\frac{h_{i,j}^3 \cdot (p_i - p_j)}{12\mu L} + \frac{\mathrm{v} h_{i,j}}{2} \right] \cdot b \tag{2.3}$$

The flows between adjacent TSVs (lateral leakage) and between TSVs and shaft (drain leakage) via the axial gap are approximated as 1D flows and modeled using combined Couette-Poiseuille equation and Poiseuille equation, respectively. To accurately model these flows, 2D CFD model is also available which forms a part of the Lateral Gap Module explained in section 2.5. However, as this dissertation is focused on developing computationally inexpensive simulation methods for design optimization purposes, the lateral and drain leakage flows are assumed to be 1D in this work.

If the fluid pressure falls below the saturation pressure, air bubbles are released in the fluid (aeration). Similarly when the fluid pressure falls below the vapor saturation pressure, vapor bubbles are generated (cavitation). The fluid aeration and cavitation effects are considered in Eq. 2.1, 2.2 and 2.3 by using effective fluid properties (bulk modulus, K, viscosity, μ and density, ρ) of the mixture of fluid, air and vapor. The details of the approach for determining the gas and vapor fraction in each CV is presented in [39].

2.2 Loading Module

After the Fluid Dynamic Module calculates the pressure in all CVs, the instantaneous forces acting on the gears in the radial plane are evaluated from the pressure distribution. The forces acting on each tooth space ($f_{x,i}, f_{y,i}$) are calculated by evaluating the product of the pressure inside the TSV and projection of the tooth space area in the Cartesian directions (Figure 2.4). These forces are then added to obtain the net force due to pressure, $\vec{F_p}$ on each gear:

$$F_{p,x} = \sum_{i}^{z} f_{x,i} \tag{2.4}$$

$$F_{p,y} = \sum_{i}^{z} f_{y,i} \tag{2.5}$$

From the information about the individual forces ($f_{x,i}, f_{y,i}$) and the line of action of these forces ((x_i, y_i), obtained from the Geometrical Module), the moment acting on each gear is calculated:

$$M = \sum_{i}^{z} f_{x,i} \cdot y_i - \sum_{i}^{z} f_{y,i} \cdot x_i \tag{2.6}$$

The moment on the driven gear is balanced by the moment due to the contact force between the gears acting along the line of action. The expression of contact force is

$$f_c = \frac{M_{driven}}{r_p \cos\alpha} \tag{2.7}$$

where r_p is the radius of the pitch circle of the gear and α is the drive pressure angle.

Thus, the net radial force acting on each gear is:

$$\vec{F_t} = \vec{F_p} + \vec{f_c} \tag{2.8}$$

The total torque at the drive shaft of the EGM, then, is the sum of the torque from fluid pressure (Eq. 2.6) and the torque from the contact force:

$$M_{shaft} = M_{drive} + f_c \cdot r_p \cos\alpha = M_{drive} + M_{driven} \tag{2.9}$$

A detailed description of the Loading Module (along with the Fluid Dynamic Module) can be found in [21].

2.3 Journal Bearing and Micromotion Module

For each gear, the journal bearing module calculates the eccentricity of the shaft with respect to the bearing from the knowledge of the net radial load and bearing geometry characteristics. This calculation is performed using a simplified approach of the mobility method [40] where the Ocvirk solution [41] is used for short-bearing configuration (width/diameter < 1) and Warner-Sommerfield solution [42] is used for

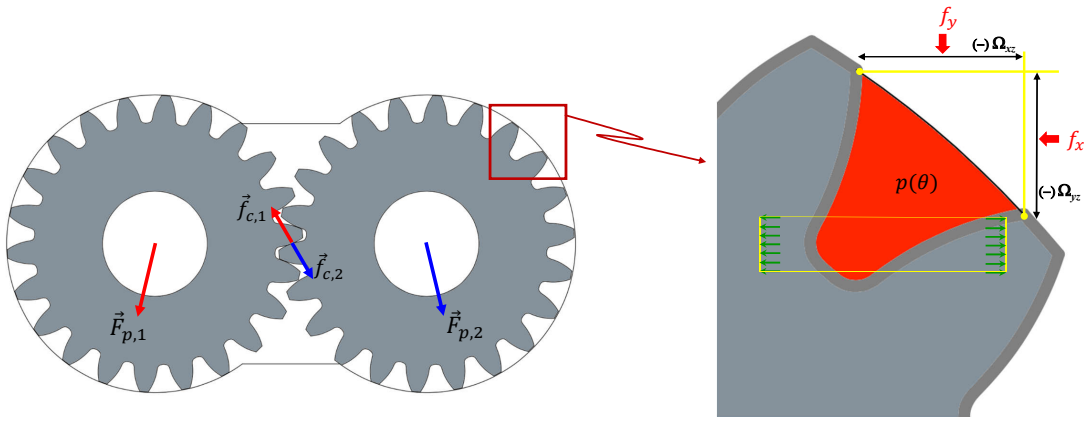

Figure 2.4. Net radial force acting on each gear. Image on right illustrates the evaluation of forces from pressure in a particular TSV. Ω_{yz} and Ω_{xz} are the projection areas of the CV in x and y directions, respectively

finite bearings (width/diameter > 1). From eccentricity of the shaft, new position of the gears is determined.

Alternate to this simple approach, a CFD model for journal bearing is also available. In the model, the fluid film in the journal bearing is discretized and Reynolds equation of lubrication [43] is solved for the pressure field. An iterative procedure is employed to obtain the journal eccentricity position that yields the pressure distribution in the film to balance the radial force on the gear. More details about this model can be found in [44].

2.4 Geometrical Module

Owing to the complexity of the geometry of EGMs, HYGESim has a dedicated module for the evaluation of the geometrical features required by other modules. This Geometrical Module uses the CAD drawings of the EGM or parametrized geometrical values as input. The algorithm in the Geometric Module then defines the morphology of each CV of the EGM and calculates its volume. This information is used in the

pressure build up equation (Eq. 2.1). The algorithm also calculates the hydraulic diameter and area of all the flow connections between different CVs. This information is used in determining the magnitude of the flow through these connections (Eq. 2.2). Finally, the algorithm evaluates the projection areas of the TSVs and their centroid locations which is used by the loading module in the calculation of pressure forces and moments acting on the gears (Eq. 2.6). For all these features, the algorithm also determines how they vary with the angular position of the gears and the location of the axes of the gears. The details of this algorithm is described in [45].

2.5 Lateral Gap Module

Lateral Gap Module is useful in the modelling of the axial compensation mechanism realized by the bushings in pressure compensated EGMs (Figure 1.2). In these EGMs, the lateral bushings are free to move and are balanced by the fluid pressure from the gear side and the casing side. The equilibrium position of the bushings is critical: if the bushing is too close to the gears, contact between the gears and bushing may occur resulting in high friction and wear. On the other hand, if the bushing is too far away from the gears, the lateral and drain leakages will become significant, reducing the volumetric efficiency of the EGM.

The Lateral Gap Module consists of multiple solvers coupled with each other. Fluid structure coupled solvers determine the pressure in the fluid domain and resulting elastic deformation in the solid domain. Fluid structure thermal coupled solvers determine temperature in the film and resulting thermoelastic deformation in the solid domain. Effects of mixed lubrication is included using an asperity contact model. Finally, axial micromotion of the gears and bushings is evaluated using the force balance solver. Detailed description of these solvers/models can be found in [46].

3. MODELLING EXTERNAL GEAR PUMPS OPERATING WITH NON-NEWTONIAN FLUIDS

In this chapter, the work done to achieve the first research goal (considering Aspect A1 in EGM modelling) is described. In particular, the methodology of modelling the operation of EGMs is described that accounts for the non-Newtonian nature of the working fluid.

In chemical and food processing industries, EGMs work in the pumping mode (hence called external gear pumps) for the purposes of fluid handling and transportation. The fluids in many of these applications are non-Newtonian with viscosity depending on the shear rate. The work in this dissertation particularly relates to the case of shear-thinning fluids, with typical viscosity profile shown in Figure 3.1. At low shear rates, the viscosity is constant and is referred to as zero shear rate viscosity μ_0. As the shear rate increases beyond a critical value, the viscosity starts to decrease following the power law $\mu = k(\dot{\gamma})^{n-1}$ where k and n are constant for a fluid ($n < 1$ for shear thinning). As the shear rate continues to increase, the viscosity slowly flattens out to a value called infinite shear rate viscosity μ_∞.

For external gear pumps operating with non-Newtonian fluids, apart from a patent on gap geometry recommendation [47], little modelling effort has been reported in literature. PumpLinx (a commercial CFD software) [33], has recently incorporated non-Newtonian capabilities in the simulation of gear pumps, but this software suffers from same limitations explained in section 1.6.

In the research work presented in this chapter, the lumped parameter modelling approach in HYGESim is extended to model the working of external gear pumps operating with non-Newtonian fluids. The developed model is validated against the results from a set of experiments conducted on the reference pump E1 (Table 1.1) with three different non-Newtonian fluids.

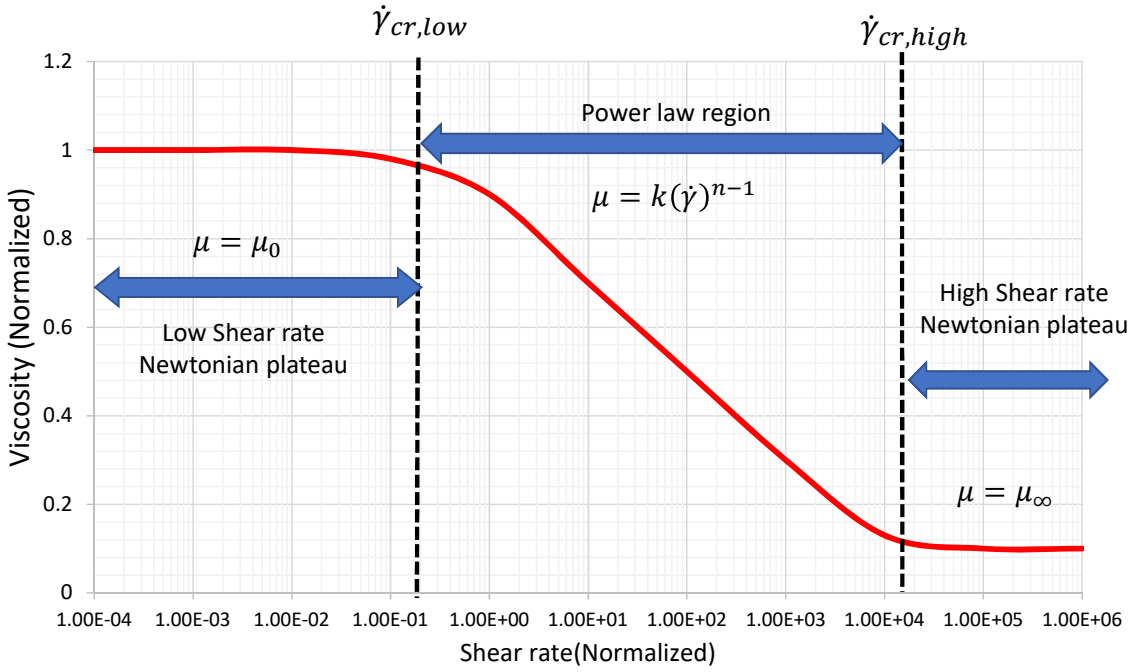

Figure 3.1. Viscosity shear rate behavior of a typical shear thinning fluid

3.1 Reference pump and fluids

The EGM used as reference in this study is Zenith B9000 external gear pump (E1 in Table 1.1). The construction of this pump is shown in Figure 1.1 and the geometric details of this pump is presented in Table 3.1. This pump is used in chemical industries where it operates with various non-Newtonian fluids like plastics, polymers, paints etc. [48]. The fluids used in this study are three different shear thinning fluids (zero shear rate viscosity varying from 5 Pa s to 100 Pa s). The identity of the fluids cannot be disclosed because of the confidentiality agreement with the industry supplying the fluids. For this reason, the fluids are referred to as fluid A, fluid B, and fluid C, fluid A being most viscous, fluid C being least viscous.

From the fluid properties provided by the industry and the mean shear rates at the internal flows (refer to Section 3.7 for more details), it is observed that the

Weissenberg number (Wi) for the flow is $Wi \approx 1$ [49]. This indicates that the non-Newtonian effects in the flow are significant during the EGM operation and thus, the flow dynamic equations for the modelling of internal flows needs to be revised.

Table 3.1.
Geometric parameters of the reference gear pump E1

Parameters	Values
Displacement	30 cc/rev
Number of teeth	22
Gear diameter	50 mm
Gear width	48 mm
Radial clearance at the tooth tip	35 μm
Journal bearing radial clearance	14 μm

3.2 Modelling of orifice flow

As explained in section 2.1, certain internal flow connections in EGMs are modelled using the orifice equation (Eq. 2.2). This form of the orifice equation, however, is only valid for Newtonian flows. So, a different orifice flow relation is needed to be determined that is suitable for non-Newtonian flows. In the following subsections, the methodology of developing the non-Newtonian orifice equation suitable for the modelling of internal flow connections in gear pumps is described.

3.2.1 Past efforts in orifice flow modelling

For non-Newtonian flows through orifices, efforts have been made in past by Salas-Valerio and Steffe [50], McNeil et al. [51], and Pal [52] to relate the orifice discharge coefficient to other flow parameters like Reynolds number. Other researchers have come up with a different method of modeling the orifice flow by relating dimension-

less pressure drop (Euler number/pressure loss coefficient/head loss) to other dimensionless quantities. Edwards et al. [53] reported head losses for flows through orifices (among other pipe fittings) and correlated it to Reynolds number for different orifice diameter ratios (β). Das and his research team [54, 55] studied the flow of aqueous solutions of sodium salt of carboxy methyl cellulose through orifices and developed a dimensionless relationship among Euler number, Reynolds number, and orifice diameter ratio β. Bohra [56] conducted experiments involving the flow through orifices of different diameters, thickness, and at different temperatures. From results of those experiments, he developed orifice flow models relating Euler number to Reynolds number for both low and high Reynolds numbers. Ntamba and Fester and Chowdhury and Fester [57,58] conducted experiments with Kaolin, carboxymethyl cellulose, and Bentonite and developed correlations between pressure loss coefficient, β, and Slatter Reynolds number [59]. The relations proposed by these researchers and their applicability are summarized in Table 3.2.

From the table, it is evident that the correlations suggested in past are applicable for orifice diameter ratio $\beta \geq 0.2$. Only Bohra's correlation is applicable for lower β, but only for orifices of finite thickness ($l/d_o \geq 0.32$). However, the connections modelled as orifices in external gear pumps are sharp orifices. Modelling these connections as sharp orifices has shown to better describe the flow dynamics by various researchers in past [60–62]. Moreover, the orifice flow is significant when the gear teeth enter the meshing zone (Figure 2.3), where this flow represents the pumping action. The flow at low orifice diameters are specifically important because that is when the TSV is decreasing in volume and the rate at which the fluid escapes the TSV determines the features of the outlet flow and the level of pressure in the TSV. This will be further illustrated with the help of results later in this chapter. So, it is important for the model to have an accurate measure of flow through orifices of lower β.

Table 3.2.

Orifice flow relations proposed by previous researchers

Researchers	**Correlations proposed**	**Applicability**
Edwards et al. [53]	$K_L = \frac{786}{Re}$	$\beta = 0.289$
	$K_L = \frac{154}{Re}$	$\beta = 0.577$
Salas-Valerio and Steffe [50]	$C_d = 0.494(1 - exp(-0.011Re)) + 0.086$	3.18 mm$\leq d_o \leq$ 7.84 mm
Pal [52]	$C_d = \sum_{i=0}^{4} A_i (logRe)^i$	$\beta = 0.594$
Das et al. [54, 55]	$\frac{\Delta p}{\rho v^2} = 0.601 Re^{-0.048} \left(\frac{d_o}{D}\right)^{-4.380}$	$0.46 \leq \beta \leq 0.71$
Bohra [56]	$Re < 6 : Eu = \frac{1}{Re^{1.203}} \left(64 (\frac{l}{d_o})^{1.502} \mu_r^{-0.47} + 36\pi\right)$	$0.023 \leq \beta \leq 0.137$
	$Re > 6 : Eu = \left[\left(\frac{64\left(\frac{l}{d_o}\right)^{1.159} \beta^{0.075} \mu_r^{-0.334} + 17.16\pi}{Re^{0.882}}\right) + \left(\frac{1-\beta^4}{C_d^2}\right)^3\right]^{\frac{1}{3}}$	$0.32 \leq l/d_o \leq 5.72$
Ntamba and Fester [57]	$K_{or} = 37.3\beta^{-2.68} Re_3^{-1} + 0.85\beta^{-4.85}$	$l/d_o < 0.75$ $0.2 \leq \beta \leq 0.7$
Chowdhury and Fester [58]	$K_{or} = \frac{170.5\beta^{-3.17}}{Re} + \left[-17\beta + 5\left(\frac{t}{d_o}\right)^{(53.77\beta^2 - 71.23\beta + 26.33)(t/d_o)^{-0.92}}\right]$	Long orifice $0.36 \leq \beta \leq 0.7$

3.2.2 Non-dimensional orifice flow model

Owing to the limitations presented in the previous subsection, a new orifice model is developed in this work that is applicable for small apertures. The model development involves identification of key dimensionless parameters influencing the orifice flow and then usage of experimental techniques to establish functional relationships among them.

The pressure drop across the orifice depends on the following parameters: the orifice diameter ratio, flow through the orifice, and fluid properties like density and viscosity.

$$\Delta p = f\Big(\frac{d_o}{D}, v, \rho, \mu\Big) \tag{3.1}$$

Using Buckingham's Π theorem, the dimensionless numbers obtained are Euler number (Eu), Reynolds number (Re), and orifice diameter ratio (β).

$$Eu = \frac{\Delta p}{0.5\rho v^2} \tag{3.2}$$

$$Re = \frac{\rho v d_o}{\mu} \tag{3.3}$$

$$\beta = \frac{d_o}{D} \tag{3.4}$$

Generalized Reynolds number used in the past to study non-Newtonian flows [51, 55, 62] has a limitation that it only accounts for the power law behavior of the fluid viscosity. However, real shear thinning fluids often have Newtonian plateaus at low and high shear rates (Fig. 3.1). Hence, in this study, Reynolds number expression is the same as that for Newtonian fluids with the exception that the viscosity is not a constant but is determined from the shear rate using Carreau-Yasuda law of viscosity.

$$\mu = \mu_\infty + (\mu_0 - \mu_\infty)\big[1 + (\lambda_n \dot{\gamma})^a\big]^{\frac{n-1}{a}} \tag{3.5}$$

where the average value of the shear rate at the orifice can be approximated as shown in [56]:

$$\dot{\gamma} = \frac{3n+1}{4n}\frac{32Q}{\pi d_o^3} \tag{3.6}$$

This law allows the viscosity to reach Newtonian plateaus at high and low shear rates and behaves as power law in between. Many real fluids (including all fluids used in this study) follow this law.

Thus, the desired orifice equation is expressed as

$$Eu = f(Re, \beta) \tag{3.7}$$

To determine this functional relationship, distinct set of experiments were conducted to obtain numerous data points for different Re (by changing flow velocity and fluid) and β (by changing orifice diameters).

3.2.3 Experimental setup

The experiments were conducted at the facility of the company sponsoring this research, so, only a brief description of the setup is provided here.

ISO schematic of the hydraulic circuit for the experimental setup is shown in Figure 3.2. An electric motor drives a positive displacement pump (here Zenith H-9000 external gear) which delivers the flow through an orifice. In experiments, the diameter of the transmission lines used was 19.05 mm. Three sharp orifices of diameters 3.175 mm, 1.5875 mm, and 0.79375 mm were used. Hence, the orifice diameter ratio was 0.16, 0.08, and 0.04. The orifices were made from 3.175 mm stock but were cut on low pressure side with 45° bevel making narrowest part sharp as knife edge. Two pressure transducers were mounted 254 mm upstream and 19.05 mm downstream of the orifice to measure the pressure drop across the orifice. A Coriolis type flow meter was placed downstream of the orifice to measure the flow rate. Three different shear thinning fluids were used with zero shear rate viscosity varying from 5 to 100 Pa s.

Figure 3.3 shows how the viscosity of fluid C varies with the shear rate. The measurement of viscosity was done on Couette type rotational and capillary viscometer to obtain the data at low and high shear rates, respectively. Such variation of viscosity

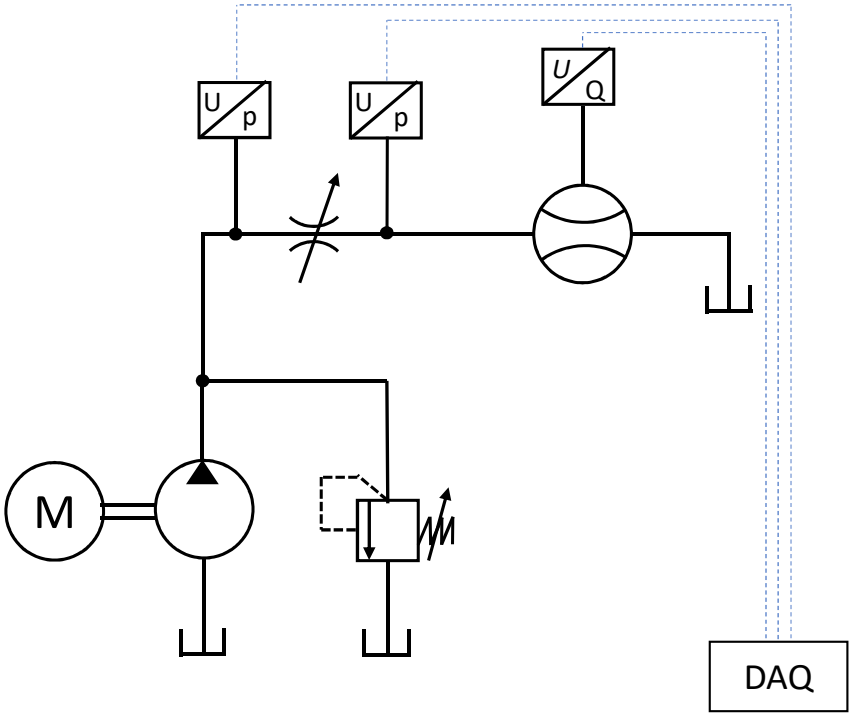

Figure 3.2. ISO schematic of the hydraulic circuit for orifice flow investigation

can be modeled by Carreau-Yasuda law (Eq. 3.5) and as shown in Fig. 3.3, this law matches very well with the experimentally obtained data.

The experiments were conducted to obtain several data points by varying the pump speed, changing the orifice plates and changing the fluid. All the experiments were conducted at 21 °C, eliminating the temperature dependence of viscosity.

3.2.4 Results and model development

From the experimental data collected, the value of dimensionless numbers Eu, Re and β were obtained for each datapoint. Figure 3.4 shows the variation of Euler number with Reynolds number. The trend of Eu versus Re is similar to what has been reported by Bohra [56] and Chowdhury and Fester [58], though difference in

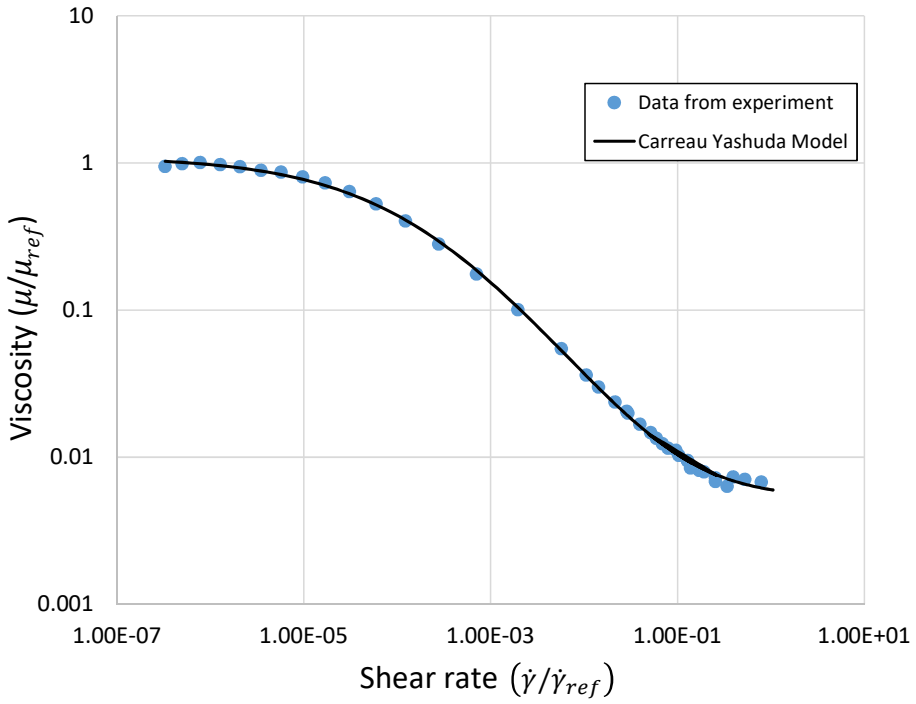

Figure 3.3. Normalized viscosity shear rate plot for fluid C. The dots indicate the data points obtained from viscometric measurements. The line is obtained from Carreau-Yashuda law.

orifice geometry and range of correlation applicability makes quantitative comparison unreasonable.

On the basis of dimensional analysis and data analysis, following correlation is proposed:

$$Eu = \frac{k_1}{Re^{k_2}\beta^{k_3}} \tag{3.8}$$

where k_1, k_2 and k_3 are constants that were determined by the regression analysis on the data collected. Since the data spans several orders of magnitude, performing regression in the logarithmic scale ensures uniform precision at both lower and higher order data. Logarithm of Eq. 3.8 was taken to obtain

$$\log Eu = \log k_1 - k_2 \log Re - k_3 \log \beta \tag{3.9}$$

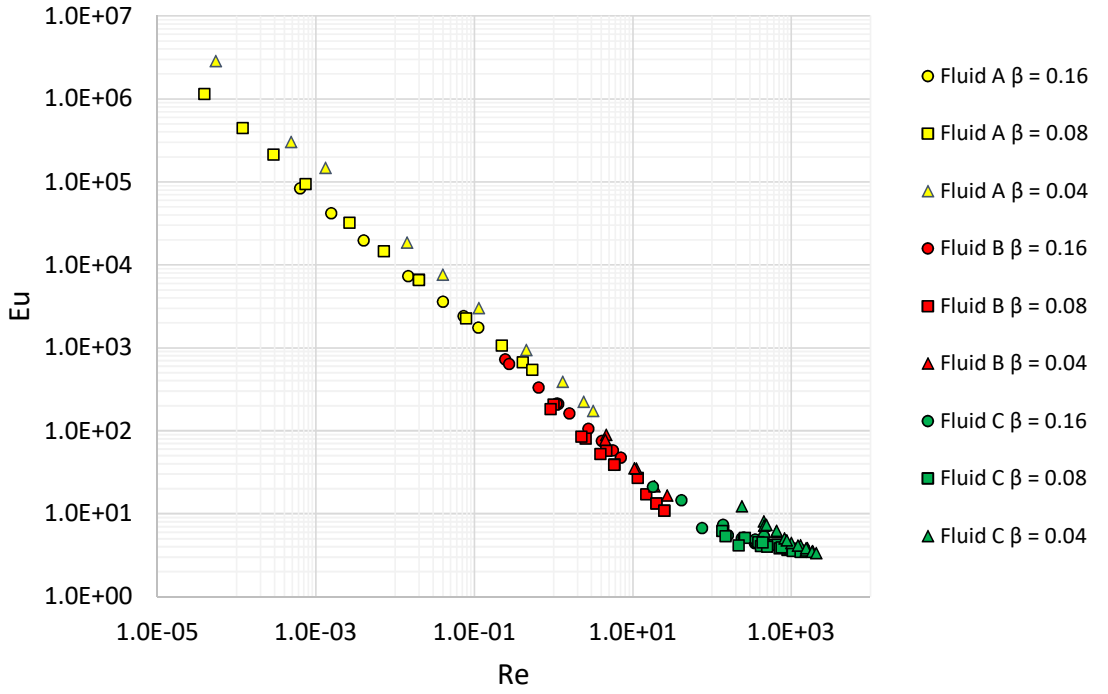

Figure 3.4. *Eu* versus *Re* for different orifice diameter ratios for different fluids

It can be seen in Figure 3.4 that $Eu - Re$ curve slope changes around $Re = 20$. So, separate regression analyses were done on the data with $Re < 20$ and $Re > 20$. For $Re < 20$, the value of constants obtained from the regression analysis is shown in Table 3.3.

Table 3.3.
Constants in Eq. 3.9 for $Re < 20$

Constants	**Value**	**Standard deviation**
$\log k_1$	1.959	0.078
k_2	0.862	0.010
k_3	0.412	0.071

The final correlation after substituting the value of the constants is:

$$Eu = \frac{91.1}{Re^{0.862}\beta^{0.412}} \tag{3.10}$$

The R squared value (goodness-of-fit measure) for this correlation is 0.9924, and standard error is 0.123.

For $Re > 20$, the value of constants obtained from the regression analysis is shown in Table 3.4.

Table 3.4.
Constants in Eq. 3.9 for $Re > 20$

Constants	**Value**	**Standard deviation**
$\log k_1$	1.187	0.062
k_2	0.330	0.020
k_3	0.339	0.051

The final correlation for $Re > 20$ is given by

$$Eu = \frac{15.4}{Re^{0.330}\beta^{0.339}} \tag{3.11}$$

The R squared value for this correlation is 0.8507, and standard error is 0.067.

Figure 3.5 shows that the Euler number predicted by the correlations closely matches the experimental data. Figure 3.6 shows Eu versus Re comparison for the measured data and that obtained from the proposed correlations which again shows a close match. These comparisons validate the correlations.

To conclude, Eq. 3.10 and Eq. 3.11 form the non-Newtonian orifice flow relation which is used in the modelling of internal connections in EGMs.

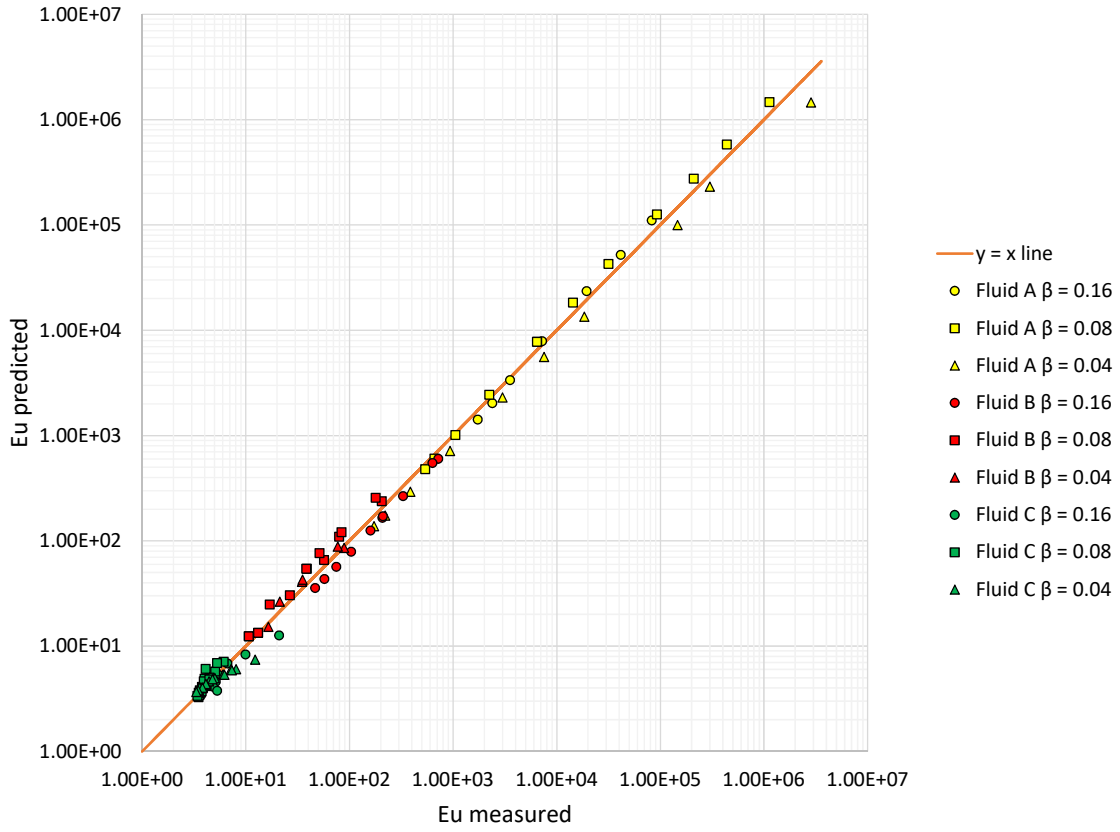

Figure 3.5. Comparison of the Euler number predicted by the correlations proposed versus the Euler number from the experimental data

3.3 Modelling of leakage flow

As explained in section 2.1, in lumped parameter approach, the tooth tip leakages (inset in Figure 1.4) and the lateral leakages in EGMs are modelled as combined Couette-Poiseuille flow. The form of Couette-Poiseuille equation in Eq. 2.3 is only valid for Newtonian flows. However, the shear thinning fluids too exhibit regions of Newtonian behavior when the shear rate in the flow is lower than"low critical shear rate", $\dot{\gamma}_{cr,low}$, or higher than "high critical shear rate", $\dot{\gamma}_{cr,high}$ (Figure 3.1). Thus, Eq. 2.3 is still valid in these regions. In the power law region, the combined Couette-

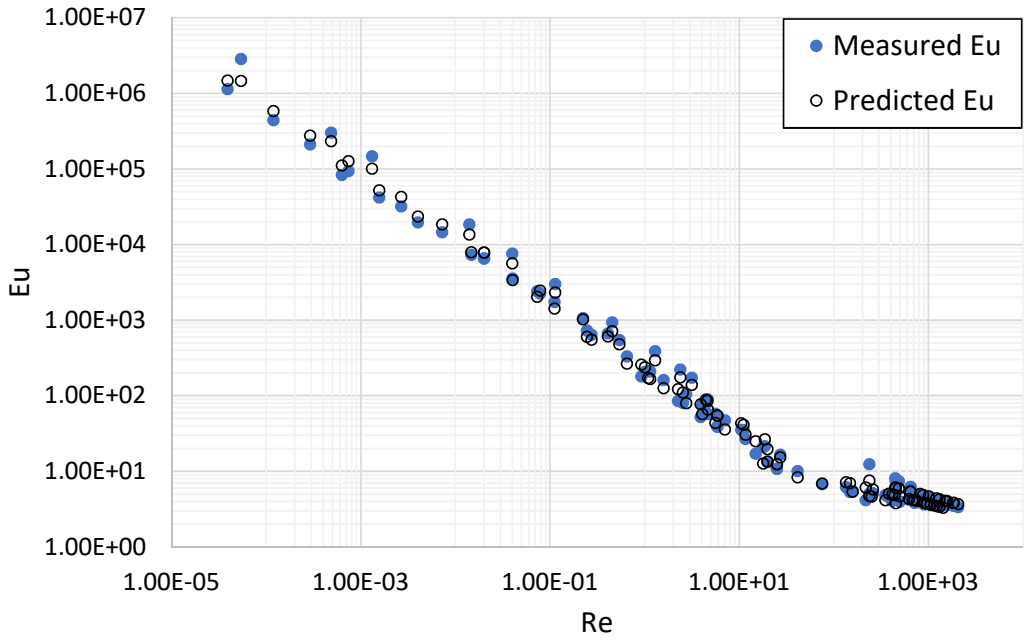

Figure 3.6. *Eu* versus *Re* comparison between experimental data and those obtained from proposed correlation

Poiseuille flow expression developed for power law fluids by Tadmor and Gogos [63] is applicable:

$$Q = \frac{\mathrm{v}bh|6G|^s \mathrm{sign}G}{(1+s)(2+s)}\Big[(1-\Lambda)|1-\Lambda|^{1+s} + \Lambda|\Lambda|^{1+s} - (2+s)|\Lambda|^{1+s}\Big] \tag{3.12}$$

where $s = 1/n$ and G is dimensionless number given by

$$G = \frac{h^{n+1}}{6k\mathrm{v}^n}\frac{\Delta p}{L} \tag{3.13}$$

and Λ is obtained from

$$|\Lambda|^{1+s} - |1-\Lambda|^{1+s} + \frac{1+s}{|6G|^s \text{sign}G} = 0 \tag{3.14}$$

For drain leakage, where only the pressure difference drives the leakage flow, the above set of expressions simplify to

$$Q = -2b\frac{|G'|^s \text{sign}G'}{s+2}\Big(\frac{h}{2}\Big)^{s+2} \tag{3.15}$$

where

$$G' = \frac{1}{k}\frac{\Delta p}{L} \tag{3.16}$$

The decision of whether to use the Newtonian formulation or the non-Newtonian formulation at any instant in the simulation is made on the basis of mean shear rate, $\overline{\dot{\gamma}}$, in the flow.

The velocity profile for Newtonian Couette-Poiseuille flow from [63] is given by

$$\frac{v}{\mathrm{v}} = \xi - 3\xi(1-\xi)\frac{h^2}{6\mu\mathrm{v}}\frac{\Delta p}{L} \tag{3.17}$$

where ξ is the dimensionless coordinate in the direction of gap height, $\xi = y/h$.

From this equation, the shear rate can be evaluated as:

$$\dot{\gamma} = \frac{dv}{dy} = \frac{\mathrm{v}}{h}\Big[1 - 3(1-2\xi)\frac{h^2}{6\mu\mathrm{v}}\frac{\Delta p}{L}\Big] \tag{3.18}$$

When the pressure difference is very small, the shear rate is nearly constant. When the pressure difference is high, the shear rate does vary from 0 to a maximum value (Figure 3.7(b)). However, the mean shear rate is still a good approximation.

Figure 3.8 shows the flowchart of the algorithm used in selecting the appropriate formulation.

3.4 Modelling of journal bearing

In EGMs, the gears are typically supported by journal bearings. In the reference pump E1, the gears and shafts are manufactured from two different parts. The drive

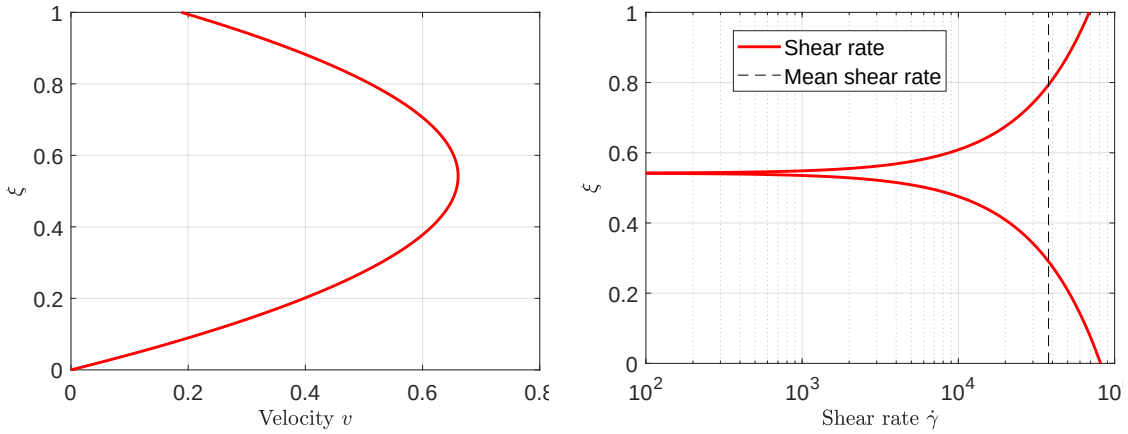

(a) Velocity profile

(b) Shear rate profile

Figure 3.7. Velocity and shear rate profile for a typical Couette-Poiseuille flow (pressure dominated)

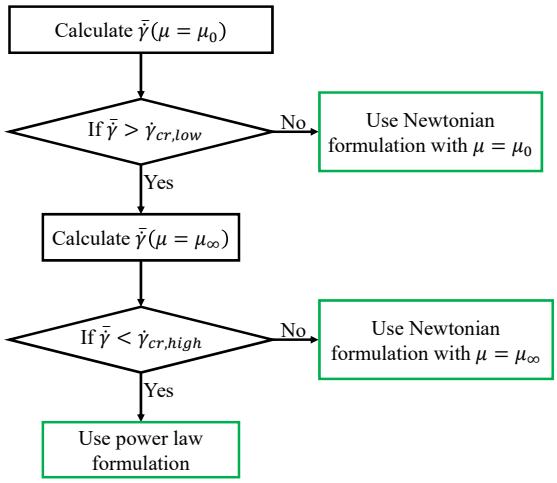

Figure 3.8. The flowchart of the algorithm used in selecting the Couette-Poiseuille flow model

gear and its shaft are rotationally locked by a key. This shaft and the holes on the front and back cover (Figure 3.9) form a journal bearing pair. On the driven side,

the shaft is fixed and the gear rotates freely on it. Hence, the hole in the driven gear and the shaft form the journal bearing pair.

For Newtonian fluids, the mobility method of determining the eccentric position of the journal in the bearing (explained in section 2.3) works very well. However, for non-Newtonian fluids, an alternate approach is required.

Dien and Elrod [64] provide a generalized Reynolds equation for non-Newtonian fluids, whose expression for journal bearings is

$$\frac{\partial}{\partial x}\frac{h^{2+n}}{n}\frac{\partial p}{\partial x} + \frac{\partial}{\partial y}\frac{h^{2+n}}{n}\frac{\partial p}{\partial y} = 6kU^n\frac{\partial h}{\partial x} \tag{3.19}$$

For a given eccentricity and speed, the term on the right is known and the differential equation can be solved for pressure. Integrating the pressure in the film gives the load carrying capacity. Solving this partial differential equation in the film requires discretization of fluid film and an iterative procedure of solving the algebraic equation at each grid point. These steps require a significant amount of time which goes against the core advantage of lumped parameter model: the simulation swiftness.

Hence, prior to the pump simulation, a batch of journal bearing simulations are conducted using the approach mentioned above to obtain a dataset which relates the journal eccentricity to the load support and speed for a given non-Newtonian fluid. Then, during the actual simulation of the external gear pump, this look up table is used to obtain the instantaneous eccentricity of the journal for the load provided by the loading module, via interpolation of the data from the table. In the lookup table, the number of data points for eccentricity and attitude angle (the angle between the load direction and the line joining the centers of the bearing and journal) are chosen as 100 and 200, respectively. These numbers are obtained from a sensitivity study. For the given nominal clearance at the bearing of the reference pump (Table 3.1), the choice of these numbers provides appropriate resolution in the journal position determination.

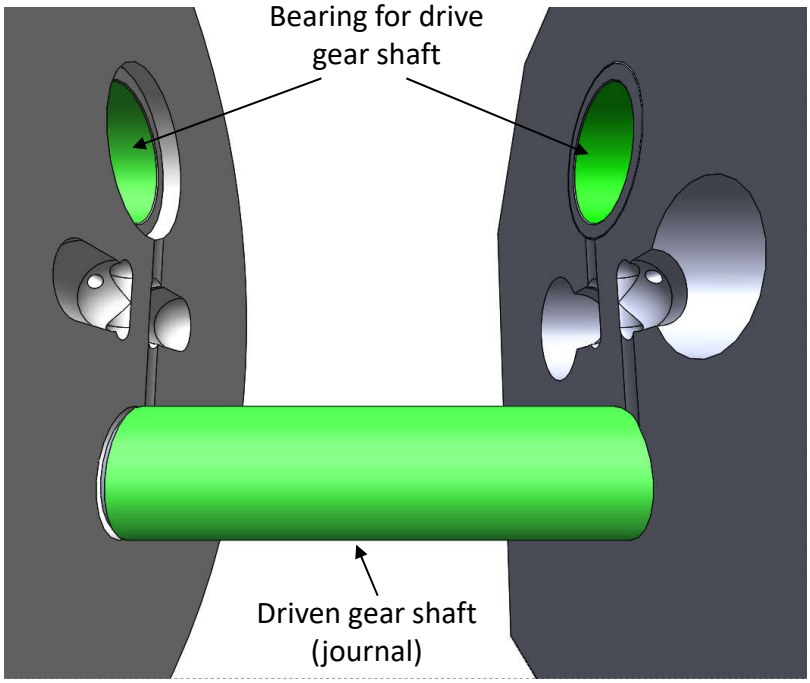

Figure 3.9. Journal bearing interfaces in the reference EGM E1 highlighted in green.

3.5 Results from non-Newtonian model implemented in HYGESim

The results discussed in this section are presented with respect to the angular position of the drive gear. Figure 2.2 shows that the angle (in HYGESim and hence results) starts from the meshing zone towards the inlet, to outlet, and back to the meshing zone. This sense of angle matches the progression of the tooth space as it rotates from the inlet region towards the outlet region. The reference pump E1 typically operates at low speeds and so, all the simulation and experimental results in this section are presented for speed < 100 rpm.

From the Geometrical Module results, a lot can be known about how different geometric quantities vary as the gears rotate. Figure 3.10 shows the volumes of a couple of mating tooth spaces for both drive and driven gear, as they rotate. The angle at which the two curves intersect near 360° represents the instant at which the

teeth pair mesh and the sum of the two working tooth space volumes is minimum. One might expect that volume of tooth space will remain constant when it is facing the pump casing. On the contrary, the micromotion of the gears leads to the variation of the tooth space volume which can be seen in this figure (in this case, the gear axes position oscillates around (-16, 5) μm and (-6, -2) μm with respect to the coordinate system in Figure 2.2).

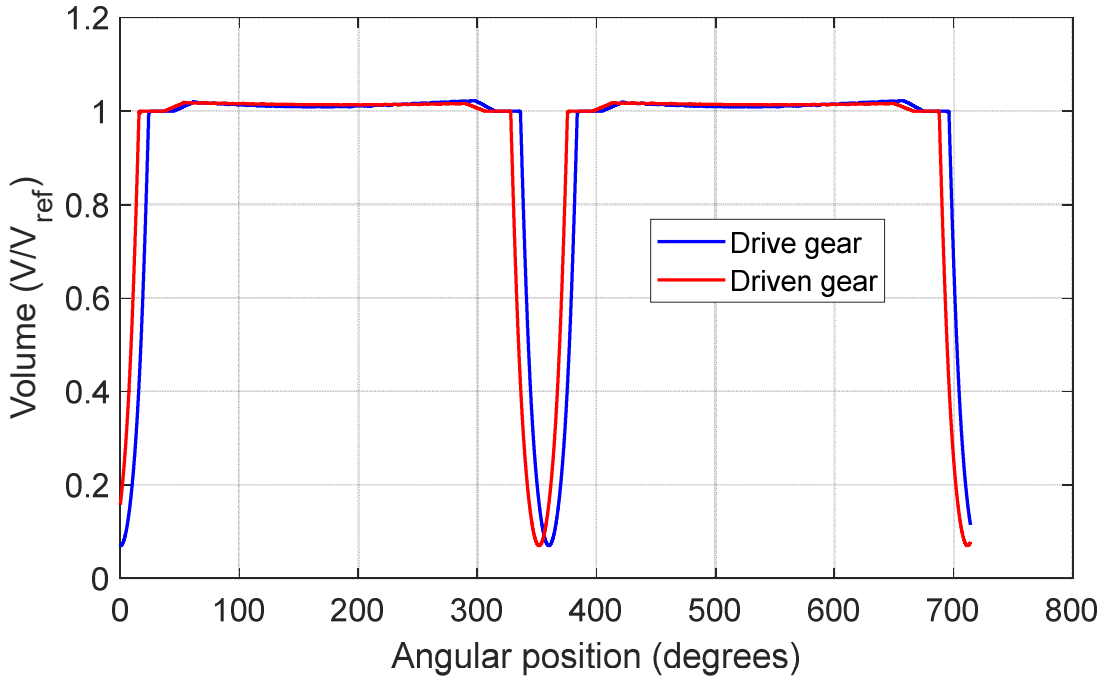

Figure 3.10. Volume variation of i^{th} tooth spaces of the drive and the driven gear as they rotate. The angle on the x axis represents the angular position of the drive tooth space.

Moreover, the Geometrical Module can also give an idea of how the areas of different orifice connections vary with angle (Figure 3.11).

Figure 3.12 shows how the areas of orifices and flow through the orifices HG1 and HV1 (determined from the Fluid Dynamic Module using Fluid A) vary with drive TSV angle. As the TSV enters the meshing zone (at 335°), its connection to outlet (via HG and HV orifices) starts to decrease. However, since the volume of tooth

space decreases too, the fluid escapes to the outlet via these orifices. That is why HG and HV orifices experience significantly high flow rates as the flow area keeps on decreasing. Accurate evaluation of these flows is important to achieve an accurate description of delivery flow and pressure inside the TSV. This further supports the claim of requiring an accurate orifice model for the determination of flow through orifices of small area, which justifies the work in Section 3.2.

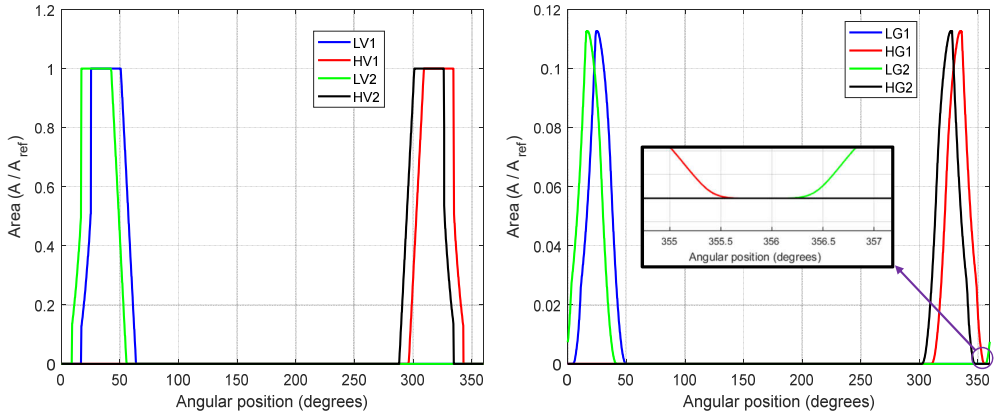

Figure 3.11. The variation of orifice connection areas (connecting TSVs to inlet/outlet region) as the gears rotate.

From Figure 3.11, it can be seen that for a brief period near 356°, all the orifices are closed. The tooth space volume is also reducing in that period. This leads to a sudden rise in pressure of the fluid in the tooth space. As a consequence, a spike in the TSV pressure occurs, as it appears in Figure 3.13 which shows the instantaneous pressure in both the drive and the driven gear tooth spaces, when the simulation is performed at reference conditions.

An interesting feature visible in Figure 3.13, is the shape of the drive gear TSV pressurization. As the TSV enters the casing, its pressure first increases and then decreases, before increasing again up to the outlet pressure level. This trend can be explained through the radial sealing realized as a consequence of the gear axis' eccentricity, with respect to the nominal gear center position. In particular, the

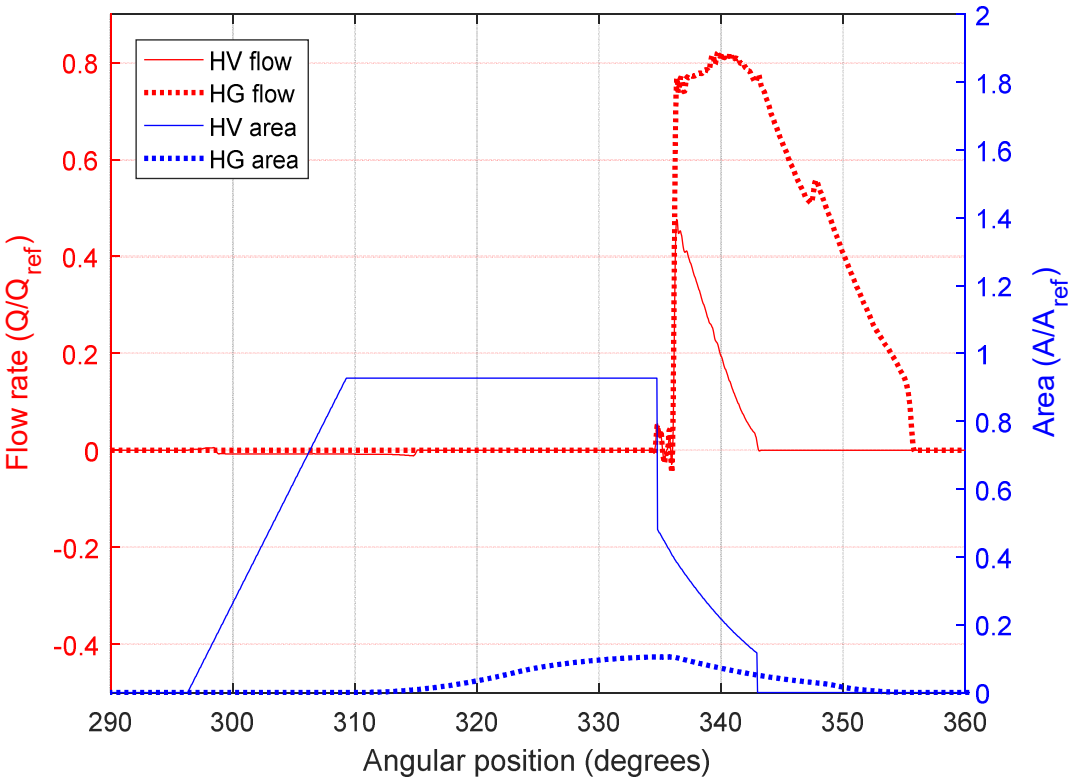

Figure 3.12. Flow rates through HG1 and HV1 grooves (from drive TSV to outlet volume) and areas of these groove openings as a function of drive TSV angle.

radial load acting on the gear (given by the fluid pressure and the contact force) is supported by the bearings through a proper eccentricity of the gear shaft with respect to the bearings (shown as vector $\overrightarrow{O_C O_S}$ in Figure 3.14). Additionally, under this loading, the gear also experiences a micromotion with respect to the shaft, $\overrightarrow{O_S O_G}$ (gear and shaft are rotationally locked by the means of a key, but there are few microns of clearance between them). This additional motion, which corresponds to the geometrical clearance of the coupling between the gear and the shaft, is superimposed to the motion given by the journal-bearing eccentricity, for the determination of the actual gap between the tooth tip and internal surface of the pump casing. The net displacement of gear with respect to its nominal position can be represented as the

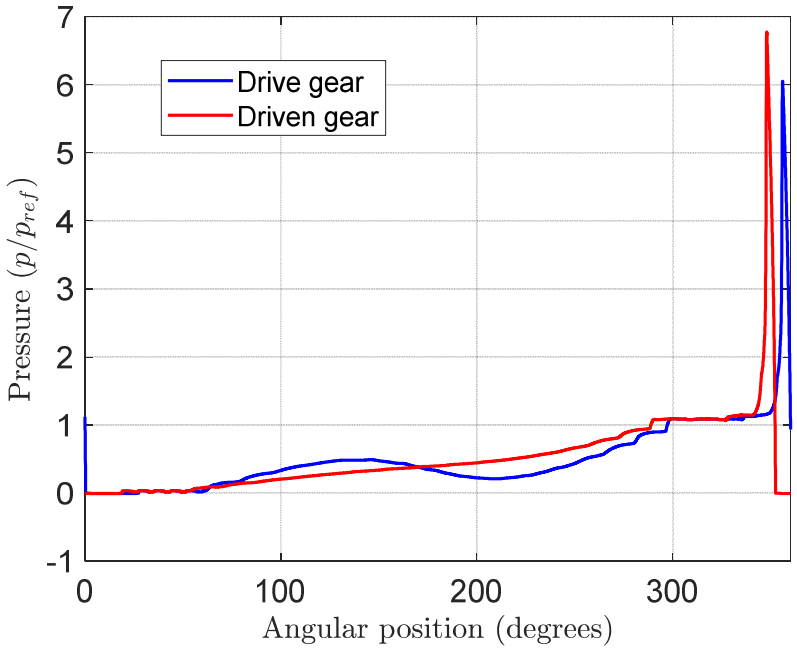

Figure 3.13. Pressurization of a tooth space volume of drive and driven gear for simulation at reference conditions. The angle on x axis corresponds to the angle of drive tooth space.

vector $\overrightarrow{O_C O_G}$ in Figure 3.14. This overall displacement has a significant effect, as shown in Figure 3.15, in terms of highly varying gap between the drive gear tooth tip and the pump casing. Therefore, when the TSV enters the casing, the tooth tip gap starts from a high value and reduces leading to a rise in the TSV pressure. The opposite happens after 160°, when the tooth tip gap starts to increase leading to a reduction in the TSV pressure.

In the reference gear pump, the driven gear shaft is fixed. The driven gear has a hole which forms a journal bearing pair with the shaft (Figure 3.9). Due to large width of the gear, the width of the fluid film in this journal bearing is larger as compared to the journal bearing at the drive shaft. Hence the eccentricity of the driven gear with respect to the shaft is low compared to the drive gear. This implies a relatively

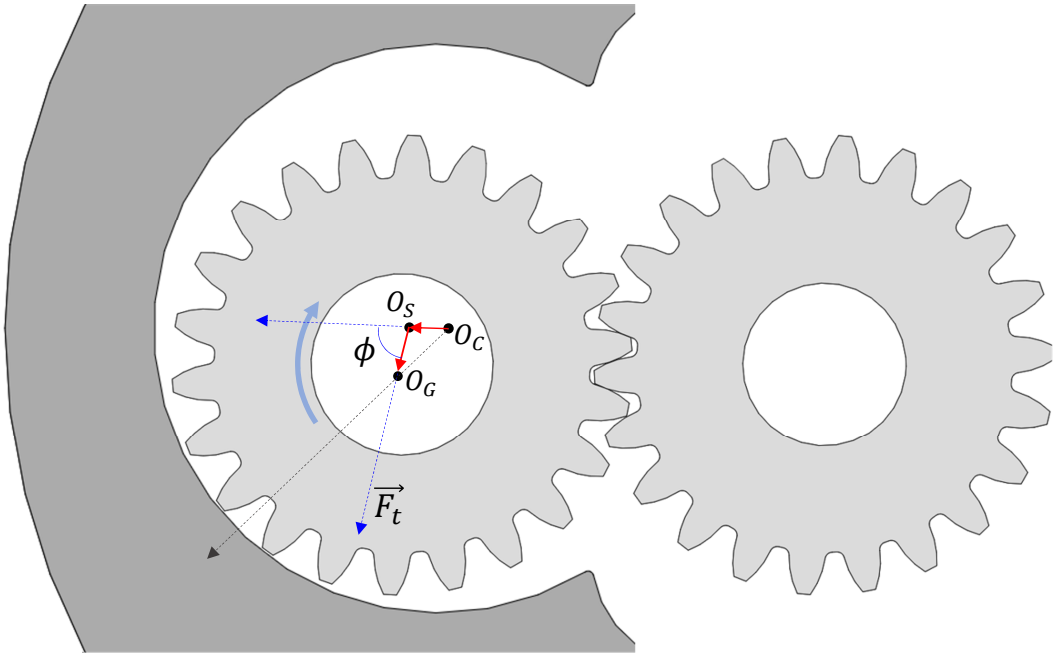

Figure 3.14. Illustration of gear micromotion. O_C, O_S and O_G are the centers of casing, shaft and gear, respectively. $\vec{F_t}$ indicates the direction of net radial force acting on the gear. The shaft achieves an eccentric position to carry the load (ϕ is the attitude angle). The gear moves in direction of $\vec{F_t}$ by the magnitude of the clearance between gear and shaft.

uniform gap at the tooth tip of the driven gear (Figure 3.15). As a consequence, the TSV pressurization at the driven gear happens at a more uniform rate (Figure 3.13).

3.6 Experimental Validation

3.6.1 Test setup

Within this research activity, experiments were performed at the industry sponsor's facility to validate the non-Newtonian EGM simulation approach developed and implemented in HYGESim. A proper validation requires comparisons against steady-state measurements of the outlet flow as a function of the shaft speed and outlet pressure as well as comparisons with dynamic measurements representative of

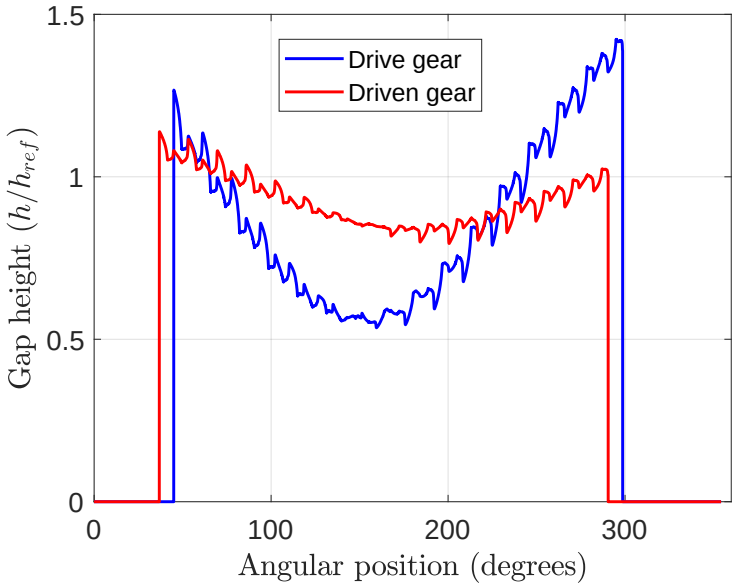

Figure 3.15. Variation of gap height at a tooth tip for drive and driven gear. The angle on x axis corresponds to the angular position of drive tooth space.

the transients characterizing the fluid displacing action realized by the gears. Steady state measurements of the flow through positive displacement machines are very common in engineering [65, 66], and they can be based on the use of an accurate loading apparatus at pump outlet along with the measurement of both the flow rate and fluid pressure at the delivery.

Dynamic measurements of the flow in positive displacement machines is still an active area of research, and measurements are less standardized. For external gear pumps, some researchers used different techniques to measure the pressure in a tooth space volume [22, 67] which would provide data to verify the plots such as the one in Figure 3.13. However, this experimental technique can be invasive and expensive. Other authors prefer to relate the dynamic features of the flow through the unit to the instantaneous pressure oscillations which can be measured in a well-defined delivery

apparatus [21, 22, 68, 69]. In this research, the delivery apparatus was designed to be similar to the apparatus in [70].

Figure 3.16 shows the ISO schematic of the hydraulic circuit built for conducting the experiments. The delivery side of the pump consists of a constant diameter outlet pipe with a sharp orifice at the end acting as the load to the pump. Two pressure transducers are mounted at the middle of the pipe: a slow response one, suitable to measure the average outlet pressure, and piezo-electric fast response transducer, suitable to measure the dynamic features of the pressure pulsations. The former one provides the steady state value of pressure whereas the latter provides the instantaneous value of pressure (which is then used to perform the pressure ripple comparisons). Downstream the loading element, a Coriolis mass flow meter was used to measure the average mass flow rate.

To perform the model validation, several experiments were conducted with the reference pump E1. The experiments were conducted at different speeds ($6 - 73$ rpm), with different reference fluids and in some cases, a back pressure regulator was used to obtain data over wide range of differential pressure ($10 - 75$ bar) across the pump.

3.6.2 Results and validation

In this section, the results from HYGESim are presented and comparison with the experimental data is shown for different fluids. The first comparison (Figure 3.17) pertains to the pressure oscillations at outlet of the pump. Figure 3.17 shows the comparison using fluid A at different speeds (and hence different pressures, resulting from the loading orifice), in both time domain (left) and frequency domain (right). As noticeable from the figure, there is a close match between experiment and simulation in terms of peak to peak values in pressure, shape of the ripple and amplitude of different harmonics.

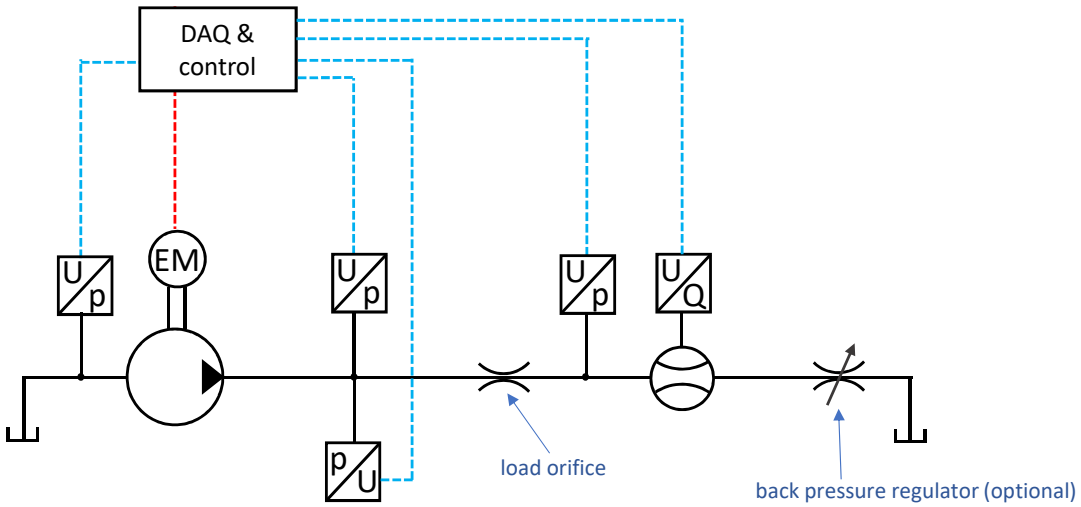

Figure 3.16. ISO Schematic of Experimental setup.

It is to be noted that the plots in Figure 3.17 show the pressure fluctuation with respect to the average pressure, and the values are not scaled. Thus, the good match in the magnitude is from the model itself. This kind of comparison constitutes an important validation of the model developed in this research. In fact, these pressure transients at the outlet of the pump are related to:

- The variations of the internal control volumes (tooth space volumes and variable internal volumes), evaluated by the Geometrical Module.
- The value and the timing of the internal connection areas, evaluated by the Geometrical Module (in particular the meshing groove areas).
- The flow equation used to determine the flow between different control volumes (the orifice equation).
- The compressibility modelling of the fluid.

The good agreement confirms that all these aspects are correctly modelled in HYGESim.

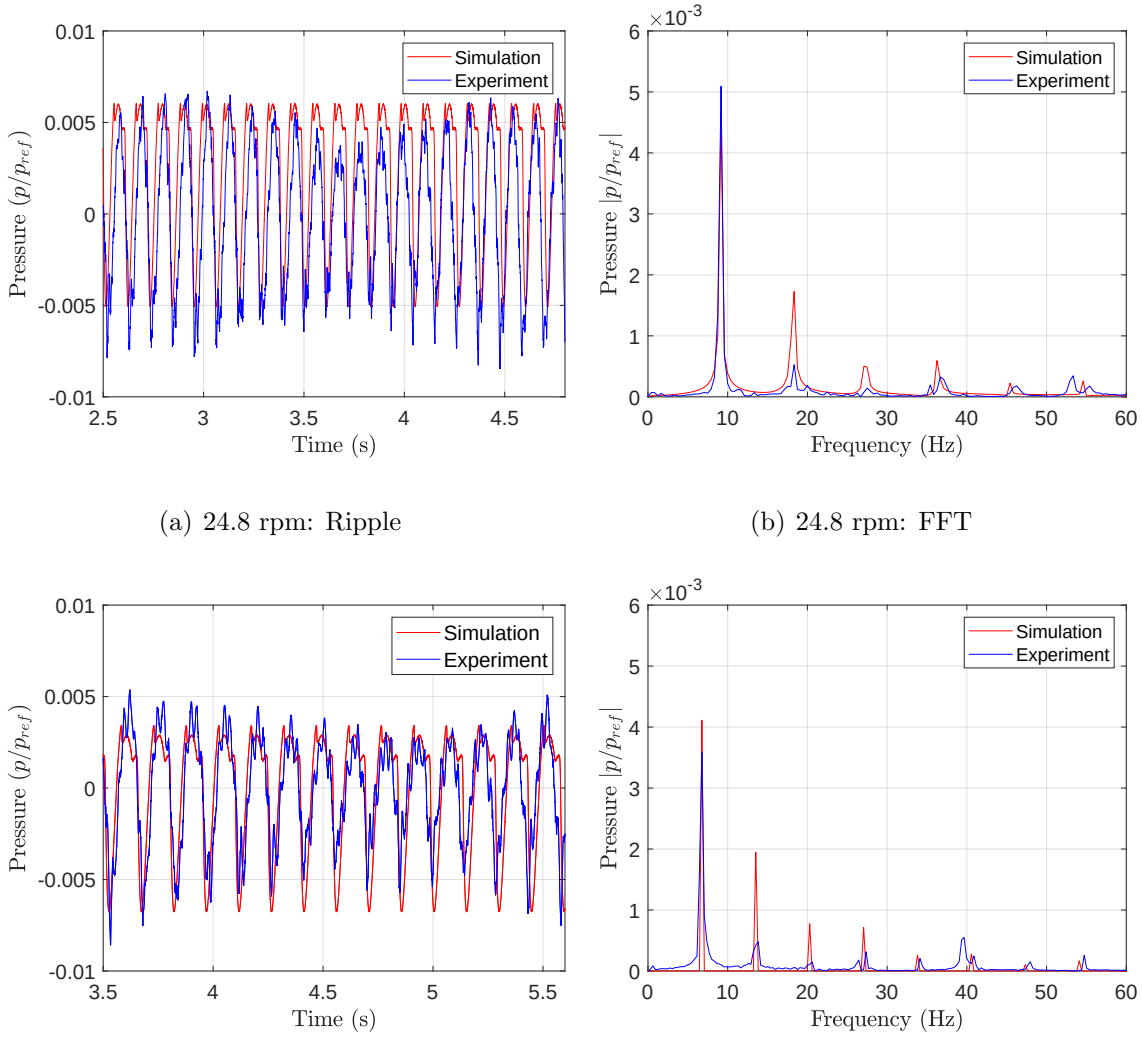

(a) 24.8 rpm: Ripple

(b) 24.8 rpm: FFT

(c) 18.5 rpm: Ripple

(d) 18.5 rpm: FFT

Figure 3.17. Pressure ripple comparison between simulation and experiment at different speeds.

The ripple comparison does not confirm the leakage modelling in HYGESim. To validate this, the predicted steady state flow rates at the pump outlet are compared with the experimental data. The comparison is shown in Figure 3.18 where a good match between experiments and HYGESim can be seen.

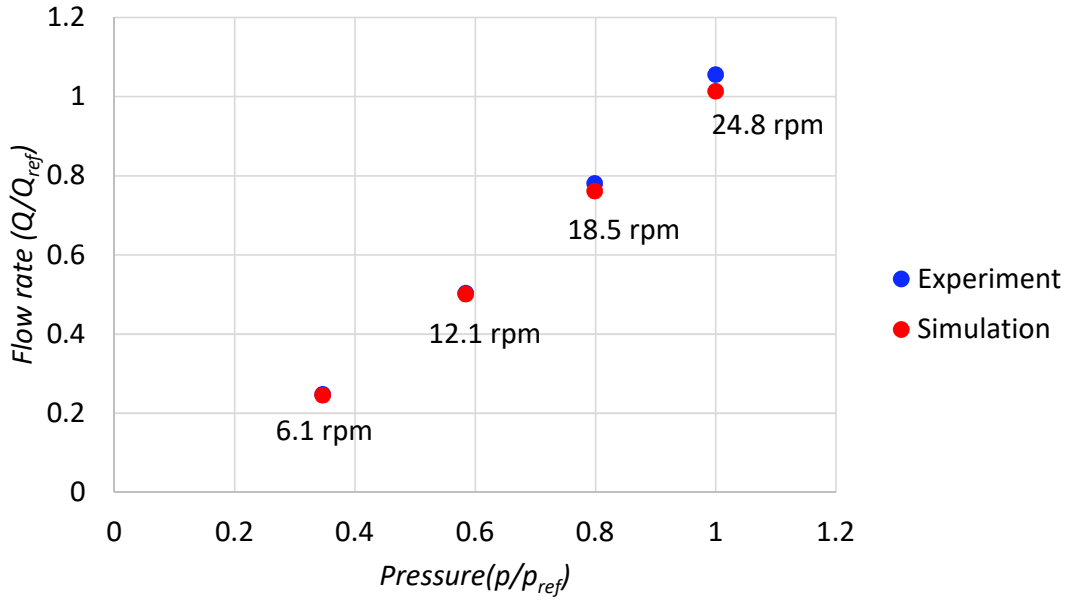

Figure 3.18. Comparison of the outlet flow rate predicted by HYGESim and measured experimentally at different pressures and speeds for fluid A.

In order to validate HYGESim for different fluids, fluid B was used to conduct the experiments. Again, as shown in Figure 3.19, HYGESim succeeds in predicting the outlet flow (and hence efficiency) at different pressures and different speeds.

Due to high viscosity of fluid A and B, the efficiency (predicted and measured) were relatively close to 100% when operated with Fluid A and B. So, it was decided to use Fluid C, a very low viscosity fluid, to conduct the experiments. Low viscosity promotes leakages lowering the volumetric efficiency. The aim was to reduce volumetric efficiency significantly and verify how close the HYGESim predictions could be.

Multiple experiments with Fluid C were done at different pressures and speeds which led to pump volumetric efficiency variation from 90% (at lower pressures) to 40% (at high pressures). Figure 3.20 shows the comparison between HYGESim prediction and experimental data which again shows a good match between the two.

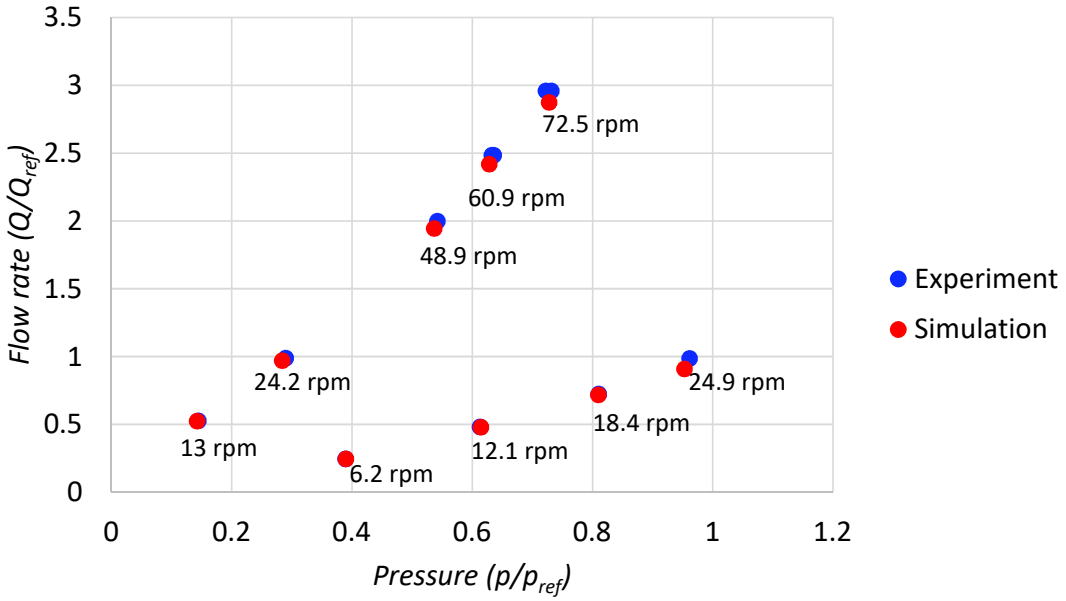

Figure 3.19. Comparison of the outlet flow rate predicted by HYGESim and measured experimentally at different pressures and speeds for fluid B.

Good comparison between experimental data and simulation results for 3 different fluids validates the modelling approach presented in this chapter and implemented in HYGESim.

3.7 Effect of fluid shear thinning on pump behavior

One of the most relevant potentials of the HYGESim tool developed in this work is that it can be used to examine the performance of the pump with different fluids ranging from Newtonian to highly non-Newtonian (i.e. extent of shear thinning). To highlight this aspect, simulations were performed with theoretical fluids of identical zero shear rate viscosity (μ_0) and consistency index (k) but different flow behavior index (n) (Figure 3.21). As it can be noticed from Figure 3.22, the outlet flow of the pump is reduced when the flow behavior index of the fluid is reduced. The reason

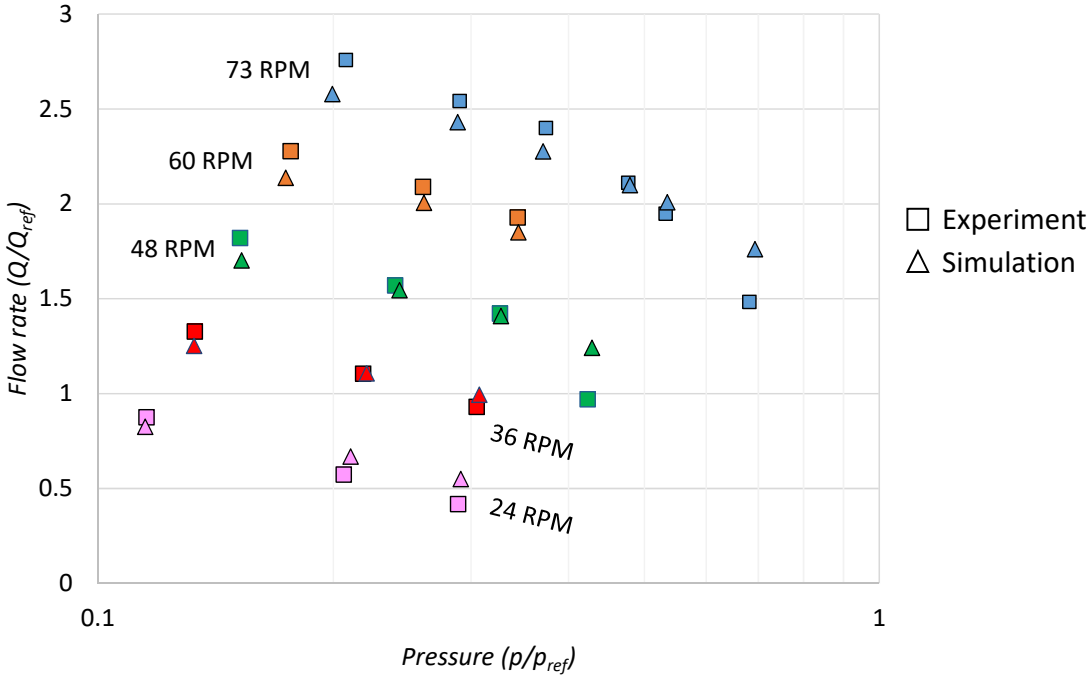

Figure 3.20. Comparison of the outlet flow rate predicted by HYGESim and measured experimentally at different pressure and speeds for fluid C.

for this behavior is given by the fact that the leakages in gear pumps are viscosity dependent. Hence, as the flow behavior index reduces, the fluid viscosity decreases at any particular shear rate, resulting in the increase of leakage flow.

It is often a matter of interest to determine the range of fluids that a pump can efficiently operate with. To determine such a range of fluids, one needs to determine the ranges of k and n such that the viscosity stays nearly the same in range of shear rates most critical to the reference pump. In the reference pump, at a reference operating condition, the mean shear rate at the leakage interfaces was found to be $\overline{\dot{\gamma}}/\dot{\gamma}_{ref} \in [10\,, 50]$.

$\overline{\dot{\gamma}}/\dot{\gamma}_{ref} = 25$ was chosen as the central point at which the viscosity would be kept constant when k and n are varied. Figure 3.23 shows the viscosity curves obtained by varying k and n, but keeping the viscosity constant at the chosen value of shear rate.

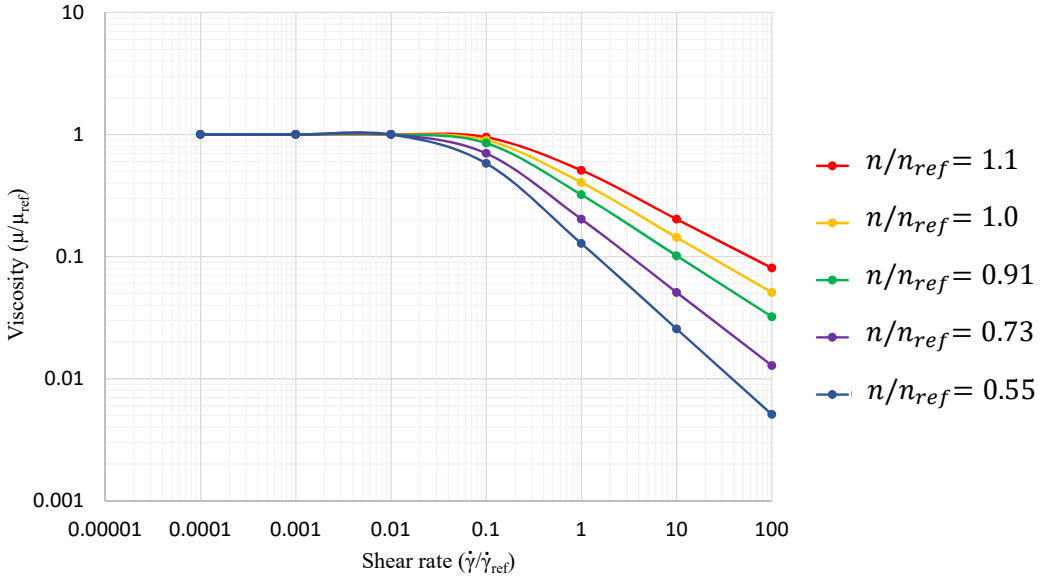

Figure 3.21. Viscosity shear rate plot of the theoretical fluids used to study the impact of shear thinning of fluid on pump performance.

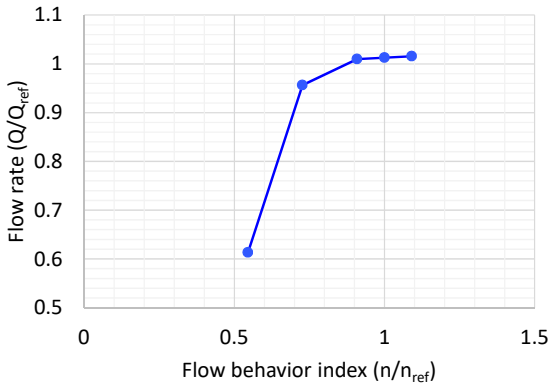

Figure 3.22. Outlet flow of the pump operating with the theoretical fluids described in Figure 3.21

It can be observed that n is increased from 0.4 (highly shear thinning) to 1 where the fluid becomes Newtonian with constant viscosity of $\mu/\mu_{ref} = 0.071$.

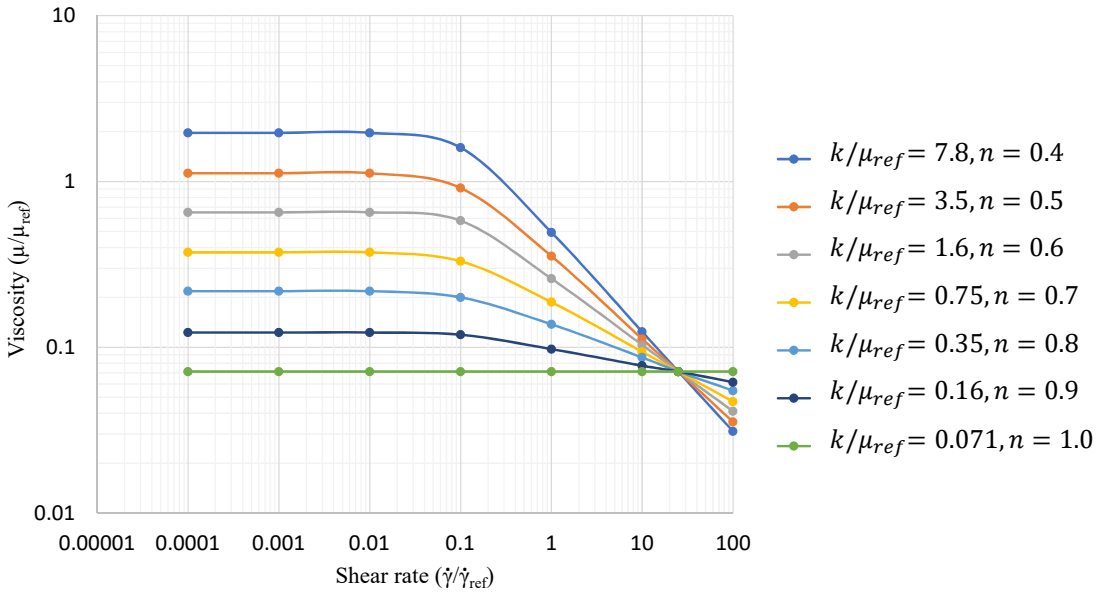

Figure 3.23. Viscosity curves of theoretical fluids with different flow consistency index k and flow behavior index n. All the fluids have same viscosity of $\mu/\mu_{ref} = 0.071$ at shear rate $\dot{\gamma}/\dot{\gamma}_{ref} = 25$, so that the viscosity remains nearly the same in the range of critical shear rates of the pump.

Simulations performed for these fluids show that the volumetric efficiency of the pump stays within 1% of variation for the considered range of fluids. This is expected since the fluids have been carefully chosen such that the viscosity at the critical regions of the pump (regions of high leakages) remain similar. Therefore, it is expected to have small variation in the leakage flows.

The TSV pressurization remain similar in all the considered cases. However, the TSV experiences higher pressure spikes at the meshing zone when the pump operates with Newtonian fluid, compared to the case of non-Newtonian fluids. Figure 3.24 shows a specific case where the drive TSV pressure for Newtonian fluid is compared to the non-Newtonian fluid with $n = 0.5$ (both fluids obtained from Figure 3.23). The cause of this higher pressure spike is the higher resistance to flow exchange between the drive gear TSV and the driven gear TSV via the gear backlash (see FG connection in Figure 2.3). Shear thinning behavior of the non-Newtonian fluid allows for higher

flows between these TSVs, when each of them is experiencing a rise in the pressure due to the reduction of volume. This flow helps reducing the pressure spike associated with the meshing process. For the case of Newtonian fluid, this flow is lower and hence, the pressure spike is high.

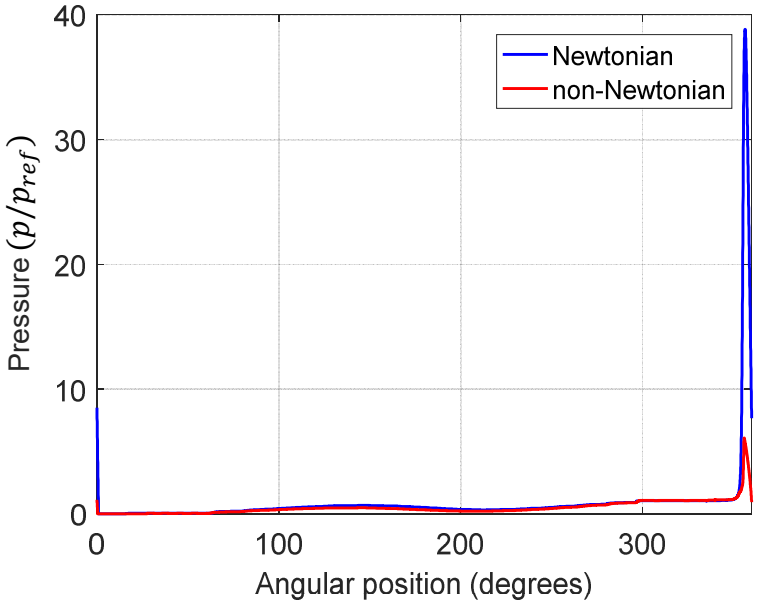

Figure 3.24. Drive gear TSV pressure comparison for Newtonian fluid and the non-Newtonian fluid with $n = 0.5$ (chosen from Figure 3.23).

4. INVESTIGATION ON THE FLOW REGIME AT THE TOOTH TIPS

In this chapter, the second crucial aspect of EGM modelling, nature of the flow regime at the tooth tip, is investigated. Careful modelling of the leakage flow over the tooth tips in EGMs (Figure 1.4) is critical for the development of accurate simulation models for EGMs. The prediction of overall performance parameters such as the volumetric efficiency highly depends on it. Moreover, this leakage flow plays a key role in determining the instantaneous pressurization of TSVs as they rotate from the inlet side towards the outlet side. The course of the TSV pressurization determines the radial pressure distribution around the gears (Figure 1.5), thus the radial force loading acting on the journal bearings supporting the gears. The location of the gear axes of rotation, and therefore the gap between each tooth and the casing, depends on these loads. Additionally, if the unit is pressure compensated, the TSV pressure distribution highly influences the behavior of the lateral gap compensation system [71].

To develop an accurate model of leakage flow over the tooth tip, it is important to have a thorough understanding of the nature of the flow over tooth tip (Aspect A2) and how it impacts the magnitude of leakage flow rate. The lumped parameter models for EGMs developed in past [9,15,17,21,72,73] assume the nature of this flow to be laminar and use Couette-Poiseuille equation to model this flow:

$$Q = \Big[-\frac{h^3 \Delta p}{12 \mu L} + \frac{\mathrm{v} h}{2} \Big] \cdot b \tag{4.1}$$

This equation is referred to as "laminar flow relation" in this chapter.

This assumption is valid for EGMs operating with high viscosity fluid and at relatively low speeds which is typical of the units used in hydraulic control systems and fluid handling systems. Past works, such as [21], show the validity of this assumption via comparison of the volumetric efficiency obtained from the model with experiments.

However, EGMs are also used widely in fuel injection applications (e.g. reference EGM E2) where the working fluid, the fuel, has much lower viscosity. Moreover, the EGM operating speeds in these applications are much higher. Thus the laminar assumption of the leakage flow over the tooth tip may no longer be valid.

In this chapter, the nature of fluid flow over the tooth tip of EGMs is investigated by simulating this flow via a CFD tool. Based on the simulation results and published work, an appropriate flow model is proposed that is applicable for a wide range of operating conditions. The new model is integrated within the HYGESim tool, using which it is shown how this model complements and in certain cases corrects the prediction made by traditional approaches.

4.1 CFD modelling of the flow over the tooth tip

The precise nature of flow (especially turbulent features) in any type of flow field can only be determined via experiments or direct numerical simulations. However, experiments that allow observing turbulent features of flow require significant efforts involving PIV methods [74–76]. Direct numerical simulation, on the other hand, requires a lot of computational time and is feasible only for low Reynolds number flows [77, 78].

Fluent simulation tool [79], instead, provides a quick way of simulating flows ranging from laminar to turbulent regimes. The flow solver in Fluent is based on Reynolds-averaged Navier-Stokes equations (RANS) approach where turbulence models are used for the Reynolds stress terms [80]. Even though the solutions to RANS equations do not resolve small scale flow features, it does capture the macroscopic features of the flow reasonably well, especially for simple flows like channel flows. Considerable amount of research has been done in the past to evaluate the accuracy of different turbulence models for various types of flows with respect to the experiments [81–84].

Thus, in the current work, the investigation of turbulence of flow over the tooth tip of EGMs is done via modelling of the flow in Fluent CFD tool using an appropriate turbulence model.

4.1.1 Computational Mesh

The flow over the tooth tip occurs at a length scale which at least two orders of magnitude smaller than the size of the EGM. That is, this phenomenon is localized at the tooth tip and hence can be isolated from the overall flow behavior of the EGM. Figure 4.1 shows the 2D computational domain designed to study the flow at the tooth tip. The domain is in the TSV frame of reference. The bottom wall represents the internal face of the casing which moves with respect to the tooth with a velocity:

$$\mathrm{v} = \frac{2\pi N_r}{60} r_g \tag{4.2}$$

where N_r is the shaft speed in rpm and r_g is the radius of the gear.

The width of the tooth tip and the inclination of flank surfaces of the gear tooth correspond to the reference EGM E2.

With the help of ANSYS meshing tool, the fluid mesh is generated which is structured in the gap region with fixed number of cells across the gap. Outside the gap region, the mesh is unstructured and its size grows with each succeeding layer of elements at the rate of 2% per layer.

In turbulent wall bounded flows, the velocity profile near the wall consists of the viscous sublayer, log layer and outer layer [84]. To accurately capture the effects of all the layers, it is important to have the grid points very close to the walls. When wall functions are not used, the dimensionless distance of the first grid point from the wall y_1^+ should be ≤ 1. The dimensionless distance is defined as

$$y^+ = \frac{y u_\tau}{\nu} \tag{4.3}$$

where, friction velocity, u_τ is

$$u_\tau = \sqrt{\frac{\tau_w}{\rho}} \tag{4.4}$$

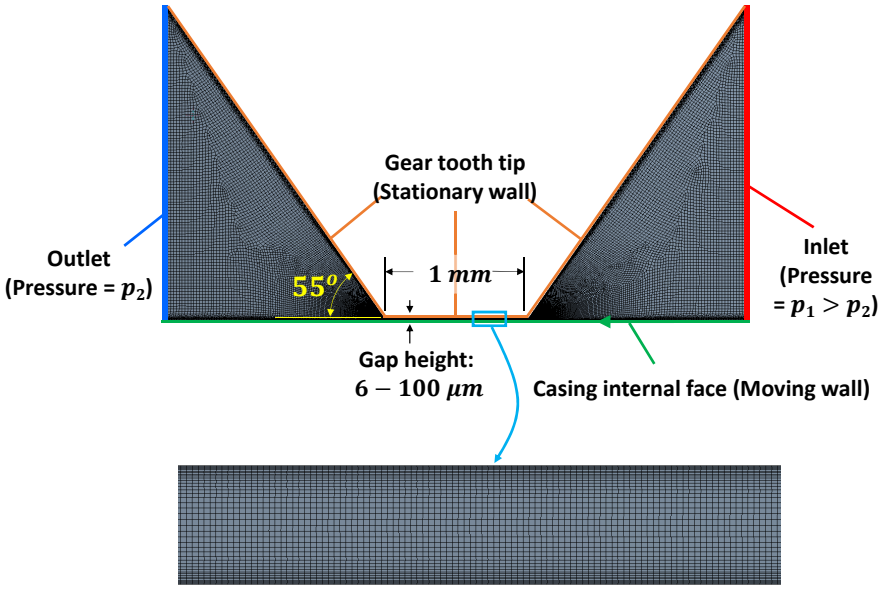

Figure 4.1. Computational domain for flow over the tooth tip. The domain is in the tooth frame of reference in which the casing surface is moving.

Hence, the distance of the first grid point from the wall, y_1, depends on wall shear stress, τ_w, which can only be reliably determined from the simulation results. Hence to determine y_1, an iterative procedure is followed involving following steps:

1. Guess a value of y_1.
2. Construct the mesh using inflation layer feature in Ansys meshing tool with this value of y_1.
3. Run the Fluent simulation.
4. Determine τ_w and correct the value of y_1. Go to step 2.

It only takes 2-3 iterations to obtain a converged value of y_1.

Multiple fluid domains are created with gap height at the tooth tip varying from 6 µm to 100 µm. Mesh sensitivity studies are conducted for each of these domains to

choose the appropriate mesh sizes. Table 4.1 shows the meshes used in the study for the domain with 20 μm gap height and Figure 4.2 shows the convergence of flow rate through the gap with mesh refinement.

Table 4.1.
Meshes used in mesh sensitivity study for fluid domain with 20 μm gap height.

Mesh identifier	Total number of cells
1	24358
2	43267
3	99720
4	163784
5	227012
6	348657

4.1.2 Fluent setup and solver

$k-\epsilon$ model and $k-\omega$ model are the most common turbulence models used in engineering. From Wilcox [84] and Fluent help [85], $k-\omega$ model performs better compared to $k-\epsilon$ model near the walls especially when flow separation is likely. In the current analysis, the flow is indeed likely to separate at the corners of the tooth tip. $k-\omega$ model however, is sensitive to freestream conditions. This problem was addressed in Menter's SST model [82] which combines the elements of $k-\epsilon$ and $k-\omega$ models. In fact, SST model accurately predicts the flow through an asymmetric plane diffuser [83,86] which has similar features of flow (e.g. wall bounded, flow separation) as the current flow of interest. In Fluent, the SST model coefficients are calibrated by the developers to accurately predict the flow separation from smooth surfaces. Hence, in this work, SST $k-\omega$ turbulence model is used.

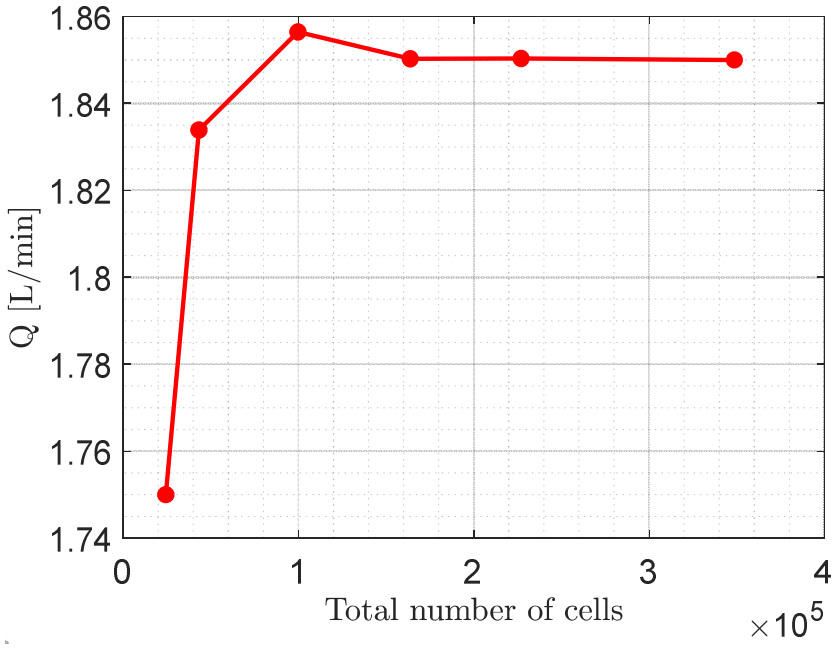

Figure 4.2. Results from mesh sensitivity study for the domain with 20 µm gap height. The simulations are conducted for v = 40 m/s, Δp = 40 bar with Jet A-1 fluid

Pressure boundary conditions are applied at the inlet and outlet of the domain (Figure 4.1). Moving wall boundary condition is applied at the bottom wall which represents the relative motion of the casing's internal surface with respect to the tooth tip.

SIMPLEC solver is used with 2nd order spatial discretization of pressure and momentum equations. The criteria of convergence is the reduction of scaled residuals [85] of continuity, x and y momentum, k and ω equations below 10^{-6}.

4.1.3 Simulation results

Figure 4.3 shows the sample results from Fluent for flow over the tooth tip where the gap height is 20 µm and the pressure difference is 40 bar. Case 1 simulates the tooth tip flow for fluid power application. It has an ISO VG 46 oil as the working

fluid and the relative velocity of the casing with respect to the tooth tip is 8 m/s. The flow streamlines for this flow case is shown in Figure 4.4. The flow rate through the gap observed in the Fluent simulation result is 0.1528 L/min which is close to 0.1526 L/min predicted from the laminar flow Eq. 4.1.

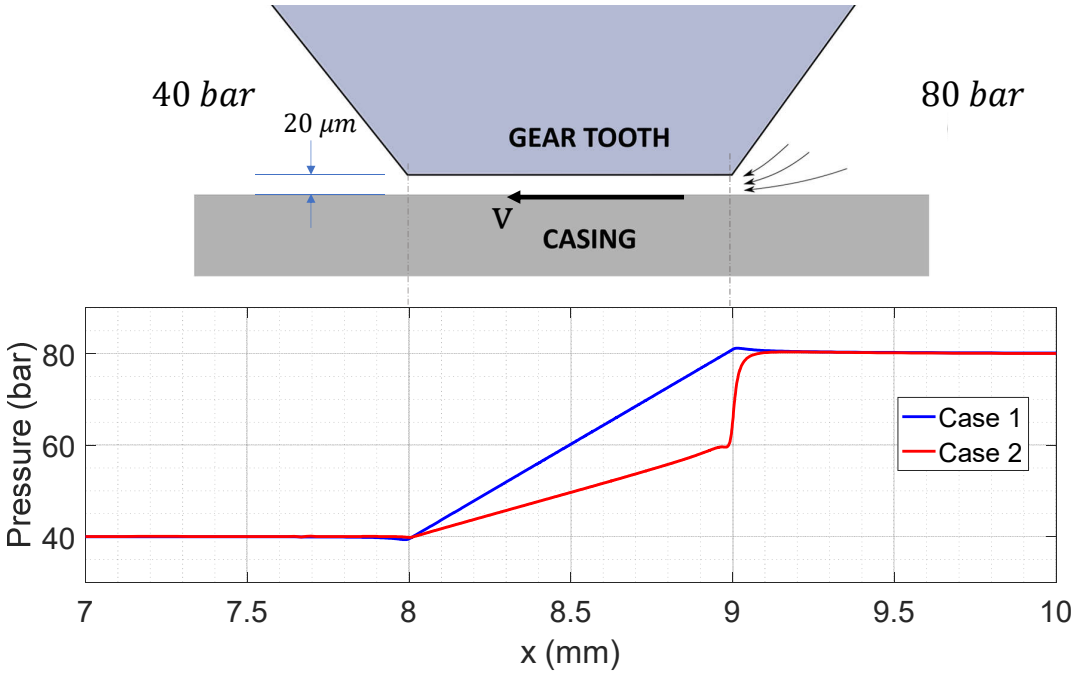

Figure 4.3. Pressure variation along the flow direction for (i) case 1: relative velocity v = 8 m/s and ISO VG 46 as working fluid (ii) case 2: relative velocity v = 40 m/s and Jet A-1 as working fluid

Case 2, in Figure 4.3, represents the flow over the tooth tip for a fuel injection application. In this case, the working fluid is Jet A-1 and the relative velocity is 40 m/s. Figure 4.5 shows the streamlines for this flow case which is significantly different on the inlet side and at the gap compared to the previous case. In particular, the flow separates from the corner of the tooth tip as it enters the gap leading to the formation of a recirculation zone. As a consequence, a significant pressure drop is observed at the entrance of the tooth tip (Figure 4.3). The flow rate through the gap observed from the Fluent simulation is 1.78 L/min which is less than half of 3.69

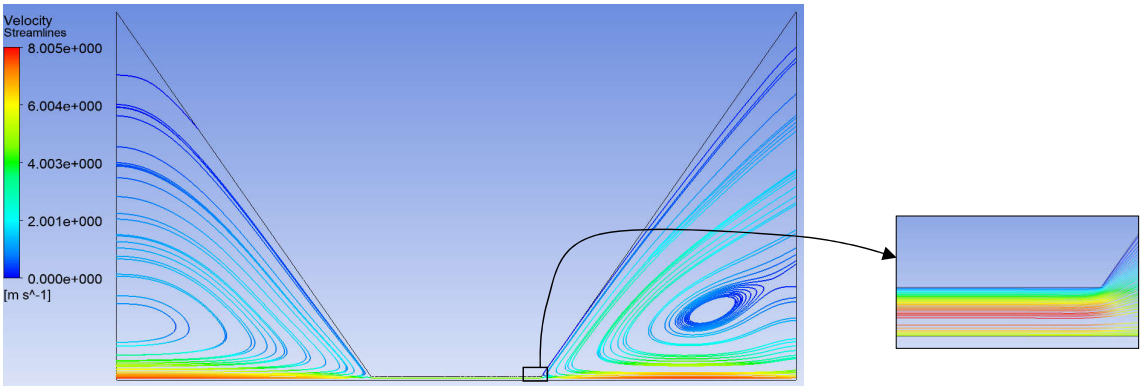

Figure 4.4. Flow streamlines for case 1: $\Delta p = 40$ bar, v = 8 m/s and ISO VG 46 as working fluid. Inset shows absence of any recirculation at the tooth tip entrance.

L/min predicted from the laminar flow Eq. 4.1 (Δp used in the laminar flow equation excludes the entrance pressure drop).

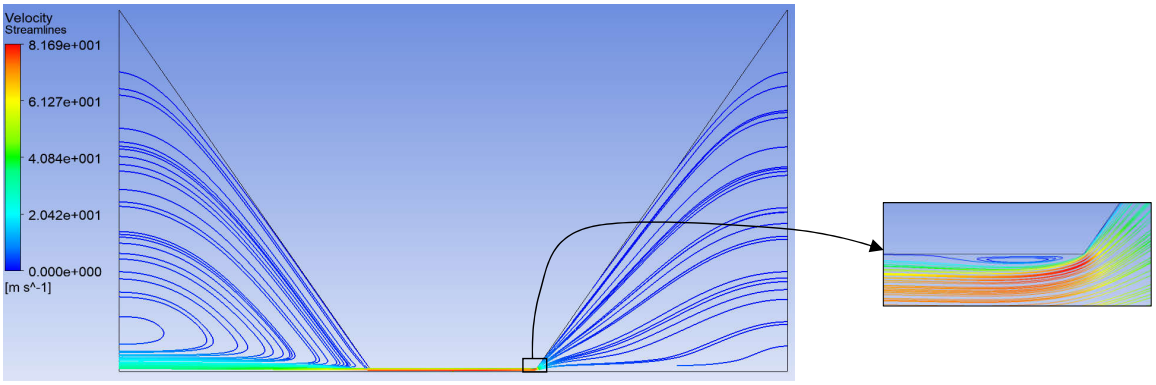

Figure 4.5. Flow streamlines for case 2: $\Delta p = 40$ bar, v = 40 m/s and Jet A-1 as working fluid. Inset shows the recirculation zone at the tooth tip entrance.

For further investigation, multiple simulations were carried out for a range of pressures (0-40 bar), surface velocities (0-40 m/s) and gap heights at the tooth tip (6-100 μm). Jet A-1 was chosen as the operating fluid. The results (a sample of which

is presented in Table 4.2) show that at low gap heights, pressures, and velocities, the flow is laminar and the flow relation of Eq. 4.1 accurately models the flow over the tooth tip. However, at higher gap heights, pressures, and velocities, the flow Reynolds number in the gap becomes very high indicating the domination of inertial effects in the flow. The flow separates at the corner of the tooth tip at the entrance of the gap and becomes turbulent in the gap region. From modelling perspective, the fluid experiences a significant pressure drop when it enters the gap at the tooth tip. Even after accounting for this pressure drop, the laminar flow relation (Eq. 4.1) significantly overpredicts the flow as compared to the flow obtained from Fluent.

Table 4.2.
Comparison of flow over the tooth tip between Fluent and Laminar flow equation

h (µm)	v (m/s)	Δp (bar)	Fluent		Laminar flow relation
			Q (L/min)	Re	Q (L/min)
6	5	5	0.3976	201	0.4015
20	20	5	0.5624	284	0.5772
40	10	40	4.3761	4418	54.9702
65	31	40	8.3468	8428	273.0760

From these observations, it is concluded that for the range of flow conditions that an EGM working in fuel injection applications has to operate with, the flow at the tooth tip becomes turbulent rendering the laminar flow relation inapplicable. Hence, there is a need of a leakage flow model suitable for turbulent flow as well as a model to predict the entrance pressure drop.

4.2 Analytical Modelling of turbulent flow over the tooth tip

Analyzing turbulent flow over the tooth tip via CFD simulations is useful in understanding the flow features, however, in lumped parameter modelling, the focus is not on understanding the detailed flow features of turbulence. The focus, instead, is to determine the flow rate at the tooth tip that can be used in the Fluid Dynamic Module. To maintain the advantage of HYGESim in terms of swift simulation of EGMs, simple analytical relations are needed that can capture the effects of turbulence at the tooth tip.

4.2.1 Turbulent flow relations for channel flow

Investigation of turbulent wall bounded flows has been an active area of research in past several decades both from experimental as well as modelling perspective. Exact analytical solution for even such simple turbulent flows does not exist. Analytical modelling of these flows are often a combination of theoretical relations and empirical correlations. Efforts related to the modelling of wall bounded flows started from Prandlt [87] and Karman [88] whose works related to the velocity profile close to wall led to now universally recognized "law of the wall" [80]. This law is applicable to a wide range of wall bounded flows. The velocity profile away from wall is heavily dependent on the flow parameters and multiple researchers [89–92] have proposed relations to model this velocity profile. For channel flow, Churchill and Chan [93] have combined the theory of flow behavior near wall with well validated empirical correlations near center of the flow to propose the expression for velocity profile in turbulent channel flows:

$$v = \left[\frac{\left(1 + y^+ - exp\{-1.75(y^+/10)^4\}\right)^3}{(y^+)^6} + \left(2.5\ln\{9.025y^+ + 1\} + \frac{15}{4}Y^2 - \frac{10}{3}Y^3\right)^{-3} \right]^{-\frac{1}{3}} \left[\frac{\tau}{\rho}\right]^{0.5} \quad (4.5)$$

where τ is the wall shear stress, $Y = y/h$, $y^+ = y(\rho\tau)^{0.5}/\mu$ and y is the distance from the wall.

However, a major limitation of these models is the fact the they do not consider the relative motion of the two walls in the channel. A simple but poor approximation for modelling Couette-Poiseuille flow can be the addition of the Couette flow velocity vY to the velocity profile in Eq. 4.5.

Significant works have also been done towards the modelling of turbulent flow in the bearings [94–96]. Mentioning this is relevant here since these approaches often start with developing a model for channel flow and then applying it to the bearings. Among them, the model developed by Ng and Pan [94] can be useful in the current work due to its non-dependence on experimental data:

$$Q = \mathrm{v}h\Big(\frac{1}{2} - G_x B_x\Big) \tag{4.6}$$

where

$$B_x = \frac{h^2}{\mu \mathrm{v}} \frac{\partial p}{\partial x} \tag{4.7}$$

and G_x is a function of vh/ν provided graphically in their original paper.

The limitation of this model is that the derivation of this model includes certain linearization steps which may lead to poor accuracy at extreme flow scenarios.

The models proposed by “Churchill and Chan” and “Ng and Pan” are appropriate for the requirement of the lumped parameter model. Due to the presence of empirical relations embedded in these models, it is obvious that these models are not applicable for all range of flow parameters. To decide which one of these is more accurate for the modelling of flow over the tooth tips in EGMs, comparison of these models with Fluent results was done for a set of flow parameters commonly encountered by EGMs. In particular, there are two drivers of flow over the tooth tip:

- Couette driver: The relative motion of the casing with respect to the tooth tip (in TSV frame of reference). This driver can be expressed with the following dimensionless number:

$$Re_c = \frac{\rho v h}{\mu} \tag{4.8}$$

- Poiseuille driver: The pressure difference across the tooth tip. Following dimensionless number represents this driver

$$b^+ = \frac{(0.5h)^{1.5}}{\mu}\left[\rho\frac{\Delta p}{L}\right]^{0.5} \tag{4.9}$$

  Here Δp excludes the pressure drop at the entrance of tooth tip gap.

The range of $Re_c \in [0, 4000]$ and $b^+ \in [0, 300]$ covers a wide range of flow conditions typically present at the tooth tip of EGMs.

Figure 4.6 shows that the model proposed by Ng and Pan performs poorly at high b^+. In contrast, the model proposed by Churchill and Chan is accurate for a wide range of b^+ and Re_c. The accuracy of this model suffers at low values of b^+ and Re_c. This happens because at low values of b^+ and Re_c, the flow is likely to be laminar and the empirical relations in the model no longer apply. The laminar relation plot in Figure 4.6 confirms this hypothesis by its good performance at low values of b^+ and Re_c.

From these results, it is concluded that the relation from Churchill and Chan should be used for modelling the flow over the tooth tip when $Re_c > 2000$ and $b^+ > 30$. For lower values of b^+ and Re_c, the laminar relation still works well.

4.2.2 Entrance Pressure Drop

As described in section 4.1.3, in turbulent flow regime, the flow experiences a pressure drop as it enters the gap at the tooth tip due to the formation of recirculation zone. From CFD simulations, it is observed that this entrance pressure drop can be up to 95 % of the pressure difference across the tooth tip. This phenomenon of entrance

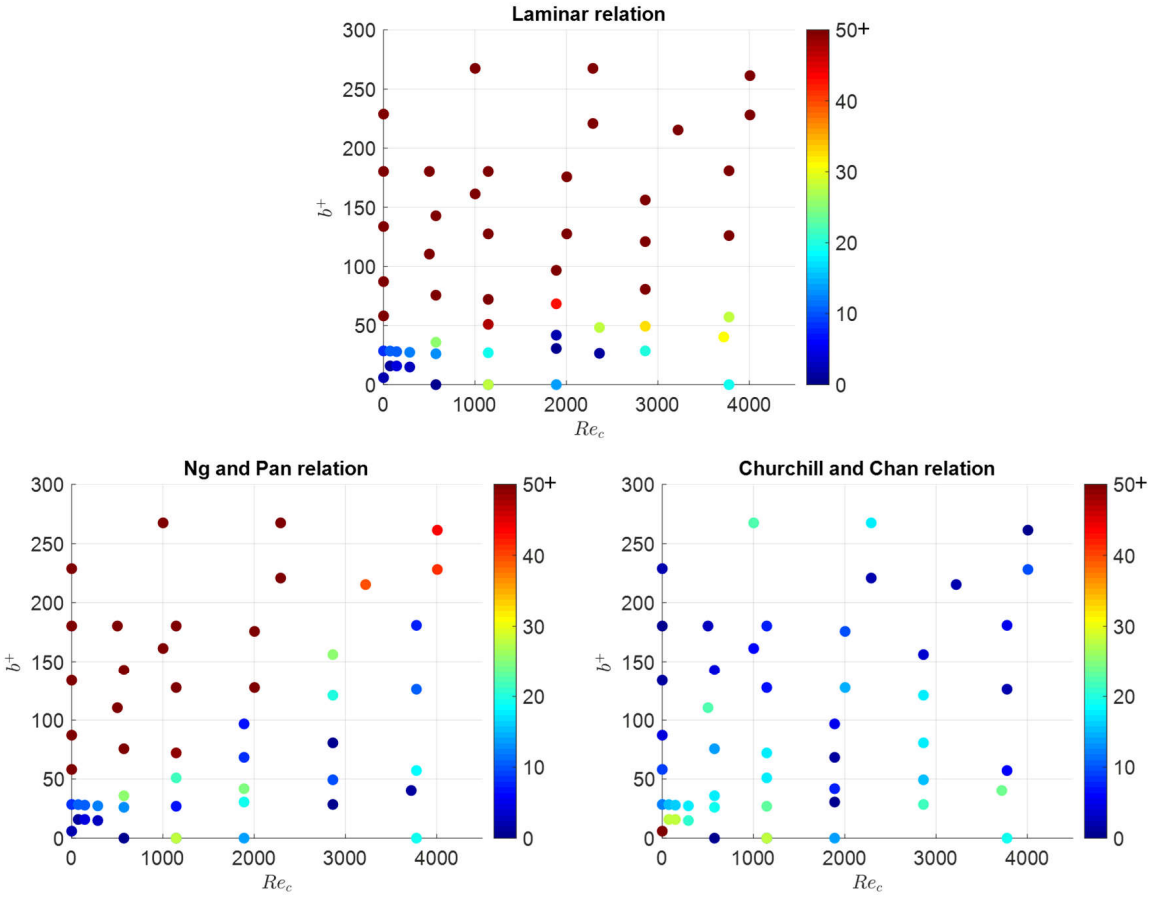

Figure 4.6. Accuracy of the flow relations (laminar flow relation Eq. 4.1, Ng and Pan [94], and Churchill and Chan [93]) for the flow through tooth tip. The color indicates percentage error of flow predicted by the relations with respect to Fluent simulations. Existence on entrance pressure drop prevents uniform distribution of points.

pressure drop has been experimentally studied in detail by Idelchik [60]. He expressed the pressure drop at the entrance by the means of resistance coefficient

$$\xi = \frac{\Delta p}{0.5\rho v^2} \tag{4.10}$$

From the Fluent simulation results, the value of $\xi = 1.2$ is able to predict the entrance pressure drop fairly accurately (Figure 4.7) for a wide range of b^+ and Re_c. Hence above formulation is included in the turbulence model for flow over the tooth tip.

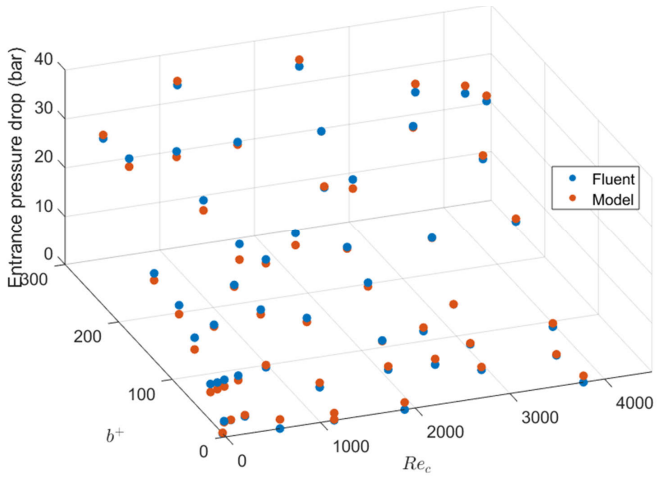

Figure 4.7. Comparison of entrance pressure drop prediction from Fluent and the Idelchik model with $\xi = 1.2$

4.3 Results from the proposed model

The tooth tip leakage flow model for turbulent flows described in section 4.2 is implemented in HYGESim's Fluid Dynamic Module such that it uses either the laminar flow model (Eq. 4.1) or the turbulent flow model based on the values of b^+ and Re_c. Simulations are conducted for the reference fuel pump (E2), details of which is provided in Table 4.3.

First, simulations are conducted with an ISO VG 46 mineral oil as the working fluid and for a range of operating conditions that emulate fluid power operation. The results show no difference between the traditional model (which assumes laminar flow over the tooth tip and no entrance loss) and the proposed model. Figure 4.8(a) shows the results obtained for the operating condition: 1000 rpm, 100 bar, where the TSV pressure can be seen to be identical between the traditional model and the one proposed in this chapter. The reason for this similarity lies in the fact that for operating conditions of lower speeds, pressures, and higher viscosity fluids, the Couette and Poiseuille flow drivers are small (Figure 4.8(b)) and laminar flow relation

Table 4.3.
Geometric parameters of the reference pump E2

Parameters	**Values**
Number of teeth	13
Gear radius	40 mm
Gear depth	25 mm
Theoretical displacement	69 cc/rev
Width of the tooth tip	1 mm
Clearance at the tooth tip	50 μm
Clearance (radial) at the bearing	35 μm

(Eq. 4.1) accurately describes the leakage flow. Hence, the results do not change with the proposed model.

Next, simulations are conducted with Jet A-1 as the working fluid and for a range of operating conditions that emulate fuel injection operation. Results show significant differences between the traditional model (which assumes laminar flow over tooth tip and no entrance loss) and the proposed model. To illustrate this, simulation results are reported for the operating condition of 8000 rpm and 100 bar pressure. Figure 4.9(a) shows the difference in pressurization of TSV for the two models. The plot can be understood in the following manner. The angle in the x axis indicates the angle of the center of the TSV from the meshing zone (shown in Figure 4.10(b)). When the TSV comes out of the meshing zone, its volume increases leading to reduction in its pressure below the inlet pressure (10 bar). From there onwards up to roughly 90°, the TSV pressure stays the same as the inlet pressure. At this angle, the TSV is cut off from the inlet i.e. both its leading and lagging teeth are facing the casing. From here onwards, The TSV pressure starts to increase, its rate being dependent on the amount of tooth tip leakage flow to that TSV. At around 145°, the leading

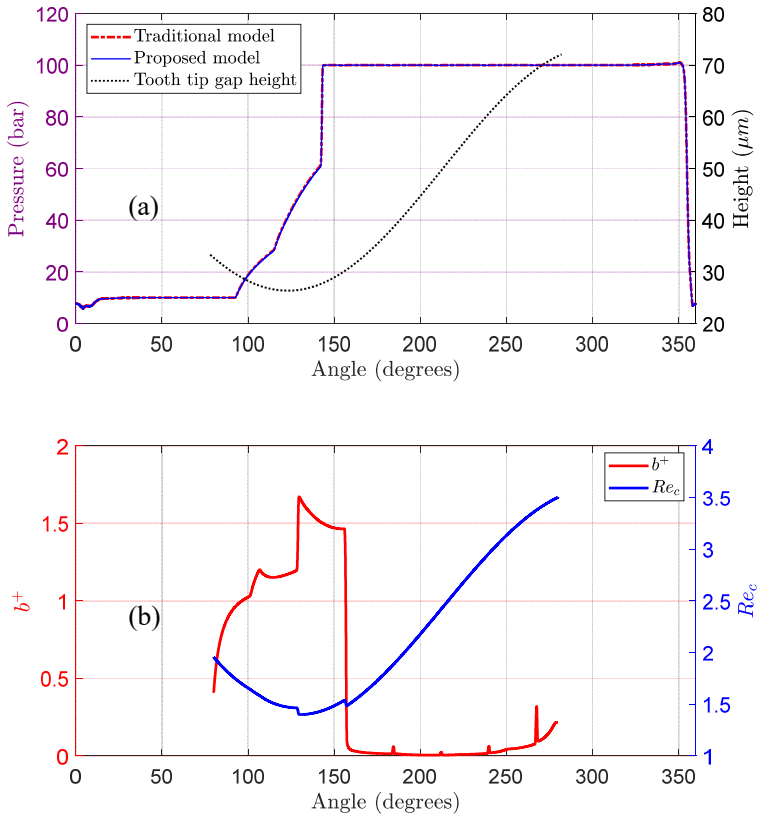

Figure 4.8. Results from HYGESim for gear pump operating with ISO VG 46 as working fluid at 1000 rpm and 100 bar pressure. (a) TSV pressure comparison between the traditional and proposed model; and variation of gap height between the tooth tip and casing. (b) Poiseuille and Couette flow driver values at a tooth tip.

tooth of the TSV reaches the backflow groove. Figure 4.10(a) shows the bushing in the reference unit with the backflow groove. This groove brings the high pressure fluid from the outlet. Hence, as soon as the TSV opens to the backflow groove, its pressure becomes equal to the outlet pressure.

Figure 4.9(b) shows that when the TSV enters the casing, the value of b^+ increases to the values higher than the critical value of 30 indicating turbulence of flow over the tooth tip. Hence the leakage flow determined from laminar flow assumption is very high compared to the new model that switches to turbulent formulation once

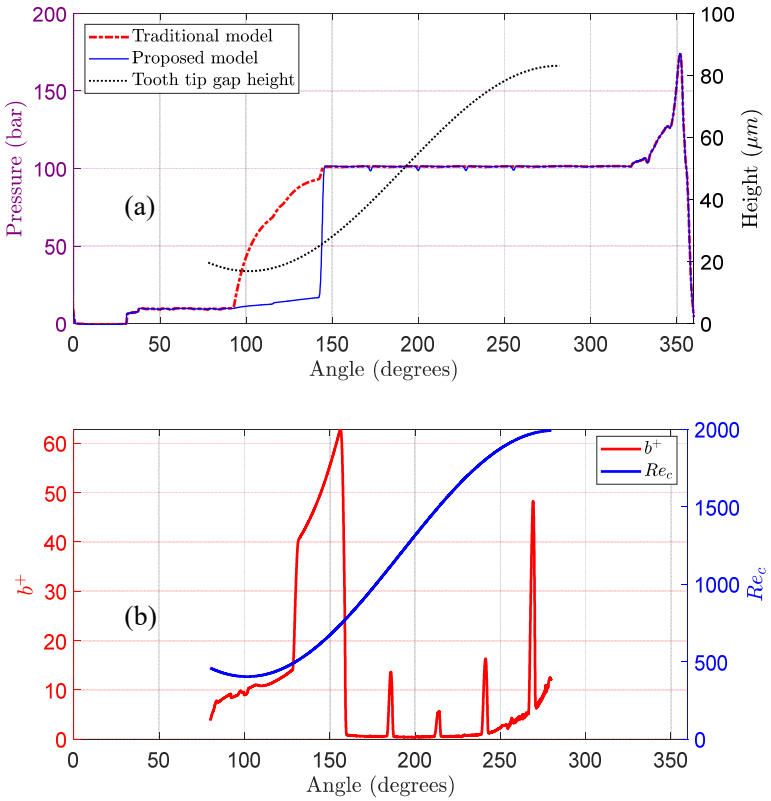

Figure 4.9. Results from HYGESim for gear pump operating with Jet A-1 as working fluid at 8000 rpm and 100 bar pressure. (a) TSV pressure comparison between the traditional model and proposed model; and variation of gap height between the tooth tip and casing for the proposed model. (b) Poiseuille and Couette flow driver values at a tooth tip.

b^+ crosses 30 (Figure 4.11). Thus, the TSV in the traditional model formulation experiences an early pressurization compared to the proposed model.

Accurate prediction of TSV pressurization is important in determining the radial loading on the gears which has to be supported by the journal bearings. The micromotion of the gears depend on this radial loading. Hence, the TSV pressurization profile ultimately effects the leakage gap at the tooth tip and associated leakage flow.

Moreover, the simulation tools for studying the axial balance in pressure compensated EGMs rely on accurate information about TSV pressurization. In fact, the

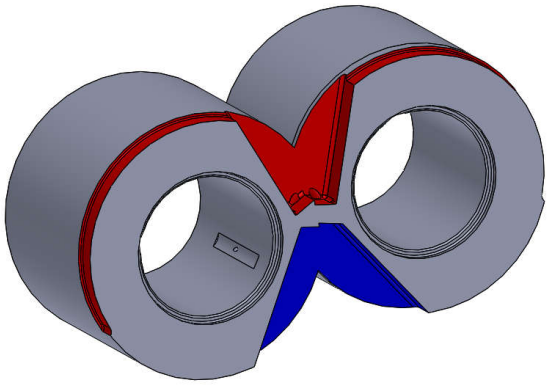

(a) Bushing with the backflow groove and high pressure relief groove highlighted in red

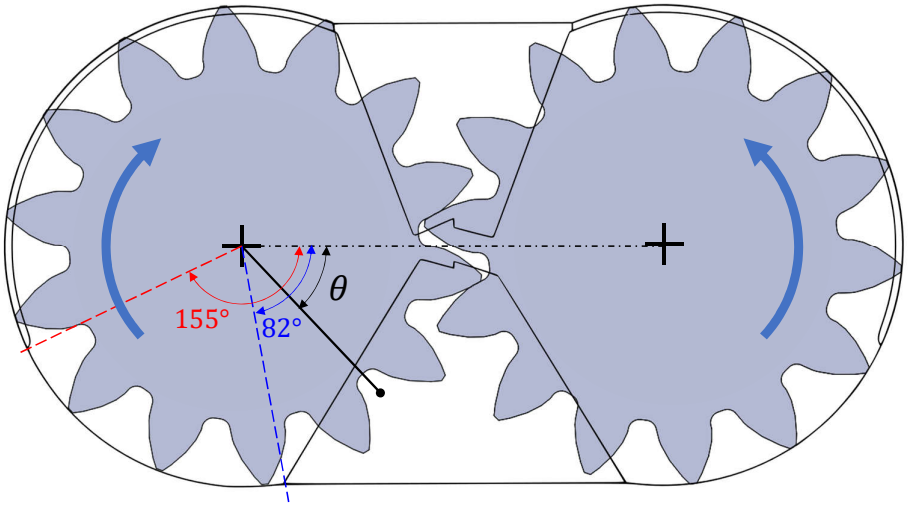

(b) 2D view of the gears with outline of the bushing overlaid. Angular position of a TSV is θ, the start angle of the casing is 82° and the start angle of the backflow groove is 155°.

Figure 4.10. Bushing on the reference unit

TSV pressure information from the model proposed here was utilized in the study of axial compensation system in the reference pump E2 by Thiagarajan [46] where a

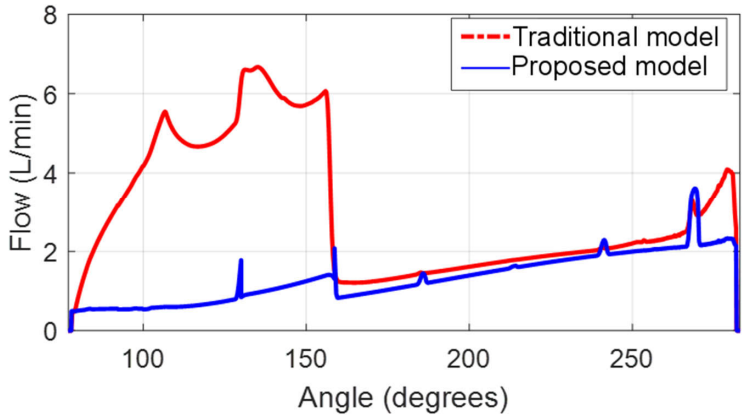

Figure 4.11. Comparison of the flow over the tooth tip for simulations with traditional and proposed models for operating condition: 8000 rpm, 100 bar with Jet A-1 as working fluid.

good match for the axial position of the bearings between experiments and simulations was observed. The equilibrium position of the bearing is achieved by a balance of pressure forces on each side of the bearing. The TSV pressure plays a significant role in determining the force from the gear side. Hence, a good match in the bearing position not only validated the Lateral Gap Module but also acted as an indirect validation for the turbulence modelling of the leakage flow at the tooth tip.

The outlet flow rate for the operating condition described earlier from the traditional model and the proposed model comes out to be 548 L/min and 553 L/min, respectively. The difference will be even bigger if the clearances at the tooth tip and bearing are such that the gap height at the tooth tip is high even after gears' micromotion towards the inlet. For example, if the clearance at the tooth tip and the bearing are set to 100 µm and 60 µm, respectively, the outlet flow with traditional model and proposed model are 460 L/min (82.2 % efficient) and 553 L/min (99.7 % efficient), respectively. This shows the significance of the proposed model for an accurate prediction of the volumetric efficiency.

Figure 4.12 shows that the outlet flow non-uniformity prediction of the simulation tool is lower with the traditional model compared to the proposed model that incor-

porates turbulent flow relations. In the hydraulic systems, the outlet flow pulsation manifests into pressure ripple that leads to noise and vibration issues. Hence, the proposed model, when integrated with the simulation tools that model noise sources in EGMs [97], has better prospects of accurately predicting the noise.

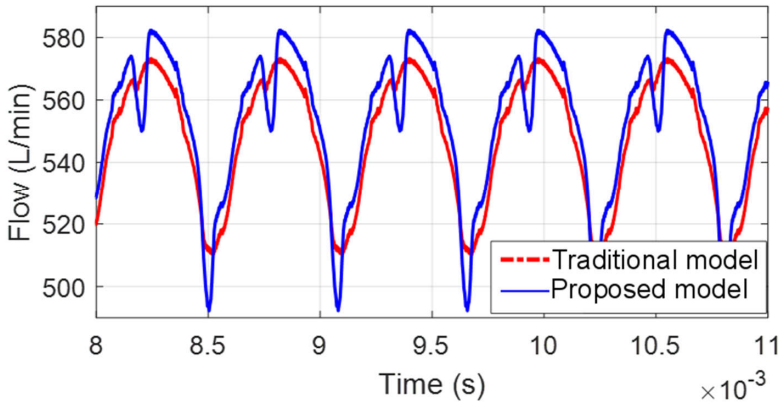

Figure 4.12. Outlet flow ripple comparison for simulations with traditional and proposed models for operating condition: 8000 rpm, 100 bar with Jet A-1 as working fluid.

5. MODELLING OF MANUFACTURING ERRORS IN EXTERNAL GEAR MACHINES

Previous couple of chapters focused on key flow aspects and their impact on EGM performance. This chapter and the next one deals with key geometric aspects of EGMs that significantly influence their performance. In this chapter particularly, common manufacturing errors on the gears are incorporated in EGM modelling (Aspect A3) and the effect of these errors on the performance of EGMs is investigated.

In the real world, a machine cannot be manufactured with exact dimensions. Various types of errors are introduced in a part during the manufacturing process. To control the extent of these errors, tolerances are specified on machine drawings as an indicator of maximum allowable error. However, the tighter a tolerance is, the higher is the cost of manufacturing.

For gears, the manufacturing processes introduce errors on various aspects of their geometry. ISO [98], DIN [99] and Agma [100] standards are used to classify the gears on the basis of these errors. Mainly, these standards deal with profile errors, pitch errors and lead errors. However, there is no emphasis on the errors related to conicity and concentricity of the (imaginary) cylinders formed by the top lands of the gears (i.e. tooth tips). These errors are typically on the order of few microns (up to few tens of microns) which is at the same order as the clearances between the gears and the casing in EGMs. Hence, these manufacturing errors impact the geometry of the clearances at the gear tooth tips, which in turn impacts the performance of EGMs. Experiments are an expensive and time consuming way to understand and establish these relationships. Numerical modelling, instead, is an inexpensive and faster method of simulating the EGM operation and study the impact of various factors on EGM performance.

However, among all the numerical models for EGMs developed in past (section1.6), none consider the impact of manufacturing errors on flow characteristics of EGMs. Furthermore, despite the existence of these models, rigorous tolerance studies are rarely found in the literature. For EGMs, only Mucchi et al. [17] consider one of the errors in gears: the tooth profile error, which might impact the noise and vibration during operation. Manufacturing errors in gears have been investigated in past in terms of their impact on the operation of gear transmissions [101–103] but those works are tangential to the goal of this research.

The goal of the work presented in this chapter is to fill the lack of numerical approaches suitable to model the effects of critical tolerances in EGMs by developing a numerical model that can permit investigating the impact of two common manufacturing errors on the volumetric performance of EGMs: the conicity error and the concentricity error. The model builds upon the HYGESim simulation tool explained in Chapter 2. However, a simplified model is also proposed that can be used within other lumped parameter based models. To validate the model, experiments are conducted on six units of the reference pump E3, each having a different combination of manufacturing errors.

5.1 Manufacturing errors considered

In this study, two common errors in the gear geometry are considered that occur during gear manufacturing: conicity and concentricity of the cylinder formed by the top land of a gear with respect to the rotational axis.

5.1.1 Conicity

Figure 5.1 shows an example of the conicity error on a gear. If a machine drawing for a gear indicates a diameter, say d, and a tolerance on the diameter, say $\pm\delta$, then an acceptable gear can have a conic shape such that the diameter on one end is $d_{max} = d + \delta$, while the diameter on the other end is $d_{min} = d - \delta$.

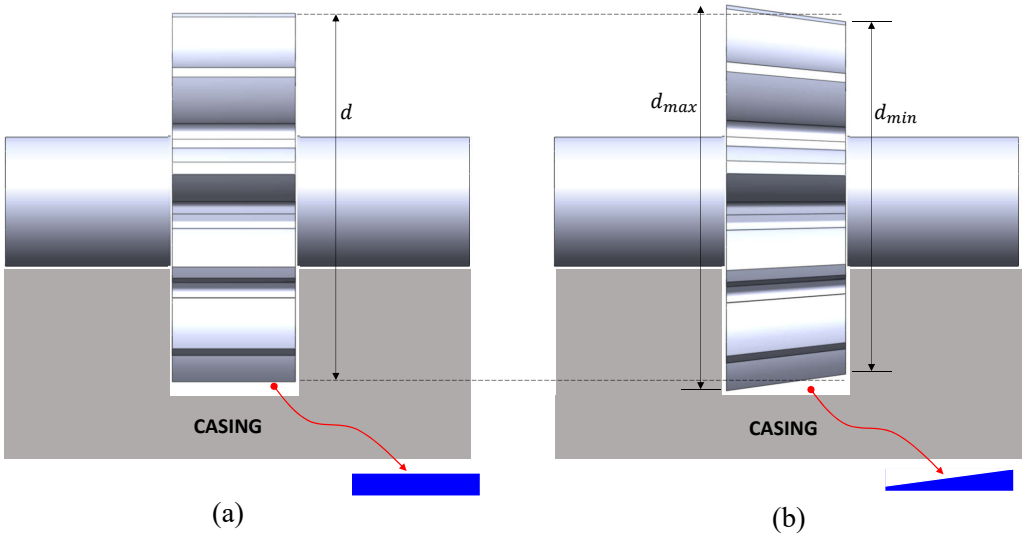

Figure 5.1. Illustration of gear conicity: (a) perfect gear (b) gear with conicity. The blue quadrilateral shows the cross section view of clearance path at a tooth tip.

This shape of the gear changes the clearance geometry at the gear tooth tip as shown via the blue quadrilaterals in Figure 5.1. Since, this clearance is responsible for the leakage flow over the tooth tip, the conicity error directly impacts the volumetric efficiency of EGMs.

5.1.2 Concentricity

In gear manufacturing, another common error that is observed is the concentricity error, where, the gear's axis is eccentric with respect to the shaft axis (Figure 5.2(b) and (c)). This error is controlled using the runout tolerance. As per ANSI Y14.5M-1982 [104], runout is the variation in a circular feature with respect to a datum axis when the part is rotated 360° around the datum. Runout covers two types of

manufacturing errors: concentricity and circularity. In this work, only concentricity of the gears is considered.

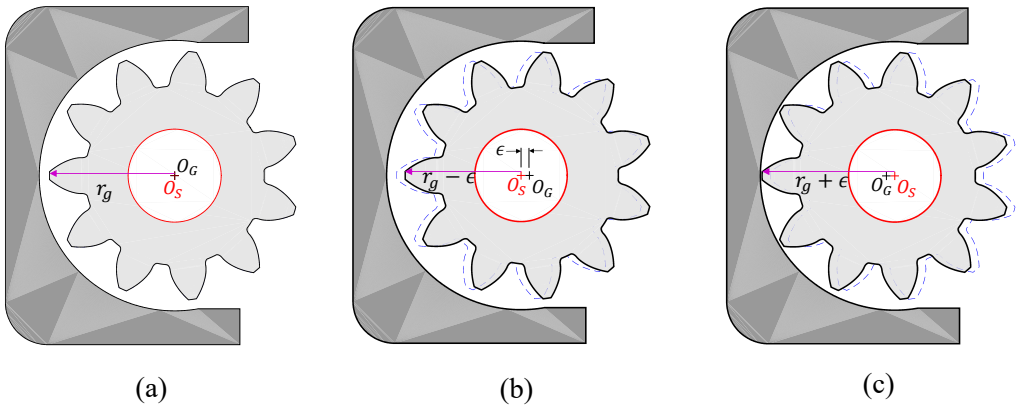

Figure 5.2. Concentricity error and its impact on the gap height at the tooth tips. (a) shows a gear with no concentricity error. (b) and (c) show Gears with the shaft axis, O_S, offset from the gear axis, O_G

Figure 5.3(a) illustrates how the runout error is measured using a height gauge. The part is rotated around the datum axis which is the axis of rotation of the part. The height gauge placed above the surface measures the runout in terms of variation of surface's instantaneous vertical position. When only concentricity error is present, the measurement from the height gauge resembles a sine wave (Figure 5.3(b)). For gears, the axis of the shaft is the datum axis, and the height gauge placed on the gear tooth tip measures the concentricity error.

It is important to note that the concentricity tolerance on a gear is independent of the diameter tolerance on the gear. This implies that, due to the concentricity error, the distance from the shaft axis to the tip of each tooth can either be higher or lower than the radius of the gear. This is illustrated in Figure 5.2 via a radius vector from the shaft center to a gear tooth tip. If the gear radius is $r_g (= d/2)$ and the distance between the shaft center and the gear center (concentricity error) is ϵ, then the distance of a gear tooth tip from the shaft center can be as low as $r_g - \epsilon$

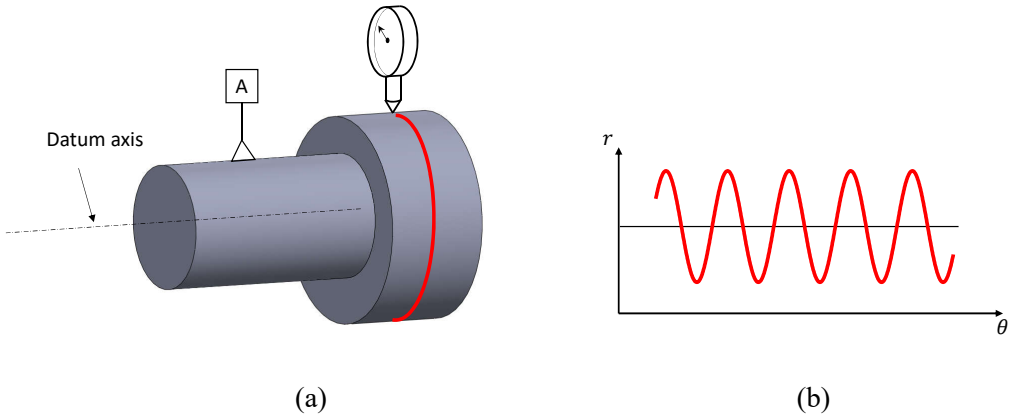

Figure 5.3. (a) Runout measurement (b) Height gauge reading for concentricity error: sine wave with period corresponding to one revolution

or as high as $r_g + \epsilon$. It has to be noted that the term "gear center" refers to the trace of the axis of the cylinder formed by the top land of the gear. The variation of distance of the gear tooth tip from the shaft center impacts the instantaneous height of the gap between the gear tooth tip and the internal surface of the casing. This can be seen qualitatively in Figure 5.2. The height of the gap at the tooth tip directly impacts the leakage flow over the tooth tip. Thus, similar to the conicity error, the concentricity affects the leakage flow and hence the volumetric efficiency of EGMs.

5.2 Modelling of manufacturing errors in HYGESim

In the EGM simulation tool HYGESim, the Fluid Dynamic Module is responsible for evaluating the leakage flow (refer section 2.1). In the current work, the leakage flow evaluation methodology is revised to incorporate the conicity and concentricity errors. The methodology is explained in the following subsections.

5.2.1 Concentricity error implementation with gear micromotion

In Figure 5.4, a section of EGM perpendicular to the rotation axis is shown. O_C is the center of the casing, O_S is the center of the shaft which is offset from O_C, due to the micromotion phenomenon. The vector $\vec{e}$ represents the magnitude and direction of the micromotion. O_G is the center of the gear which is offset from O_s, due to concentricity error. The vector $\vec{\epsilon}$ represents the magnitude and direction of the concentricity error. During EGM operation, the magnitude and direction of $\vec{e}$ does not change significantly [21]. In contrast, during operation, $\vec{\epsilon}$ has a constant magnitude, but it rotates with the gear rotation (θ indicates the instantaneous angular position of $\vec{\epsilon}$). Now $\vec{r_g}$ is the radius vector indicating the position of a tooth tip, P, from gear's center, then, its position from shaft's center is

$$\vec{r_S} = \vec{r_g} + \vec{\epsilon} \tag{5.1}$$

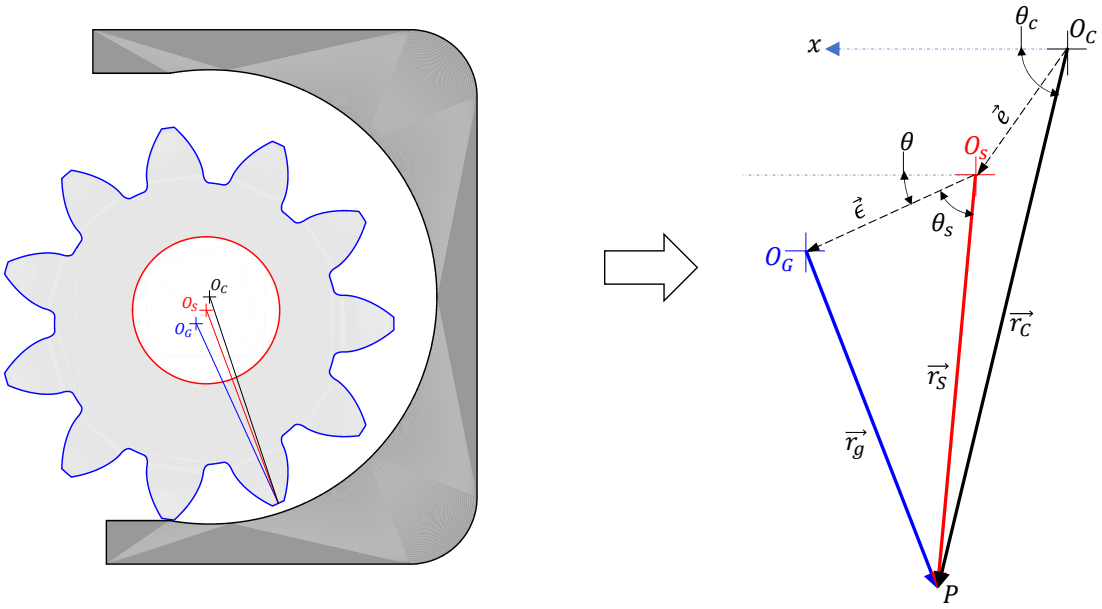

Figure 5.4. Evaluation of distance of a tooth tip from the casing center (clearance exaggerated for clarity)

In algebraic form, if θ_S is the angular position of this tooth tip from $\vec{\epsilon}$, then using cosine rule and solving for r_S, following expression for the magnitude of $\vec{r_S}$ is obtained.

$$r_S = \sqrt{r_g^2 - \epsilon^2 \sin^2 \theta_S} + \epsilon \cos \theta_S \tag{5.2}$$

Now, the position of this tooth tip with respect to the casing center can be expressed as

$$\vec{r_C} = \vec{r_S} + \vec{e} \tag{5.3}$$

Now, if $\overrightarrow{R_C}$ is the radius vector of the casing passing through P, then, the instantaneous gap height at the tooth tip P, is

$$h = \left|\overrightarrow{R_C} - \vec{r_C}\right| \tag{5.4}$$

Here, R_C is constant when the casing's internal surface is perfectly circular. However, if an EGM is designed such that the gear tooth tip touches the casing causing the wearing of the casing, then R_C varies with angular position.

5.2.2 Conicity error implementation

Conicity error results in a trapezoidal geometry of the gap at the tooth tip as shown in Figure 5.1(b). If the height of the gap on one end of the tip is h and and conicity error is δ, then the height on the other end will be $h + \delta$ (Figure 5.5). The flow through the gap is driven by the pressure difference across the gap and the motion of the tooth tip (both flow drivers are in x direction). Since there is no flow or pressure gradient in z direction, the flow can still be considered planar. Now, consider a differential section of the width of the gap, dz, at a distance z from the side of the gap where height is h. Then, the two differential surfaces at the top and the bottom of this section can be approximated as parallel surfaces. Therefore, the expression for differential flow through this section of the gap will be a differential form of Eq. 2.3:

$$dQ = \frac{h(z)^3}{12\mu L}\Delta p dz + \frac{\mathrm{v}h(z)}{2}dz \tag{5.5}$$

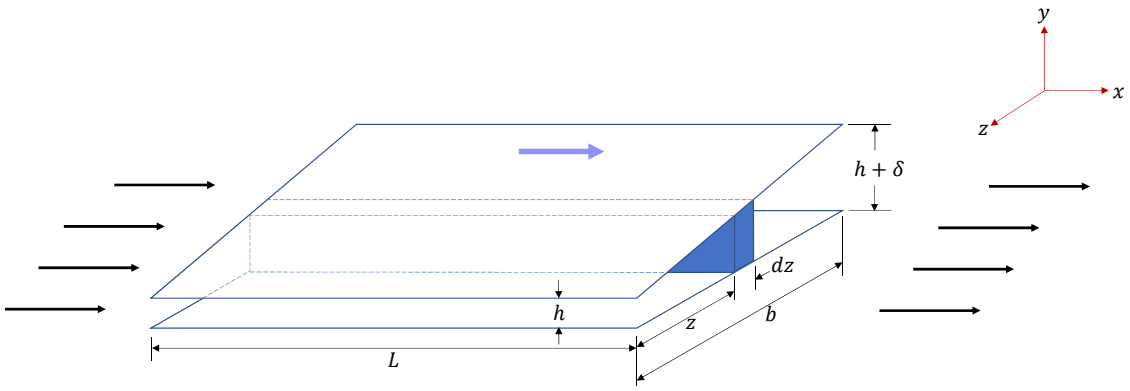

Figure 5.5. Geometry of the gap at the tooth tip due to conicity error ($b \gg L$). Flow direction is shown in black parallel arrows

Here,

$$h(z) = h + \frac{z}{b}\delta \tag{5.6}$$

Then, integrating the flow over the whole width of the gap, b,

$$Q = \frac{\Delta p}{12\mu L}\int_0^b \left(h + \frac{z}{b}\delta\right)^3 dz + \frac{\mathrm{v}}{2}\int_0^b \left(h + \frac{z}{b}\delta\right) dz \tag{5.7}$$

$$\implies Q = b\Big[\frac{\Delta p}{48\mu L}(4h^3 + 6h^2\delta + 4h\delta^2 + \delta^3) + \frac{\mathrm{v}}{2}\Big(h + \frac{\delta}{2}\Big)\Big] \tag{5.8}$$

When both conicity and concentricity errors are present, the strategies explained in subsections 5.2.1 and 5.2.2 can be superimposed. Due to conicity, the two axial faces of gears will have two different radii, therefore, the steps detailed in the section 5.2.1 for each face will yield different height of the gap at a tooth tip at each face. Then the steps outlined in section 5.2.2 can be used to evaluate the leakage flow over the tooth tip.

5.3 Effective gap height approach

The modelling approach described in section 5.2 is developed to be compatible with the HYGESim tool. However, in this section, an alternate approach of modelling

the manufacturing errors is proposed that can be used in any simple lumped parameter based simulation models. This approach originates from the idea that for any EGM with conicity and concentricity errors, an effective constant gap height at the tooth tip should exist. That is, an EGM with this effective gap height but no manufacturing errors will exhibit same volumetric performance as an EGM with the actual non-uniform gap height due the presence of these manufacturing errors.

This approach has an additional benefit that if the effective gap heights can be obtained for a set of EGMs, a qualitative volumetric efficiency comparison can be made without having to experimentally test the EGMs or conduct simulations.

It is to be noted that in this approach, the flow over the tooth tip due to its motion with respect to the casing's internal surface, i.e. Couette flow is neglected. During the operation of most EGMs, the Couette flow over the gear tooth tip is very small compared to the Poiseuille flow, so, this simplification is acceptable.

5.3.1 Conicity error

When only the conicity error exists, the determination of the effective gap height is straight forward. Eq. 5.8 represents the leakage flow over a tooth tip where the height on one side of the gear is h and on the other side is $h + \delta$. If the gear has no conicity error and the height at the tooth tip is h_{eff}, then the leakage flow rate expression becomes:

$$Q = b\frac{\Delta p}{12\mu L}h_{eff}^3 \tag{5.9}$$

Neglecting the Couette term in Eq. 5.8 and comparing it with Eq. 5.9, the expression of the effective gap height that takes the conicity error into account is

$$h_{eff} = \sqrt[3]{\frac{1}{4}(4h^3 + 6h^2\delta + 4h\delta^2 + \delta^3)} \tag{5.10}$$

This equation can be transformed in terms of the mean gap height and conicity error (as illustrated in Figure 5.6).

$$h_{eff} = \sqrt[3]{h_{mean}(h_{mean}^2 + (\delta/2)^2)} \tag{5.11}$$

This gives an interesting insight related to the effect of conicity error on the performance of EGMs. For a given mean diameter of the gear, the effective gap height increases with an increase in the conicity error. This implies that the volumetric efficiency of the EGM decreases with an increase in the conicity error.

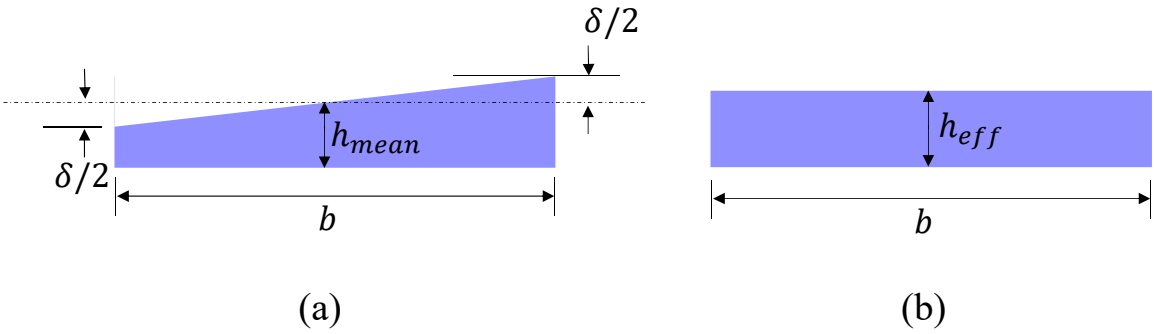

Figure 5.6. Geometry of the gap at the tooth tip. (a) gear with conicity error (b) gear with no error

5.3.2 Concentricity error

In contrast to the conicity error (which leads to an identical change in the gap height at all the tooth tips), the concentricity error leads to changes in the gap height at each tooth in a dissimilar manner. So, in order to determine an effective gap height, the interaction among gap heights at all the teeth must be considered.

The leakage flows over the tooth tips essentially form a flow connection from the inlet of the EGM to the outlet. Figure 5.7(b) shows the hydraulic circuit for the leakage flows over the tooth tips for the driven gear. In this circuit, the purple colored orifices represent the resistance to the flow formed by the gaps at the tooth tips. V_1 is the TSV that is connected to the inlet and V_{N+1} is the TSV connected to the outlet. Since the area of the flow connections between V_1 and inlet, and V_{N+1} and the outlet are very large, the pressure in the volume V_1 will be close to the inlet pressure and

pressure in the volume V_{N+1} will be close to the outlet pressure. So, in the current analysis, the hydraulic circuit from V_1 to V_{N+1} is considered (Figure 5.7(c)).

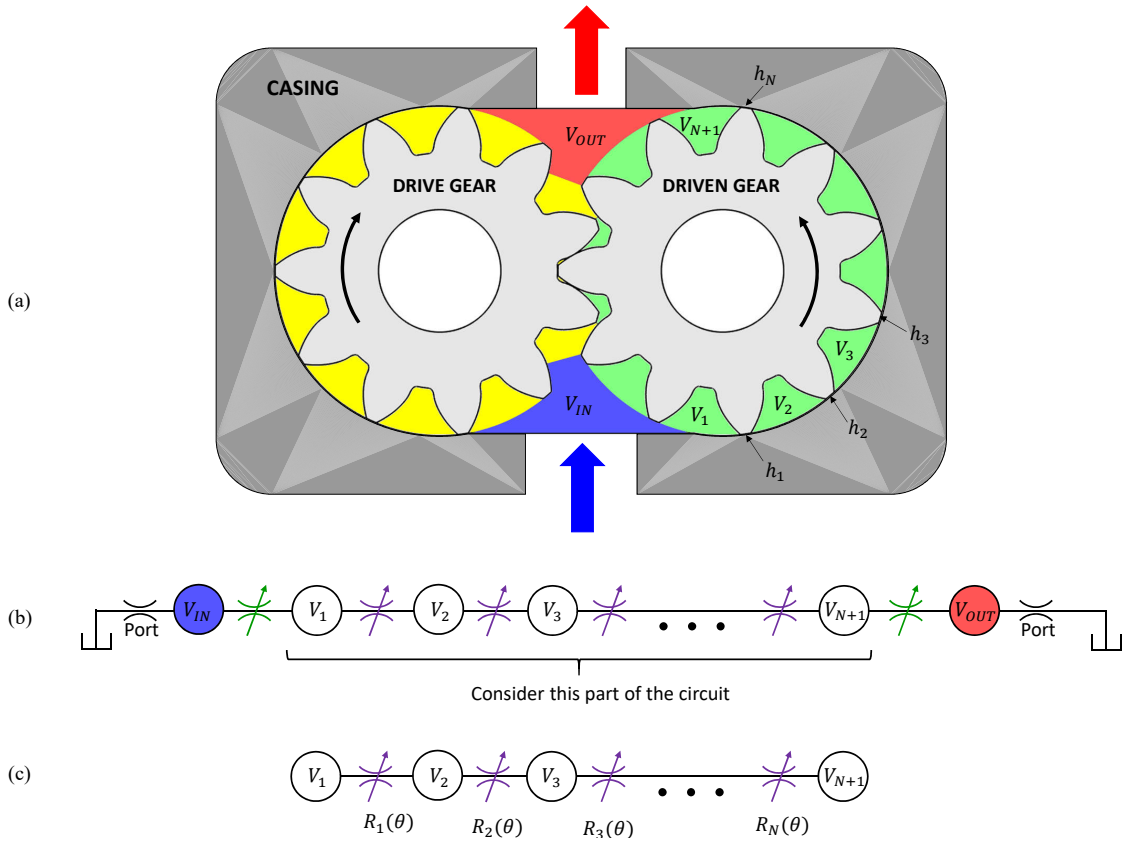

Figure 5.7. (a) Identification of TSVs and gap height at each tooth tip (b) Equivalent hydraulic circuit for leakage flow over the tooth tips (c) Part of the hydraulic circuit analyzed

In this circuit, all the chambers are TSVs and all resistances are the constrictions formed by the casing's internal surface and the tooth tips. These resistances vary for each tooth tip and with the angle of rotation (θ) of each tooth tip. Instantaneous resistance of i^{th} tooth tip at an angular position θ can be expressed as:

$$\mathcal{R}_i(\theta) = \frac{12\mu L}{b h_i^3(\theta)} \tag{5.12}$$

Here $h_i(\theta)$ is the instantaneous gap height at i^{th} tooth tip that can be determined by performing the same steps presented in section 5.2.1. Note that $h_i(\theta)$ accounts not only for the concentricity error, but also for the micromotion of the gears. Since all the resistances are in series, the total resistance of the hydraulic circuit (Figure 5.7(c)) is:

$$\mathcal{R}(\theta) = \sum_{i=1}^{N(\theta)} \mathcal{R}_i(\theta) \tag{5.13}$$

It is notable that number of resistances (N) varies with the angular position. This is because the number of tooth tips forming a clearance interface with the casing's internal surface varies with the angular position. This is illustrated in Figure 5.8 where N is 6 or 7 depending on the angular position of the gear.

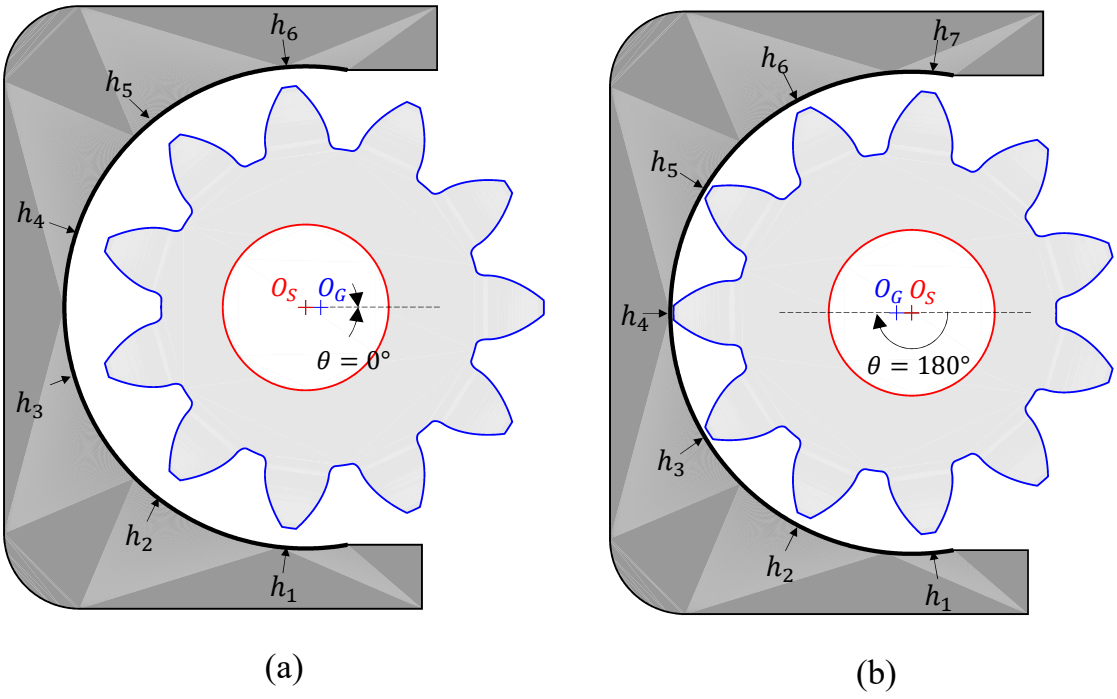

Figure 5.8. Two angular positions of a gear with concentricity error showing the number of casing - tooth tip interfaces and qualitative gap heights (exaggerated for illustration) for each configuration

Now, if an EGM with constant gap height at the tooth tips (h_{eff}) has the same volumetric efficiency as the actual EGM (with concentricity error and gear micromotion), then the average leakage flow over the full revolution will be the same for both cases.

$$Q_{leak,avg} = \left\langle \frac{\Delta p}{N(\theta)\mathcal{R}_{eff}} \right\rangle = \left\langle \frac{\Delta p}{\sum_{i=1}^{N(\theta)} \mathcal{R}_i(\theta)} \right\rangle \tag{5.14}$$

$$\implies \frac{\Delta p b h_{eff}^3}{12\mu L} \left\langle \frac{1}{N(\theta)} \right\rangle = \frac{\Delta p b}{12\mu L} \left\langle \frac{1}{\sum_{i=1}^{N(\theta)} \frac{1}{h_i^3}} \right\rangle \tag{5.15}$$

$$\implies h_{eff} = \left(\frac{\left\langle \frac{1}{\sum_{i=1}^{N(\theta)} \frac{1}{h_i^3}} \right\rangle}{\left\langle \frac{1}{N(\theta)} \right\rangle} \right)^{\frac{1}{3}} \tag{5.16}$$

In above equations (5.14)-(5.16), $\langle ... \rangle$ indicates the average of the quantity over one revolution of the gear.

Equations 5.11 and 5.16 present the expressions for the effective gap height in the presence of conicity and concentricity errors with the effect of micromotion included.

Thus, for any EGM, an effective gap height can be determined using Eq. 5.11 and 5.16. This provides a yardstick to compare the efficiency of the units with same design but different manufacturing errors. Moreover, this effective gap height can be incorporated in any simple lumped parameter models to quickly evaluate the volumetric efficiency of an EGM.

There are few limitations of this alternate approach:

1. This approach neglects the flow over the tooth tip due to relative motion of the tooth with respect to the casing. In most EGMs, this flow is typically small compared to the pressure driven flow. However, the readers are advised to verify the same before using this model. In an analytical form, this constraint can be expressed as

$$\frac{\Delta p h^3}{12\mu L} \gg \frac{\mathrm{v} h}{2} \tag{5.17}$$

$$\implies F_{cp} = \frac{\pi \mu L N_r r_g}{5 \Delta p h^2} \ll 1 \tag{5.18}$$

2. To use Eq. 5.16 in a lumped parameter model, the micromotion magnitude and direction has to be determined beforehand. To do that, the net force on the gears can be approximated using a simplified approach (e.g. assuming certain TSV pressurization profile and integrating it over the gear's radial surface). Then, if the bearing at the shaft is of the journal type, the mobility method [40] can be used to determine the micromotion magnitude and direction. If the bearing is of the roller type, then the magnitude of the micromotion is the radial clearance between the shaft and its bearing and the direction of micromotion is the direction of the net force on the gear.

3. Apart from the leakage flow at the tooth tip, another source of flow loss in EGMs is the flow through the gap between the gear and the elements on its axial sides. This flow is influenced by the course of pressurization of TSVs whose accuracy is affected in this effective gap height approach. In particular, in this approach, the gap height at all the tooth tips is uniform, which leads to a linear pressurization of a TSV as it moves from the inlet side to the outlet side. However, in reality, the EGM has a variable gap at the tooth tip which causes a non-linear pressurization. Hence, using this effective gap height model will lead to a poor estimation of the leakage at the axial sides of the gears.

5.4 Experimental investigation

In order to validate the modelling approach developed in section 5.2, an experimental strategy was devised. The following subsections describe the details of experimental work done in this research.

5.4.1 Reference pumps

To perform the experimental tests, six units of concentric GC series external gear pumps (E3) were obtained. All units were disassembled and the gears were taken

out (Figure 5.9). A machining operation was done on the tooth tips of the gears to introduce varying amounts of conicity and concentricity errors (Figure 5.10).

(a) Reference pump (E3)

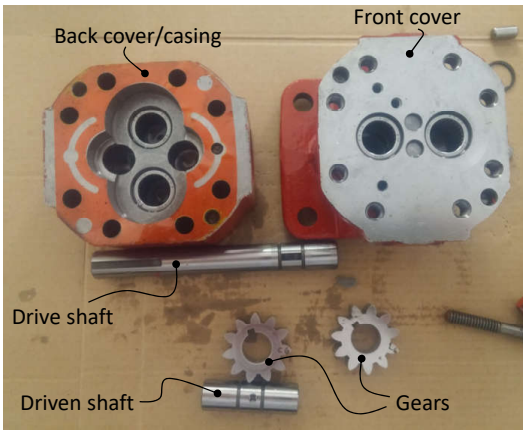

(b) Components upon disassembly

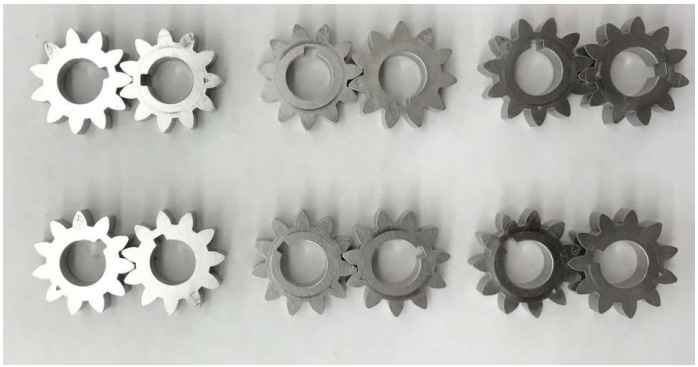

(c) Twelve gears belonging to 6 units of the reference pump

Figure 5.9. Reference pump disassembled and gears obtained from six such units.

The errors on the gears were measured using a gear metrology machine (Figure 5.11). The measurement of conicity and concentricity errors are summarized in Figure 5.12. Gearset 6 has the least amount of errors. Gearsets 1 and 4 have medium and high amounts of conicity error, respectively, but a low concentricity error. In contrast, gearsets 5 and 3 have medium and high amounts of concentricity error, respectively,

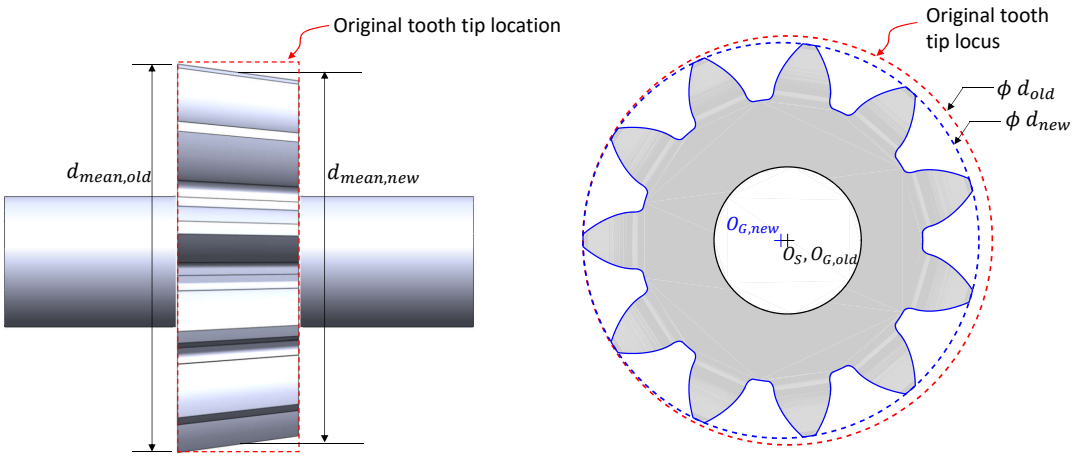

(a) Conicity error. (b) Concentricity error.

Figure 5.10. Error introduction on the gears

but a low conicity error. Finally, gearset 2 has medium amounts of both conicity and concentricity errors. The uncertainties in the measurements of conicity and concentricity errors were ±1.25 μm and ±0.75 μm, respectively. It is important to note that the machining operation reduced the diameters of the gears. The mean diameters of the gears after machining are presented in Table 5.1.

Table 5.1.
Mean diameters of all the gears used in the tests

Gearset	1: drive	1: driven	2: drive	2: driven	3: drive	3:driven
d_{mean} (mm)	29.551	29.543	29.539	29.550	29.542	29.536
Gearset	4: drive	4: driven	5: drive	5: driven	6: drive	6: driven
d_{mean} (mm)	29.547	29.558	29.563	29.562	29.582	29.583

To eliminate any variability in the pump geometry (apart from the manufacturing errors on the gears), only one pump casing was used throughout the experiments.

Figure 5.11. Measurement of conicity and concentricity errors on the gears with Wenzel WGT 350 gear metrology machine.

The relevant geometrical parameters of the pump that stayed the same across all the experiments is shown in Table 5.2

5.4.2 Experimental setup

A hydraulic circuit was built to permit the measurement of volumetric efficiency of the pump for a range of operating speeds and pressures. From the schematic shown in Figure 5.13(a), the needle valve at the end of the circuit was used to increase the pressure at the pump outlet. An ISO VG 46 mineral oil was used in the tests which were conducted at 35 °C. The pump flow was measured using a flow meter. Pressure transducers and thermocouples were used to monitor pressures and temperatures at the inlet and the outlet of the pump. The details of the sensors used are provided in

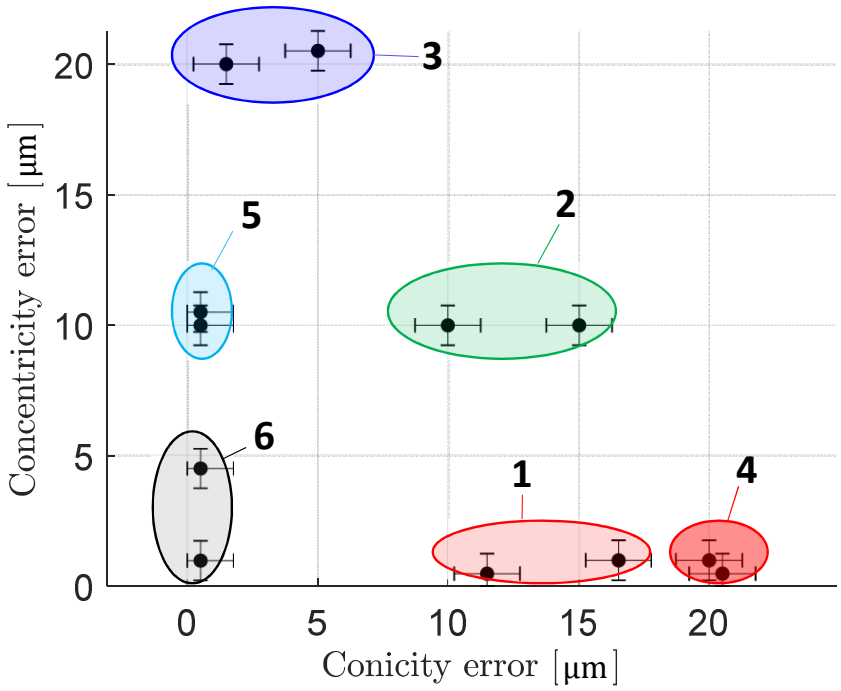

Figure 5.12. Manufacturing errors introduced to 6 gearsets

Table 5.2.
Geometric parameters of the pump common to all gearsets

Casing radius (of internal surface)	14.827 mm
Casing depth	9.507 mm
Clearance between the shafts and the bearings	23 µm
Clearance between the gears and the casing on axial side	30 um
Number of teeth on each gear	11
Geometric displacement	3.25 cc/rev

Table 5.3. At the outlet of the pump, two pressure sensors were mounted: a Wika pressure sensor to measure the average value of pressure and a Kistler piezoelectric pressure sensor (sampling frequency: 50 kHz) to measure the dynamics of pressure.

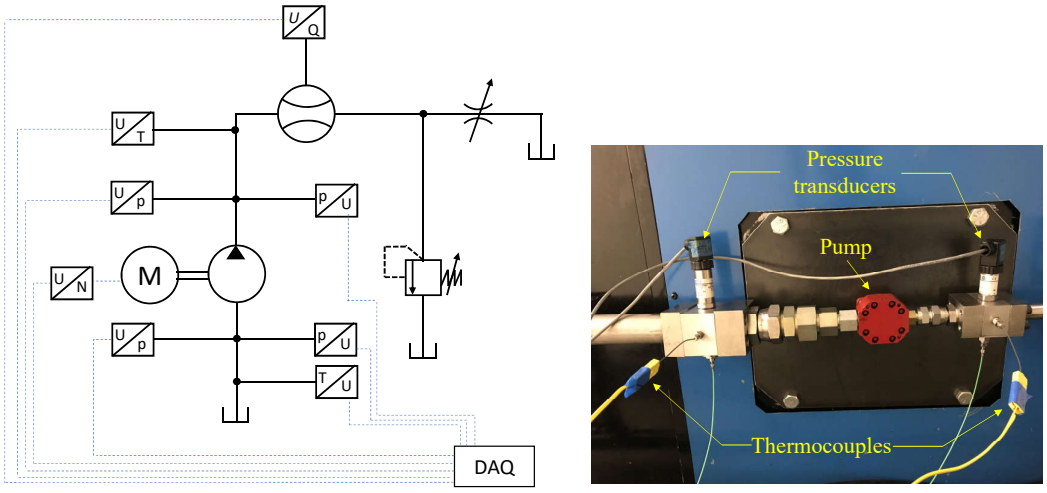

(a) ISO schematic of the hydraulic circuit.

(b) Picture of actual test setup

Figure 5.13. Experimental setup

Table 5.3.
Specification of the sensors used in the tests

Sensor	Model	Specifications	Accuracy
Pressure	Wika S-10	0 to 400 bar	±5 % of span
transducer	Kistler	0 to 600 bar	
Thermocouple	Omega K-type	-5 to 200 ° C	±1 °C
Flow meter	VSE VS02	0.1 to 120 L/min	±0.3%

5.4.3 Experimental Results

The results obtained from the tests are presented in Figures 5.14, 5.15 and 5.16 in terms of volumetric efficiency. Figure 5.14 shows that the efficiency decreases with the increase in the conicity error. The efficiency plot for the gearsets 1 and 4 are similar, which is confusing at first. However, geometric measurements show that the mean radius of the driven gear in the gearset 1 is smaller than that in the gearset 4

(Table 5.4). Therefore, the two effects, (a) increase in leakage due to smaller radius and (b) decrease in leakage due to lower conicity error (from Eq. 5.11), balance each other. The effective gap height data presented in Table 5.4 is obtained using Eq. 5.11 and 5.16. From the effective gap height information for each gear, the mean gap height at the tooth tips for a gear pump is calculated by evaluating their cubic mean:

$$h_{mean} = \sqrt[3]{0.5(h^3_{eff,drive} + h^3_{eff,driven})} \tag{5.19}$$

Cubic mean is the appropriate method of evaluating the mean here since the leakage flow has a cubic relationship with the gap height. The difference between the average gap height for the gearsets 1 and 4 is $< 3\,\mu$m. This explains why the results obtained from these two gearsets are very similar.

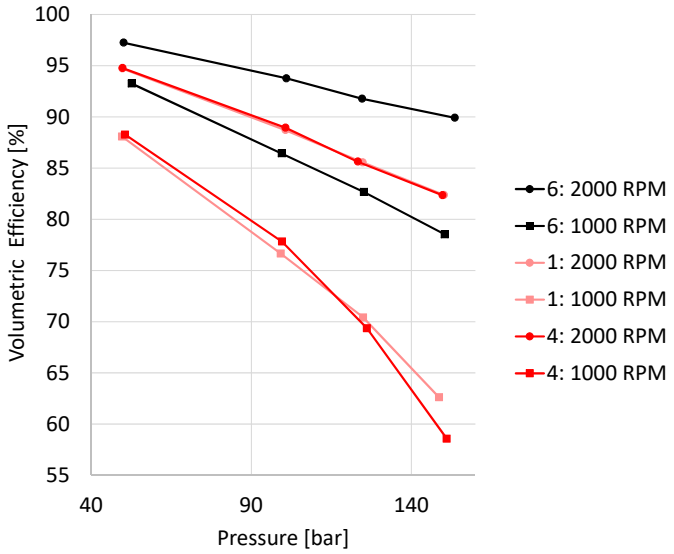

Figure 5.14. Results from experiments on gearsets 6, 1 and 4 showing the effect of conicity error

Figure 5.15 shows the effect of concentricity error on the volumetric efficiency of the pump. Finally, Figure 5.16 shows the combined effect of conicity and concentricity errors on the volumetric efficiency of the pump. These results show that with the

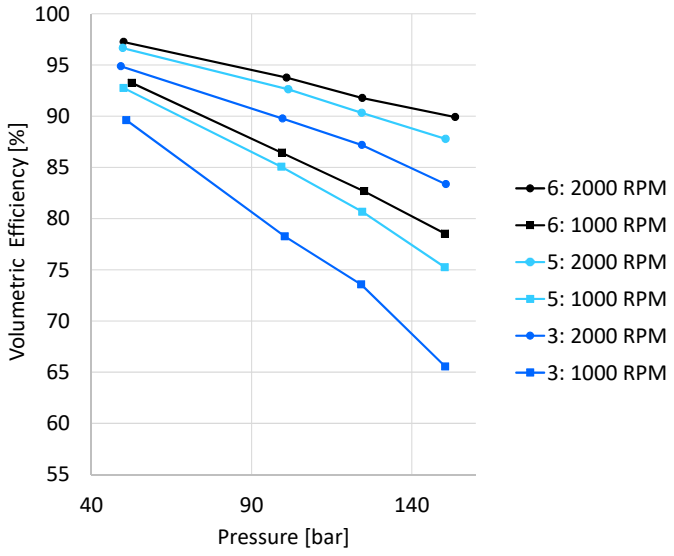

Figure 5.15. Results from experiments on gearsets 6, 5 and 3 showing the effect of concentricity error

Table 5.4.
Comparison of dimensions for gearset 1 and 4

	Gearset 1		Gearset 4	
	Drive	Driven	Drive	Driven
Mean gear radius (mm)	14.775	14.771	14.774	14.779
Conicity error (μm)	16.5	11.5	20	20.5
Concentricity error (μm)	1	0.5	1	0.5
Effective gap height (μm)	44.4	48.2	46.9	39.7
Mean gap height (μm)	46.4		43.6	

increase in the conicity and the concentricity errors, the volumetric efficiency of the pump is decreased. It is important to note, however, that with introduction of the manufacturing errors, the mean diameters of the gears have reduced as illustrated in

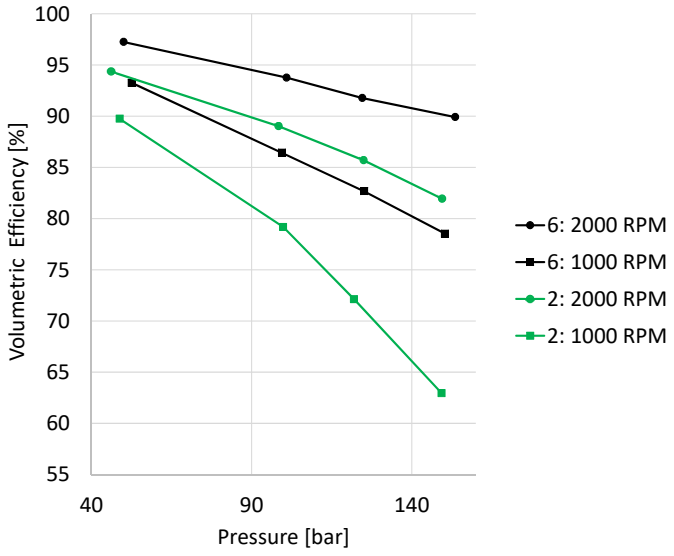

Figure 5.16. Results from experiments on gearsets 6 and 2 showing the effect of both conicity and concentricity error

Figure 5.10 and tabulated in Table 5.1. So, the trends shown in Figures 5.14, 5.15 and 5.16 are expected.

Figure 5.17 shows the outlet pressure pulsation comparison between the gearsets 6 and 3 when the pump was operating at 1000 rpm and 100 bar. The effect of high concentricity error is observed in terms of a shaft frequency (16.67 Hz) appearing in the frequency spectrum of the pulsation signal. The explanation of this phenomenon is provided in section 5.5.3.

5.5 Simulation results and validation

5.5.1 Validation of error model implemented in HYGESim

To test the validity of the manufacturing error model implemented in the HYGESim tool (described in section 5.2), multiple simulations were conducted using the actual pump geometries and the operating conditions mimicking the actual experi-

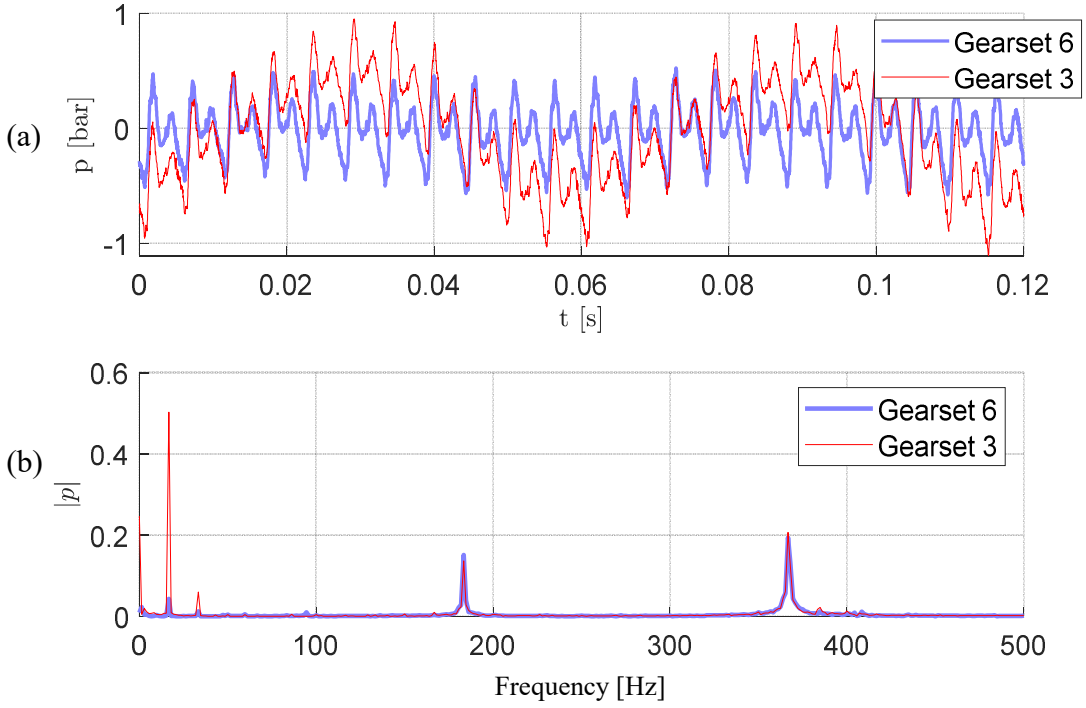

Figure 5.17. Pressure pulsation at the pump outlet for the gearset 6 and 3. Operating condition: 1000 rpm, 100 bar: (a) Time domain (b) Frequency domain

ments. In Figure 5.18, the comparison between the results from the simulations and the experiments is presented in terms of volumetric efficiency. The simulation results agree with the experiments across all the operating conditions and across all the gearsets considered in this study. As explained in section 5.1, the manufacturing errors considered in this study effect the leakage path at the tooth tips hence impacting the leakage flow and the volumetric efficiency of the unit. Thus, a good comparison between the simulations and the experiments across all operating conditions for all the gearsets with varying amounts of manufacturing errors validates the model for manufacturing errors developed in this work and integrated in the HYGESim tool.

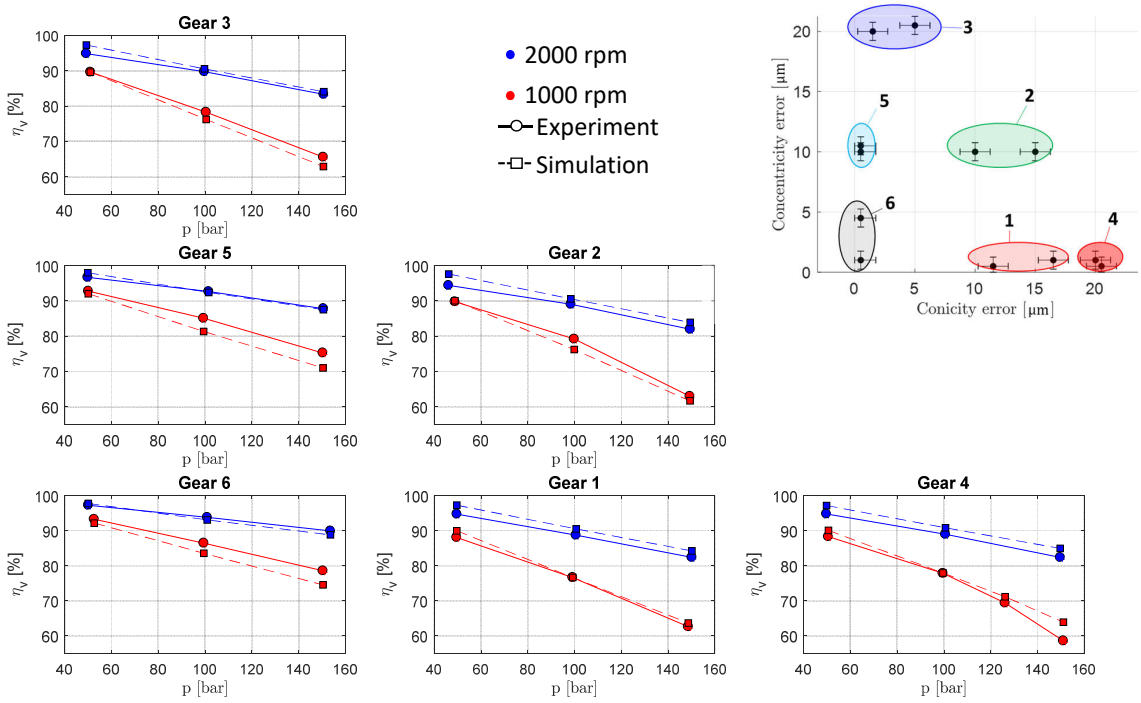

Figure 5.18. Comparison of simulation results with experiments for all six gearsets in terms of volumetric efficiency

5.5.2 Validation of effective gap height approach

The effective gap height approach presented in section 5.3 is a simplified method for implementing both the conicity and the concentricity errors in any lumped parameter based model. This approach is validated against HYGESim (with error model implemented) via 3 sets of simulations: one with no errors, one with high conicity error (50 µm) and one with high concentricity error (40 µm). The pump macroscopic geometry used in these simulations corresponds to the pump tested in this work (presented in section 5.4). The nominal clearance at the tooth tip (difference in the radius of the casing and the radius of the gear) is set to 65 µm. In this pump, due to the clearance between the shaft and the bearing, the center of a perfect gear moves by 23

µm from the center of the casing. Moreover, this pump uses needle roller bearings; therefore, unlike in journal bearings where the motion of the journal is at a different angle compared to the load direction, for roller bearings, the motion of the shaft and the gear can be assumed with a good approximation to be in the direction of the load. From simulations, this motion is determined to be typically at an angle of $\sim 75^{\circ}$ from the line connecting the centers of the gears towards the pump inlet. This information is utilized by the effective gap height model.

Simulations were conducted at 1000 rpm and 50, 100 and 150 bar pressures. The mean radius of the gears was kept constant across all the simulations. Acknowledging the fact that the axial flow will not be accurately predicted by the effective gap height model, the axial gap heights were set to zero in these simulations.

The results in Figure 5.19 show nearly a perfect match between the HYGESim model and the effective gap height model. This validates the effective gap height approach. As explained in section 5.3, the Couette drag at the tooth tip is not considered in the effective gap model. However, for these set of simulations, $F_{cp} < 0.18$ (refer Eq. 5.18), so, the Couette drag was a minor component of the flow over the tooth tip.

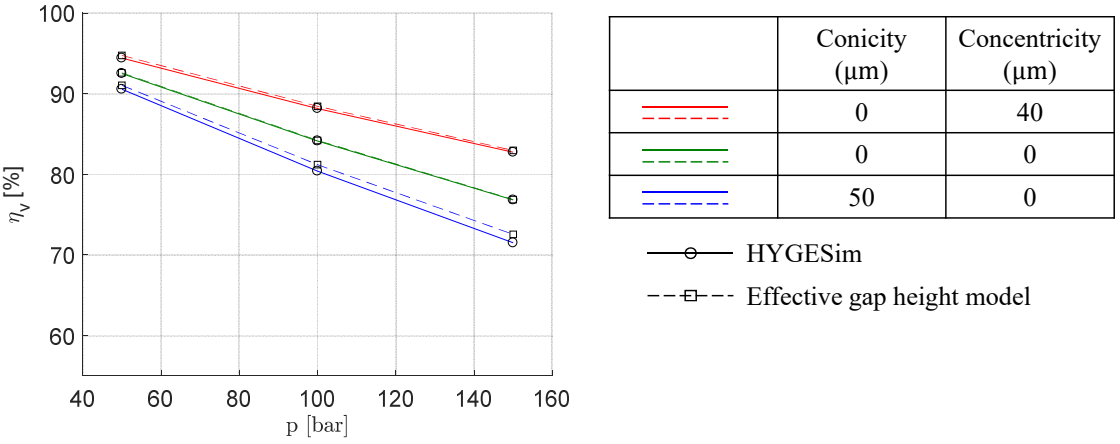

Figure 5.19. Comparison of the results from the effective gap height model with HYGESim tool

If the real axial gap height (which is 30 μm for the pump considered) is used in the simulations, the effective gap height model overpredicts the volumetric efficiency by $2-5\%$ (compared to HYGESim) owing to the limitation (iii) discussed in section 5.3.

5.5.3 Effect of concentricity error on EGM performance

It can be seen in Figure 5.19 that the volumetric efficiency of the EGM increases with the increase in the concentricity error. This may seem counterintuitive, but this effect is indeed real. The concentricity error causes the offset of the gear's axis from the shaft's axis. So, as it can be seen in Figure 5.8, at some angular positions, the gap heights at the tooth tips are high when the offset is away from the casing. For other angular positions, however, when the offset is towards the casing, the heights at the tooth tips are low. For each angular position, the "equivalent gap height", h_{eq}, can be defined as the uniform gap height value (uniform across all tooth tips) that will lead to the same instantaneous leakage flow as the actual gap height configuration. This equivalent gap height can be calculated by referring to Figure 5.7(c) and equating the total resistance arising from this uniform gap height, h_{eq}, and the total actual resistance in the actual leakage flow circuit:

$$N(\theta)\mathcal{R}_{eq} = \sum_{i=1}^{N(\theta)} \mathcal{R}_i(\theta) \tag{5.20}$$

$$\implies \frac{N(\theta)}{h_{eq}^3} = \sum_{i=1}^{N(\theta)} \frac{1}{h_i^3} \tag{5.21}$$

$$\implies h_{eq}(\theta) = \sqrt[3]{\frac{N(\theta)}{\sum_{i=1}^{N(\theta)} \frac{1}{h_i^3}}} \tag{5.22}$$

Figure 5.20 shows how this equivalent gap height, h_{eq}, varies with the angular position when the nominal gap height at the tooth tip (difference in the radius of the casing and the radius of the gear), h_{nom}, is 50 μm and the concentricity error, ϵ, is 20 μm. The shaft is assumed to be concentric with respect to the casing for simplicity. This

plot shows that at 0° angular position (gear's axis offset away from the casing), the equivalent gap height is higher than the nominal gap height which is qualitatively visible in Figure 5.8(a). However, as the shaft rotates, the gear axis rotates around the shaft axis and h_{eq} decreases. At 180° angular position, the axis offset is towards the casing (Figure 5.8(b)) and hence, the equivalent gap height is around its lowest. The plot in Figure 5.20 is discontinuous because the number of the tooth tips forming the leakage interface with the casing, $N(\theta)$, keeps jumping between 6 and 7. When this equivalent gap height is integrated over a full revolution, the effective gap height, h_{eff}, is obtained.

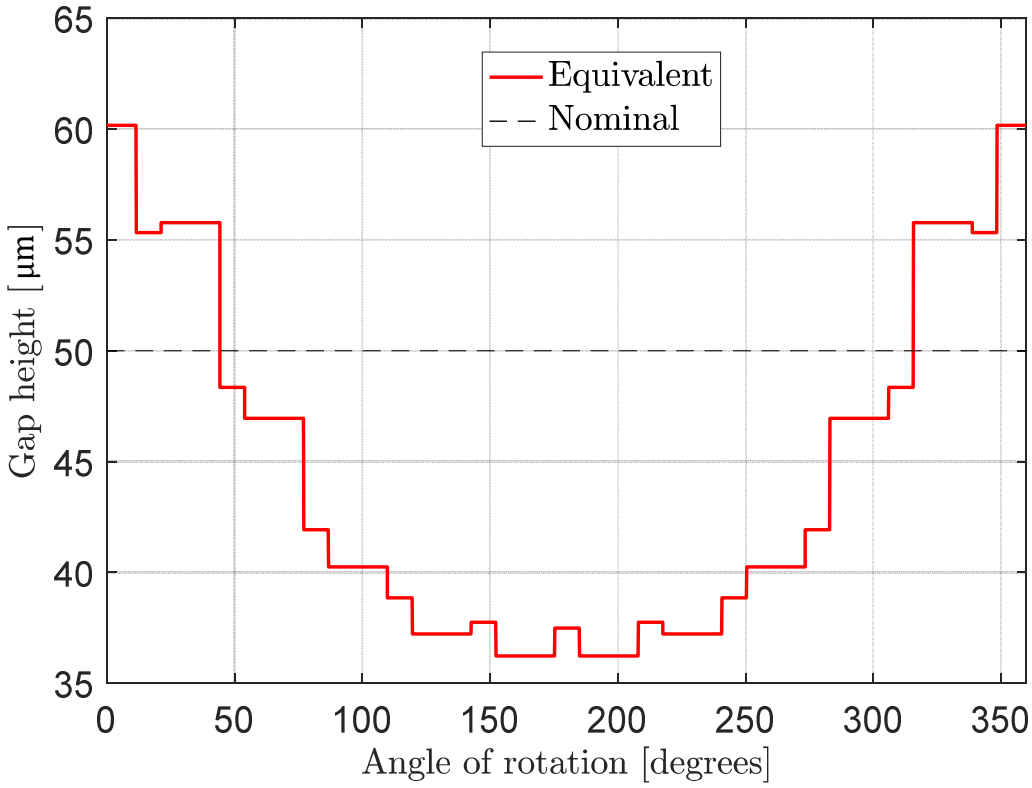

Figure 5.20. Variation of the equivalent gap height at the tooth tip when the nominal gap height is 50 μm and the concentricity error is 20 μm

The factors that influence how the effective gap height at the tooth tip varies with the concentricity error are (i) the angular span of the casing (∠C) and (ii) the

number of teeth in a gear (z). The angular span of the casing is the central angle of the arc forming the leakage interface with the tooth tip (shown by thick black curves in Figure 5.8). For the pump used in this study ($\angle C = 206^{\circ}$, z=11), when $h_{nom} = 50$ μm and $\epsilon = 20$ μm, h_{eff} =46 μm. Indeed, the effective gap height at the tooth tip decreases when the concentricity error in present. This causes a reduction of the leakage at the tooth tip and hence an improvement in the volumetric efficiency.

It is important to note, however, that this advantage of an improved volumetric efficiency with the concentricity error only works until the tooth tip starts to touch the casing. So, if h_{nom} is the difference in the radius of the casing and the gear and e is the magnitude of gear micromotion, then the maximum concentricity error that will help with the volumetric efficiency is $h_{nom} - e$. Figure 5.21 shows how the effective gap height varies with the concentricity error, ϵ, when $h_{nom} = 50$ μm and $e = 0$. For $\epsilon = 0$, $h_{eff} = h_{nom} = 50$ μm. The effective gap height decreases with the increase in the concentricity error until $\epsilon = h_{nom} = 50$ μm, where $h_{eff} = 35.9$ μm. As the concentricity error is further increased, the gear tooth tip breaks into the casing, increasing its radius, hence the effective gap height starts to increase.

This trend of increasing volumetric efficiency with the concentricity error is not reflected in the experiments due to the nature of the error introduced on the gears before testing. As explained in section 5.4, the concentricity error was achieved by machining of the gear tooth tips. This machining caused a reduction of the gear diameter (Figure 5.10). Hence, when comparing the results from gearsets 6 to 5 and 3, two effects come into play: the increase in the volumetric efficiency due to higher concentricity error and the decrease in the volumetric efficiency due to lower gear radius. The latter effect dominates and hence, a decrease in the volumetric efficiency from the gearset 6 to the gearsets 5 and 3 is observed.

Although the concentricity error leads to an increase in the volumetric efficiency, there is a crucial downside. Due to the concentricity error, the equivalent gap height at the tooth tip varies with the gear angular position (Figure 5.20) which results in the oscillation of the instantaneous leakage flow over the tooth tip. This is reflected in

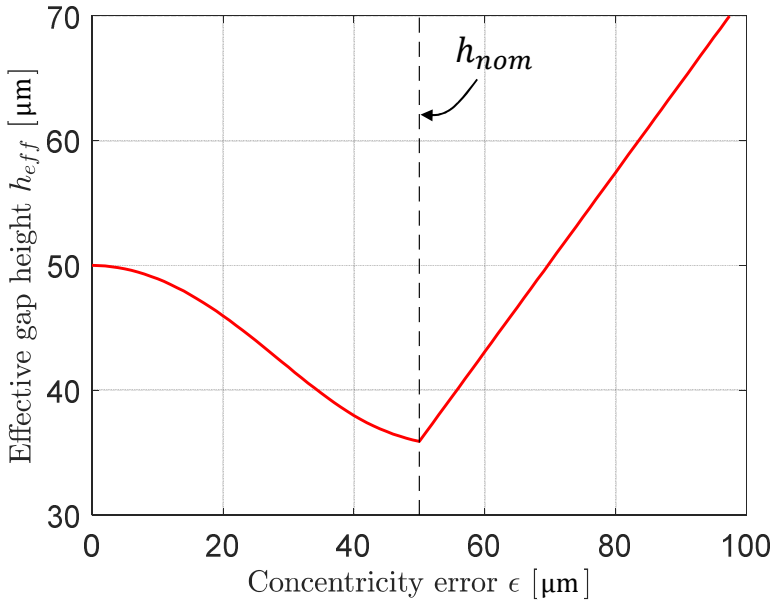

Figure 5.21. Variation of the effective gap height with concentricity error ($h_{nom} = 50$ µm, $e = 0$). The dotted line is at $\epsilon = h_{nom} = 50$ µm.

the oscillation of the outlet flow. Figure 5.22 shows the comparison of the simulated pulsation of the outlet flow for two cases: $\epsilon = 0$ and $\epsilon = 20$ µm. The simulations were run for 1000 rpm. The concentricity error introduces the shaft frequency of 16.67 Hz in the flow pulsation frequency spectrum (Figure 5.22(b)) which adds to the original flow pulsation. This phenomenon is seen in the experimental results as well in terms of the pressure pulsation at the pump outlet (Figure 5.17).

The flow pulsation at the outlet of the EGM is an undesirable phenomenon. It is a source of unwanted noise and vibration in the hydraulic system. The increment of the flow non-uniformity due to the concentricity error adds to these concerns.

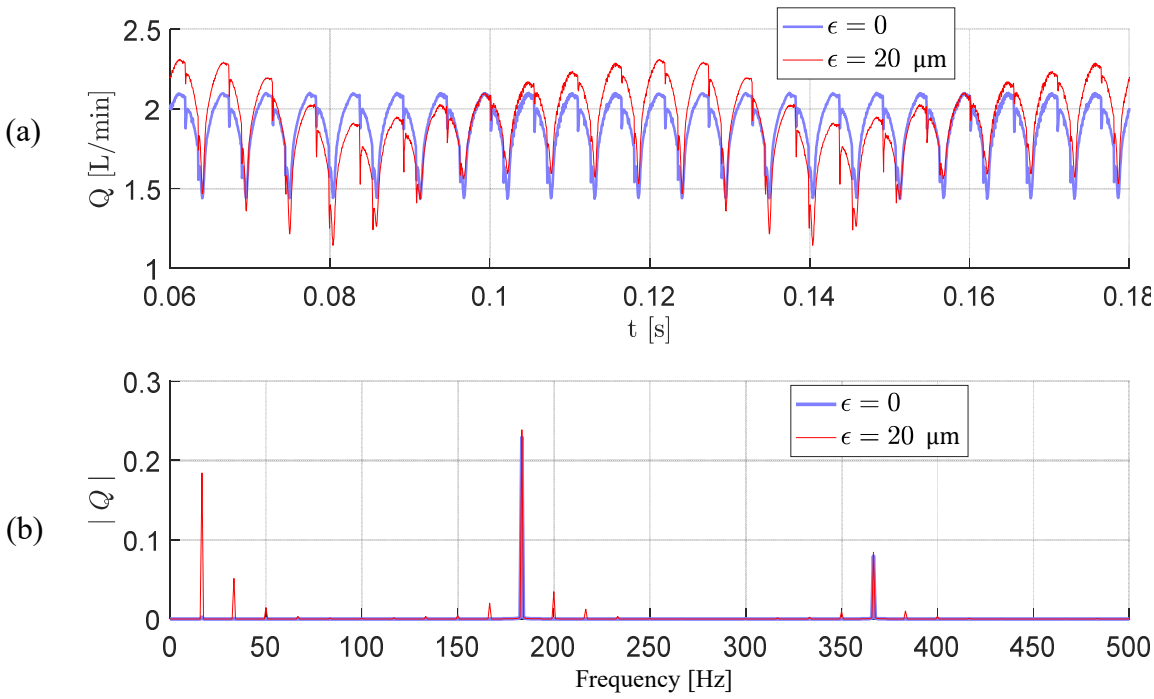

Figure 5.22. Simulated outlet flow pulsation of the gear pump with zero and non-zero concentricity. (a) Time domain (b) Frequency domain

6. MODELLING OF LEAKAGE FLOW THROUGH CURVED GEOMETRIES

In previous chapters, the modelling of EGMs considered the tooth tip leakage flow to be the flow between flat surfaces (Figure 1.4). However, in some EGMs like continuous contact gear machines, the tooth tip geometry is different. As shown in Figure 6.1, Continuous-Contact Helical Gear Pumps (CCHGPs) consist of gears with circular arcs at the tip. Thus, the leakage flow geometry consists of two arcs of different curvatures. This chapter focuses on developing a numerical technique to the model the flow through such curved geometries (Aspect A4).

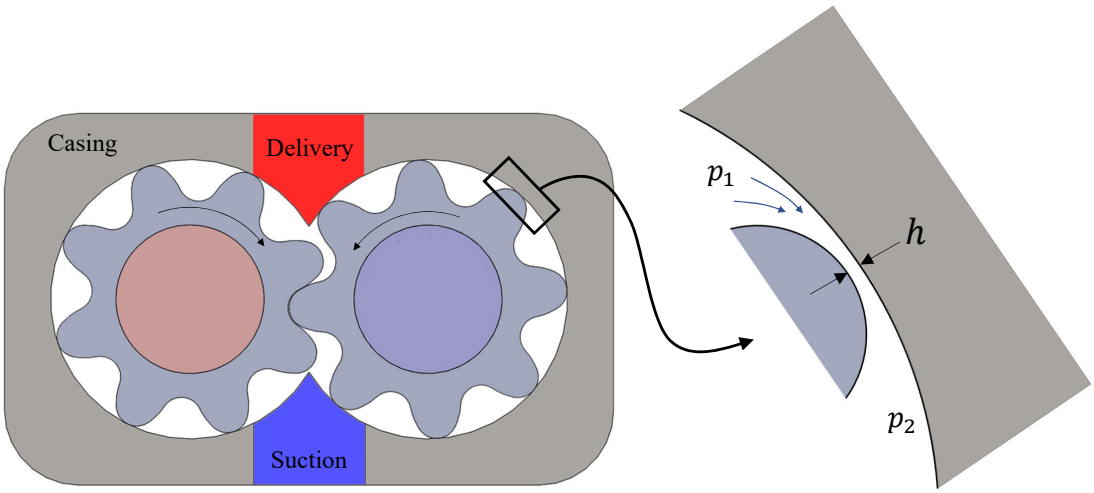

Figure 6.1. Components in a CCHGP. The clearance between gear and casing is highlighted in the illustration on the right.

Flow through curved geometries exists in the traditional EGMs too, at the inter-teeth flow connection (flow path connecting drive and driven gear TSVs at the meshing region) as shown in Figure 6.2. The only difference is the fact that in EGMs, the curvatures of the two walls are in opposite direction, whereas in CCHGPs, the curvature of the two walls are in the same direction. This inter-teeth flow connec-

tion allows cross port flow which, similar to the tooth tip leakage flow, affects the volumetric performance of the EGM. Moreover, as this flow path establishes the connection between the pumping TSVs, this flow also impacts the dynamic features of the outlet flow. This becomes critical for EGMs with very low gear backlash where the magnitude of the inter-teeth flow is decisive in predicting the presence or absence of dual-flank behavior in the outlet flow [45].

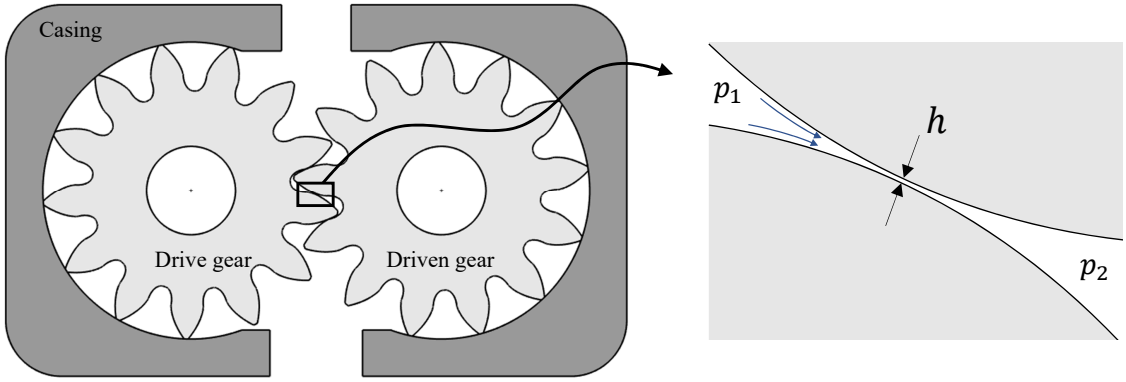

Figure 6.2. Inter-teeth flow connection in EGM.

Apart from EGMs, the leakage flow through curved geometries is also present in another class of gear machines: gerotors (Figure 6.3). A gerotor consists of two gears (also called rotors) one of which is internal toothed and other is external toothed. In pumping operation, the shaft drives the inner gear which in turn drives the outer gear. As seen in Figure 6.3, the gears are located at an eccentric position to each other. This eccentricity allows a variation of the TSV with gear rotation. As the gears rotate, the volume near the inlet side increases in size leading to the suction of flow. This fluid is then carried to the outlet side where the TSV decreases leading to the delivery of the flow to the outlet.

As the gears rotate, there is relative motion between the gears' surfaces. To avoid high friction due to this relative motion, the gears are designed such that there always

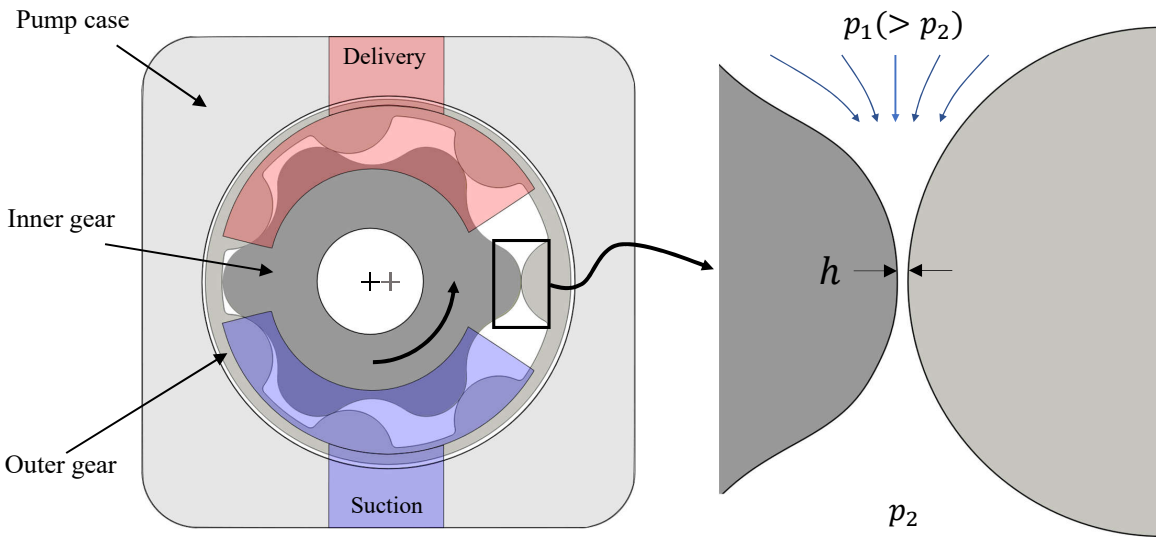

Figure 6.3. Components in a gerotor. The clearance between the gears is highlighted in the illustration on the right.

exists a clearance between the inner gear and the outer gear. An example of such a clearance is shown in Figure 6.3. This clearance allows establishing lubrication at the gear-gear interface. However, this also permits the fluid to leak from the high pressure side to the low pressure side. Similar to CCHGPs and EGMs, this leakage geometry consists of two arcs.

In past, the tooth tip flow in CCHGPs and the inter-teeth flow in traditional EGMs have been modelled using the orifice equation [21, 25]. However, the orifice equation is accurate only when there are sudden constrictions in the flow geometry. Instead, the geometry of aforementioned flows consists of smoothly varying cross section. Thus, using orifice equation to model this flow is an oversimplification and negatively impacts the modelling accuracy.

For gerotors, approaches with different levels of complexity have been used by researchers towards the modelling of leakage flow over the tooth tips. Manco et al. [105, 106] proposed an approach from the lubrication theory that involves numerically solving the Reynolds equation of lubrication in the leakage gap. However, this

approach has a high computational time which is undesirable for lumped parameter models. In contrast to Manco et al., Schweiger et al. [107] simply used the orifice equation to model this leakage flow which as discussed above, is not an accurate method. Recently, Pellegri et al. [108–110] proposed a multidomain simulation model for gerotors. In this model, the tooth tip leakage was approximated as the flow between two parallel plates where the length of the plate is tuned via experiments.

In short, there is a scarcity of the model for the flow through curved geometries which can be accurate as well as computationally cheap. For computational swiftness, researchers have often resorted to certain approximations which is a significant limitation and hinders accurate performance prediction.

The work presented in this chapter aims at overcoming this limitation by proposing a model for flow through curved geometries. The proposed model is developed by identifying the key geometric and flow parameters that influence the leakage flow characteristics. Using Buckingham's Π theorem, analytical methods and CFD simulations, functional relationships between the relevant dimensionless parameters are established. The non-dimensional model is then validated against experiments using a unique test apparatus designed specifically for this task.

6.1 Non-dimensional model development

The flow over the tooth tip of CCHGPs and gerotors and the inter-teeth flow in EGMs are essentially the flow through a constriction characterized by curved walls with a certain gap height at the constriction. The geometric parameters that influence this flow are the radii of curvature of the walls and the value of minimum gap height h. From Figure 6.4, for gerotors and traditional EGMs, R_1 and R_2 are the radii of curvature of the two gears at the location of the constriction, respectively. Instead for CCHGPs, R_1 is the radius of curvature of the gear tooth tip and R_2 is the radius of curvature of the internal surface of the casing. It is to be noted that the internal

surface of the casing has a negative curvature. Hence, R_2 will be a negative quantity in Figure 6.4(b).

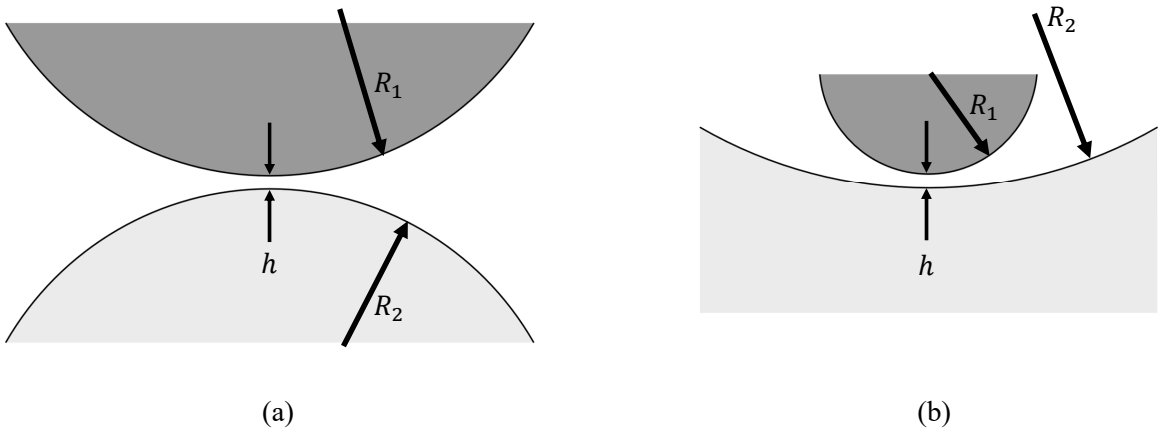

Figure 6.4. (a) The geometry of leakage gap at the tooth tip of gerotors and the geometry of inter-teeth flow in EGMs. (b) The geometry of tooth tip leakage gap in CCHGPs.

It is argued that, in fact, the flow is influenced only by the equivalent curvature of the flow geometry which is the sum of curvatures of the two bounding walls:

$$\kappa_{eq} = \kappa_1 + \kappa_2 \tag{6.1}$$

$$\implies \frac{1}{R_{eq}} = \frac{1}{R_1} + \frac{1}{R_2} \tag{6.2}$$

In other words, if the radii of individual walls vary such that equivalent radius of curvature R_{eq} stays the same, then the flow too stays the same. This idea is well accepted in the field of lubrication [43,111]. Nevertheless, this idea has been validated using CFD simulations which will be described in detail in section 6.3.

Moving away from the geometry, the pressure difference across the constriction obviously plays a major part in deciding the amount of flow through the constriction.

The height of the gap at the constriction is in the order of few microns, so, if the operating fluid has high viscosity, the flow through the constriction will be laminar

and only the viscosity of the fluid will be important in deciding the flow rate through the gap. However, as discussed in Chapter 4, for low viscosity fluids, the flow through the constriction can become turbulent and the density of the fluid should also influence the flow.

First, for laminar flow through the constriction,

$$v = \mathrm{f}(h, R_{eq}, \Delta p, \mu) \tag{6.3}$$

where v is the mean flow velocity at the location of the constriction.

Using Buckingham's Π theorem, the dimensionless numbers obtained are:

$$\Pi_v = \frac{\mu v}{h \Delta p} \tag{6.4}$$

$$\Pi_h = \frac{h}{R_{eq}} \tag{6.5}$$

Here Π_h is a geometrical dimensionless parameter, whereas as Π_v is the dimensionless number related to the flow. In fact, Π_v is the inverse of the product of Reynolds number and Euler number:

$$\Pi_v = \frac{\mu v}{h \Delta p} = \frac{\mu}{\rho v h} \cdot \frac{\rho v^2}{\Delta p} = \frac{1}{Re \cdot Eu} \tag{6.6}$$

Now, as Reynolds number is the ratio of inertia forces to viscous forces and Euler number is the ratio of pressure forces to inertia forces, Π_v becomes the ratio of viscous forces to pressure forces. Although, Re and Eu are commonly known dimensionless parameters, their product cancels out the inertia force term, thus, these dimensionless numbers lose their individual significance. Hence, Π_v is used as the flow dimensionless parameter in this work.

Since Π_v contains the mean flow velocity term, it is the independent dimensionless number. Hence, the desired relationship is of the form:

$$\frac{\mu v}{h \Delta p} = \mathrm{F}\Big(\frac{h}{R_{eq}}\Big) \tag{6.7}$$

Here, F is an unknown functional relationship that must be determined.

Next, for turbulent flow through the constriction,

$$v = \mathrm{f}(h, R_{eq}, \Delta p, \mu, \rho) \tag{6.8}$$

Using Buckingham's Π theorem, the dimensionless numbers obtained are:

$$\Pi_v = \frac{\mu v}{h \Delta p} \tag{6.9}$$

$$\Pi_h = \frac{h}{R_{eq}} \tag{6.10}$$

$$\Pi_p = \frac{h^2}{\mu^2} \Delta p \rho \tag{6.11}$$

Thus, the desired relationship is of the form:

$$\frac{\mu v}{h \Delta p} = \mathrm{F}\Big(\frac{h}{R_{eq}}, \frac{h^2}{\mu^2} \Delta p \rho\Big) \tag{6.12}$$

As compared to Eq. 6.7, this equation involves extra dimensionless number Π_p, thus this parameter accounts for the dominance of inertial effects in the flow.

It can be observed that Π_p can be expressed in terms of commonly known dimensionless numbers: Euler number and Reynolds number.

$$\Pi_p = \frac{h^2}{\mu^2} \Delta p \rho = \frac{\Delta p}{\rho v^2} \cdot \frac{\rho^2 v^2 h^2}{\mu^2} = Eu \cdot Re^2 \tag{6.13}$$

In fact, instead of flow velocity, if the pressure drop across the constriction is taken as the dependent parameter, then, the Buckingham's Π theorem results in following three dimensionless numbers:

$$\Pi_v = \frac{\mu v}{h \Delta p} \tag{6.14}$$

$$\Pi_h = \frac{h}{R_{eq}} \tag{6.15}$$

$$Re = \frac{\rho v h}{\mu} \tag{6.16}$$

and the non-dimensional relationship will be

$$\frac{\mu v}{h \Delta p} = \mathrm{F}\Big(\frac{h}{R_{eq}}, Re\Big) \tag{6.17}$$

Presence of Reynolds number in Eq. 6.17 makes it more intuitive than Eq. 6.12, however in current analysis, Eq. 6.12 is preferred. In HYGESim and all other lumped parameter based models, the leakage flow model is supposed to provide the flow information which is then used in the pressure build up equation to determine the pressure in the CVs. Equation 6.17 is an implicit function with respect to the flow velocity whereas Eq. 6.12 is an explicit function with respect to it. Hence, Eq. 6.12 is the required flow model of interest.

It can be noticed that the effect of relative motion between the walls is not considered in the current analysis. EGMs (including CCHGPs) typically operate at speeds $\leq$ 2000 rpm and at pressures of $\sim$ 200 bar. At such operating conditions, the flow due to the relative motion between the bounding walls is small compared to the flow due to the pressure difference. Moreover, in gerotors, since both rotors are in motion, the relative motion of the two walls at the constriction region is small.

6.2 Laminar relation derivation from Reynolds Equation

If the flow through the curved constriction falls under the laminar flow regime, the functional relationship can be determined analytically from the Reynolds equation of lubrication [43] by making proper simplifications.

Using the theory of equivalence of curvature (Eq. 6.2), this flow can be modelled as flow between two surfaces: a flat surface and a curved surface with radius of curvature R (Figure 6.5). Here $x = 0$ is the location of the constriction. Then, the variation of gap height in the direction of flow, $h'(x)$ can be expressed as

$$h'(x) = h + R - (R^2 - x^2)^{(1/2)} = h + R - R\Big[1 - \Big(\frac{x}{R}\Big)^2\Big]^{(1/2)} \tag{6.18}$$

$$\implies h'(x) = h + \frac{1}{2}\Big(\frac{x^2}{R}\Big)\Big[1 + \frac{1}{4}\Big(\frac{x}{R}\Big)^2 + \frac{1}{8}\Big(\frac{x}{R}\Big)^4 + ...\Big] \tag{6.19}$$

In the curve-constricted flow geometry, since, the equivalent radius of curvature $R \gg x$, the higher order terms in Eq. 6.19 can be neglected. Thus,

$$\implies h'(x) = h + \frac{x^2}{2R} \tag{6.20}$$

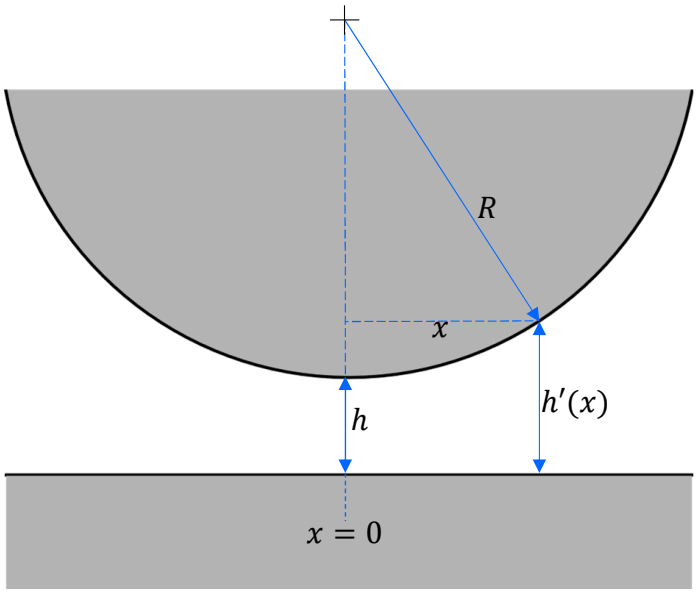

Figure 6.5. Flow geometry consisting of one curved and one flat wall

Now, the Reynolds equation [43] under the assumptions of negligible spanwise flow and relative motion of the walls, can be simplified to

$$\frac{\partial}{\partial x}\left(h'(x)^3 \frac{\partial p}{\partial x}\right) = 0 \tag{6.21}$$

If the fluid pressure far from the constriction is known, say, $p(x = -0.5R) = p_1$, $p(x = 0.5R) = p_2$, then using this information as boundary conditions, the differential Eq. 6.21 can be solved to obtain

$$p = \frac{p_1 + p_2}{2} - \frac{(8h + R)^2 \Delta p}{K^+}\left[\frac{3\sqrt{2R}}{2}\tan^{-1}\left(\frac{\sqrt{2}x}{2\sqrt{Rh}}\right) + \frac{R\sqrt{h}x(3x^2 + 10hR)}{(x^2 + 2hr)^2}\right] \tag{6.22}$$

where

$$K^+ = 160h^{1.5}R + 12h^{0.5}R^2 + 3\sqrt{2}R^0.5(8h + R)^2 \tan^{-1}\left(\frac{\sqrt{2}}{4}\sqrt{\frac{R}{h}}\right) \tag{6.23}$$

Now, flow velocity at the constriction ($x = 0$)

$$v = -\frac{h^2}{12\mu}\frac{\partial p}{\partial x}\Big|_{x=0} \tag{6.24}$$

$$\implies v = \frac{\Delta p h^{1.5}\left(\frac{8h}{R}+1\right)^2}{3\mu R^{0.5}\left[160\left(\frac{h}{R}\right)^{1.5} + 12\left(\frac{h}{R}\right)^{0.5} + 3\sqrt{2}\left(\frac{8h}{R}+1\right)^2 \tan^{-1}\left(\frac{\sqrt{2}}{4}\sqrt{\frac{R}{h}}\right)\right]} \tag{6.25}$$

As $h \ll R$, h/R terms can be neglected and $\tan^{-1}\left(\frac{\sqrt{2}}{4}\sqrt{\frac{R}{h}}\right) \longrightarrow \frac{\pi}{2}$. This yields,

$$v = \frac{\Delta p h^{1.5}}{(9\sqrt{2}\pi/2)\mu R^{0.5}} \tag{6.26}$$

$$\implies v = \frac{0.05 h^{1.5}}{\mu R^{0.5}}\Delta p \tag{6.27}$$

Rearranging,

$$\frac{\mu v}{h\Delta p} = 0.05\sqrt{\frac{h}{R}} \tag{6.28}$$

$$\text{or,} \quad \Pi_v = 0.05\sqrt{\Pi_h} \tag{6.29}$$

From this relation, the flow rate over through the constriction can be determined as:

$$Q = \frac{0.05\, b h^{2.5}}{\mu R_{eq}^{0.5}}\Delta p \tag{6.30}$$

It is important to note that this flow relation is only applicable in the laminar flow regime. The subsequent sections describe the methodology for the determination of the flow relation(s) applicable for the complete flow regime.

6.3 CFD modelling of the flow through curved constriction

To investigate the characteristics of flow through the curved constriction over the complete range of flow regimes, CFD simulations of the flow was conducted using ANSYS CFD tool, Fluent [79].

Multiple computational domains were constructed with different radii of curvature of the walls and minimum gap height. Figure 6.6 shows one of the 2D computational

domains with $R_1 = 5$ mm, $R_2 = \infty$ and $h = 30\,\mu$m. The computational domains were discretized into meshes with structured and unstructured regions with finer grids near the walls. To capture the near wall flow behavior in turbulent flow cases, the mesh was refined at the walls to ensure that $y^+ \leq 1$ (similar to section 4.1).

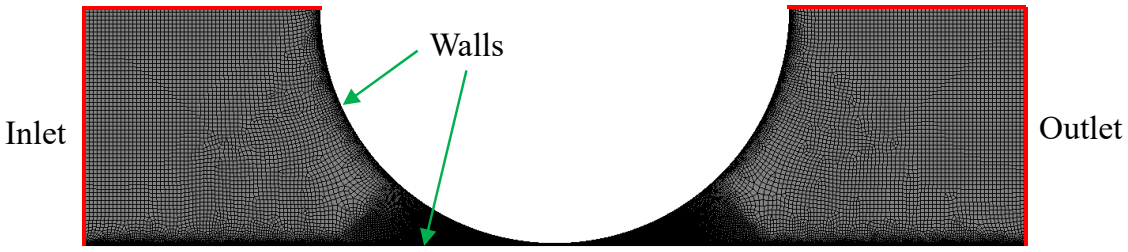

Figure 6.6. Computational domain for the analysis of gap flow through curved constriction ($R_1 = 5$ mm, $R_2 = \infty$ and $h = 30\,\mu$m)

Appropriate mesh convergence study was done for each of the computational domains to determine the level of refinement that would yield accurate solution in low computational time. Figure 6.7 shows the results from the mesh convergence study (in terms of convergence of the flow rate through the gap) on the domain with $R_1 = 5$ mm, $R_2 = \infty$ and $h = 30\,\mu$m.

Pressure boundary condition was imposed at the inlet and the outlet of the flow domain (Figure 6.6). Apart from this, no slip boundary condition was employed on the walls. Reynolds-averaged Navier-Stokes equations (with SST $k - \omega$ turbulence model) were solved using SIMPLEC algorithm. The criteria for convergence was the reduction of residual of these equations below 10^{-6}.

6.3.1 Equivalence of curvature

First, the concept of equivalence of curvature (Eq. 6.2) was tested. Three sets of simulations were conducted (Table 6.1), where, in each set, the radius of each wall was

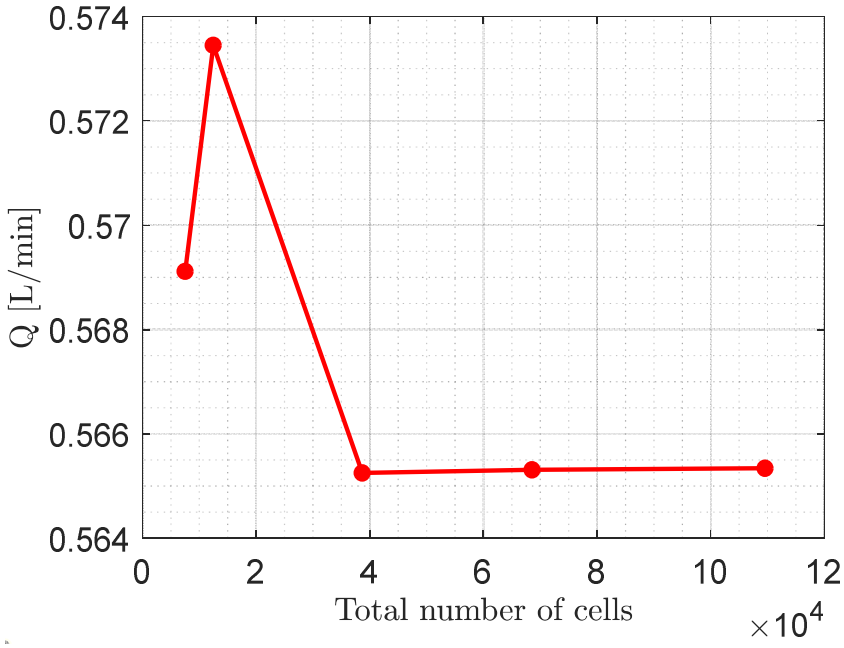

Figure 6.7. Convergence of gap flow with mesh refinement. Gap geometry: $R_1 = 5$ mm, $R_2 = \infty$ and $h = 30\,\mu$m. The simulations were conducted at 10 bar pressure difference with fluid properties of ISO VG 46 mineral oil. The flow rate is calculated assuming the depth of the gap as 70 mm.

varied such that equivalent radius of curvature remained unchanged. One simulation case in each set was such that the radius of curvature of one wall was infinite, meaning a flat wall (Figure 6.6). The height of the gap for all the simulations was kept at 25 microns. Figure 6.8 shows that flow rate through curved constrictions is independent of the radius of curvature as long as the equivalent radius of curvature remains the same. This validates the concept of equivalence of curvature. So, from the geometry standpoint, the equivalent radius of curvature (R_{eq}) and the minimum gap height (h) is enough to describe the flow.

Table 6.1.
Simulation cases to test the equivalency of curvatures

Set	R_1 (mm)	R_2 (mm)	R_{eq} (mm)	R_1/R_2
1.1	4	-20	5	-0.2
1.2	5	∞	5	0
1.3	7.5	15	5	0.5
1.4	10	10	5	1
2.1	2.4	-12	3	-0.2
2.2	3	∞	3	0
2.3	4.5	9	3	0.5
2.4	6	6	3	1
3.1	0.8	-4	1	-0.2
3.2	1	∞	1	0
3.3	1.5	3	1	0.5
3.4	2	2	1	1

6.3.2 Functional relationship

At this point, to determine the functional relationships described in section 6.1, multiple CFD simulations were conducted in Fluent. For simplicity, one wall of the flow geometry was kept flat, while the radius of curvature of other wall was varied. From considerations based on literature [112–114] and past experience, it has been noticed that radius of curvature of most gear profiles fall in the range of 0.4 mm to 10 mm. Thus, as per Eq. 6.2, the range of equivalent radius of curvature is 0.2 mm to 5 mm. Moreover, typical CCHGPs and gerotors have tooth tip clearances ranging from 5 to 50 microns. This gives us the range of dimensionless parameter Π_h as 0.001 to 0.25. So, multiple domains were constructed with different wall curvatures and gap heights in aforementioned range. A wide range of pressure (0 to 200 bar) and

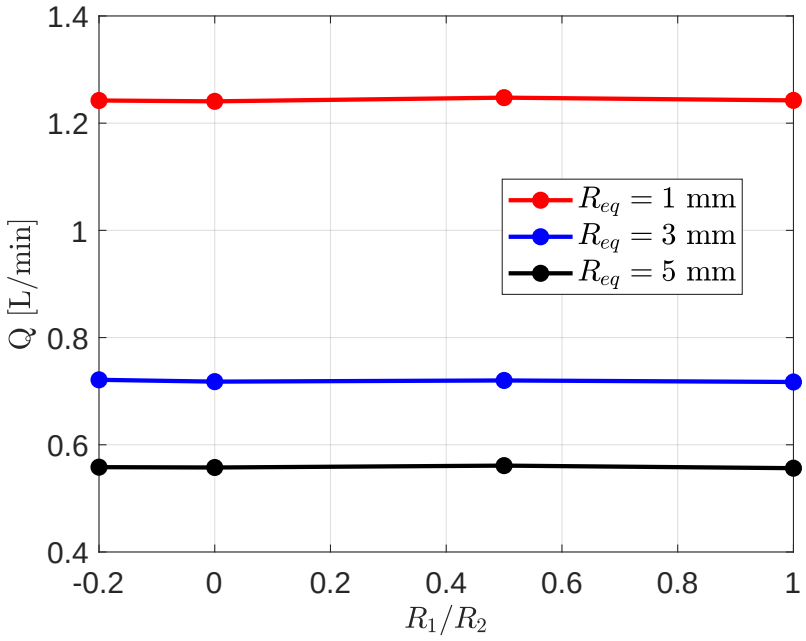

Figure 6.8. Flow rate through the constrictions for a range of curvatures of walls

fluid properties was used in the simulations to obtain a wide range of dimensionless number Π_p.

The results show that for lower values of Π_p and Π_h, the flow remains attached to the walls (Figure 6.9(a)). However, at high values of Π_p and Π_h, the flow separates from the curved wall (Figure 6.9(b)).

The flow data from the results are used to evaluate Π_v (Eq. 6.4) and the same is plotted against Π_p for a range of $\Pi_h\,(= h/R_{eq})$ values in Figure 6.10. At lower values of Π_p and Π_h, (when the flow remains attached to the walls), Π_v is seen to be independent of Π_p and is only influenced by Π_h. On the other hand, at higher values of Π_p and Π_h (when flow separation occurs), Π_v becomes independent of Π_h and is only dependent on Π_p.

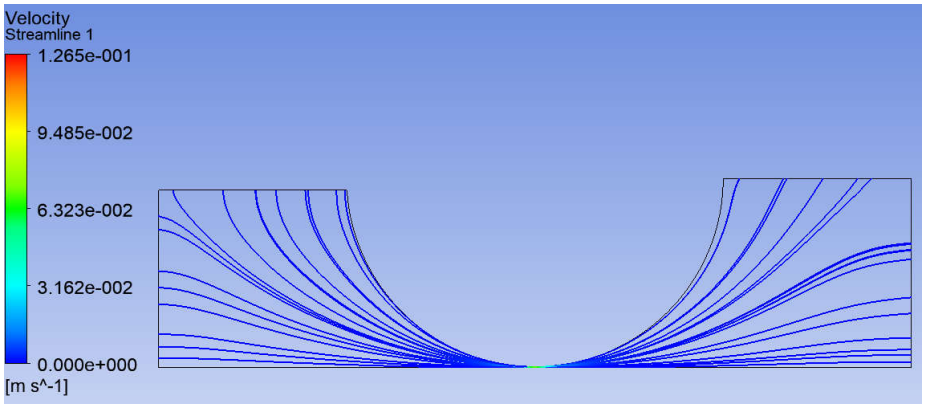

(a) $\Pi_h = 0.002$, $\Pi_p = 12.2$

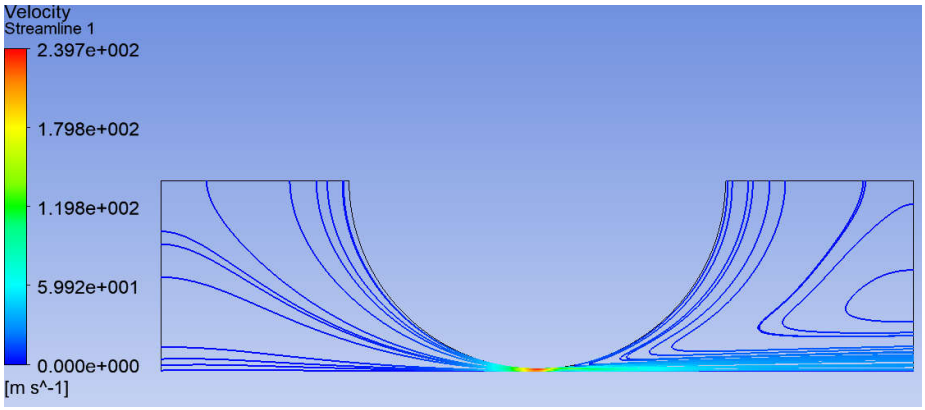

(b) $\Pi_h = 0.01$, $\Pi_p = 5.21 \times 10^6$

Figure 6.9. Streamlines of the flow through the curved constriction for two different flow conditions

From Figure 6.10, below the line $\Pi_v = \sqrt{1/(2\Pi_p)}$, Π_v only depends on Π_h. This dependence is shown in Figure 6.11. From the plot, the functional relationship obtained via curve fitting is:

$$\frac{\mu v}{h\Delta p} = 0.05\sqrt{\frac{h}{R_{eq}}} \tag{6.31}$$

The R squared value (goodness-of-fit measure) for this relation is 0.9974. Notably, this is the same relation obtained analytically from the Reynolds equation of lubrication in section 6.2.

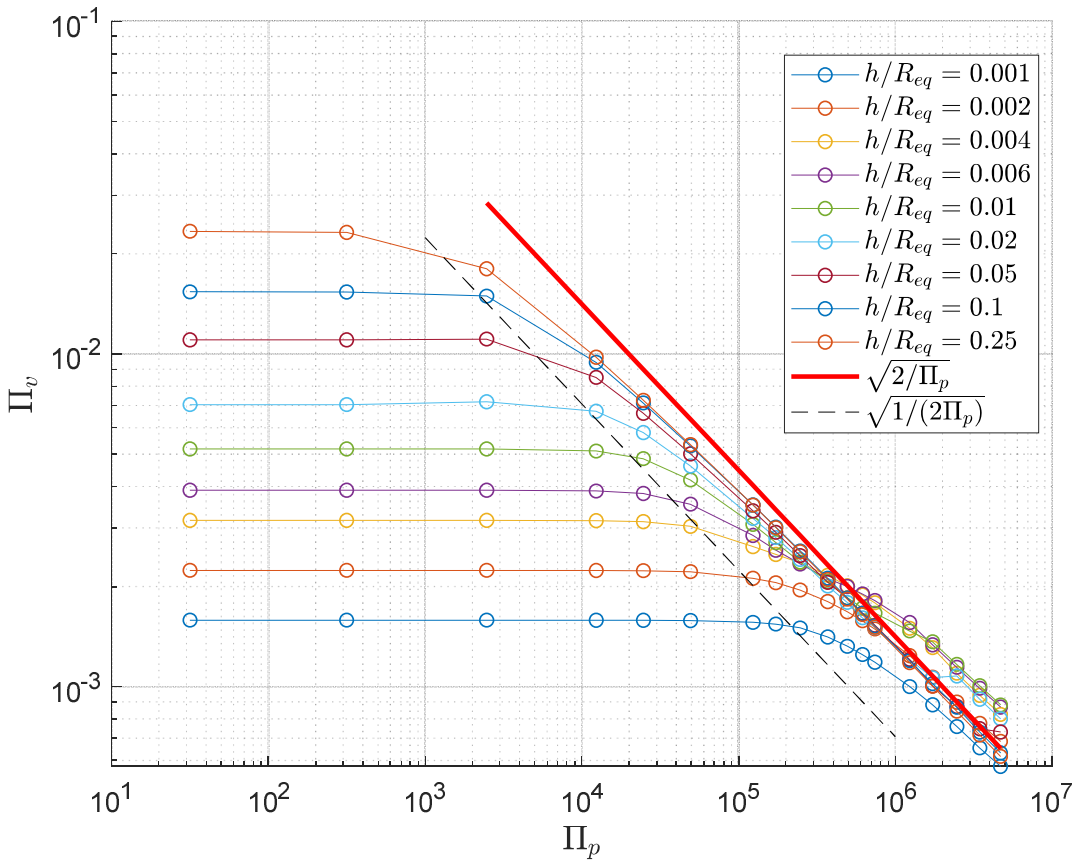

Figure 6.10. Variation of Π_v with Π_p for a range of Π_h $(= h/R_{eq})$.

This relation is valid below $\Pi_v = \sqrt{1/(2\Pi_p)}$ line (Figure 6.10), i.e. when

$$\Pi_v < \sqrt{\frac{1}{2\Pi_p}} \tag{6.32}$$

$$\implies \Pi_{hp} = 0.05\sqrt{2\Pi_h\,\Pi_p} < 1 \tag{6.33}$$

In Figure 6.10, it can be observed that at high values of Π_p, all the curves collapse around a single line whose equation is:

$$\Pi_v = \sqrt{\frac{2}{\Pi_p}} \tag{6.34}$$

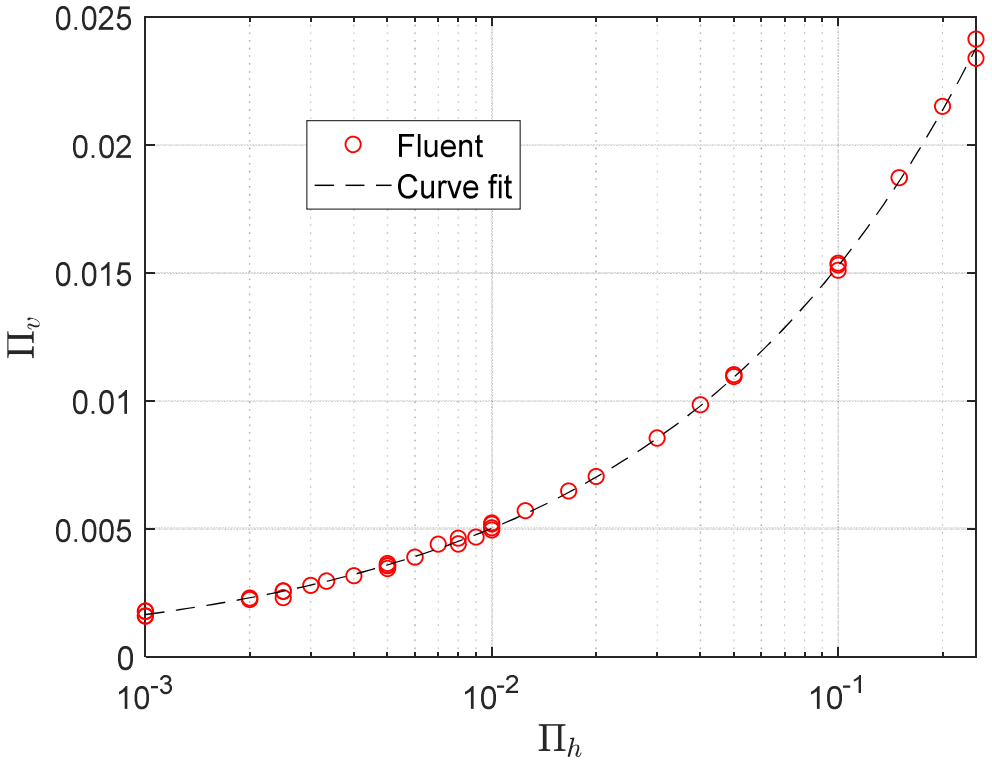

Figure 6.11. Variation of Π_v with Π_h for laminar flow conditions

Expanding and simplifying above equation, following relation is obtained:

$$v = \sqrt{\frac{2\Delta p}{\rho}} \tag{6.35}$$

$$\implies Q = \Omega\sqrt{\frac{2\Delta p}{\rho}} \tag{6.36}$$

This is indeed the orifice equation (Eq. 2.2) with $C_f = 1$. The orifice flow coefficient, C_f is 1 because the shape of the curved constriction is similar to a venturi which has $C_f = 0.99$ [115]. Moreover, the flow coefficient is a measure of contraction of the flow after the constriction throat (called vena contracta). Figure 6.12 shows the absence of contraction of flow after the throat justifying the value of C_f being 1.

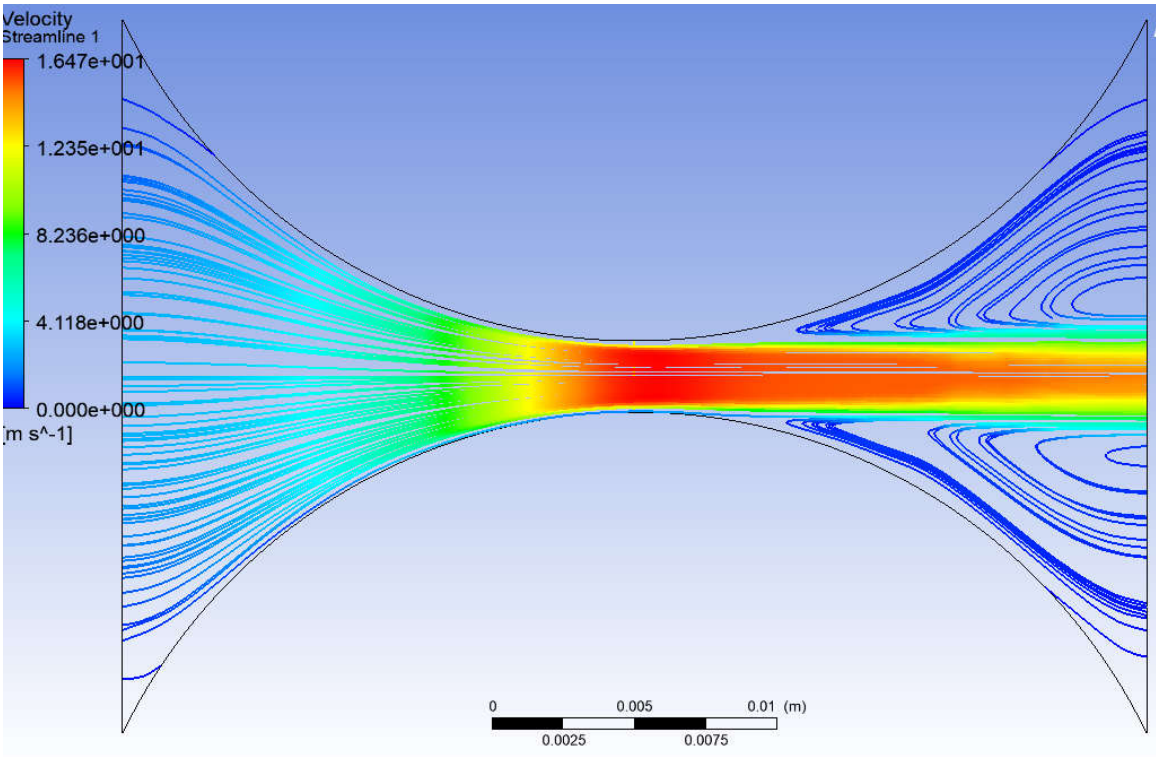

Figure 6.12. Streamlines of a flow with $\Pi_h = 0.25$ and $\Pi_p = 8 \times 10^5$ showing the absence of vena contracta due to which $C_f = 1$

To summarize, the relation describing the flow through the curved constriction is

$$\Pi_v = \begin{cases} 0.05\sqrt{\Pi_h} & \text{, when } \Pi_{hp} < 1 \\ \sqrt{\frac{2}{\Pi_p}} & \text{, when } \Pi_{hp} \gg 1 \end{cases} \tag{6.37}$$

These two relationships can be combined using a tanh function:

$$\Pi_v = (0.05\sqrt{\Pi_h})^{\zeta_1} \left(\sqrt{\frac{2}{\Pi_p}}\right)^{\zeta_2} \tag{6.38}$$

where,

$$\zeta_1 = 0.5 - 0.5\tanh\left(c_1 \log(\Pi_{hp}) + c_2\right) \tag{6.39}$$

$$\zeta_2 = 0.5 + 0.5\tanh\left(c_3 \log(\Pi_{hp}) + c_4\right) \tag{6.40}$$

Here, $c_1 = 0.67$, $c_2 = 0.61$, $c_3 = -0.096$, $c_4 = 0.062$

6.4 Effect of cavitation

The flow model presented in the previous subsection was developed for non-cavitating conditions. However, in turbulent flow regime, the flow separates from the walls (Figure 6.12) creating low pressure regions where there is a possibility of pressure falling below the gas saturation pressure of the fluid. In such a scenario, the gases normally dissolved in the fluid, come out of the solution in the form of bubbles (referred to as aeration). Next, if the pressure falls below the vapor pressure of the fluid, the fluid experiences a phase change from the liquid state to gaseous state (vaporous cavitation). Generally, the term cavitation encompasses aeration and vaporous cavitation. The energy consumed during the cavitation process (i.e. air bubble formation and phase change) occurring in the flow channel should result in a lower power level at the outlet of the channel. That is, lower flow should be expected for a given pressure difference.

To study these effects of cavitation on the flow behavior, flow simulations were conducted using the commercial CFD software PumpLinx [33]. This tool is preferred over ANSYS Fluent for cavitation studies since this tool has a robust cavitation model that accounts for both aeration and vaporous cavitation. The cavitation model is based on the homogenous fluid approximation where the fluid is considered as a mixture of liquid, vapor and gases. The evolution of vapor and gas fractions in the flow is determined from a reduced form of Rayleigh-Plesset equation for bubble dynamics, based on the work by Singhal et al. [116].

The computational domain was similar to what was described in section 6.3 and multiple simulations were conducted for similar range of geometries and flow conditions.

The results from the simulations confirm the fact that the flow separation is accompanied with a significant drop of pressure. Figure 6.13 shows two such instances where the pressure drops well below the outlet pressure. From the simulation results, it was observed that for same values of Π_h and Π_p, when the pressure in the flow

domain stays above the saturation pressure, 0 bar or 1.013 barA (Figure 6.13(a)), the flow relations from the previous section predict Π_v very well. However, when the pressure in the domain falls below the saturation pressure (Figure 6.13(b)), Π_v obtained from the simulations is lower than that predicted from the non-cavitating model. This is expected because of the energy consumption in the cavitation process.

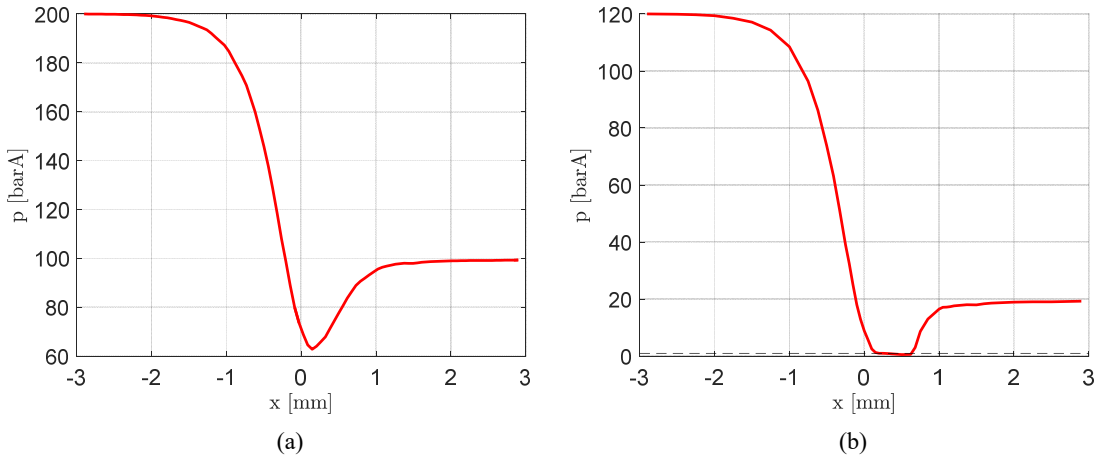

Figure 6.13. Variation of pressure along the flow direction. $x = 0$ is the location of constriction. $\Pi_h = 0.05$, $\Pi_p = 1.9 \times 10^5$ (a) $p_{in} = 200$ bar, $p_{out} = 100$ bar (b) $p_{in} = 120$ bar,$p_{out} = 20$ bar, dotted line indicates 1.013 barA

It is further observed that the ratio of the inlet to outlet pressure dictates the extent of the drop of pressure at flow separation. For instance, in Figure 6.13, this ratio is 2 for non-cavitating case and 6 for cavitating case. From this observation, a cavitation non-dimensional parameter Π_c is proposed:

$$\Pi_c = \frac{p_{in}}{p_{out}} \tag{6.41}$$

such that the tendency of the flow to cavitate increases with Π_c. A simulation campaign was carried out where for each Δp across the flow geometry, multiple simulations with varying Π_c were conducted. Table 6.2 shows a sample of operating conditions illustrating how Π_c variation was achieved.

Table 6.2.
Pressure boundary conditions applied to vary Π_c

p_{in} (barA)	p_{out} (barA)	Π_c
$\Delta p = 10$ bar		
40	30	1.33
20	10	2
15	5	3
12	2	6
11	1	11
10.5	0.5	21
10.1	0.1	101
$\Delta p = 100$ bar		
200	100	2
150	50	3
120	20	6
110	10	11
105	5	21
100.5	0.5	201

Figure 16.14 shows the results in terms of $\Pi_v/\Pi_{v,nc}$ vs Π_c where $\Pi_{v,nc}$ is the Π_v value obtained for the non-cavitating case. Clearly, as Π_c increases, the flow and hence Π_v decreases. The trend flattens out at higher values of Π_c since at such high values, doubling Π_c causes a minimal change in the actual pressure boundary conditions. For instance, for $\Delta p = 200$ bar, $\Pi_c = 101$ means $p_{in} = 202$ barA and $p_{out} = 2$ barA, whereas $\Pi_c = 201$ means $p_{in} = 201$ barA and $p_{out} = 1$ barA.

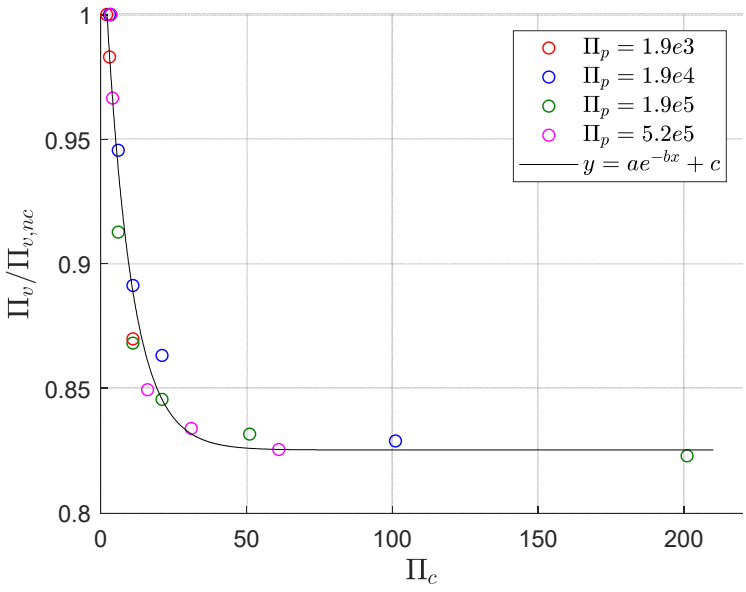

Figure 6.14. Simulation results quantifying the effect of cavitation

Based on these results, the following formulation for Π_v is proposed that acts as the correction to the relation in Eq. 6.37:

$$\Pi_v = \Pi_{v,nc} \cdot \zeta_c \tag{6.42}$$

where

$$\zeta_c = c_5 e^{-c_6 \Pi_c} + c_7 \tag{6.43}$$

Here, $c_5 = 0.22$, $c_6 = 0.11$ and $c_7 = 0.83$.

6.5 Experimental tests

6.5.1 Test apparatus design

To validate the leakage flow model developed in previous sections, a novel experimental apparatus was designed, fabricated and tested. The actual flow geometry involves gap heights as small as 5 microns. Designing a setup at such scale would

require very tight tolerances which would have significantly increased the cost of the apparatus. To avoid that, the flow geometry has been scaled by a factor of 50. So, the gap height would vary from 0.25 mm to 2.5 mm and the radius of curvature would vary from 10 mm to 250 mm.

Figure 6.15 shows the front and the side view of the experimental apparatus. The block in the figure have been made transparent so that the slider and the flow geometry is visible. The block has a rectangular cavity on the top in which the slider can slide in. The apparatus utilizes the equivalency of curvature discussed in previous sections. The bottom curved surface of the slider and the flat surface of the block (shown in red lines in Figure 6.15) form the flow geometry of interest. Since only equivalent curvature of the walls matters in the flow analysis, the flat surface of the block is used throughout all experiments. To achieve variable curvature of the flow geometry, three different sliders are manufactured with radius of curvature as 10 mm, 50 mm, and 250 mm. This covers the whole range of the scaled radius of curvature described in previous paragraph.

The gap height is varied by realizing a vertical motion of the slider. To realize that, a tapered hole has been machined in the slider such that the bottom face of the hole is horizontal, but the upper face is inclined at an angle of 3.8° (Figure 6.16). This allows achieving a wedge-shaped element (red element in Figure 6.17) to lift the slider as the wedge is moved horizontally. For each millimeter raising of the slider, the wedge needs to move horizontally by 15 mm. This magnification of motion permits a precise control of the slider position.

To accurately determine the instantaneous position of slider (and hence the height of the gap), a high-resolution micrometer (resolution of 2.5 μm) is mounted on the support element. Figure 6.18 shows how the micrometer allows the indirect measurement of the height of the gap. First, when the slider touches the block (height = 0), the micrometer reading, z_0 is recorded. After that, the slider is raised and the new reading, z, is recorded. The difference $z_0 - z$ provides the gap height value.

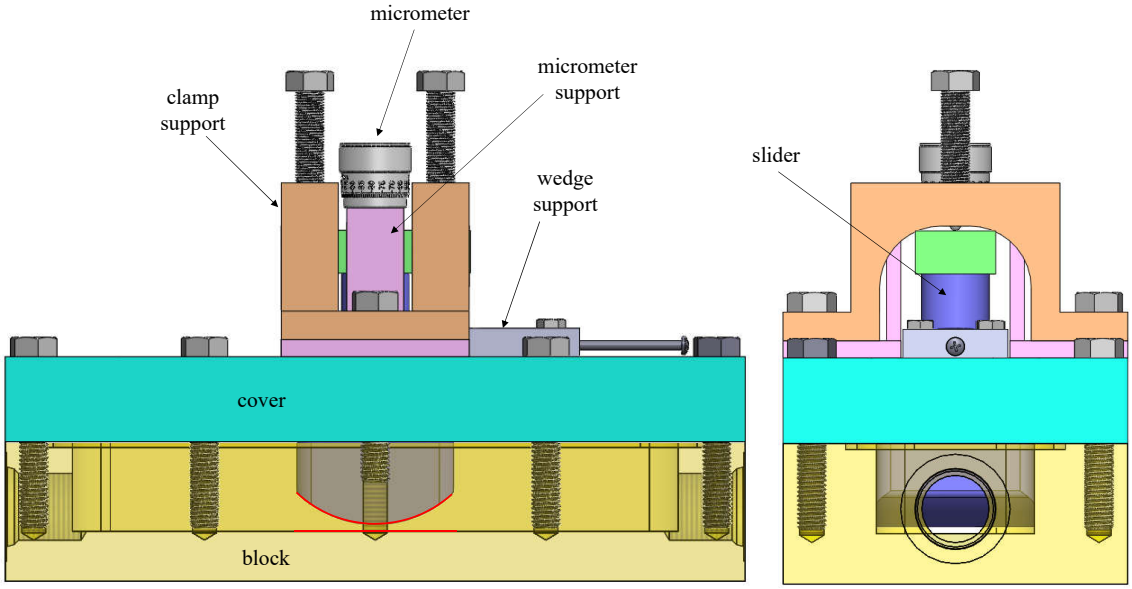

Figure 6.15. Front and side view of the test apparatus with slider of radius 50 mm. The flow geometry is marked in red lines.

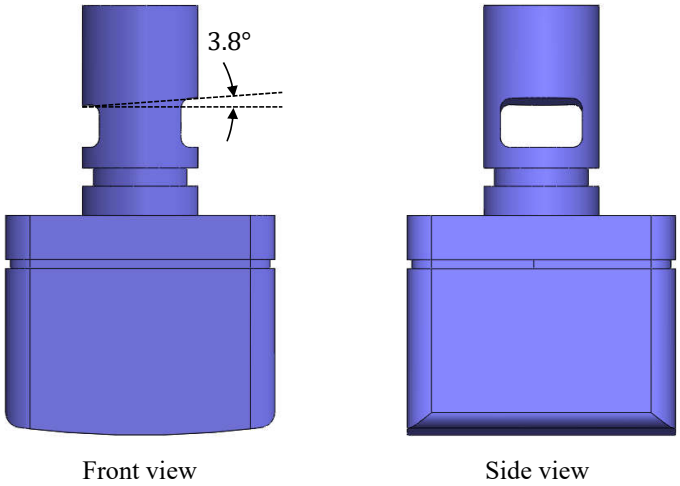

Figure 6.16. CAD of the slider ($R = 250$ mm)

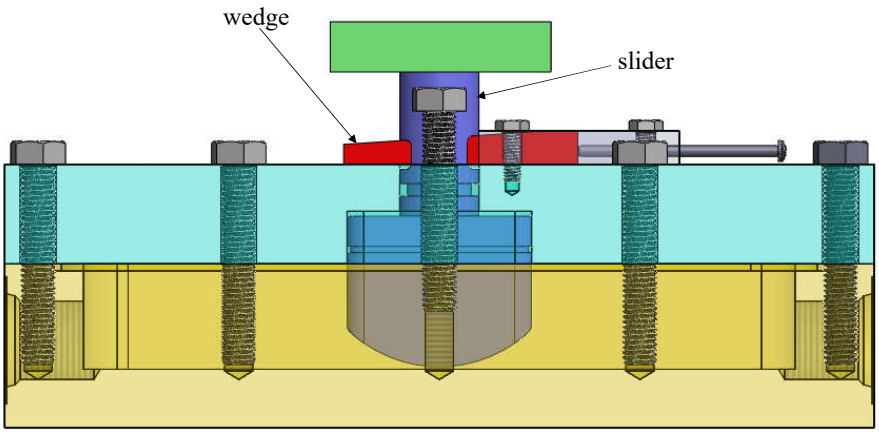

Figure 6.17. Test apparatus with multiple parts hidden to show the slider, wedge and interaction between them.

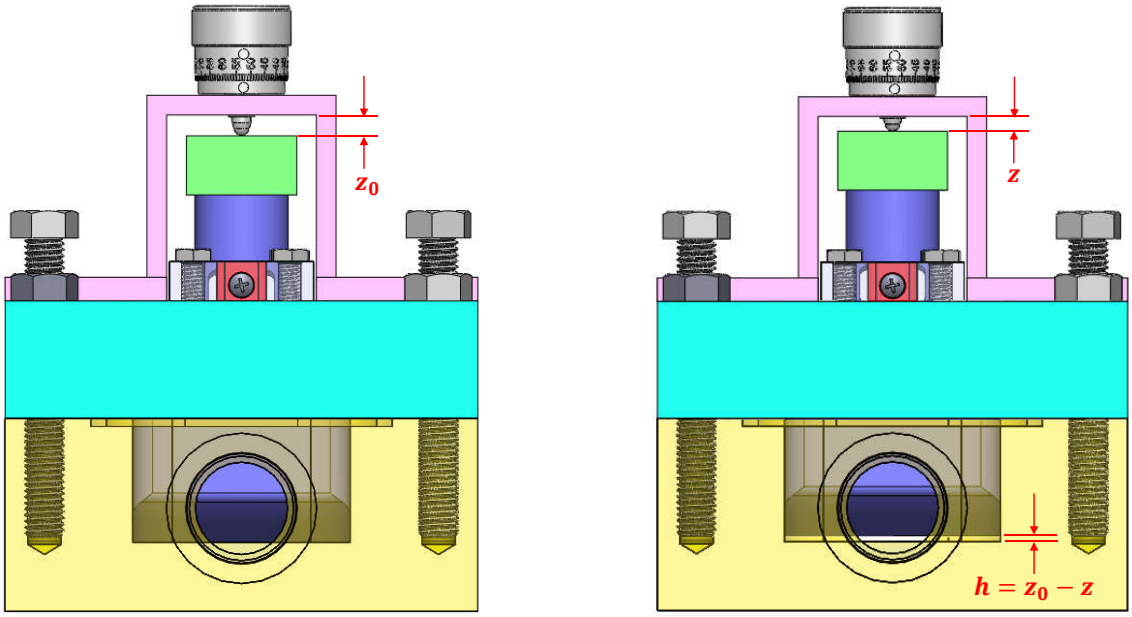

Figure 6.18. Illustration of using micrometer to determine the height of the gap

The slider is clamped from the top via two bolts on the clamp support (Figure 6.15). This prevents the slider from moving up in response to the high fluid pressure below it (between the slider and the block). To allow the motion of the slider within the block cavity, there is a clearance fit between them. The block and slider were designed and manufactured such that this clearance is $\leq 76.2\,\mu m$. Such a low clearance ensures that the flow through this lateral gap is negligible compared to the main flow over the bottom face of the slider.

6.5.2 Hydraulic circuit

A proper hydraulic circuit was designed to perform the experiments necessary to validate the model discussed in previous sections. The ISO schematic of the circuit is shown in Figure 6.19. Pressure and temperature sensors are mounted just before and right after the test apparatus to obtain the pressure difference across the apparatus and monitor the fluid temperature, respectively. The flow rate through the test apparatus is measured via the flow meter mounted downstream of it. As the flow rate in the experiments is varied significantly, two flow meters of different ranges were used in the experiments. The details of these flow meters and other sensors used in the experiments are presented in Table 6.3. For flow rates < 120 L/min, VS02 model was used, whereas for flow rates ≥ 120 L/min, VS10 model was used. Figure 6.20 shows the picture of the apparatus on the test rig.

Table 6.3.
Sensors used in the tests.

Sensor	Model	Specifications	Accuracy
Pressure transducer	Wika S-10	0 to 400 bar	± 0.5% of span
Thermocouple	Omega K-type	-5 to 200 °C	1 °C
Flow meter	VSE VS02	0.1 to 120 L/min	± 0.3%
Flow meter	VSE VS10	1.5 to 525 L/min	± 0.3%

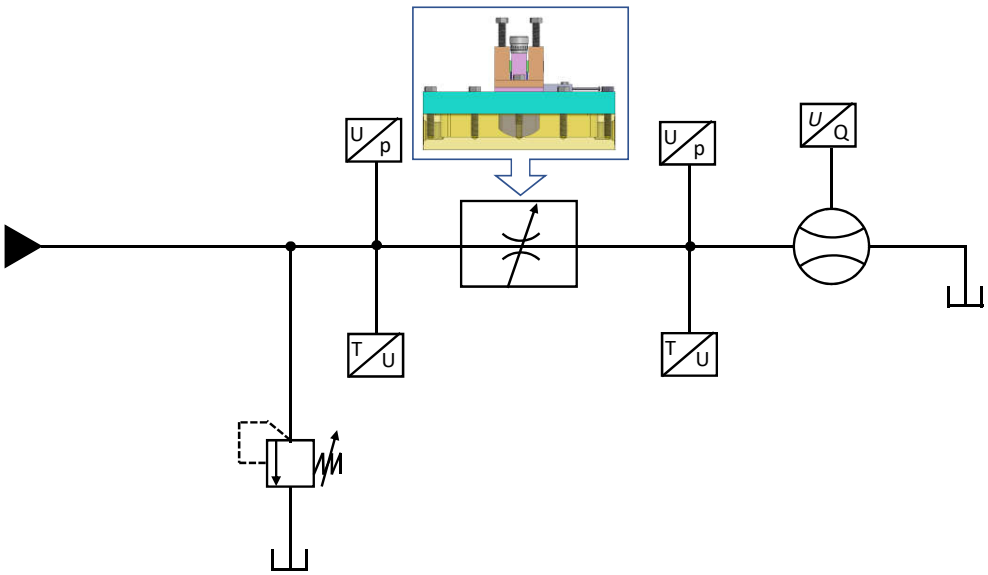

Figure 6.19. ISO schematic of the hydraulic circuit used in the experiments.

An ISO VG 46 mineral oil was used as the operating fluid in the tests. Multiple tests were conducted using each of the three sliders by varying the slider position and then varying the flow rate at the source for each slider position.

The experiments were conducted in three sets. In set A, the experiments were performed to validate the model for laminar flow conditions, i.e. Eq. 6.31. As discussed in section 6.3, this equation is valid for low values of Π_p. To ensure this, experiments were conducted at

- low temperature (20 °C) : this raised the viscosity of the fluid, and
- low flow rates : this allowed a lower pressure drop across the constriction

In set B, the experiments were performed to validate the turbulent flow model and the behavior of the transition from laminar to turbulent flow regime. As the transition and turbulent flows occur at higher values of Π_p, the experiments were conducted at higher temperatures (30-75 °C) and high flow rates.

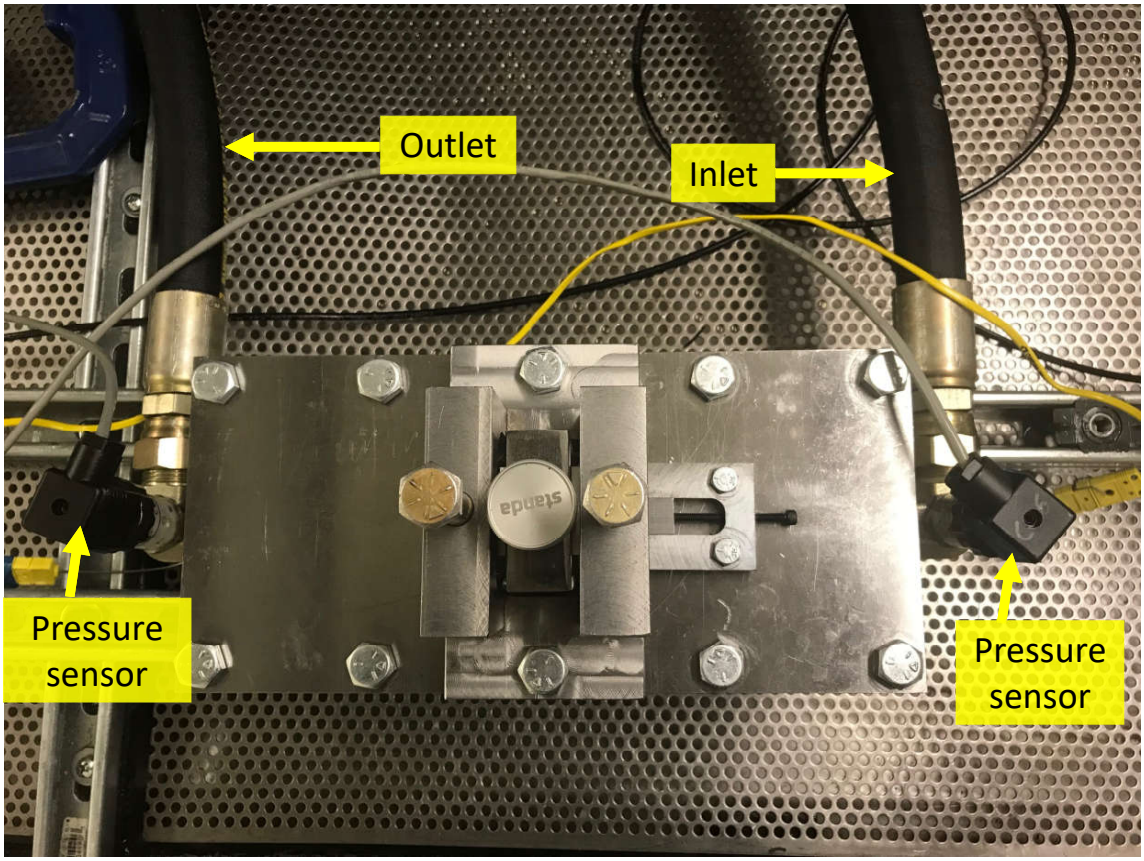

Figure 6.20. Picture of the test apparatus in the hydraulic circuit.

Finally, in set C, the experiments were conducted to validate the cavitation correction of the model. To allow the occurrence of localized cavitation (predicted via the variation of Π_c), the hydraulic circuit was modified as shown in Figure 6.21. In this circuit, when the ball valve is open, there is nearly zero resistance to the flow downstream of the apparatus. Thus, when the flow rate is increased at the source, pressure at the inlet increases, promoting Π_c and hence, localized cavitation. On the other hand, when the ball valve is closed, the apparatus outlet pressure increases owing to the resistance at the needle valve resulting in lowering Π_c and eliminating cavitation.

To obtain the results for a range of Π_c, the flow source was set to a constant flow rate value and data were recorded for different positions (closed/open) of the ball and needle valves. The procedure was then repeated for different flow rate values.

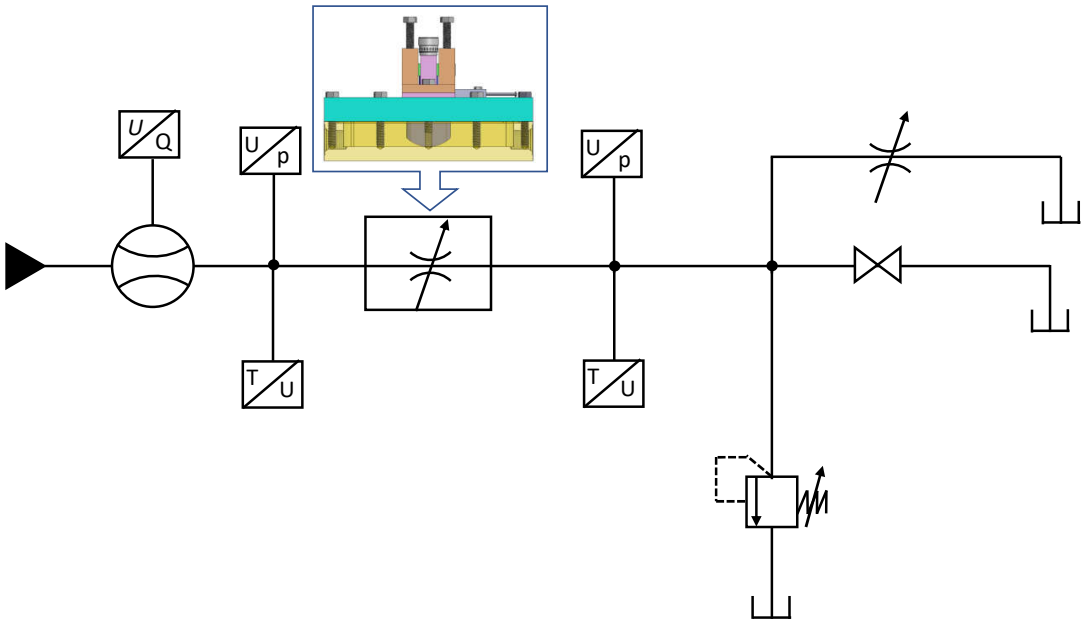

Figure 6.21. ISO schematic of the hydraulic circuit used in the experiments for set C.

6.6 Results and discussion

6.6.1 Laminar flow

In this section, results from the experiments in set A are presented. Figure 6.22 shows the results obtained by using the slider with radius of curvature of 50 mm. As expected, as the gap height increases, for the same flow rate, the amount of pressure drop across the slider decreases. So, in order to obtain same pressure drop, higher flow rate is needed. At gap height of 1 mm, 84 L/min of flow was required to obtain a pressure drop of 3.7 bar. Similar results were also obtained for other two sliders with radius of curvature of 250 mm (Figure 6.23) and 10 mm (Figure 6.24). The nature of

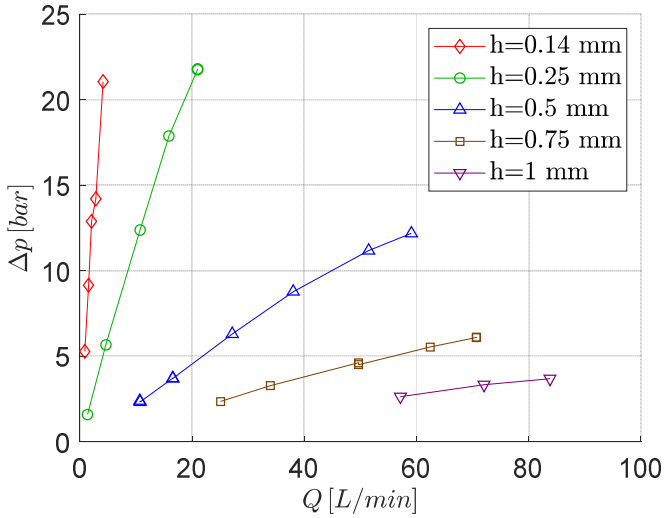

Figure 6.22. Flow pressure characteristics for the flow geometry with $R_{eq} = 50$ mm

the curve changes a little towards the upper end of each curve. This happens because of micron level deformation of the gap geometry at high pressures leading to slight increase in the gap height.

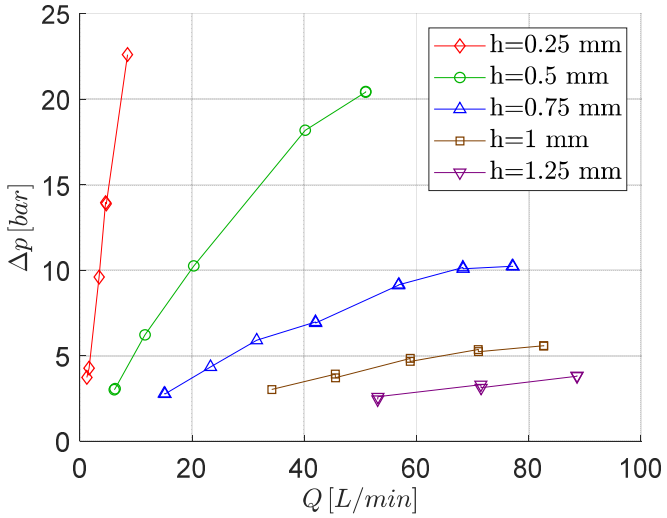

Figure 6.23. Flow pressure characteristics for the flow geometry with $R_{eq} = 250$ mm

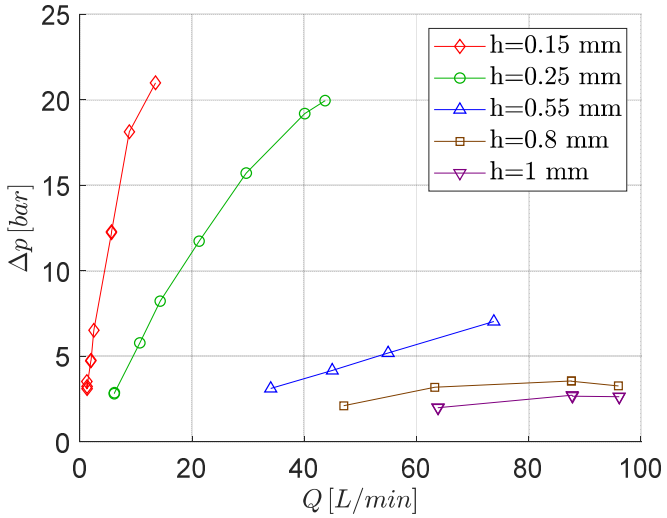

Figure 6.24. Flow pressure characteristics for the flow geometry with $R_{eq} = 10$ mm

The data recorded from the experiments is transformed into the dimensionless numbers Π_h and Π_v. Figure 6.25 shows the plot of Π_v vs Π_h obtained from experimental tests. The functional relationship for laminar flow (Eq. 6.31) is plotted in dotted lines. The figure shows a good match between experiments and the model. Thus, the non-dimensional leakage flow relation for laminar flow is validated. For $h/R_{eq} > 0.08$, the experiments deviate from the model. This is because at such high values of Π_h, very low values of Π_p is required to keep $\Pi_{hp} < 1$. Such low values of Π_p would either need very low pressure difference across the gap (which would be lower than the accuracy of the sensors) or very high viscosity (which would require temperature < 20 °C; this is not attainable in the test rig).

Comparison with Pellegri et al.'s leakage flow model

In their lumped parameter based fluid dynamic model, Pellegri et al. [108–110] assume laminar nature of the flow over the tooth tip of gerotor and use the equation for flow between parallel plates to model the tooth tip gap flow. The actual gap

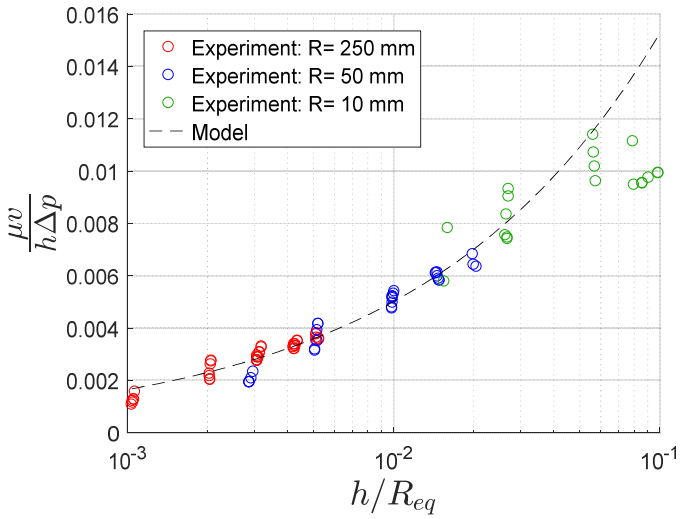

Figure 6.25. Results from the experiments and comparison with the laminar flow model

geometry is anything but parallel plates, however, the comparison of the laminar model developed in this work with Pellegri et al.'s model does provide an interesting insight. Pellegri et al. propose that flow over the tooth tip is given by the following equation:

$$Q = \frac{bh^3}{12\mu L_t}\Delta p \tag{6.44}$$

where, L_t is the distance between two regions where the gap height increases from the minimum gap height, h to $h(1+\epsilon_h)$. Here, ϵ_h is a tunable parameter.

From Eq. 6.44, the dimensionless parameter

$$\Pi_v = \frac{\mu v}{h\Delta p} = \frac{h}{12L_t} \tag{6.45}$$

Π_v from above equation and Π_h are evaluated for a range of geometrical parameters, and the results are compared against the laminar non-dimensional model developed in this work (Eq. 6.31). Figure 6.26 shows the comparison for multiple values of ϵ_h. In [110], Pellegri et al. choose $\epsilon_h = 0.1$ and in [117], Pellegri suggests the range of ϵ_h between 0.08 and 0.15. However, according to Figure 6.26, ϵ_h=0.36 matches the model accurately (the mean error for $h/R_{eq} \in [10^{-3}, 10^{-1}]$ is 2%). Thus,

although, the simplifications in Pellegri et al.'s leakage flow model can be questioned, it is interesting to note that for certain value of the parameter ϵ_h, it matches the laminar model developed and validated in this work.

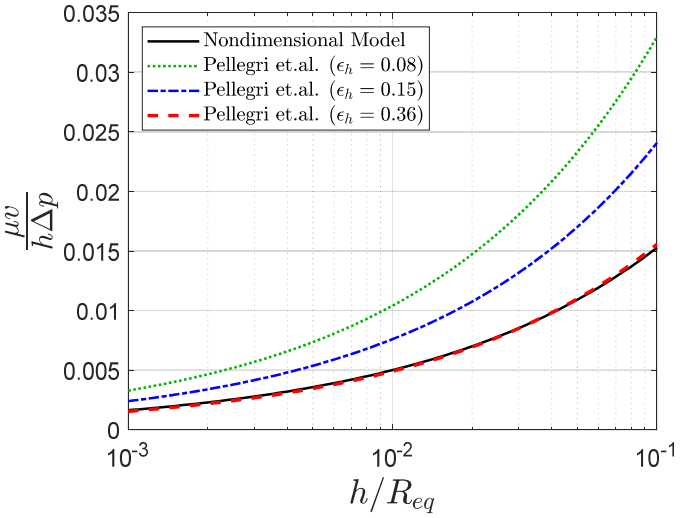

Figure 6.26. Comparison of the laminar flow model developed in this work with Pellegri et al. [108, 109]

6.6.2 Transition and turbulent flows

The flow experiments in set B encompass the transition and turbulent flow regimes. For fully turbulent flows ($\Pi_p > 10^6$ as per Figure 6.10), the pressure-flow characteristic is observed to be quadratic ($\Delta p \propto Q^2$). This behavior is typical of turbulent flows. In Figure 6.27, the experimental results match the dimensional turbulence flow relation (Eq. 6.36) in their quadratic behavior.

The experimental data for both the transition and turbulent flow regimes is transformed into the dimensionless form and is compared against the combined flow model (Eq. 6.38). Figure 6.28 shows a good match between the two which validates the curve-constricted flow model developed in this work.

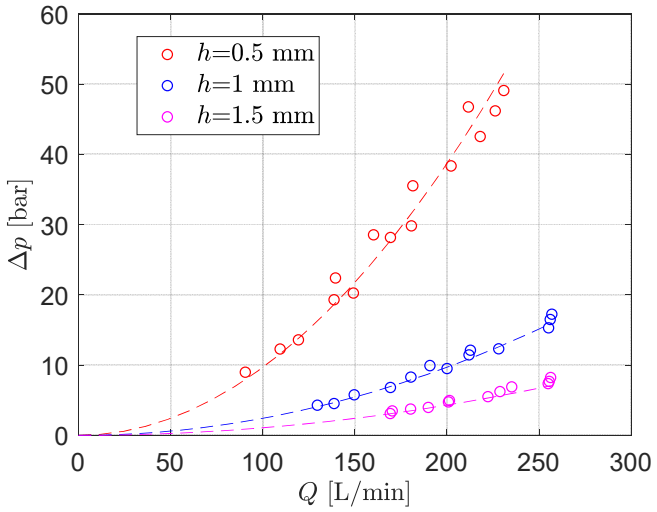

Figure 6.27. Pressure-flow characteristics from a subset of experiments in set B. The dotted lines indicate the characteristics predicted from the dimensional turbulent flow relation in Eq. 6.36.

6.6.3 Effect of cavitation

Finally, the results from the experiments in set C are presented. Figure 6.29(a) shows the results in terms of pressure difference across the apparatus vs the pressure at the outlet of the apparatus for three different flow rates. The variation in the outlet pressure is achieved by changing the positions of the ball and needle valves. When p_{out} is close to 0 bar (1.013 barA), Π_c is high, predicting localized cavitation. Thus, for a given flow rate, the pressure drop across the apparatus is high. As p_{out} is increased, Π_c decreases reducing the extent of cavitation and thus, lowering Δp for a given flow rate. The last two datapoints for each curve have nearly the same Δp indicating the absence of cavitation.

The experimental data is transformed into dimensionless quantities and are compared against the model (Eq. 6.42 and 6.43). Figure 6.29(b) shows a good match between the two that validates the model for cavitation correction.

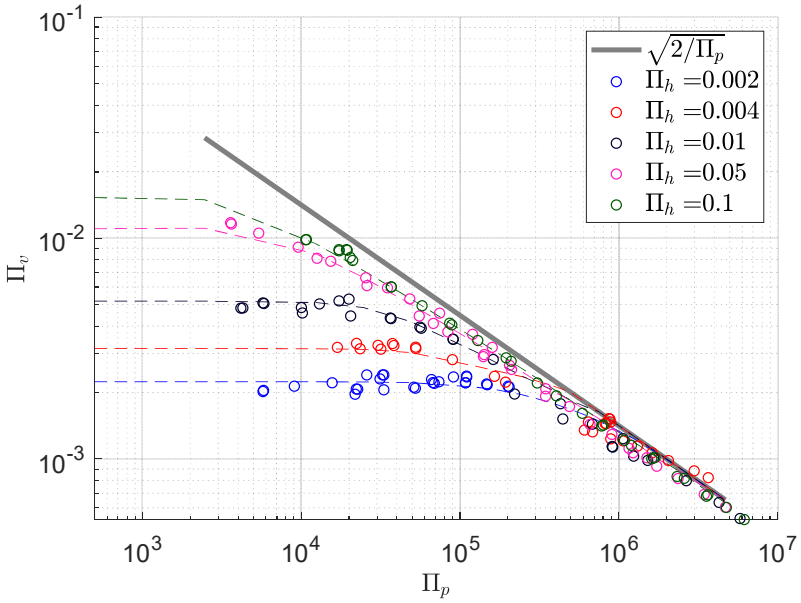

Figure 6.28. Comparison between the experimental data (circles) and the combined flow model (dotted line). The solid line indicates the model for fully turbulent flow.

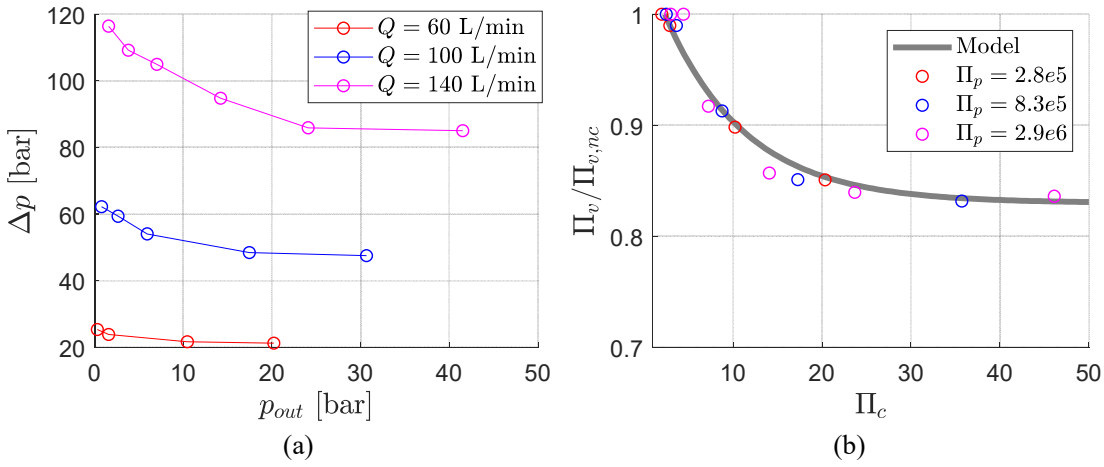

Figure 6.29. Results showing the effects of cavitation on flow: (a) pressure data from the experiments and (b) comparison between the experimental data and the cavitation correction model.

7. PREDICTION OF HYDRO-MECHANICAL EFFICIENCY IN EXTERNAL GEAR MACHINES

In previous chapters, the focus has been on the accurate modelling of internal flows in gear machines. This is important in the prediction of volumetric efficiency of these machines. However, an equally important performance characteristic of EGMs is the hydro-mechanical efficiency (also referred to as the torque efficiency). The total efficiency of an EGM is the product of volumetric and hydro-mechanical efficiencies. Hence, the capability of the prediction of hydro-mechanical efficiency is a critical attribute of an EGM simulation tool. However, this attribute is absent in almost all the state-of-the-art EGM simulation tools. Thus, the work presented in this chapter forms a key contribution to the field of EGM modelling.

To determine the hydro-mechanical efficiency of a unit, all the sources of torque losses must be identified and loss models must be developed for each of these sources. In EGMs, the key sources of torque losses are friction at the gear tooth tips, friction at the lateral leakage interfaces, friction at the bearings and friction between the gears during their meshing.

The torque loss models proposed by the researchers in 20^{th} century, for positive displacement machines in general, were semi-empirical in nature [118–122]. Even for EGMs in particular, early models were based on experimental data [123]. The first numerical model for the prediction of torque losses in EGMs (that was not dependent on experimental data) was developed by Thiagarajan and Vacca [124]. However, this model involves 2D CFD based modelling of the lateral lubricating interfaces that makes it computationally expensive. Moreover, the model makes certain assumptions on the evaluation of the meshing friction which can be a major contributor to the torque losses. The most recent work in this topic is the one published by Zardin et al. [125]. However, their approach has few limitations related to the friction at the

journal bearings and the meshing interface. In particular, for journal bearing, the shaft is assumed to be concentric to the bearing, thereby neglecting the micromotion phenomenon (which as discussed in section 1.6, significantly impacts the EGM performance). Moreover, for the evaluation of the meshing friction, ISO standard for gearboxes is used whose applicability is debatable for EGMs where significantly high levels of pressures are observed.

The work presented in this chapter aims to overcome these limitations without sacrificing the simulation swiftness. In this work, a new methodology for the evaluation of torque losses at key interfaces in EGMs is developed. The loss models are then integrated in the HYGESim simulation tool and validated against the experimental data. The reference machine used in this work is Casappa PHP20 pump (E5).

7.1 Friction at the tooth tip

As described in previous chapters, the micron level gaps between the gear tooth tips and casing allow the fluid flow across the tooth driven by relative motion of the surfaces and pressure difference across the adjacent TSVs. As the reference EGM E5 works with mineral oils and operates at moderate speeds (1000-2500 rpm), the flow over the tooth tip stays laminar (Figure 7.1). For laminar Couette-Poiseuille flow over the tooth, the flow velocity can be expressed as:

$$v = \frac{\mathrm{v}y}{h} - \frac{1}{2\mu} y(h-y)\frac{dp}{dx} \tag{7.1}$$

Then, the shear stress on the gear tooth tip:

$$\tau_w = \frac{\mu \mathrm{v}}{h} + \frac{h}{2}\frac{dp}{dx} \tag{7.2}$$

$$\implies \tau_{w,i} = \frac{\mu\omega r_g}{h} + \frac{h(p_{i+1} - p_i)}{2L} \tag{7.3}$$

From shear stress, the shear force on each tooth tip can be calculated as

$$F_i = \tau_{w,i} L b \tag{7.4}$$

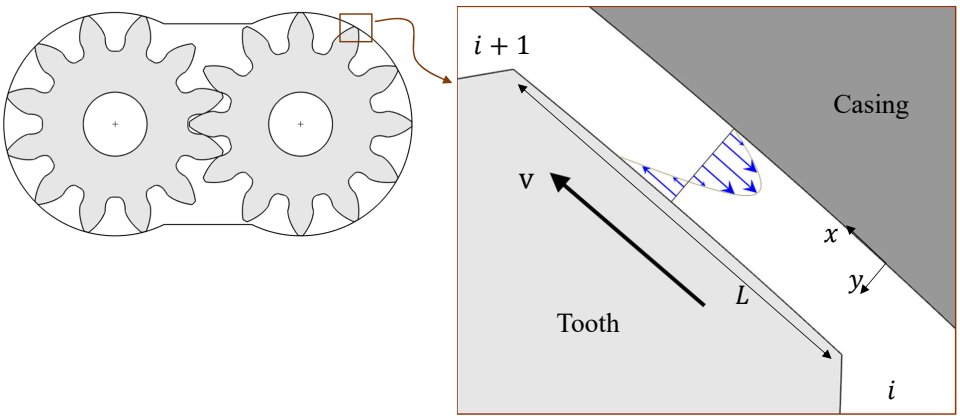

Figure 7.1. reference pump E5: Gap at the tooth tip with local coordinate system for theoretical analysis.

Finally, the torque from the friction at the tooth tip,

$$M_{f,tip} = \sum_i F_i r_g = Lbr_g \sum_i \tau_{w,i} \tag{7.5}$$

This approach works when the gap height is higher than the surface roughness. However, in EGMs, due to the asymmetric loading of the gears, the gears move towards the low pressure side (gear micromotion). Often, the gears wear into the casing and then maintain a low gap height at the tooth tip. This is desirable from the leakage reduction perspective. However, such low height means that the surface roughness can no longer be neglected.

Patir and Cheng [126,127] have investigated lubrication under mixed friction conditions where due to surface roughness, friction between the two surfaces arise from a combination of viscous shear and asperity contacts (Figure 7.2). They proposed the following model of shear stress for the conditions of mixed friction:

$$\tau = \frac{\mu \mathrm{v}}{h}(\phi_f + \phi_{fs}) + \phi_{fp}\frac{h}{2}\frac{dp}{dx} \tag{7.6}$$

where

$$\phi_f = h\boldsymbol{E}(1/h_T) \tag{7.7}$$

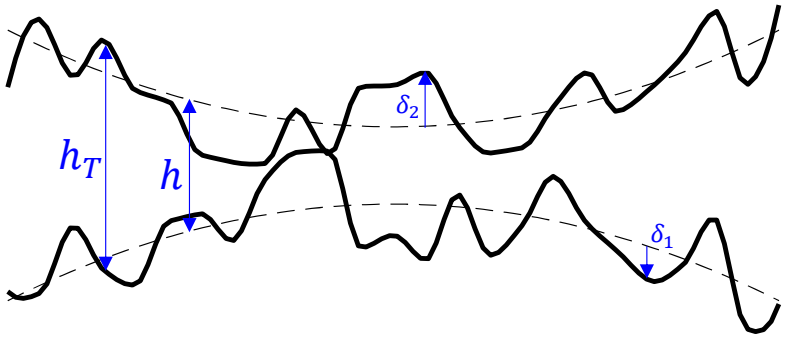

Figure 7.2. Illustration of typical gap geometry where gap height is in the order of the surface roughness (adapted from [126])

Here $\boldsymbol{E}$ is the expectation function which is obtained by integration of the roughness distribution over the film region. Next, h is the mean gap height, whereas, h_T is the actual film thickness accounting for surface roughness (Figure 7.2):

$$h_T = h + \delta_1 + \delta_2 \tag{7.8}$$

The analytical approximate expression of ϕ_f for Gaussian distribution is present in [127]. Figure 7.3(a) shows its variation with non-dimensional film thickness h/σ. Here,

$$\sigma = \sqrt{\sigma_1^2 + \sigma_2^2} \tag{7.9}$$

where $\sigma_{1,2}$ is the standard deviation of roughness of the surface 1,2.

In Eq. 7.6 $\phi_{fs} = 0$ for surfaces with longitudinal roughness patterns. This is indeed the case with tooth tip-casing interface. The tooth tip wears into the casing creating roughness pattern along the direction of the motion.

Finally, ϕ_{fp} is the pressure correction term whose variation with non-dimensional film thickness was determined by Patir and Cheng [127] and is shown in Figure 7.3(b).

Thus, in the presence of mixed friction, Eq. 7.2 is replaced by Eq. 7.6 and then Eq. 7.5 is used to evaluate the friction torque at the tooth tips of EGMs.

Figure 7.4 shows the effect of σ on the friction torque. Black line indicates the torque for ideal surfaces with zero roughness. In that case, the full film is preserved

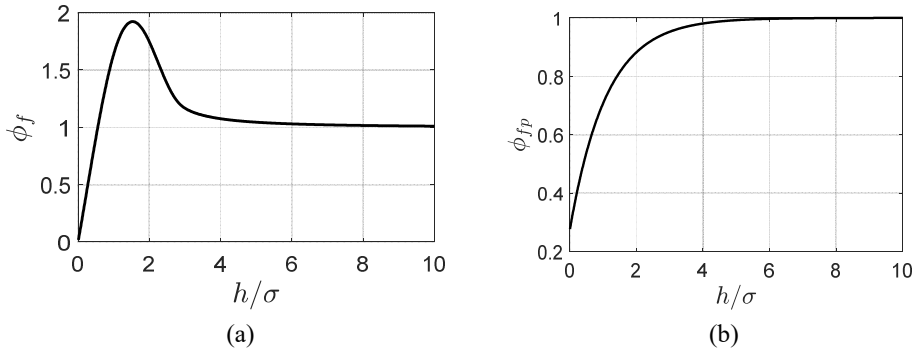

Figure 7.3. variation of factors ϕ_f and ϕ_{fp} with film thickness

even for very low gap heights, $h \to 0$. Thus, as per Eq. 7.2, the shear stress and hence friction torque $\to \infty$ as $h \to 0$. In contrast, for higher surface roughness (increasing σ), the friction at $h \to 0$ is bounded due increase in the size of regions under asperity contacts compared to regions under full film.

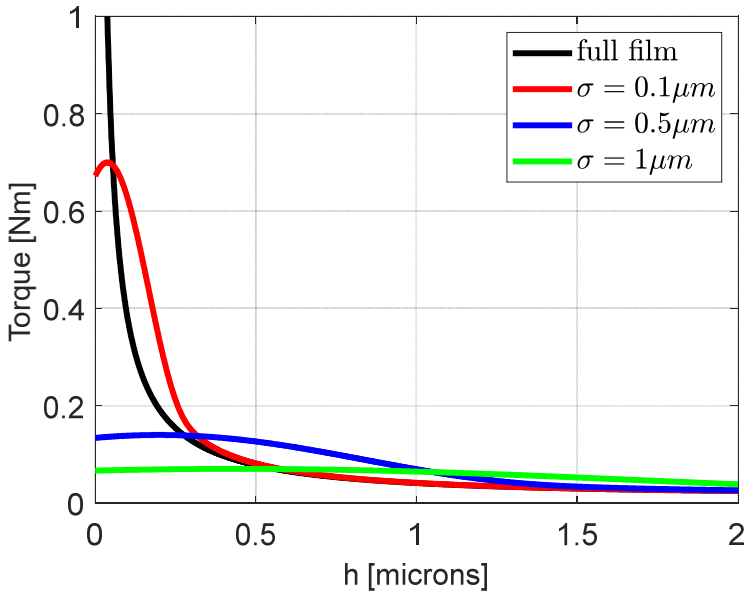

Figure 7.4. Effect of surface roughness on torque

7.2 Friction at the lateral gaps

Figure 7.5 shows the lateral gap between the gears and the bushings for the reference EGM E5. To study the friction at this interface, the lateral gap is divided into two interfaces as per the primary direction of flow: lateral leakage interface and drain leakage interface (Figure 7.6)

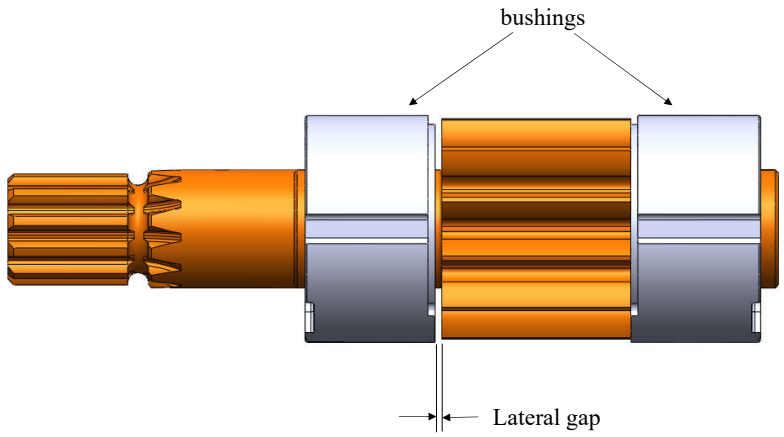

Figure 7.5. Illustration of lateral gap in the reference pump E5

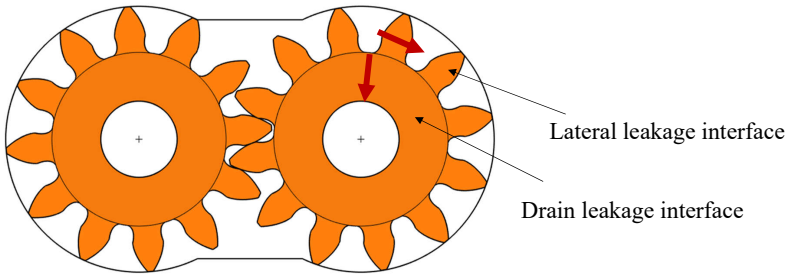

Figure 7.6. Lateral and drain leakage interface (direction of flow is indicated in brown arrows)

In the following subsections, the formulations for the evaluation of friction in each of these interfaces is described.

7.2.1 Friction at the lateral leakage interface

The lateral leakage occurs between adjacent TSVs via the gap on the lateral side of the gears. As the gap height is in the order of microns, similar to the flow at the tooth tip, this leakage flow stays laminar and Eq. 7.2 is an appropriate relation for shear stress. In Figure 7.7, considering a differential slice of tooth at distance from gear center of r and thickness dr, Eq. 7.2 can be written as

$$\tau_w = \frac{\mu\omega r}{h} + \frac{h\Delta p}{2L(r)} \tag{7.10}$$

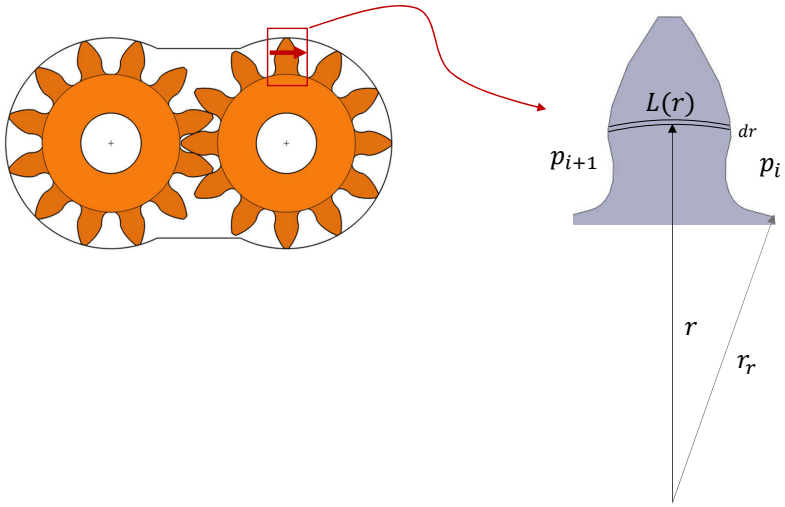

Figure 7.7. Lateral leakage interface: a differential slice of the tooth for the evaluation of shear stress

It is to be noted that the length of the gap $L(r)$ clearly varies with distance of the slice from the gear center. Now, the differential shear force acting on this slice is

$$dF = \tau_w L(r) dr \tag{7.11}$$

Thus, the shear force acting over one tooth is

$$\implies F = \int_{r_r}^{r_g} \tau_w L(r) dr = \frac{\mu\omega}{h} \int_{r_r}^{r_g} rL(r) dr + \frac{h(p_{i+1} - p_i)}{2}(r_g - r_r) \tag{7.12}$$

and, the friction torque from the shear stress over the tooth is

$$M_{f,l} = \int_{r_r}^{r_g} r dF = \int_{r_r}^{r_g} \tau_w r L(r) dr \tag{7.13}$$

$$M_{f,l} = \frac{\mu\omega}{h} \int_{r_r}^{r_g} r^2 L(r) dr + \frac{h(p_{i+1} - p_i)}{4}(r_g^2 - r_r^2) \tag{7.14}$$

The integral terms in Eq. 7.12 and Eq. 7.14 cannot be evaluated analytically. However, as the integrands contain only geometric quantities, they can be evaluated numerically offline and can be considered as input parameters for HYGESim.

It is to be noted that Eq. 7.14 assumes that the gap height h is constant over the full revolution of the gear. However, in reality, the bushing is often tilted with respect to the gears owing to high pressure in the TSVs on the outlet side (Figure 7.8). In such cases, for a given mean gap height h_0 and tilt angle ϕ, the gap height becomes

$$h(r, \theta) = h_0 - r \tan\phi \sin\theta \tag{7.15}$$

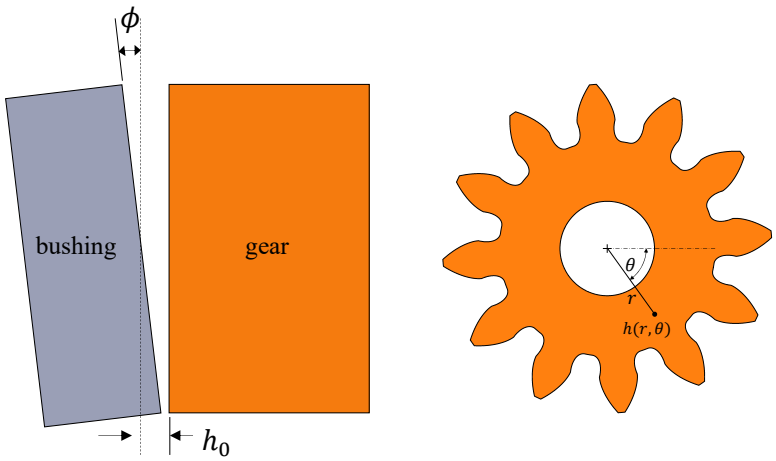

Figure 7.8. Tilting of the busing and evaluation of local gap height

Thus, Eq. 7.10 becomes

$$\tau_w = \frac{\mu\omega r}{h(r, \theta)} + \frac{h(r, \theta)\Delta p}{2L(r)} \tag{7.16}$$

Then, the equation for shear force over one tooth becomes

$$F = \mu\omega \int_{r_r}^{r_g} \frac{rL(r)}{h_0 - r\tan\phi\sin\theta} dr + \frac{(p_{i+1} - p_i)}{2}\Big[h_0(r_g - r_r) - \frac{\tan\phi\sin\theta}{2}(r_g^2 - r_r^2)\Big] \quad (7.17)$$

and the equation for friction torque over one tooth becomes

$$M_{f,l} = \mu\omega \int_{r_r}^{r_g} \frac{r^2 L(r)}{h_0 - r\tan\phi\sin\theta} dr + \frac{(p_{i+1} - p_i)}{2}\Big[\frac{h_0}{2}(r_g^2 - r_r^2) - \frac{\tan\phi\sin\theta}{3}(r_g^3 - r_r^3)\Big] \quad (7.18)$$

The integrals in Eq. 7.17 and Eq. 7.18 are now dependent on operating conditions too (h_0, ϕ). For implementation of these equations in HYGESim, integral tables are generated as a preprocessing step. This tables are in the form of text files that store the numerical evaluation of these integrals for a set of values of h_0, ϕ and θ. HYGESim interpolates the data from this table to determine the instantaneous value of the integrals.

7.2.2 Friction at the drain leakage interface

In the drain leakage interface, the pressure driven leakage flow is along the radial direction (Figure 7.9). Thus, the shear stress due to this flow does not generate any friction torque. The friction torque only occurs due to the Couette flow arising from the relative motion of the gear with respect to the bushing. Considering a differential slice of this interface with radius r and thickness dr, the expression of shear stress is simply

$$\tau_w = \frac{\mu\omega r}{h} \quad (7.19)$$

Now, the differential shear force acting on this slice is

$$dF = \tau_w \cdot 2\pi r dr \quad (7.20)$$

Due to radial symmetry, the net shear force on the drain leakage interface is zero.

The friction torque acting on this interface is

$$M_{f,d} = \int_{r_d}^{r_r} r dF = \int_{r_d}^{r_r} \tau_w \cdot 2\pi r^2 dr \quad (7.21)$$

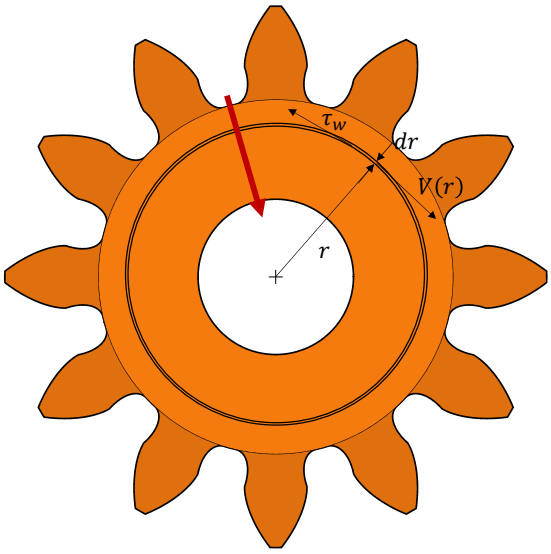

Figure 7.9. Drain leakage interface: a differential slice for the evaluation of shear stress

$$\implies M_{f,d} = \frac{\pi\mu\omega}{2h}(r_r^4 - r_d^4) \tag{7.22}$$

Eq. 7.22 is applicable for constant gap height over the whole interface. However, when the bushing tilts, the gap height varies in the interface as per Eq. 7.15. For such a case, the differential slice is now a rectangular area shown in Figure 7.10. The differential force acting on this slice is

$$dF = \tau_w \cdot r d\theta dr \tag{7.23}$$

Then, the shear force acting on the whole drain leakage interface in x direction is

$$F_x = -\int_{r_d}^{r_r}\int_0^{2\pi} \tau_w \sin\theta \cdot r d\theta dr \tag{7.24}$$

$$= -\mu\omega \int_{r_d}^{r_r}\int_0^{2\pi} \frac{r^2 \sin\theta}{h_0 - r\tan\phi\sin\theta} dr d\theta \tag{7.25}$$

$$= -\mu\omega \cdot \frac{2\pi}{\tan\phi}\int_{r_d}^{r_r} \frac{r}{\sqrt{1 - r^2\left(\frac{\tan\phi}{h_0}\right)^2}} - r\, dr \tag{7.26}$$

$$\implies F_x = -\mu\omega \cdot \frac{2\pi}{\tan\phi}\Big[\frac{1}{m}\big(\sqrt{1-mr_d^2} - \sqrt{1-mr_r^2}\big) - \frac{r_r^2 - r_d^2}{2}\Big] \tag{7.27}$$

where, $m = (\tan\phi/h_0)^2$.

As the bushing tilt is symmetric along y axis, $F_y = 0$.

Next, the friction torque is evaluated as

$$M_{f,d} = \int_{r_d}^{r_r}\int_0^{2\pi} r dF = \int_{r_d}^{r_r}\int_0^{2\pi} \tau_w r^2 d\theta dr \tag{7.28}$$

$$\implies M_{f,d} = \mu\omega \int_{r_d}^{r_r}\int_0^{2\pi} \frac{r^3}{h_0 - r\tan\phi\sin\theta} dr d\theta \tag{7.29}$$

$$= \mu\omega \cdot \frac{2\pi}{h_0}\int_{r_d}^{r_r} \frac{r^3}{\sqrt{1 - r^2\left(\frac{\tan\phi}{h_0}\right)^2}} dr \tag{7.30}$$

$$\implies M_{f,d} = \frac{2\pi\mu\omega}{h_0}\frac{1}{3m^2}\Big[\sqrt{1-mr_d^2}(2+mr_d^2) - \sqrt{1-mr_r^2}(2+mr_r^2)\Big] \tag{7.31}$$

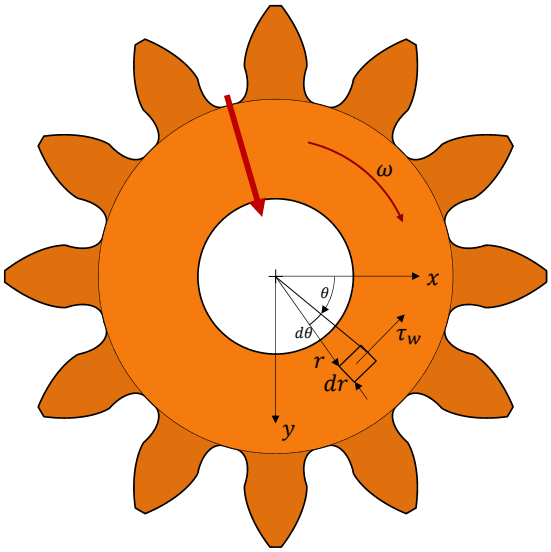

Figure 7.10. Drain leakage interface: a differential slice for the evaluation of shear stress for tilted bushing

7.3 Friction at the bearings

In the reference unit E5, there are four journal bearings formed by the gears' shafts and holes in the bushings. A simple equation for the evaluation of friction torque on the shaft of journal bearing was provided by Petrov [43]:

$$M_{f,s,Petrov} = \frac{2\pi\mu r_s^3 b_b \omega}{c} \tag{7.32}$$

A critical limitation of this equation is that it assumes the journal (gear shaft) to be concentric to the bearing. In reality however, to support the external load acting on the journal, the journal achieves an eccentric position with respect to the bearing (Figure 7.11).

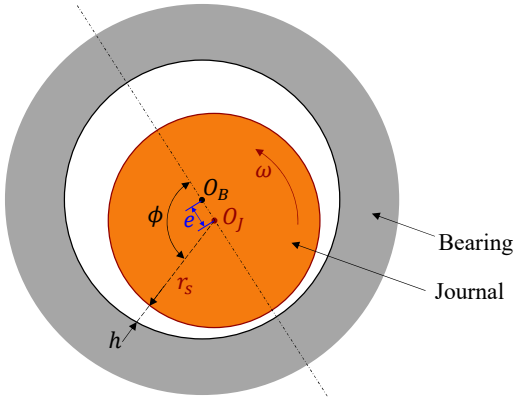

Figure 7.11. Journal Bearing geometry showing eccentricity of the journal (shaft) with respect to the bearing.

It is important to note that the flow in the journal bearing fluid film can again be considered to be laminar (due to micron level film thickness) and Eq. 7.2 can be used for the evaluation of shear stress. However, a key challenge is the determination of the pressure in the fluid film.

In his study of short bearing approximation for journal bearings, Ocvirk [41] proposed that under the short bearing assumption ($b_b < 2r_s$), the pressure term in

Eq. 7.2 can be neglected. Thus, the shear stress at an angular position ϕ on the journal is

$$\tau = \frac{\mu\omega r_s}{h(\phi)} \tag{7.33}$$

where h is the thickness of the fluid film in the journal bearing. h can be expressed in terms of the journal bearing nominal radial clearance, c and the journal eccentricity, e as

$$h = c + e\cos\phi = c(1 + \epsilon\cos\phi) \tag{7.34}$$

where ϵ is the eccentricity ratio that varies from 0 (no eccentricity) to 1 (maximum eccentricity).

The shear force on the shaft can then be determined by integrating the shear stress in Eq. 7.33 over the whole angular span:

$$F_s = b_b \int_0^{2\pi} \tau r_s d\phi \tag{7.35}$$

Consequently, the friction torque on shaft is

$$M_{f,s} = r_s b_b \int_0^{2\pi} \tau r_s d\phi \tag{7.36}$$

$$\implies M_{f,s,Ocvirk} = \frac{2\pi\mu r_s^3 b_b \omega}{c} \cdot \frac{1}{(1-\epsilon^2)^{0.5}} \tag{7.37}$$

It is notable that as $\epsilon \to 0$, the Ocvirk expression for friction converges to Petrov's equation.

Another alternate approach for the determination of the friction torque at journal bearings is to consider the pressure term in Eq. 7.2 and use for pressure expression from half Sommerfeld solution [43]. This solution is obtained under that assumption that the bearing is infinitely long and the pressure in the film is non-zero only in half of the film (π film). The aforementioned pressure expression is

$$p = \frac{\mu\omega r_s^2}{c^2} \cdot \frac{6\epsilon\sin\phi(2 + \epsilon\cos\phi)}{(2+\epsilon^2)(1+\epsilon\cos\phi)^2}, \quad 0 \le \phi \le \pi \tag{7.38}$$

Starting from Eq. 7.2, the shear stress at an angular position ϕ on the journal is

$$\tau = \frac{h}{2r_s}\frac{dp}{d\phi} + \frac{\mu\omega r_s}{h} \tag{7.39}$$

From this expression of shear stress, the expression of friction torque on the shaft is determined to be

$$M_{f,s,Som} = \frac{r_s b_b}{2} \int_0^{\pi} h \frac{dp}{d\phi} d\phi + \frac{2\pi\mu r_s^3 b_b \omega}{c} \cdot \frac{1}{(1-\epsilon^2)^{0.5}} \tag{7.40}$$

The integral in this equation could not be evaluated analytically.

It is to be noted that each of the two approaches described above (Ockvirk and Sommerfeld) have certain assumptions. In fact, the two approaches represent the two extremes of the solution. The former approach is suitable for short bearings, whereas, the latter approach is suitable for long bearings. The bearings present in the reference unit E5 have $b_b \approx 2r_s$. Thus, the actual solution of friction torque must lie between the values predicted by the two approaches.

To determine the friction torque without any assumptions on the bearing length, the Reynolds equation of lubrication needs to be solved numerically over the fluid domain. For journal bearing, the Reynolds equation simplifies to

$$\frac{\partial}{\partial\phi}\left(h^3 \frac{\partial p}{\partial\phi}\right) + r_s^2 h^3 \frac{\partial^2 p}{\partial y^2} = -6\mu\omega_b r_s^2 c\epsilon \sin\phi \tag{7.41}$$

Figure 7.12 shows the pressure distribution obtained from the numerical solution of Eq. 7.41. From this pressure solution, the shear stress is evaluated using Eq. 7.39 and subsequently, the friction torque is determined.

Figure 7.13 shows the comparison between the results obtained from the three approaches. (The integral in Eq. 7.40 was solved numerically to determine the friction torque from Sommerfeld approach.) As expected, the torque obtained from the numerical solution of Reynolds equation lies between the torques obtained from Ocvirk and Sommerfeld approaches.

This figure also highlights the fact that the journal eccentricity has a significant effect on the friction torque. The loads on the journals in EGMs are typically on the order of few kiloNewtons and thus the eccentricity ratios of the journals are around 0.9-0.95. Consequently, Petrov's equation (used by Zardin et al. [125]) significantly underestimates the bearing torque.

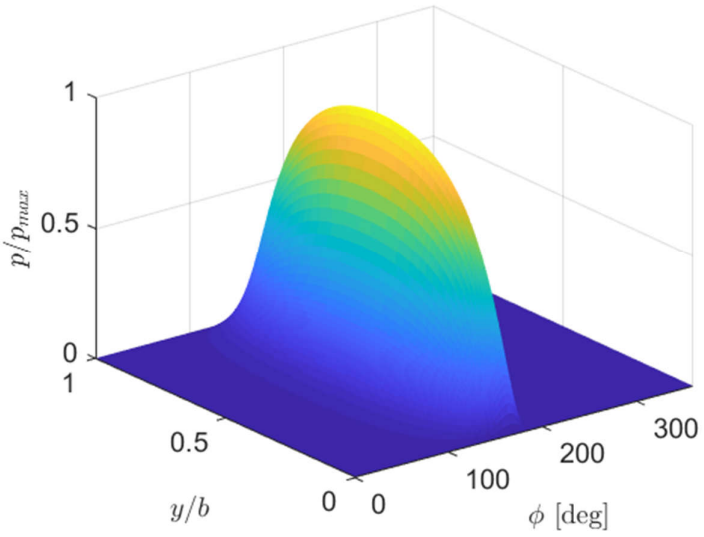

Figure 7.12. Pressure distribution in the journal bearing fluid film obtained from the solution of Reynolds equation. Reference case: bearing of pump E5, ω=1000 rpm, ϵ=0.9

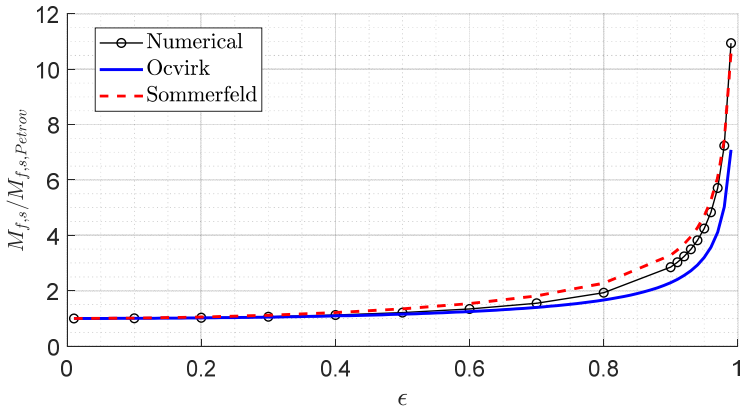

Figure 7.13. Comparison of the bearing friction torque obtained from the three approaches. Reference case: bearing of pump E5, ω=1000 rpm

The Ocvirk solution is preferred for implementation in HYGESim due to its analytical nature. However, to obtain a match with the numerical solution, a correction factor to the Ocvirk solution needs to be determined. For the reference unit E5, the correction factor was found to be $0.43\epsilon^4 + 1$. That is,

$$M_{f,s,Oc,mod} = (0.43\epsilon^4 + 1) \cdot M_{f,s,Ocvirk} \tag{7.42}$$

Figure 7.14 shows a good match between the numerical solution and the modified Ocvirk solution of Eq. 7.42.

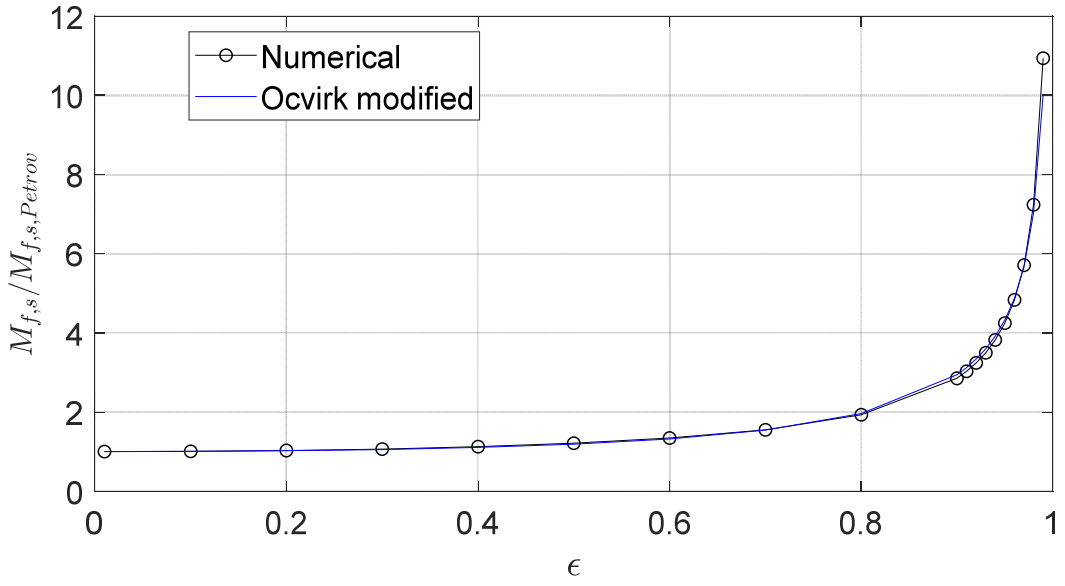

Figure 7.14. Comparison between the numerical solution and the modified Ocvirk solution

7.4 Friction in the meshing of gears

The friction in the meshing of the gears originate from the rolling and sliding motion of the gear teeth surfaces with respect to each other. The gears in EGMs experience high contact force that is required to provide the torque to the driven gear

to displace the fluid against high pressure. Such forces result in elastic deformation of the contact surfaces. Thus, the condition of elastohydrodynamic lubrication (EHL) exists at these surfaces.

Jacobson and Hamrock [128] developed an EHL model for rectangular contacts considering the non-Newtonian behavior of the fluid and the wall slip at high shear stresses. In particular, they employed a fluid model that includes the limiting shear stress of the fluid (τ_L in Figure 7.15). When the shearing imposed is higher than this value, fluid slippage occurs.

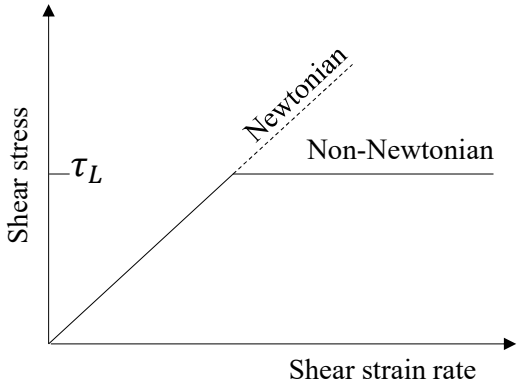

Figure 7.15. Model of fluid shearing behavior adopted by Jacobson and Hamrock [128]

The limiting shear stress increases with pressure as per the following relation:

$$\tau_L = \tau_0 + \gamma p \tag{7.43}$$

where, τ_0 is the initial shear strength.

Jacobson and Hamrock conducted several EHL simulations and based on the results, they proposed a relation for the friction coefficient for surfaces under EHL contact:

$$\mu_{f1} = 0.67 \times 10^{-6} (U^*)^{0.81} U^{0.26} (WG^2)^{3.32} \tag{7.44}$$

If $\mu_{f1} > 0.8\gamma$

$$\mu_f = 0.8\gamma + 0.021 \tanh\left[\frac{\mu_{f1}}{\gamma} - 0.8\right] \tag{7.45}$$

Here,

$$U^* = \frac{u_d}{u_s} \tag{7.46}$$

$$U = \frac{\mu_0 u_s}{E'R} \tag{7.47}$$

$$W = \frac{w_z}{E'R} \tag{7.48}$$

$$G = \alpha_1 E' \tag{7.49}$$

In Eq. 7.46, u_d is half of the relative sliding speed. In Eq. 7.46 and Eq. 7.47, u_s is the average speed of the two surfaces. In Eq. 7.47, R is the equivalent radius of curvature of the two surfaces and E' is the effective elastic modulus of the material:

$$E' = \frac{E}{1 - \nu_p^2} \tag{7.50}$$

In Eq. 7.48, w_z is the load per unit length of the contact. In Eq. 7.49, α_1 is the pressure-viscosity coefficient in the relation describing the dependence of fluid viscosity on pressure:

$$\mu = \mu_0 e^{\alpha_1 p} \tag{7.51}$$

Figure 7.16 shows the orientation of contact forces acting on the drive and driven gears. The contact force is evaluated by balancing the moments from (a) the fluid pressure acting on the driven gear (Eq. 2.6) and (b) the shear forces acting on the driven gear's surfaces:

- tooth tips of the gear (Eq. 7.4)
- lateral surfaces of the gear (Eq. 7.17 and Eq. 7.27)
- shaft of the gear (Eq. 7.36)

The friction force is then calculated from the contact force as

$$F_f = \mu_f F_c \tag{7.52}$$

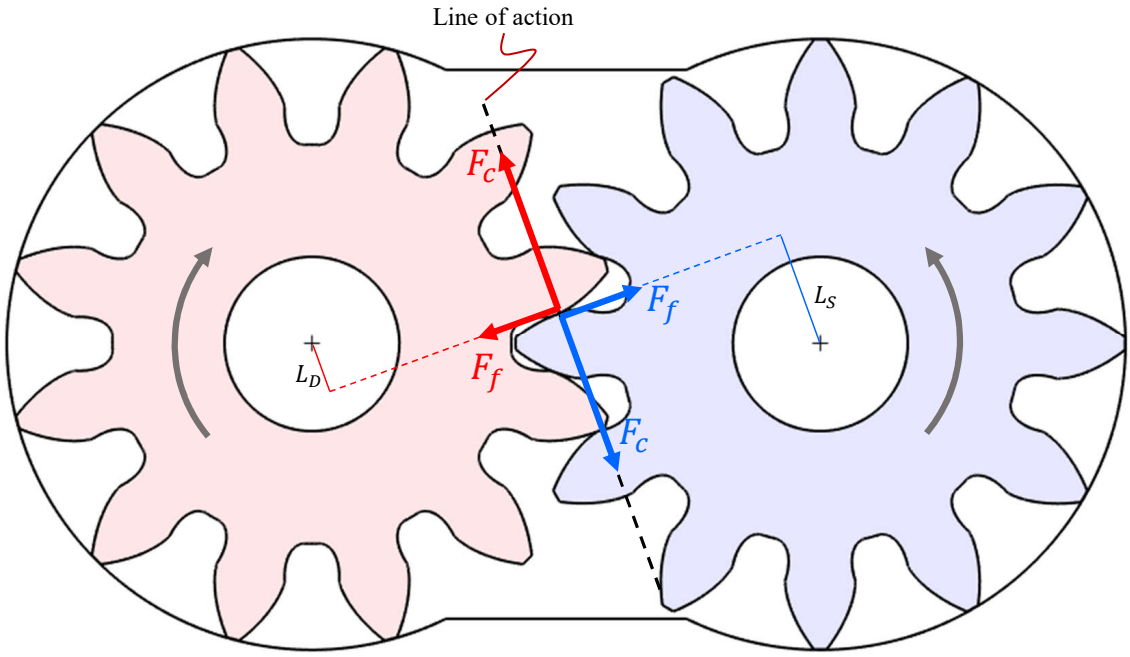

Figure 7.16. Contact force, friction force and friction torque on the gears

Finally, the meshing friction torque from this friction force on drive and driven gears are calculated as

$$M_{f,m,D} = F_f L_D \tag{7.53}$$

$$M_{f,m,S} = F_f L_S \tag{7.54}$$

For the driven gear, this friction torque is balanced by additional contact force

$$F_{c,f} = \frac{M_{f,m,S}}{r_p \cos\alpha} \tag{7.55}$$

Thus, the net meshing friction torque is the sum of the meshing friction torque on the drive gear and the moment from $F_{c,f}$:

$$M_{f,m} = M_{f.m,D} + F_{c,f} r_p \cos\alpha \tag{7.56}$$

$$\Longrightarrow \; M_{f,m} = M_{f,m,D} + M_{f,m,S} \tag{7.57}$$

7.5 Results and experimental validation

The shear force and friction torque formulations developed in the previous sections were implemented in HYGESim and simulations were conducted for the reference unit E5 for a range of operating speeds and pressures. In this section, first, the torque loss results obtained from the simulations are presented. Next, the hydro-mechanical efficiency results are compared against the experimental data (provided by the sponsor of the project). Due to confidentiality agreement with the sponsors, the results presented are normalized with respect to the reference speed: $N_{ref} \sim \mathcal{O}(1000$ rpm, reference pressure: $p_{ref} \sim \mathcal{O}(100$ bar) and reference torque: $M_{ref} = V_D p_{ref}$.

7.5.1 Meshing friction results

The results from the simulations help explain certain observations in regards to the meshing friction. In particular, when the gears are in a configuration shown in Figure 7.16, the meshing friction torque on drive gear is clockwise which is in the same direction as the gear rotation. That is, the meshing friction assists in the motion of the gear which seems counter-intuitive. However, the meshing friction torque on the driven gear is clockwise too which is in the opposite direction of the gear rotation. The simulation results (Figure 7.17(a)) show that at this angular position of gearsets (360°), the resistive meshing friction torque on driven gear is higher than the assistive meshing friction torque on the drive gear such that the net meshing friction torque (Eq. 7.57, shown in Figure 7.17(b)) is always resistive.

Figure 7.17 also shows that the net meshing friction torque becomes instantaneously zero at certain angular positions. At those angular positions, the contact surfaces have same velocity tangential to the contact ($\theta = 367.5°$ in Figure 7.18), thus the relative sliding speed becomes zero.

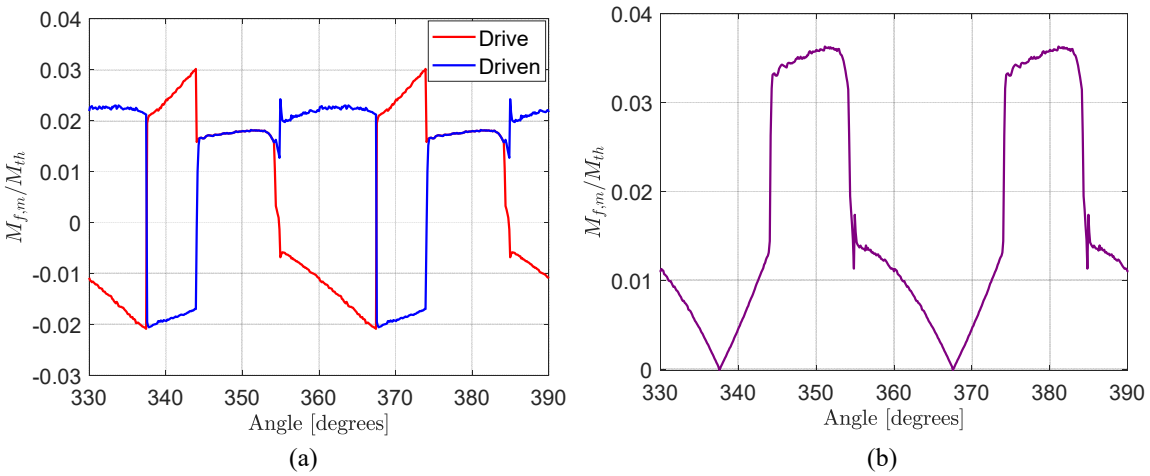

Figure 7.17. Meshing friction torque obtained from the simulation of the reference unit E5 at the reference speed and pressure: (a) Meshing friction torque on drive and driven gears, (b) net meshing friction torque. Positive and negative values of torque correspond to resistive and assistive torque to the motion, respectively.

7.5.2 Friction torque results from all the sources considered

Figure 7.19 shows the trends of friction torque at different interfaces obtained from the simulation of the reference EGM. The friction torque at the tooth tip experiences sudden increase from $p = 0.2p_{ref}$ to $p = 0.4p_{ref}$. This happens due to the fact that at $p = 0.2p_{ref}$, the tooth tip gap height stays high enough to avoid mixed friction. However, as the pressure is increased, the magnitude of gear micromotion increases lowering the tooth tip gap height resulting in the rise of the friction. At this pressure level, the tooth tip and casing surfaces interact in mixed friction regime. On further increase of pressure, the tooth tip gap height lowers further, however, as shown in Figure 7.4, the friction torque stays bounded in mixed friction regime. Thus, the further increase in friction torque is gradual and is primarily caused by increasing dp/dx term in Eq. 7.6.

The friction torque at the lateral leakage interface increases linearly with pressure and speed. This is in accordance with the Eq. 7.18 which governs the friction torque

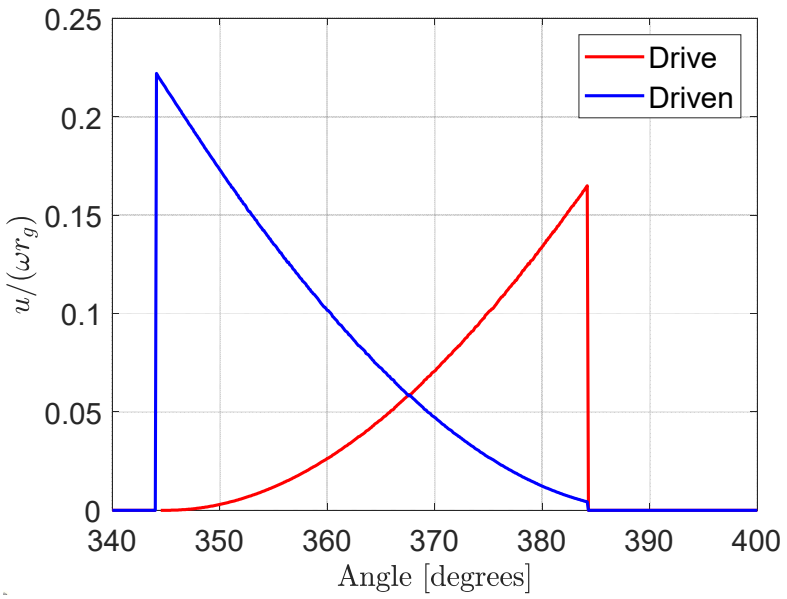

Figure 7.18. Velocity (tangential to the contact) of the two surfaces during gear meshing

at this interface. The friction torque at the drain leakage increases linearly with speed as per Eq. 7.31. The slight increase with pressure is observed which occurs due to increase in fluid viscosity with pressure.

The friction torque at the bearing too exhibits the linear behavior, however, the trends are more steep with pressure. This is because, with the increase in pressure, the load on the bearing increases and hence the eccentricity of the journal increases. Thus, the bearing friction torque increases as per Eq. 7.37.

The meshing friction torque increases significantly with pressure but marginally with speed. This is because the meshing friction torque depends directly on the contact force which increases with the pressure to balance the increasing moment on the driven gear. At higher speeds, the pressure in the TSVs trapped in meshing zone increases, resulting in a slight increase in the moment on the driven gear that has to be balanced by higher contact force.

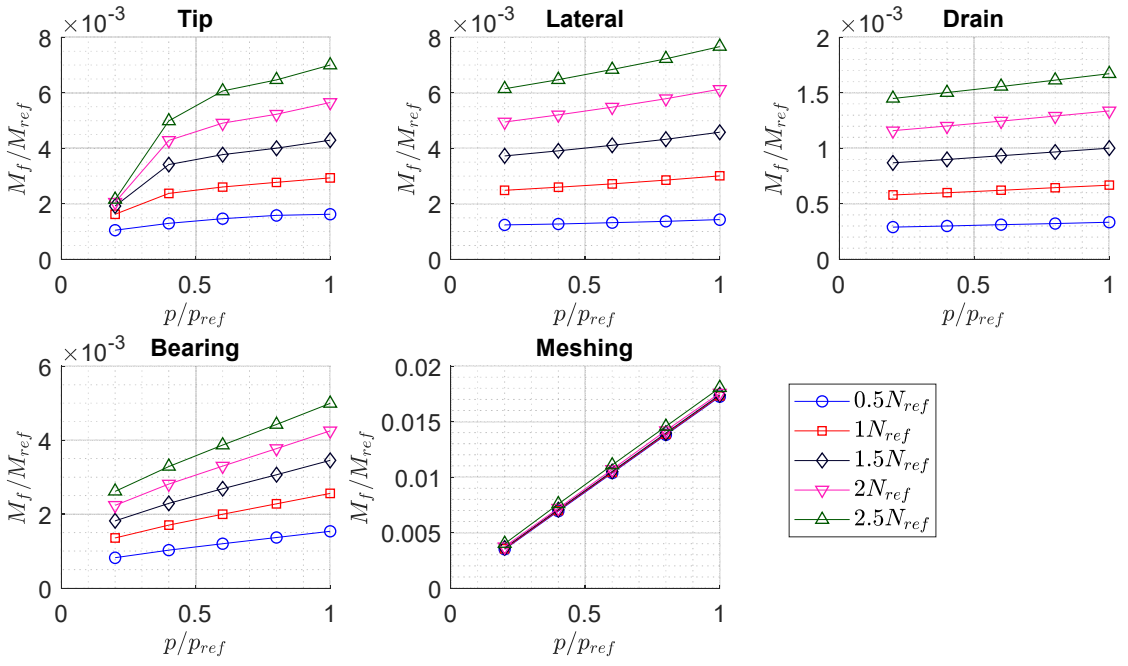

Figure 7.19. Friction torque at each interface obtained from the simulation of E5 unit for a set of operating conditions

Figure 7.20 shows the comparison of the torque losses at all the interfaces considered. The trends with pressure is shown in Figure 7.20(a) and the trends with speed is shown in 7.20(b). Clearly, meshing friction torque is the major contributor to the overall torque loss.

In Figure 7.20, the torque losses are observed to be increasing with pressure. However, it is important to note that the theoretical torque increases with pressure too (Eq. 1.4). Thus, it is more informative to represent these torque losses in terms of the fraction of the theoretical torque. To achieve that, the torque loss quantities at each operating condition are normalized by the theoretical torque at that operating condition. Thus, the fractional torque loss is defined as:

$$M_{f,fractional} = \frac{M_f}{M_{th}} \tag{7.58}$$

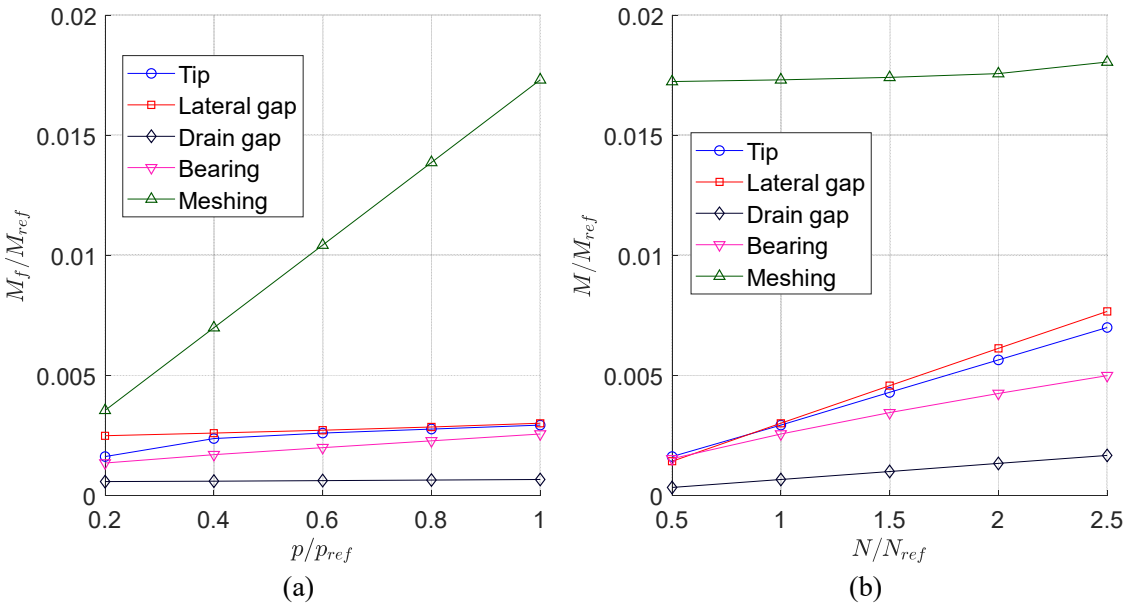

Figure 7.20. Comparison of different sources of torque losses obtained from the simulation of the reference unit E5. (a) trends with pressure obtained at $N = N_{ref}$. (b) trends with speed obtained at $p = p_{ref}$

As per the confidentiality agreement with the project sponsors, the pump efficiency data needs to remain confidential. To ensure this, the fractional torque loss is normalized by the fraction of total torque loss at the reference operating condition:

$$M_f^* = \frac{M_{f,fractional}}{[M_{f,total,fractional}]_{ref}} \tag{7.59}$$

where $M_{f,total} = M_{f,t} + M_{f,l} + M_{f,d} + M_{f,b} + M_{f,m}$.

This normalized fractional torque loss for each source is presented in Figure 7.21. The fractional meshing torque loss is observed to be almost constant with pressure, whereas other torque losses, as a fraction of the theoretical torque, decrease with pressure and increase with speed. In particular, the trend with pressure is $\sim 1/p$. This is because the friction torque equations for these sources of losses are of the type

$$M_f \approx \mathrm{f}_1(\omega) + \mathrm{f}_2(\Delta p) \tag{7.60}$$

$$\implies \frac{M_f}{M_{th}} \approx \frac{1}{\Delta p}\mathrm{f}_1(\omega) + \mathrm{f}_2(1) \tag{7.61}$$

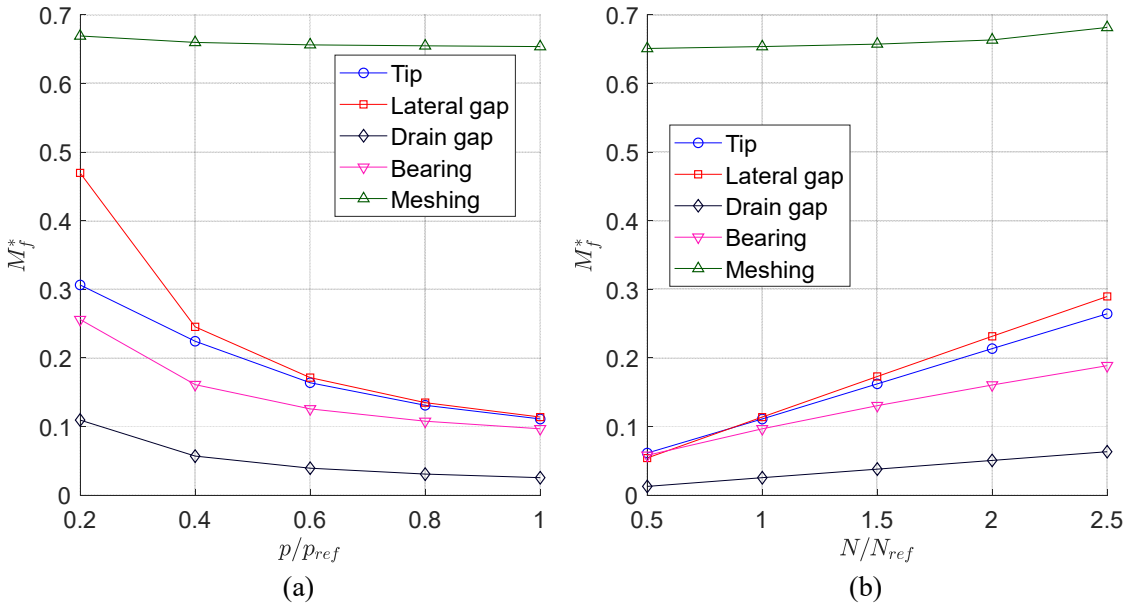

Figure 7.21. Normalized fractional torque losses obtained from the simulation of the reference unit E5. (a) trends with pressure obtained at $N = N_{ref}$. (b) trends with speed obtained at $p = p_{ref}$

7.5.3 Comparison between simulation results and experiments

From the torque losses results, the hydro-mechanical efficiency is determined as per Eq. 1.3. For the results shown in this subsection, the hydro-mechanical efficiency at all operating conditions are normalized by the hydro-mechanical efficiency at the reference condition (N_{ref}, p_{ref}).

Figure 7.22 shows the comparison between the hydro-mechanical efficiency obtained from HYGESim and that obtained from the experimental data (provided by the project sponsor). A good match between the simulations and experiments is observed. The overall trend is an increase in hydro-mechanical efficiency with pressure.

This follows directly from the trend of the fractional torque losses in Figure 7.21(a), where the losses decrease with pressure.

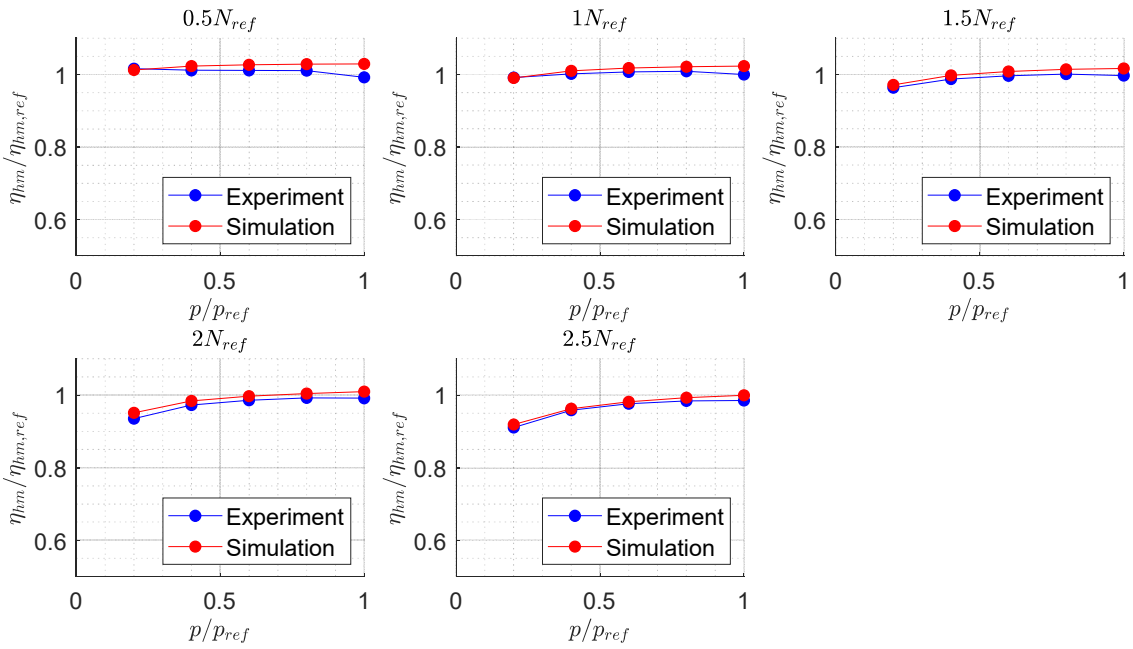

Figure 7.22. Hydro-mechanical efficiency comparison between the simulations and experiments for the reference pump E5: Trends with pressure.

Figure 7.23 shows the comparison between the simulations and experiments where the trends are presented with respect to the operating speed. Again, a good match in the values as well as the trends is observed. The results show that the hydro-mechanical efficiency of the reference unit decreases with speed. This again follows directly from the trend of the fractional torque losses in Figure 7.21(b), where the losses increase with speed.

Figure 7.24(a) presents the hydro-mechanical efficiency map of the reference unit obtained from the simulation results and experimental data.

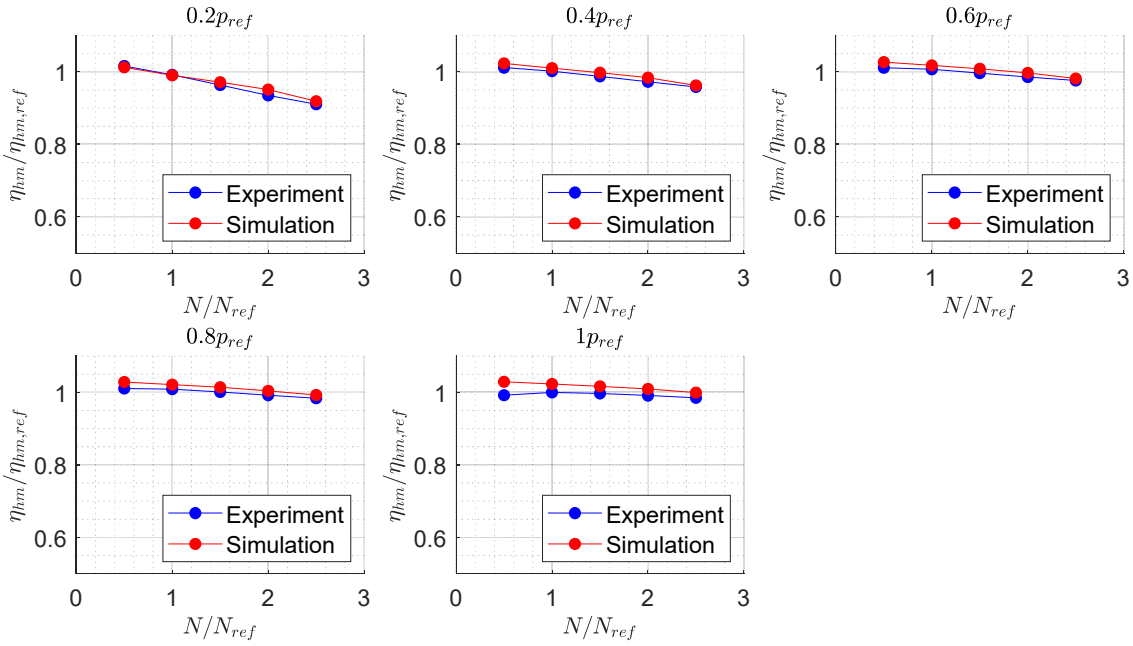

Figure 7.23. Hydro-mechanical efficiency comparison between the simulations and experiments for the reference pump E5: Trends with speed.

The error in the prediction of the hydro-mechanical efficiency by HYGESim is defined as:

$$\epsilon_{hm} = \frac{|\eta_{hm,sim} - \eta_{hm,exp}|}{\eta_{hm,exp}} \times 100\% \tag{7.62}$$

The error over the whole range of operating conditions is shown in 7.24(b). Except for one data point, the error at all the data points is $< 2\%$.

Thus, a good match between the simulation results and data measured in the experiments over the whole range of operating conditions validates the hydro-mechanical efficiency model developed in this work.

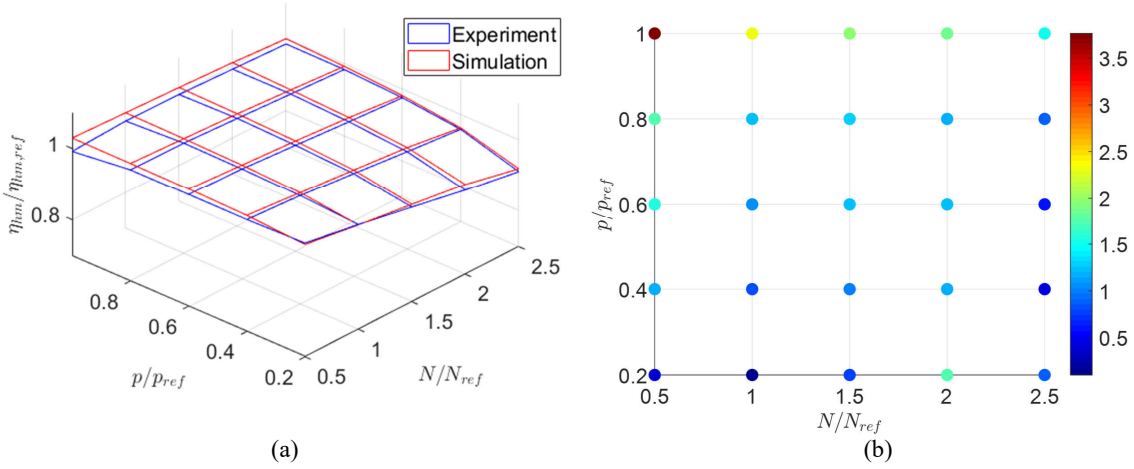

Figure 7.24. (a) Efficiency map over the considered range of speed and pressure (b) Error in the prediction of the hydro-mechanical efficiency. The colorbar indicates the error percentage.

8. THERMAL MODELLING OF EXTERNAL GEAR MACHINES

This chapter deals with the final relevant aspect related to EGMs (as described in the research objective of this dissertation): fluid temperature. In the operation of an EGM, temperature of the working fluid is a critical parameter. The viscosity of the working fluids is a strong function of temperature. For instance, for ISO VG 46 mineral oils, when temperature is increased from 30 °C to 50 °C, the fluid viscosity reduces by a factor of 2.2. It can be seen from the leakage flow models described and developed in previous chapters that the fluid viscosity directly impacts the leakage flow. As explained in Chapter 4, leakage flow has a significant impact on the EGM performance in terms of the volumetric efficiency as well as the axial compensation of floating elements. Moreover, as described in Chapter 7, the torque losses in EGMs (and hence the hydro-mechanical efficiency of EGMs) are dependent on fluid viscosity too.

The fluid temperature in EGMs is affected by two factors:

- Compression of the fluid during the pumping action and expansion of the fluid during the motoring action,
- Power losses in EGMs comprising volumetric losses (from leakage flows) and torque losses (from friction at the interfaces in relative motion).

Due to these factors, the temperature of the fluid in the EGM can vary significantly. In fact, the experiments always show an increase in the temperature of the fluid leaving the EGM. This elevated fluid temperature at the outlet of the EGM impacts the performance of other hydraulic components connected downstream of the EGM.

In view of these facts, a key limitation of the lumped parameter based models for EGMs developed in past is that they assume isothermal flow conditions in EGMs.

This assumption negatively impacts the accuracy of the simulation model. In practice, to improve the accuracy of the results obtained from the model, the simulations of EGMs are conducted using these models at a temperature which is the mean of the temperatures at the inlet and the outlet ports of the EGM. However, this port temperature information has to be obtained from the experiments. This dependence on the experimental data hampers the predictive capability of the simulation models. Moreover, these models cannot be used to predict the temperature of the outlet flow which, as mentioned in the previous paragraph, is critical to the performance of the components downstream of the EGM.

First research work that involved the port temperatures of EGMs was related to the development of the thermodynamic model for the prediction of the pump efficiency based on port pressure and temperature measurements [129]. Similar model was developed by Casoli et al. [130] for axial piston pumps. These models, however, are not predictive as they rely on the outlet temperature measurements. The efforts towards the development of thermal models that can allow the prediction of the outlet temperatures have been made by Zecchi et al. [131] and Shang and Ivantysynova [132] for axial piston machines. For EGMs, thermal effects have been considered in the modelling of the axial balance of floating elements in pressure compensated units [133, 134]. However, this approach too requires accurate temperature information from the lumped volumes of EGM which cannot be provided by the state-of-the-art EGM lumped parameter models.

The goal of the work presented in this chapter is to overcome this scarcity by developing a thermal model of EGMs based on the lumped parameter approach. In this work, the thermal modelling of the elementary hydraulic components (chamber and hydraulic resistance) of the lumped parameter model is based on the thermal-hydraulic library of the commercial tool Simcenter Amesim [135].

The thermal model developed in this work is able to predict the temperature in all the control volumes (CVs) of the EGM including the temperature at the outlet. The instantaneous temperature information can then be used to update the local fluid

properties in the CVs hence permitting an accurate evaluation of internal flows and the performance of EGMs.

In this chapter, a detailed description of the thermal model developed in this work is provided. This includes the governing equations for pressure and temperature in CVs, internal enthalpy flows between the CVs and power losses. The thermal model is then validated against the data obtained from the experiments conducted on the reference EGM E3.

8.1 Conservation laws for control volumes in EGMs

In this section, the laws of conservation of mass and energy are used to derive the governing equations for pressure and temperature in the control volumes of EGMs. The CVs in a typical EGM was shown in Figure 2.2. However, for the sake of convenience, the CVs for the EGM used as reference in this chapter are shown in Figure 8.1.

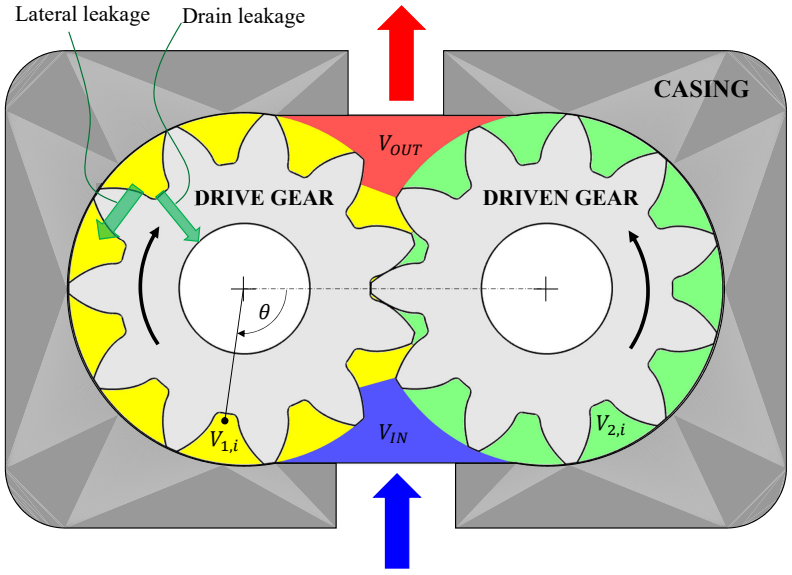

Figure 8.1. Reference EGM with CVs shown in different colors: Blue and red CVs are the inlet and outlet chambers, respectively. Yellow and green CVs correspond to the drive and driven gear TSVs, respectively.

For the analysis presented in this section, a generic CV is considered (Figure 8.2). The CV has N number of ports via which the exchange of mass (mass flow rate $\dot{m}$) and energy (enthalpy flow rate $\dot{H}$) occurs. Moreover, the volume of the CV is changing at the rate of dV/dt.

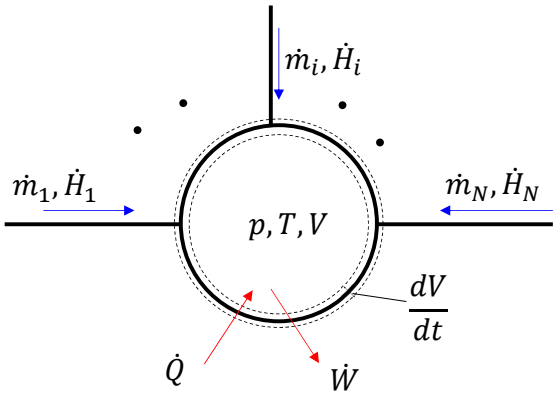

Figure 8.2. Schematic of a typical CV in EGM with N number of ports and varying volume

8.1.1 Conservation of mass

The conservation of mass equation for the CV in Figure 8.2 can be written as

$$\frac{dm}{dt} = \sum_i \dot{m}_i \tag{8.1}$$

Applying chain rule:

$$\frac{dm}{dt} = \frac{d(V\rho)}{dt} = V\frac{d\rho}{dt} + \rho\frac{dV}{dt} \tag{8.2}$$

$$\implies \frac{d\rho}{dt} = \frac{\sum_i \dot{m}_i - \rho\frac{dV}{dt}}{V} \tag{8.3}$$

Now, the total derivative of density can be written as

$$\frac{d\rho}{dt} = \left(\frac{\partial\rho}{\partial p}\right)_T \frac{dp}{dt} + \left(\frac{\partial\rho}{\partial T}\right)_p \frac{dT}{dt} \tag{8.4}$$

$$\implies \frac{dp}{dt} = \frac{1}{\left(\frac{\partial\rho}{\partial p}\right)_T}\left[\frac{d\rho}{dt} - \left(\frac{\partial\rho}{\partial T}\right)_p \frac{dT}{dt}\right] \tag{8.5}$$

For the working fluid, isothermal bulk modulus is defined as:

$$K_T = \rho\Big(\frac{\partial \rho}{\partial p}\Big)_T^{-1} \tag{8.6}$$

and isobaric thermal expansion coefficient is defined as:

$$\alpha_p = -\frac{1}{\rho}\Big(\frac{\partial \rho}{\partial T}\Big)_p \tag{8.7}$$

Thus, Eq. 8.5 becomes

$$\frac{dp}{dt} = K_T\left[\frac{1}{\rho}\frac{d\rho}{dt} + \alpha_p \frac{dT}{dt}\right] \tag{8.8}$$

Substituting $d\rho/dt$ from Eq. 8.3 in Eq. 8.8,

$$\frac{dp}{dt} = K_T\left[\frac{\sum_i \dot{m}_i - \rho\frac{dV}{dt}}{\rho V} + \alpha_p \frac{dT}{dt}\right] \tag{8.9}$$

It is notable that Eq. 8.9 is the same as the pressure build up equation described in Chapter 2 (Eq. 2.1) except the dT/dt term. This term accounts for the effect of fluid temperature on the pressure in the CV. Thus, Eq. 8.9 can be referred to as the non-isothermal pressure build up equation.

8.1.2 Conservation of energy

The conservation of energy equation for the CV in Figure 8.2 can be written as

$$\frac{d}{dt}(mu) = \dot{Q} - \dot{W} + \sum_i \dot{H}_i \tag{8.10}$$

where u is the internal energy of the CV which can be expressed in terms of the specific enthalpy h as

$$u = h - pV/m \tag{8.11}$$

The boundary work done by the CV is pdV. Thus,

$$\frac{d}{dt}(mh - pV) = \dot{Q} - p\frac{dV}{dt} + \sum_i \dot{H}_i \tag{8.12}$$

Upon simplification,

$$\frac{d\mathsf{h}}{dt} = \frac{1}{\rho V}\left[\dot{Q} + \sum_i \dot{H}_i - \mathsf{h}\sum_i \dot{m}_i\right] + \frac{1}{\rho}\frac{dp}{dt} \tag{8.13}$$

Now, the specific enthalpy can be expressed as a function of temperature and pressure as

$$\frac{d\mathsf{h}}{dt} = c_p\frac{dT}{dt} + \Big(\frac{1-\alpha_p T}{\rho}\Big)\frac{dp}{dt} \tag{8.14}$$

Detailed derivation of this relationship can be found in [132].

Eliminating $d\mathsf{h}/dt$ from Eq. 8.13 and 8.14, the governing equation for the temperature in a CV is obtained:

$$\frac{dT}{dt} = \frac{\dot{Q} + \sum_i \dot{H}_i - \mathsf{h}\sum_i \dot{m}_i}{\rho c_p V} + \frac{\alpha_p T}{\rho c_p}\frac{dp}{dt} \tag{8.15}$$

This equation is referred to as the temperature rise equation for a CV. In this equation, the first term represents the rise of temperature in the CV from external heat and the inflow/outflow at the ports. In particular,

$$\sum_i \dot{H}_i - \mathsf{h}\sum_i \dot{m}_i = \sum_i m_i(\mathsf{h}_i - \mathsf{h}) \tag{8.16}$$

Thus, this term accounts for the rise/fall in the temperature of the fluid in the CV due to the difference in the specific enthalpy of the fluid in the CV and the fluid entering the CV. The last term in Eq. 8.15 accounts for the effect of the fluid pressure in the CV on the fluid temperature in the CV.

8.2 Enthalpy Flow through hydraulic resistances

As described in section 2.1, in the lumped parameter based Fluid Dynamic Module, the CVs are connected by hydraulic resistances (which are modelled as either orifices or combined Couette-Poiseuille flow connections). Figure 8.3 shows the schematic of a hydraulic resistance connecting two lumped volumes. The fluid flowing through the resistance has the enthalpy of the upstream CV. Thus, the enthalpy flow rate associated with the mass flow through these resistances is calculated as:

$$\dot{H}_{1-2} = \dot{m}_{1-2} \cdot \mathsf{h}_{1-2} \tag{8.17}$$

where h_{1-2} is evaluated at the pressure and temperature of the upstream CV. The assumption associated with this relation is that there is no heat gain/loss to the environment in this flow. This assumption is revisited in section 8.4.

As these resistances encompass the leakage flows in EGMs, Eq. 8.17 accounts for the power losses in EGMs due to volumetric losses.

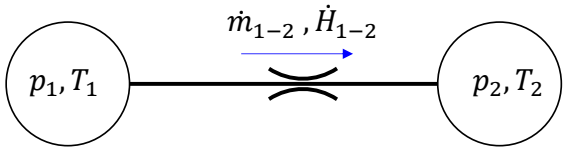

Figure 8.3. Schematic of a hydraulic resistance connecting two lumped volumes at pressures p_1 and p_2 and temperatures T_1 and T_2

8.3 Power losses due to friction

In Chapter 7, a detailed methodology was described for the evaluation of friction torque at the interfaces that are the key sources of torque losses in EGMs. From the expressions of friction torques, the power losses can be evaluated as the product of the friction torque and shaft speed.

$$P_{loss,f} = M_f \omega \tag{8.18}$$

8.4 Heat loss to the environment

Researchers in past have commented that during the operation of EGMs, the heat transfer to the environment is negligible compared to the energy flow in the EGM [129, 130]. However, to confirm this theory for the reference machine E3, a simple steady state thermal analysis of the EGM casing was conducted in ANSYS Mechanical [136].

Figure 8.4(a) shows the CAD of the solid bodies used in the thermal analysis. The bodies include the mounting plate used to mount the reference EGM on the test rig during the experiments (details in Section 5.4.2). Including the mounting plate is important as it provides higher surface area for free convection of heat. For simplicity, the fluid in the interior of the pump was assumed to be at the temperature of 45 °C which is couple of degrees higher than the maximum outlet temperature measured in the experiments. The air temperature around the casing and the mounting plate was assumed to be 20 °C (lower end of the room temperature range). Thus, these boundary conditions act as the upper bound (or the worst case scenario) for the heat loss to the environment.

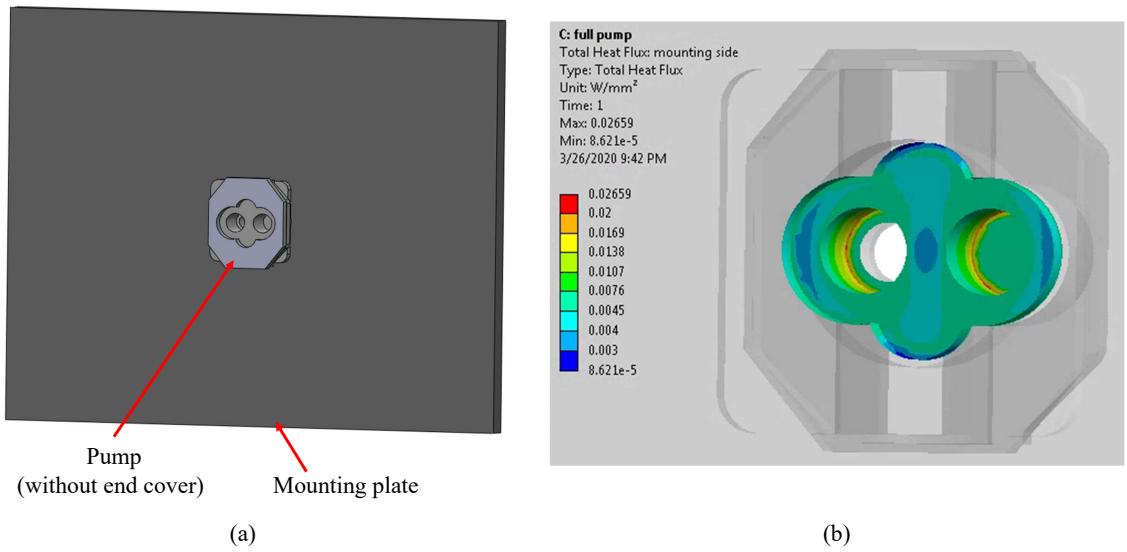

Figure 8.4. (a) CAD of the reference EGM (end cover removed to show the interior domain) and the mounting plate used in the steady state thermal analysis. (b) Heat flux at the interior surfaces obtained from the results of thermal simulation in ANSYS.

The results from this thermal analysis confirm that the heat flux to the environment from the interior surfaces of the EGM (Figure 8.4(b)) is indeed much lower than the rate of energy flow in the EGM. For instance, the radial heat flux from the

internal periphery of the casing is $q'' \approx 4.8 \times 10^{-3}$ W$/mm^2 \implies \dot{Q}_{loss} = 1.24$ watts. This is negligible compared to the circumferential energy flow $= \dot{m}\boldsymbol{h} = 2674$ watts (at 1000 rpm). Similarly, the heat flux in the axial direction (at lateral lubrication interface) is $q'' \approx 4.6 \times 10^{-3}\, W/mm^2$. Thus, the heat losses over the area of lateral and drain leakage interface (for single tooth) are 6.4×10^{-2} watts and 4.7×10^{-2} watts, respectively. These values are insignificant compared to the levels of enthalpy flow rates at these interfaces (Figure 8.5).

From this analysis, it is concluded that for the reference EGM, the heat loss to the environment is inconsequential in the thermal analysis of EGM and thus is neglected in the lumped parameter based thermal model developed in this chapter.

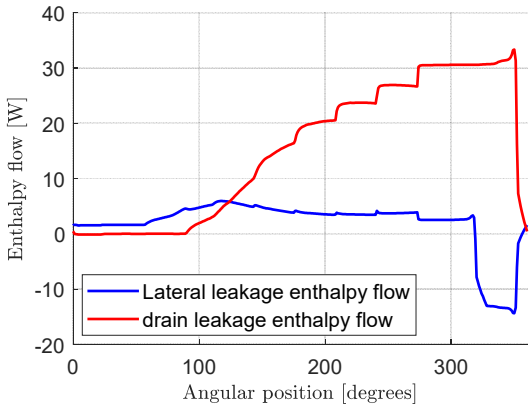

Figure 8.5. Enthalpy flow rates at the lateral and drain leakage interfaces for one tooth over its full revolution. The results are obtained from the simulation of the reference EGM at $N = 1000$ rpm, $p_{out} = 150$ bar, $T_{inlet} = 35$ °C. The angle convention is shown in Figure 8.1.

8.5 Results and comparison with experiments

The thermal model developed in this work is integrated in the Fluid Dynamic Module of HYGESim and thereafter the simulations are conducted for the reference EGM E3. In this section, the results obtained from the simulations are described

and are compared against the experimental data. Comparison is also done with the traditional isothermal model to highlight the significance of the proposed thermal model.

8.5.1 Key results from the thermal model

Figure 8.6 shows the hydraulic circuit simulated in HYGESim. The pressure boundary conditions for the pump being simulated is 0 bar at the inlet tank and 150 bar at the outlet port. The temperature at the inlet tank is set to 35 °C.

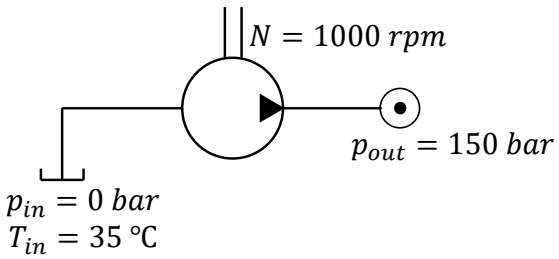

Figure 8.6. Hydraulic circuit simulated in HYGESim

Figure 8.7 shows the evolution of the temperature at the inlet ($T_{CV,in}$), outlet ($T_{CV,out}$) and drain chambers ($T_{CV,dr}$) of the pump. The inlet and outlet chambers were shown as blue and red regions, respectively, in Figure 8.1. The drain chambers in the reference EGM (not shown in the figure) are located on the end of the gear shafts that collect the drain leakage flow (shown in Figure 8.1) and provide the flow back to the inlet chamber.

From Figure 8.7, the temperature at all the chambers increase with the progression of the simulation (expressed in the terms of the shaft revolution). $T_{CV,dr}$ increases as the drain chamber collects high enthalpy drain leakage flows from the TSVs. $T_{CV,in}$ increases as it receives high enthalpy flows from the tooth tip and lateral leakage interfaces as well as drain flow from the drain chamber. However, rate of increase and the steady state value of $T_{CV,in}$ is low as the majority of the flow entering the

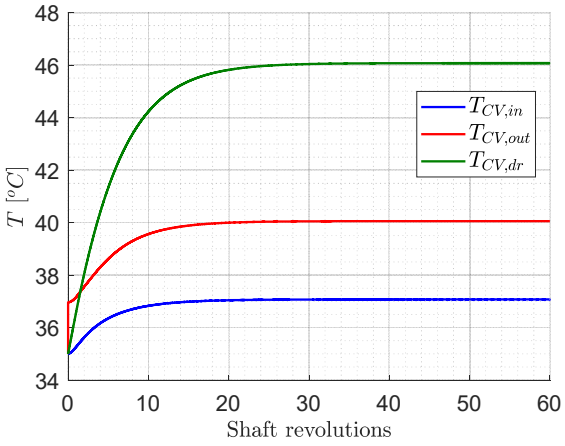

Figure 8.7. Evolution of temperatures at the inlet, outlet and drain chambers of the EGM obtained from the simulation setup in Figure 8.6

inlet chamber is the low enthalpy flow from the inlet port of the pump. The outlet chamber's temperature, $T_{CV,out}$, (which is also the temperature of the outlet flow of the pump) reaches the steady state value of 40 °C. The rise of $T_{CV,out}$ is attributed to the high enthalpy flow delivered by the TSVs.

Figure 8.8 shows the variation of pressure and temperature in a TSV for two shaft revolutions. As the TSV, V_i, enters the casing at the angular position $\approx 90°$, the leakage flow from the leading TSV, V_{i+1}, via the gaps at the tooth tip and the lateral sides of the gear pressurizes the fluid in the TSV, V_i. Since the leading TSV, V_{i+1}, is at a higher pressure, the leakage flows have higher enthalpy. The high enthalpy inflow combined with the pressurization of the TSV, V_i, results in the increase of the temperature in the TSV, V_i. The trend of the temperature in the TSV stays similar to the pressure trend until the TSV reaches the meshing zone (angular position = 360°). After 360°, a second spike in the TSV temperature is observed. This spike is caused by two factors:

- Lateral leakage flow from the lagging TSV, i.e. from V_{i-1} to V_i in Figure 8.9(c). The fluid in V_{i-1} has higher pressure and temperature, and thus, has higher specific enthalpy as compared to the fluid in V_i. Thus, the lateral leakage flow

carries the high specific enthalpy fluid to a low specific enthalpy environment raising the temperature of the latter. This effect is mathematically captured by the terms $(\sum \dot{H} - h \sum \dot{m})$ in the temperature rise equation (Eq. 8.15). From Figure 8.9(b), the leakage enthalpy flow $\dot{H}_{i-1,i}$ is higher than the product of the specific enthalpy of the fluid in V_i and the leakage mass flow rate $(h_i \cdot \dot{m}_{i-1,i})$. Thus, the aforementioned terms in the temperature rise equation yield a positive value promoting dT/dt.

- Friction heating due to the meshing of the gear teeth (black curve in Figure 8.9(b)). In the temperature rise equation (Eq. 8.15), this factor appears as a positive $\dot{Q}$ promoting dT/dt.

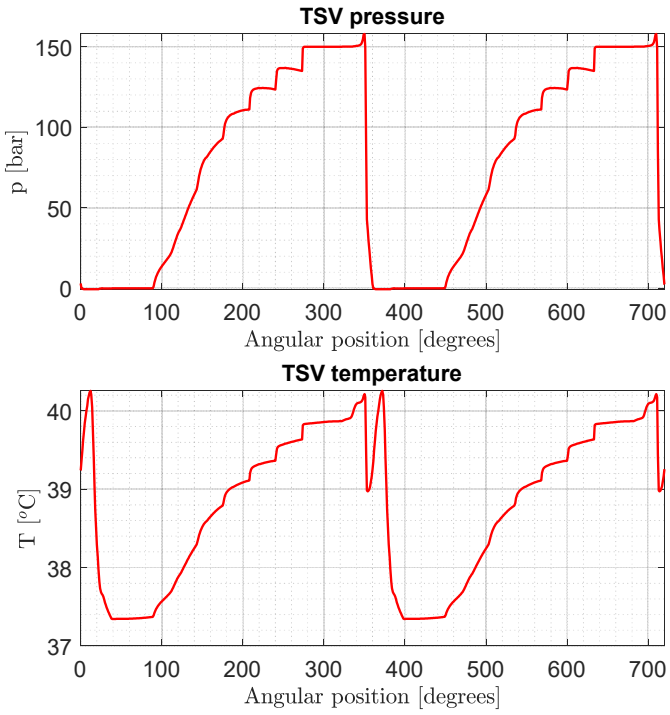

Figure 8.8. Pressure and temperature variation in a TSV over two shaft revolutions

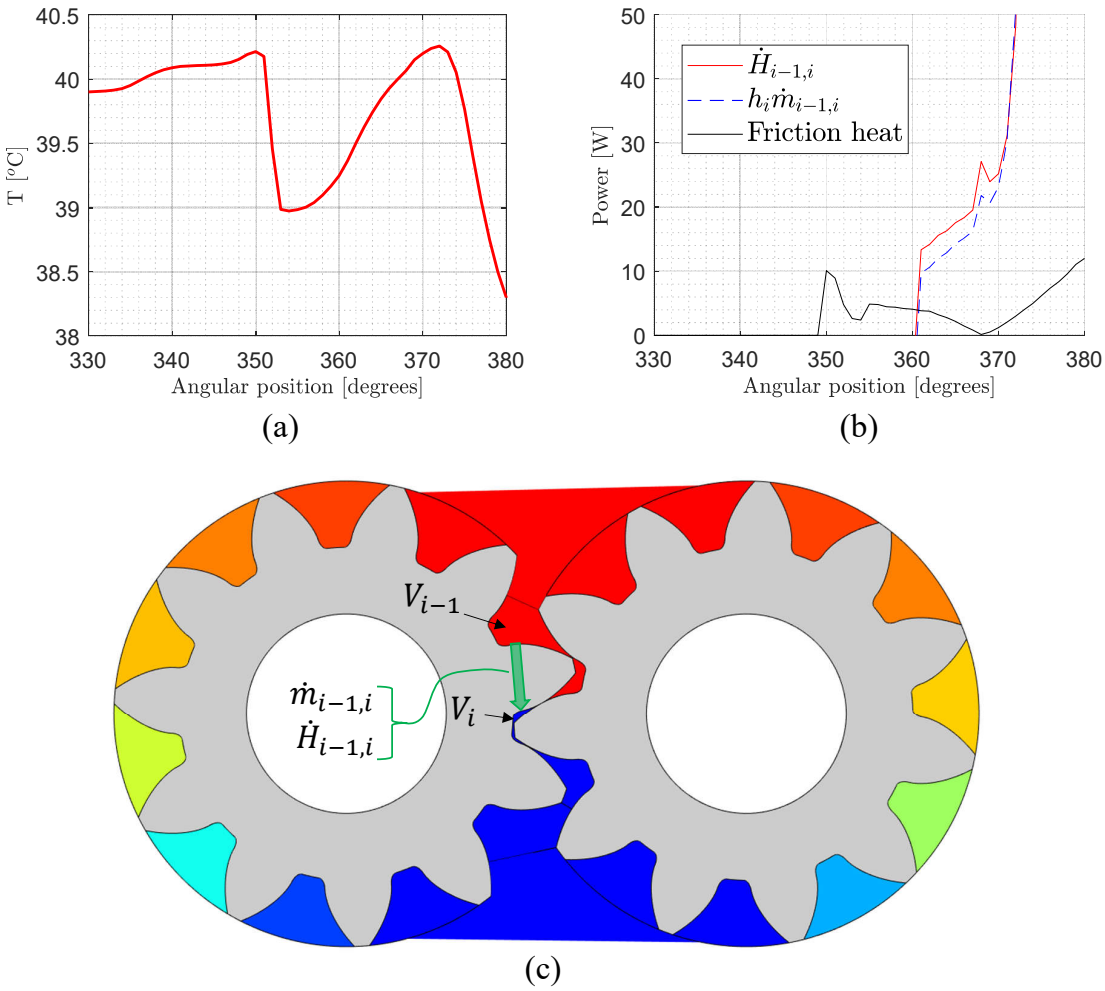

Figure 8.9. (a) TSV temperature in the meshing region. (b) Plot of different terms in the temperature rise equation (Eq. 8.15). $\dot{H}_{i-1,i}$ and $\dot{m}_{i-1,i}$ are the leakage enthalpy and mass flow rates, respectively, from V_{i-1} to V_i, h_i is the specific enthalpy of the fluid in V_i. (c) Illustration of the lateral leakage flow (green arrow) from TSV, V_{i-1}, to the TSV under investigation, V_i. The color of CVs are the qualitative indicators of the fluid pressure.

8.5.2 Validation of the thermal model

One of the main capabilities of the thermal model developed in this work is the prediction of the outlet temperature. Thus, to validate the thermal model, the outlet

temperature obtained from the simulation of the reference pump is compared against the outlet temperature measured in the experiments.

The details of the experiments conducted with the reference pump E3 was described in section 5.4. In brief, steady state flow experiments were conducted using the reference pump for a range of operating speeds and pressures. In the experiments, six different gearsets were used where each gearset had different magnitudes of manufacturing errors. In the experimental setup, two thermocouples were mounted at the inlet and outlet of the pump (Figure 5.13(b)). Via the inlet thermocouple, it was ensured that the inlet temperature stayed at 35 °C. The outlet thermocouple allowed the measurement of the outlet temperature.

Figure 8.10 shows that the outlet temperature obtained from the simulations agree with the experimental data across all the operating conditions and all the gearsets. It is notable that the outlet temperature level is affected by the compression of the fluid and power losses in the EGM from leakage flows and friction. Thus, a good agreement of the outlet temperature confirms the accuracy of these modelling aspects and thereby, validates the overall thermal model developed in this work.

8.6 Significance of the thermal model

A key merit of the thermal model developed in this work is that it provides the information about the temperature distribution in the EGM. This allows an accurate evaluation of the fluid properties in different regions of the EGM. This is particularly important for the viscosity of the fluid which exhibits a significant variation with temperature. The viscosity of the fluid impacts the leakage flow in the EGM which in turn affects the volumetric efficiency of the EGM. Thus, using the thermal model improves the accuracy of the prediction of volumetric efficiency.

To highlight the difference between the traditional isothermal HYGESim tool and the thermal model integrated HYGESim tool (referred to as non-isothermal HYGESim from this point onwards in the dissertation), three sets of simulations were

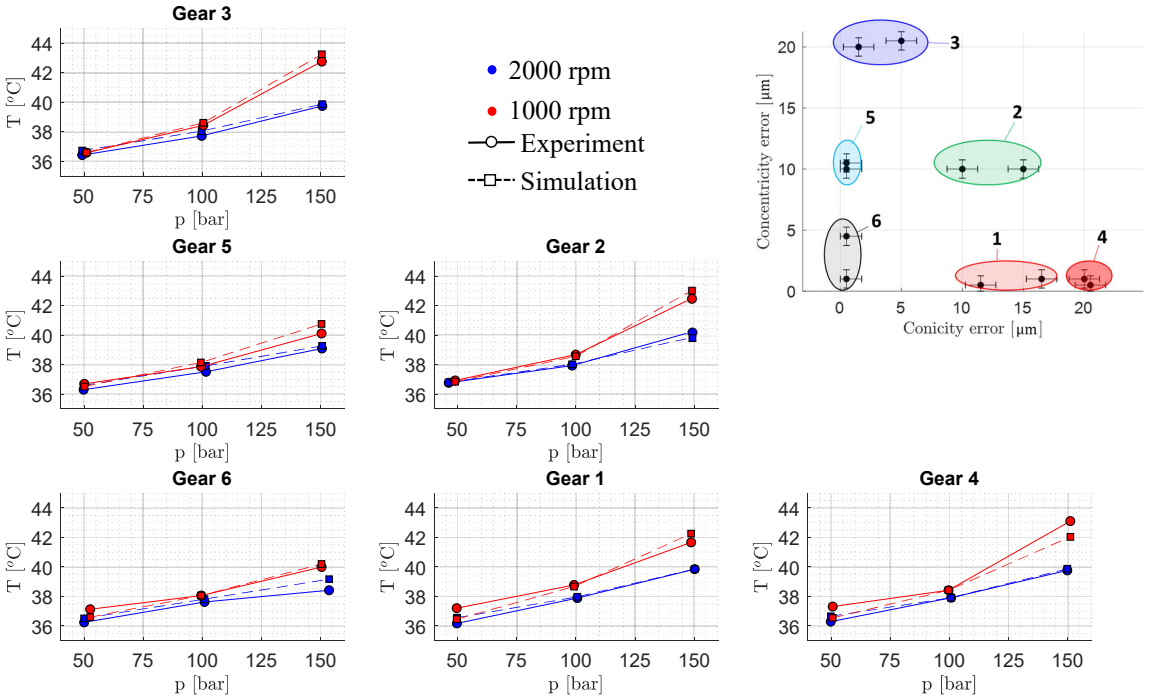

Figure 8.10. Comparison of the outlet temperature predicted by the simulations and the outlet temperature measured in the experiments for all six gearsets.

conducted using EGM E3 as the reference. To magnify the difference, the clearance at the tooth tip was increased from the nominal value of 30 μm to 55 μm. Typically, EGMs experience similar increase in clearances due to wearing out of the internal components over time.

First set of simulations were conducted using the isothermal HYGESim tool with the temperature set to $T_{pump} = 35$ °C. Second set of simulations were conducted using the non-isothermal HYGESim tool with the inlet temperature set to $T_{inlet} = 35$ °C. From the results of these simulations, the outlet temperatures were recorded and the mean temperatures for each of these simulations were calculated, $T_{mean} = 0.5(T_{inlet} + T_{outlet})$. These mean temperatures were used as T_{pump} in the third set of simulations which were conducted using the isothermal HYGESim tool. This third

set is identical to the simulations conducted in past to compare the model results with the experimental data, where mean temperatures obtained from the experiments are used as T_{pump} in the isothermal model.

Figure 8.11 shows that at high efficiency operating conditions, the three sets yield similar efficiency results. Especially, the results from set 3 (isothermal model with mean temperatures) are within 3 % of the results obtained from non-isothermal HYGESim for efficiency levels > 70 %. Thus, the traditional isothermal HYGESim is still an acceptable tool for modelling moderately efficient EGMs.

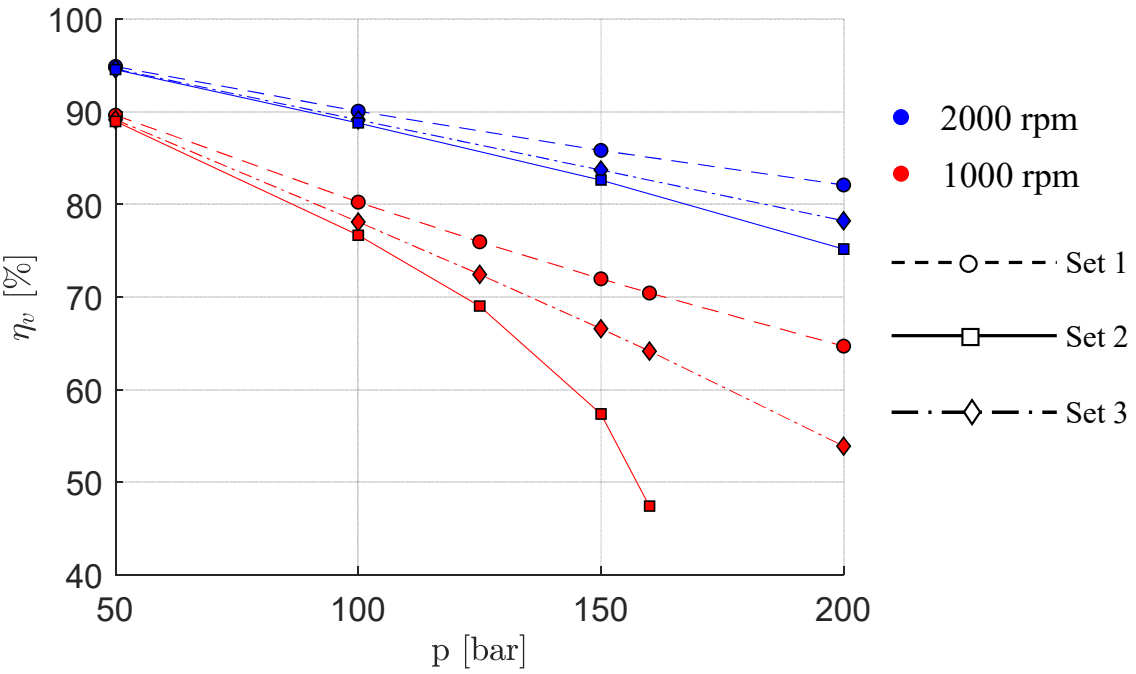

Figure 8.11. Comparison of the results in terms of volumetric efficiency from three sets of simulations: Set 1: isothermal (T_{pump} = 35 °C), Set 2: non-isothermal (T_{inlet} = 35 °C), Set 3: isothermal ($T_{pump} = 0.5(T_{inlet} + T_{outlet})$) where T_{inlet} and T_{outlet} are obtained from Set 2 simulation results.

However, at low efficiency conditions (η_v < 70 %), the isothermal models (even the one with mean temperatures), significantly overpredict the volumetric efficiency. This is expected since, at low efficiency conditions, there is a significant amount of

power loss in the EGM. This power loss is converted into heat raising the temperature of the fluid. As a consequence, the viscosity of the fluid is reduced, increasing the leakage flows and hence further lowering the volumetric efficiency. This phenomenon is not considered in the isothermal model due to which it overpredicts the volumetric efficiency.

At 1000 rpm, 200 bar, the non-isothermal model predicts zero volumetric efficiency (the leakage flow exceeds the delivery flow) indicating that the EGM is inoperable at that operating condition. However, the isothermal models predict $\eta_v > 50\,\%$.

Thus, the non-isothermal HYGESim tool is critical in the accurate efficiency prediction of the EGMs that exhibit low efficiency. This tool is especially crucial in the prediction of the operability of the EGMs at extreme operating conditions (e.g. high temperatures and high pressures) and EGMs with worn out internal components.

9. SUMMARY

This dissertation presents the numerical methodologies for the modelling of key aspects of EGM operation that play significant roles in describing the performance of the reference EGMs selected in this work. The aspects considered in this work comprises the nature of the working fluid (A1), regime of the leakage flow (A2), gear manufacturing errors, (A3) tooth tip geometry (A4), frictional losses (A5) and thermal effects (A6). The methodologies developed in this work are integrated with HYGESim, a lumped parameter based simulation tool developed by Dr. Vacca's research team.

In this dissertation, the methodology of modelling external gear pumps operating with non-Newtonian fluids was described (Aspect A1). In particular, a new set of fluid dynamic equations were developed which are suitable to describe the flow of shear thinning fluids through internal connections of the reference pump E1. In order to validate the modelling approach, experiments were conducted on the reference pump using three different fluids. A good match of volumetric efficiency between the model and experiment was observed which indicates the validity of the leakage flow modelling approach. Moreover, a good match of pressure pulsation between the model and experiment was observed too which indicates the validity of the modelling of internal orifice connections that determine the main pumping action realized by the external gear pump.

Next, the nature of fluid flow over the tooth tips of EGMs operating with low viscosity fluids and at high speeds was investigated (Aspect A2). Using CFD simulations, turbulent nature of the fluid flow over the tooth tip was observed and methods to model the leakage flow with turbulent behavior was described. Using this turbulent leakage flow model, it was shown that the nature of flow regime at the tooth tip has a significant impact on the volumetric efficiency of EGMs and the course of TSV pressurization. Accurate prediction of TSV pressurization is important in deter-

mining the radial loading on the gears which impacts the radial micromotion of the gears ultimately affecting the leakage flow itself. Moreover, accurate TSV pressurization information is useful in the analysis of the axial balance of floating elements in pressure compensated EGMs.

Further, a novel technique for studying the impact of manufacturing errors on the performance of EGMs was presented (Aspect A3). In particular, two common errors involved in gear manufacturing: conicity and concentricity errors were considered. The technique developed in this work was validated via experiments on gearsets with varying amounts of manufacturing errors. The results show that for a constant mean gear diameter, an increase in the conicity error leads to a reduction in the volumetric efficiency. On the other hand, an increase in the concentricity error leads to an increase in the volumetric efficiency. This increase, however, occurs as long as the concentricity error does not cause contact between the gear teeth and the internal surface of the casing, as it can happen for the EGMs subjected to case-wear. Furthermore, an increase in the concentricity error leads to an increase of the outlet flow non-uniformity.

Next, the methodology to model the inter-teeth flow in gear machines with curved tooth geometry was described (Aspect A4). Via analytical methods and CFD simulations, the leakage flow model was developed for such curved geometries that is applicable for a wide range of flow regimes including localized cavitation. To validate the model, an experimental apparatus was designed and manufactured with a 50:1 scale that mimics the actual flow geometry at the tooth tip. Multiple tests were conducted for a wide range of both geometry and flow parameters. The results from the tests were found to match the non-dimensional relationships, which validates the leakage flow model.

Afterwards, methodology for the evaluation of torque losses due to friction at key interfaces in EGMs was presented (Aspect A5). In particular, the friction at the gear tooth tips, lateral interfaces, bearings and meshing regions were considered. The results obtained from the simulation of the reference EGM E5 show that the meshing

friction is the dominant source of torque losses. The results from the simulations were shown to agree with the experimental data in terms of the hydro-mechanical efficiency for a wide of range of operating speeds and pressures which validates the methodology developed in this work.

Finally, the thermal model of EGM was developed to predict the temperature distribution in the EGM (Aspect A6). The governing equations for pressure and temperature were derived and the approach for the modelling of internal enthalpy flows and power losses were described. The model validation was achieved via a good agreement of the outlet temperature between the simulation results and the experimental data. From the model results, it was shown that while the traditional isothermal model is sufficient for modelling moderately efficient EGMs, the thermal model is indispensable for accurately modelling the performance of EGMs with poor efficiency and predicting the operability of EGMs at extreme operating conditions.

The numerical techniques for modeling the operation of EGMs developed in this work has multiple potentials:

- The industries using external gear pumps in the handling of non-Newtonian fluids often struggle with the performance concerns of these units. The techniques developed are going to be helpful in understanding and analyzing various issues faced by the industries in existing pumping operations. The modelling capability can also help researchers in future to perform various sensitivity studies and understand the range of non-Newtonian fluids that can be pumped with specific external gear pumps without any performance concerns.

- For EGMs operating with low viscosity fluids, the turbulence model for leakage flow developed in this work is going to be useful in precise prediction of volumetric efficiency, radial loading and axial balance of floating elements for a wide range of operating conditions.

- To ensure a cost effective manufacturing of EGMs, the decision on the level of tolerance is of paramount importance. The work presented in this dissertation

will be valuable to the pump designers in making informed decisions about the level of the tolerances on the gear geometry. This work will also be useful in accurate analysis of the performance of EGMs whose gears exhibit conicity and concentricity errors.

- The leakage flow model developed for curved tooth tip geometry has significance in furthering the research on CCHGPs and gerotor units. The model is going to be helpful for pump designers in understanding the impact of gear profile and clearances on the volumetric efficiency of these units. This will assist them in developing more efficient gear machines. The model can also be readily used in lumped parameter based numerical tools that will permit an accurate prediction of leakages and volumetric efficiency of these units.

- The torque loss model developed in this work will provide the industries an accurate and reliable method for the prediction of the hydro-mechanical efficiency of their EGMs. It will also help the pump designers in analyzing the effect of key pump parameters on the hydro-mechanical performance of the unit, thereby helping them in designing energy efficient EGMs from torque loss perspective.

- The thermal model developed in this work will be helpful for industries and researchers in accurately modelling the performance of EGMs exhibiting poor efficiency, thus allowing them to properly analyze the causes of low efficiency of such EGMs and make appropriate modifications in the EGM design. Moreover, the outlet temperature prediction capability of the model will help hydraulic system designers in accurate modelling of the hydraulic systems containing EGMs and thus optimizing their performance.

- Finally, all the techniques developed in this work can readily be integrated in common EGM simulation tools and can be used in optimization algorithms. This will allow the development of novel EGM designs for various applications with the goal to improve their performance over wide range of operating conditions.

10. FUTURE RESEARCH DIRECTIONS

The research work presented in dissertation has opened new doors for further research towards developing better performing EGMs as well as novel designs suited for new trends in hydraulic technology. Developing such EGMs would require optimization studies which is beyond the scope of this research which primarily focuses on modelling. However, the models developed in this work for EGMs working in fluid handling applications and fuel injection applications can be used in optimization algorithms for developing novel EGM designs optimized for such applications. Moreover, these algorithms can use the manufacturing error model developed in this work to determine the tolerance levels for these novel gear designs optimized for efficiency and cost. Similar optimization studies could be done on CCHGPs that use the leakage flow model developed in this work. Finally, these optimization tools can incorporate the torque loss and thermal models developed in this work for developing novel EGM designs that are optimal from both volumetric and hydro-mechanical perspective.

There are other aspects influencing the EGM performance that were not important for the reference EGMs studied in this work (Table 1.1), but can be significant for other units. Some of those aspects are listed below:

- For EGMs with long gears, pressure induced deformation of the gears can change the leakage flow geometry and hence the efficiency of EGMs.
- If EGMs working with non-Newtonian fluids operate at higher speeds and/or with high viscosity fluids, the tooth space volumes may not fill completely during the suction operation causing aeration or possibly cavitation.
- The flow through the lateral leakage interfaces and bearings may become turbulent for certain flow and operating conditions which can significantly influence the performance of EGMs.

- For EGM designs with zero-backlash between the gears (dual flank designs), the contact force in the meshing of the gears may become very high and fall outside the range of applicability of the EHL friction relation used in this work.
- For certain EGM designs, the heat loss to the environment may not be negligible.

These aspects can be investigated in future by other researchers and numerical methodologies can be developed to incorporate their effects in the modelling of EGMs.

REFERENCES

REFERENCES

[1] Sujan Dhar and Andrea Vacca. A novel cfd–axial motion coupled model for the axial balance of lateral bushings in external gear machines. *Simulation Modelling Practice and Theory*, 26:60–76, 2012.

[2] U.S. Energy Information Administration. International energy outlook 2018. *IEO*, 2018.

[3] K Mitome and K Seki. A new continuous contact low-noise gear pump. *Journal of Mechanisms, Transmissions, and Automation in Design*, 105(4):736–741, 1983.

[4] TE Beacham. High-pressure gear pumps. *Proceedings of the Institution of Mechanical Engineers*, 155(1):417–452, 1946.

[5] C Bonacini. Sulla portata delle pompe ad ingranaggi. *L'Ingengnere*, 9, 1961.

[6] Jaroslav Ivantysyn and Monika Ivantysynova. *Hydrostatic pumps and motors: principles, design, performance, modelling, analysis, control and testing*. Tech Books International, 2003.

[7] Noah D Manring and Suresh B Kasaragadda. The theoretical flow ripple of an external gear pump. *Journal of dynamic systems, measurement, and control*, 125(3):396–404, 2003.

[8] K Foster, R Taylor, and IM Bidhendi. Computer prediction of cyclic excitation sources for an external gear pump. *Proceedings of the Institution of Mechanical Engineers, Part B: Management and engineering manufacture*, 199(3):175–180, 1985.

[9] S Mancò and N Nervegna. Simulation of an external gear pump and experimental verification. In *Proceedings of the JFPS International Symposium on Fluid Power*, volume 1989, pages 147–160. The Japan Fluid Power System Society, 1989.

[10] M Eaton, KA Edge, and PS Keogh. Modelling and simulation of pressures within the meshing teeth of gear pumps. In *International Conference on Recent Advances in Aerospace Actuation Systems and Components*, 2001.

[11] MKPEK Eaton, PS Keogh, and KA Edge. The modelling, prediction, and experimental evaluation of gear pump meshing pressures with particular reference to aero-engine fuel pumps. *Proceedings of the Institution of Mechanical Engineers, Part I: Journal of Systems and Control Engineering*, 220(5):365–379, 2006.

[12] Massimo Borghi, Massimo Milani, Fabrizio Paltrinieri, and Barbara Zardin. The influence of cavitation and aeration on gear pumps and motors meshing volumes pressures. In *ASME 2006 International Mechanical Engineering Congress and Exposition*, pages 47–56. American Society of Mechanical Engineers, 2006.

[13] B Zardin, F Paltrinieri, M Borghi, and M Milani. About the prediction of pressure variation in the inter-teeth volumes of external gear pumps. In *Proceedings of the 3rd FPNI-PhD symposium on fluid power, Spain*, 2004.

[14] Barbara Zardin and Massimo Borghi. Modelling and simulation of external gear pumps and motors. In *5th FPNI-PhD Symposium on Fluid Power*, volume 1. Cracow University of Technology (CUT), Institute of Machine Design, 2008.

[15] S Falfari and P Pelloni. Setup of a 1d model for simulating dynamic behaviour of external gear pumps. Technical report, SAE Technical Paper, 2007.

[16] Paolo Casoli, Andrea Vacca, and Gian Luigi Berta. Potentials of a numerical tool for the simulation of flow in external gear machines. In *The Tenth Scandinavian International Conference on Fluid Power*, volume 7, pages 2007–21. SICFP, 2007.

[17] Emiliano Mucchi, Giorgio Dalpiaz, and A Fernandez Del Rincon. Elastodynamic analysis of a gear pump. part i: Pressure distribution and gear eccentricity. *Mechanical Systems and Signal Processing*, 24(7):2160–2179, 2010.

[18] Emiliano Mucchi, Giorgio Dalpiaz, and A Rivola. Elastodynamic analysis of a gear pump. part ii: meshing phenomena and simulation results. *Mechanical Systems and Signal Processing*, 24(7):2180–2197, 2010.

[19] Emiliano Mucchi, Giorgio Dalpiaz, and A Fernàndez Del Rincòn. Elastodynamic analysis of a gear pump–part iv: Improvement in the pressure distribution modelling. *Mechanical Systems and Signal Processing*, 50:193–213, 2015.

[20] Emiliano Mucchi and Giorgio Dalpiaz. Elasto-dynamic analysis of a gear pump–part iii: Experimental validation procedure and model extension to helical gears. *Mechanical Systems and Signal Processing*, 50:174–192, 2015.

[21] Andrea Vacca and Marco Guidetti. Modelling and experimental validation of external spur gear machines for fluid power applications. *Simulation Modelling Practice and Theory*, 19(9):2007–2031, 2011.

[22] Junjie Zhou, Andrea Vacca, and Paolo Casoli. A novel approach for predicting the operation of external gear pumps under cavitating conditions. *Simulation Modelling Practice and Theory*, 45:35–49, 2014.

[23] Yash Shah, Andrea Vacca, and Sadegh Dabiri. Air release and cavitation modeling with a lumped parameter approach based on the rayleigh–plesset equation: The case of an external gear pump. *Energies*, 11(12):3472, 2018.

[24] Thomas M Ransegnola, Andrea Vacca, Mario Antonio Morselli, Andrzej Kowalski, and Richard Muizelaar. A simulation model for a tandem external gear pump for automotive transmission. Technical report, SAE Technical Paper, 2018.

[25] Xinran Zhao and Andrea Vacca. Analysis of continuous-contact helical gear pumps through numerical modeling and experimental validation. *Mechanical Systems and Signal Processing*, 109:352–378, 2018.

[26] Ram Sudarsan Devendran and Andrea Vacca. Optimal design of gear pumps for exhaust gas aftertreatment applications. *Simulation Modelling Practice and Theory*, 38:1–19, 2013.

[27] Xinran Zhao and Andrea Vacca. Formulation and optimization of involute spur gear in external gear pump. *Mechanism and Machine Theory*, 117:114–132, 2017.

[28] Wayne Strasser. Cfd investigation of gear pump mixing using deforming/agglomerating mesh. *Journal of Fluids Engineering*, 129(4):476–484, 2007.

[29] R Castilla, PJ Gamez-Montero, N Ertürk, A Vernet, M Coussirat, and E Codina. Numerical simulation of turbulent flow in the suction chamber of a gearpump using deforming mesh and mesh replacement. *International Journal of Mechanical Sciences*, 52(10):1334–1342, 2010.

[30] D Del Campo, R Castilla, GA Raush, PJ Gamez Montero, and E Codina. Numerical analysis of external gear pumps including cavitation. *Journal of fluids engineering*, 134(8):081105, 2012.

[31] R Castilla, Pedro Javier Gamez-Montero, D Del Campo, G Raush, Mercedes Garcia-Vilchez, and E Codina. Three-dimensional numerical simulation of an external gear pump with decompression slot and meshing contact point. *Journal of Fluids Engineering*, 137(4):041105, 2015.

[32] OpenCFD. Openfoam, https://openfoam.org/, 2018.

[33] Simerics. Pumplinx, https://www.simerics.com/pumplinx/, 2018.

[34] Aaron S Heisler, John J Moskwa, and Frank J Fronczak. Simulated helical gear pump analysis using a new cfd approach. In *ASME 2009 Fluids Engineering Division Summer Meeting*, pages 445–455. American Society of Mechanical Engineers, 2009.

[35] Feng Qi, Sujan Dhar, Varun Haresh Nichani, Chiranth Srinivasan, De Ming Wang, Liang Yang, Zhonghui Bing, and Jinming Jim Yang. A cfd study of an electronic hydraulic power steering helical external gear pump: Model development, validation and application. *SAE International Journal of Passenger Cars-Mechanical Systems*, 9(2016-01-1376):346–352, 2016.

[36] P Casoli, A Vacca, and Berta GL. Optimization of relevant design parameters of external gear pumps. In *Proceedings of the JFPS International Symposium on Fluid Power*, volume 2008, pages 277–282. The Japan Fluid Power System Society, 2008.

[37] Sidhant Gulati, Andrea Vacca, and Manuel Rigosi. A general method to determine the optimal profile of porting grooves in positive displacement machines: the case of external gear machines. In *10th International Fluid Power Conference. Dresden*, 2016.

[38] Donaldson McCloy and Hugh Robert Martin. Control of fluid power: analysis and design. *Chichester, Sussex, England, Ellis Horwood, Ltd.; New York, Halsted Press, 1980. 505 p.*, 1980.

[39] YG Shah, A Vacca, S Dabiri, and E Frosina. A fast lumped parameter approach for the prediction of both aeration and cavitation in gerotor pumps. *Meccanica*, 53(1-2):175–191, 2018.

[40] JF Booker. Dynamically loaded journal bearings: mobility method of solution. *Journal of Basic Engineering*, 87(3):537–546, 1965.

[41] Fred W Ocvirk. Short-bearing approximation for full journal bearings. *NASA Technical Report*, 1952.

[42] Paul C Warner. Static and dynamic properties of partial journal bearings. *Journal of Basic Engineering*, 85(2):247, 1963.

[43] Bernard J Hamrock, Steven R Schmid, and Bo O Jacobson. *Fundamentals of fluid film lubrication*. CRC press, 2004.

[44] Matteo Pellegri and Andrea Vacca. A cfd-radial motion coupled model for the evaluation of the features of journal bearings in external gear machines. In *ASME/BATH 2015 Symposium on Fluid Power and Motion Control*, pages V001T01A025–V001T01A025. American Society of Mechanical Engineers, 2015.

[45] Xinran Zhao and Andrea Vacca. Numerical analysis of theoretical flow in external gear machines. *Mechanism and Machine Theory*, 108:41–56, 2017.

[46] Divya Thiagarajan. *Analysis and design of lubricating interfaces in external gear machines for high and low viscous working fluids*. PhD thesis, Purdue University, West Lafayette, 2018.

[47] Katsuji Kishimoto. Gear pump for non-newtonian fluid, May 17 1994. US Patent 5,312,236.

[48] Zenith pumps. Zenith 9000 series gear pump, www.zenithpumps.com, 2015.

[49] Robert Byron Bird, Robert C Armstrong, and Ole Hassager. *Dynamics of polymeric liquids. Vol. 1: Fluid mechanics*. John Wiley and Sons, Inc, Hoboken, New Jersey, second edition, 1987.

[50] Walter F Salas-Valerio and James F Steffe. Orifice discharge coefficients for power-law fluids. *Journal of Food Process Engineering*, 12(2):89–98, 1990.

[51] David A McNeil, Jack Addlesee, and Alastair Stuart. An experimental study of viscous flows in contractions. *Journal of loss prevention in the process industries*, 12(4):249–258, 1999.

[52] Rajinder Pal. Flow of oil-in-water emulsions through orifice and venturi meters. *Industrial & engineering chemistry research*, 32(6):1212–1217, 1993.

[53] MF Edwards, MSM Jadallah, and R Smith. Head losses in pipe fittings at low reynolds numbers. *Chemical Engineering Research and Design*, 63(1):43–50, 1985.

[54] Arun Kumar Samanta, Tapan Kumar Banerjee, and Sudiv Kumar Das. Pressure losses in orifices for the flow of gas-non-newtonian liquids. *Canadian journal of chemical engineering*, 77:579–579, 1999.

[55] Tarun Kanti Bandyopadhyay and Sudip Kumar Das. Non-newtonian pseudoplastic liquid flow through small diameter piping components. *Journal of Petroleum Science and Engineering*, 55(1-2):156–166, 2007.

[56] Lalit Kumar Bohra. *Flow and pressure drop of highly viscous fluids in small aperture orifices*. PhD thesis, Georgia Institute of Technology, 2004.

[57] Butteur Ntamba Ntamba and Veruscha Fester. Pressure losses and limiting reynolds numbers for non-newtonian fluids in short square-edged orifice plates. *Journal of Fluids Engineering*, 134(9):091204, 2012.

[58] MR Chowdhury and Veruscha G Fester. Modeling pressure losses for newtonian and non-newtonian laminar and turbulent flow in long square edged orifices. *Chemical Engineering Research and Design*, 90(7):863–869, 2012.

[59] Paul Slatter. The role of rheology in the pipelining of mineral slurries. *Mineral Procesing and Extractive Metallurgy Review*, 20(1):281–300, 2000.

[60] Isaak E Idelchik. Handbook of hydraulic resistance. *Israel Program for Scientific Translations*, 1966.

[61] Duqiang Wu, Richard Burton, and Greg Schoenau. An empirical discharge coefficient model for orifice flow. *International journal of fluid power*, 3(3):13–19, 2002.

[62] Ammar Zeghloul, Abdelwahid Azzi, Faiza Saidj, Abdelkader Messilem, and Barry James Azzopardi. Pressure drop through orifices for single-and two-phase vertically upward flow—implication for metering. *Journal of Fluids Engineering*, 139(3):031302, 2017.

[63] Zehev Tadmor and Costas G. Gogos. *Principles of polymer processing*. John Wiley and Sons, Inc, Hoboken, New Jersey, first edition, 1979.

[64] IK Dien and HG Elrod. A generalized steady-state reynolds equation for non-newtonian fluids, with application to journal bearings. *Journal of Lubrication Technology*, 105(3):385–390, 1983.

[65] ISO 10767-1. Hydraulic fluid power – determination of pressure levels generated in systems and components – part 1: Precision method for pumps, 1996.

[66] ISO 10767-2. Hydraulic fluid power – determination of pressure levels generated in systems and components – part 2: Simplified method for pumps, 1996.

[67] S Mancò and N Nervegna. Pressure transients in an external gear hydraulic pump. In *Proceedings of the JFPS International Symposium on Fluid Power*, volume 1993, pages 221–227. The Japan Fluid Power System Society, 1993.

[68] Dario Buono, Daniela Siano, Emma Frosina, and Adolfo Senatore. Gerotor pump cavitation monitoring and fault diagnosis using vibration analysis through the employment of auto-regressive-moving-average technique. *Simulation Modelling Practice and Theory*, 71:61–82, 2017.

[69] D Nigel Johnston and JE Drew. Measurement of positive displacement pump flow ripple and impedance. *Proceedings of the Institution of Mechanical Engineers, Part I: Journal of Systems and Control Engineering*, 210(1):65–74, 1996.

[70] Andrea Vacca, Germano Franzoni, and Paolo Casoli. On the analysis of experimental data for external gear machines and their comparison with simulation results. In *ASME 2007 International Mechanical Engineering Congress and Exposition*, pages 45–53. American Society of Mechanical Engineers, 2007.

[71] Sujan Dhar and Andrea Vacca. A fluid structure interaction—ehd model of the lubricating gaps in external gear machines: Formulation and validation. *Tribology International*, 62:78–90, 2013.

[72] Massimo Borghi, Barbara Zardin, and Emiliano Specchia. External gear pump volumetric efficiency: Numerical and experimental analysis. Technical report, SAE Technical Paper, 2009.

[73] Shu Wang, Hisatoshi Sakura, and Aditya Kasarekar. Numerical modelling and analysis of external gear pumps by applying generalized control volumes. *Mathematical and Computer Modelling of Dynamical Systems*, 17(5):501–513, 2011.

[74] J Zhang, B Tao, and J Katz. Turbulent flow measurement in a square duct with hybrid holographic piv. *Experiments in Fluids*, 23(5):373–381, 1997.

[75] Laurent Graftieaux, Marc Michard, and Nathalie Grosjean. Combining piv, pod and vortex identification algorithms for the study of unsteady turbulent swirling flows. *Measurement Science and technology*, 12(9):1422, 2001.

[76] J Sheng, H Meng, and RO Fox. A large eddy piv method for turbulence dissipation rate estimation. *Chemical engineering science*, 55(20):4423–4434, 2000.

[77] Gary N Coleman and Richard D Sandberg. A primer on direct numerical simulation of turbulence-methods, procedures and guidelines. *Technical Report AFM-09/01a*, 2010.

[78] Parviz Moin and Krishnan Mahesh. Direct numerical simulation: a tool in turbulence research. *Annual review of fluid mechanics*, 30(1):539–578, 1998.

[79] ANSYS. Academic research fluent, release 19.1, 2018.

[80] Stephen B Pope. *Turbulent flows*. Cambridge university press, 2000.

[81] David C Wilcox. Comparison of two-equation turbulence models for boundary layers with pressure gradient. *AIAA journal*, 31(8):1414–1421, 1993.

[82] Florian R Menter. Two-equation eddy-viscosity turbulence models for engineering applications. *AIAA journal*, 32(8):1598–1605, 1994.

[83] Teryn DalBello, Vance Dippold III, and Nicholas J Georgiadis. Computational study of separating flow in a planar subsonic diffuser. *Technical report NASA/TM-2005-213894*, 2005.

[84] David C Wilcox. *Turbulence modeling for CFD*, volume 3. DCW industries La Canada, CA, 2006.

[85] 19.1 ANSYS Fluent. Help system, fluent user's guide, 2018.

[86] Samy M El-Behery and Mofreh H Hamed. A comparative study of turbulence models performance for separating flow in a planar asymmetric diffuser. *Computers & Fluids*, 44(1):248–257, 2011.

[87] Ludwig Prandtl. Bericht uber untersuchungen zur ausgebildeten turbulenz. *Zs. angew. Math. Mech.*, 5:136–139, 1925.

[88] TH Von Karman. Mechanische ahnlichkeit und turbulenz. *Math.-Phys. Klasse*, 1930.

[89] Hans Reichardt. Vollständige darstellung der turbulenten geschwindigkeitsverteilung in glatten leitungen. *ZAMM-Journal of Applied Mathematics and Mechanics/Zeitschrift für Angewandte Mathematik und Mechanik*, 31(7):208–219, 1951.

[90] Robert G Deissler. Analysis of turbulent heat transfer, mass transfer, and friction in smooth tubes at high prandtl and schmidt numbers. *NACA Tech. Rep. 1210*, 1955.

[91] Donald Coles. The law of the wake in the turbulent boundary layer. *Journal of Fluid Mechanics*, 1(2):191–226, 1956.

[92] DB Spalding. A single formula for the "law of the wall". *Journal of Applied Mechanics*, 28(3):455–458, 1961.

[93] Stuart W Churchill and Christina Chan. Theoretically based correlating equations for the local characteristics of fully turbulent flow in round tubes and between parallel plates. *Industrial & engineering chemistry research*, 34(4):1332–1341, 1995.

[94] Chung-Wah Ng and CHT Pan. A linearized turbulent lubrication theory. *Journal of Basic Engineering*, 87(3):675–682, 1965.

[95] HG Elrod and CW Ng. A theory for turbulent fluid films and its application to bearings. *Journal of Lubrication Technology*, 89(3):346–362, 1967.

[96] GG Hirs. A bulk-flow theory for turbulence in lubricant films. *Journal of Lubrication Technology*, 95(2):137–145, 1973.

[97] Sangbeom Woo, Timothy Opperwall, Andrea Vacca, and Manuel Rigosi. Modeling noise sources and propagation in external gear pumps. *Energies*, 10(7):1068, 2017.

[98] ISO 1328-1. Cylindrical gears — iso system of flank tolerance classification — part 1: Definitions and allowable values of deviations relevant to flanks of gear teeth, 2013.

[99] DIN 3962. Tolerance for cylindrical gear teeth, 1978.

[100] AGMA 2015-1-A01. Accuracy classification system - tangential measurements for cylindrical gears, 2014.

[101] Gill-Jeong Cheon and Robert G Parker. Influence of manufacturing errors on the dynamic characteristics of planetary gear systems. *KSME international journal*, 18(4):606–621, 2004.

[102] Endo Hiroaki and Sawalhi Nader. Gearbox simulation models with gear and bearing faults. In *Mechanical engineering*. IntechOpen, 2012.

[103] H Ligata, A Kahraman, and A Singh. An experimental study of the influence of manufacturing errors on the planetary gear stresses and planet load sharing. *Journal of Mechanical Design*, 130(4):041701, 2008.

[104] ANSI Y14.5. Dimensioning and tolerancing, 1982.

[105] S Mancò, N Nervegna, M Rundo, G Armenio, C Pachetti, and R Trichilo. Gerotor lubricating oil pump for ic engines. *SAE transactions*, pages 2267–2283, 1998.

[106] Salvatore Mancò, Nicola Nervegna, and Massimo Rundo. A contribution to the design of hydraulic lube pumps. *International Journal of Fluid Power*, 3(1):21–32, 2002.

[107] Wolfgang Schweiger, Werner Schoefmann, and Andrea Vacca. Gerotor pumps for automotive drivetrain applications: a multi domain simulation approach. *SAE International Journal of Passenger Cars-Mechanical Systems*, 4(2011-01-2272):1358–1376, 2011.

[108] Matteo Pellegri, Andrea Vacca, E Dautry, and B Ginsberg. A lumped parameter approach for gerotor pumps: Model formulation and experimental validation. In *Proceedings of the 10th IFK International Fluid Power Conference, Dresden, Germany*, pages 8–10, 2016.

[109] M Pellegri and A Vacca. Numerical simulation of gerotor pumps considering rotor micro-motions. *Meccanica*, 52(8):1851–1870, 2017.

[110] Matteo Pellegri, Andrea Vacca, Emma Frosina, Dario Buono, and Adolfo Senatore. Numerical analysis and experimental validation of gerotor pumps: A comparison between a lumped parameter and a computational fluid dynamics-based approach. *Proceedings of the Institution of Mechanical Engineers, Part C: Journal of Mechanical Engineering Science*, 231(23):4413–4430, 2017.

[111] Ilya I Kudish. On formulation of a non-steady lubrication problem for a non-conformal contact©. *Tribology transactions*, 42(1):53–57, 1999.

[112] Soon-Man Kwon, Mu Seong Kim, and Joong-Ho Shin. Analytical wear model of a gerotor pump without hydrodynamic effect. *Journal of Advanced Mechanical Design, Systems, and Manufacturing*, 2(2):230–237, 2008.

[113] Soon-man Kwon, Chang-Hyun Kim, and Joong-ho Shin. Optimal rotor wear design in hypotrochoidal gear pump using genetic algorithm. *Journal of Central South University of Technology*, 18(3):718–725, 2011.

[114] K Biernacki and J Stryczek. Analysis of stress and deformation in plastic gears used in gerotor pumps. *The Journal of Strain Analysis for Engineering Design*, 45(7):465–479, 2010.

[115] Philip J Pritchard, John W Mitchell, and John C Leylegian. *Fox and McDonald's Introduction to Fluid Mechanics, Binder Ready Version*. John Wiley & Sons, 2016.

[116] Ashok K Singhal, Mahesh M Athavale, Huiying Li, and Yu Jiang. Mathematical basis and validation of the full cavitation model. *J. Fluids Eng.*, 124(3):617–624, 2002.

[117] Matteo Pellegri. *A study on the operation of gerotor type units considering Fluid structure and mechanical interaction effects*. PhD thesis, Purdue University, West Lafayette, 2018.

[118] WE Wilson. Rotary-pump theory. *Trans. ASME*, 68(4):371–384, 1946.

[119] Warren Elvin Wilson. Performance criteria for positive displacement pumps and fluid motors. *Trans. ASME*, 71(2):115–120, 1949.

[120] WMJ Schlösser. The overall efficiency of positive-displacement pumps. *Hydraulic pneumatic power*, 15(173):272–280, 1969.

[121] A Hibi and T Ichikawa. Torque performance of hydraulic motor in whole operating condition from start to maximum speed and its mathematical model. In *4th International Fluid Power Symposium, UK*, 1975.

[122] GL Zarotti and N Nervegna. Pump efficiencies: approximation and modeling. *Fluidics quarterly*, 14(3):1–20, 1982.

[123] Paul W Michael, Hassan Khalid, and Thomas Wanke. An investigation of external gear pump efficiency and stribeck values. Technical report, SAE Technical Paper, 2012.

[124] Divya Thiagarajan and Andrea Vacca. Investigation of hydro-mechanical losses in external gear machines: Simulation and experimental validation. In *BATH/ASME 2016 Symposium on Fluid Power and Motion Control*. American Society of Mechanical Engineers Digital Collection, 2016.

[125] Barbara Zardin, Emiliano Natali, and Massimo Borghi. Evaluation of the hydro—mechanical efficiency of external gear pumps. *Energies*, 12(13):2468, 2019.

[126] Nadir Patir and HS Cheng. An average flow model for determining effects of three-dimensional roughness on partial hydrodynamic lubrication. *Journal of Tribology*, 100:12–17, 1978.

[127] Nadir Patir and HS Cheng. Application of average flow model to lubrication between rough sliding surfaces. *Journal of Tribology*, 101:220–229, 1979.

[128] BO Jacobson and BJ Hamrock. Non-newtonian fluid model incorporated into elastohydrodynamic lubrication of rectangular contacts. *Journal of Tribology*, 106(2):275–282, 1984.

[129] Eduardo Dalla Lana and Victor Juliano De Negri. A new evaluation method for hydraulic gear pump efficiency through temperature measurements. Technical report, SAE Technical Paper, 2006.

[130] Paolo Casoli, Federico Campanini, Andrea Bedotti, Mirko Pastori, and Antonio Lettini. Overall efficiency evaluation of a hydraulic pump with external drainage through temperature measurements. *Journal of Dynamic Systems, Measurement, and Control*, 140(8), 2018.

[131] M Zecchi, A Mehdizadeh, and M Ivantysynova. A novel approach to predict the steady state temperature in ports and case of swash plate type axial piston machines. In *13th Scandinavian International Conference on Fluid Power; June 3-5; 2013; Linköping; Sweden*, pages 177–187. Linköping University Electronic Press, 2013.

[132] L Shang and M Ivantysynova. Port and case flow temperature prediction for axial piston machines. *International Journal of Fluid Power*, 16(1):35–51, 2015.

[133] Sujan Dhar, Andrea Vacca, and Antonio Lettini. A novel fluid–structure–thermal interaction model for the analysis of the lateral lubricating gap flow in external gear machines. In *ASME/BATH 2013 Symposium on Fluid Power and Motion Control*. American Society of Mechanical Engineers Digital Collection, 2013.

[134] Sujan Dhar and Andrea Vacca. A novel fsi–thermal coupled tehd model and experimental validation through indirect film thickness measurements for the lubricating interface in external gear machines. *Tribology International*, 82:162–175, 2015.

[135] Siemens. Simcenter amesim, version 16, 2018.

[136] ANSYS. Academic research mechanical, release 19.1, 2018.

PUBLICATIONS

PUBLICATIONS

Journal Publications

- Rituraj and Vacca A., Thermal modelling of external gear pumps and experimental validation. (in preparation)
- Rituraj and Vacca A., Modeling and validation of hydro-mechanical losses in external gear machines. (in preparation)
- Rituraj and Vacca A., A novel formulation of flow through curved constrictions for the modelling of leakage flows in hydraulic gear machines. (in preparation)
- Rituraj and Vacca A. (2020), An investigation of tooth tip leakages in gerotor pumps: Modelling and Experimental Validation. *Journal of Verification, Validation and Uncertainty Quantification*, 5(1), 011001.
- Rituraj, Vacca A. and Morselli M. (2019), Modelling of manufacturing errors in external gear machines and experimental validation, *Mechanism and Machine Theory*, 140, 457-478.
- Rituraj and Vacca A. (2018), External gear pumps operating with non-Newtonian fluids: Modelling and experimental validation, *Mechanical Systems and Signal Processing*, 106, 284-302.
- Rituraj, and Vacca A. (2018), Modeling the Flow of Non-Newtonian Fluids Through Sharp Orifices, *Journal of Fluids Engineering*, 140(5), 054501.

Conference Publications

- Rituraj and Vacca A. (2019), Modelling and validation of tooth tip leakages in gerotor pumps, *ASME-JSME-KSME 2019 8th Joint Fluids Engineering Conference*, San Francisco, USA.

- Rituraj, Ransegnola T. and Vacca A. (2018), An Investigation on the Leakage Flow and Instantaneous Tooth Space Pressure in External Gear Machines, *Global Fluid Power Society (GFPS) PhD Symposium*, Samara, Russia.

VITA

VITA

Rituraj grew up in Ranchi, India. He received his Bachelor of Technology degree from Indian Institute of Technology (IIT) Guwahati in 2013. After working in industry for couple of years, he moved to United States in 2015 and joined Maha Fluid Power Research Center at Purdue University for his direct PhD study under Prof. Andrea Vacca. His research during his PhD study was on the numerical modelling of external gear machines with specific focus on key flow and geometric aspects. His research resulted in the publication of several papers in international journals and conferences. His research interests through graduate work and beyond include numerical modelling and experimental analysis of hydraulic components and systems.